The non-resonant streaming instability : from theory to experiment

Alexis Marret

PSL UNIVERSITÉ PARIS

THÈSE DE DOCTORAT

DE L'UNIVERSITÉ PSL

Préparée à l'Observatoire de Paris

L'instabilité non-résonnante de dérive : de la théorie à l'expérience

The non-resonant streaming instability: from theory to experiments

Soutenue par

Alexis MARRET

Le 15 Novembre 2021

École doctorale n°127

Astronomie et Astrophysique d'Ile de France

Spécialité

Astronomie et Astrophysique

Composition du jury :

Laurence REZEAU, Professeur Laboratoire LPP, Ecole polytechnique	*Présidente*
Anatoly SPITKOVSKY, Professeur Dep. of Astrophysical Sciences, Princeton Univ.	*Rapporteur*
Emmanuel D'HUMIÈRES, Professeur Université de Bordeaux	*Rapporteur*
Nuno LOUREIRO, Professeur Dep. of Nuclear Science & Engineering, MIT	*Examinateur*
Fabien CASSE, Professeur Laboratoire AstroParticule & Cosmologie	*Examinateur*
Katia FERRIÈRE, Directrice de recherche Lab. IRAP, Université Toulouse-III-Paul-Sabatier	*Examinatrice*
Andrea CIARDI, Maître de conférences Laboratoire LERMA, Observatoire de Paris	*Directeur de thèse*
Roch SMETS, Maître de conférences Laboratoire LPP, Ecole Polytechnique	*Directeur de thèse*
Julien FUCHS, Directeur de recherche Laboratoire LULI, Ecole Polytechnique	*Invité*

l'Observatoire de Paris | PSL

Remerciements

Cette thèse m'a énormément apporté, sur le plan scientifique bien sûr, mais également sur le plan personnel.

Je voudrais tout d'abord remercier Andrea Ciardi, pour m'avoir encouragé à aller toujours plus loin. Je suis heureux d'avoir eu la chance de pouvoir apprendre de ses extraordinaires qualités scientifiques et humaines pendant plus de trois ans. Roch Smets, également, pour son encadrement ainsi que son aide précieuse, et pour avoir répondu inlassablement à mes nombreuses questions. Je remercie Julien Fuchs de m'avoir fait confiance depuis le début.

Merci à vous, Franck, Weipeng et Konstantin, pour votre bonne humeur et pour les discussions toujours enrichissantes. La recherche scientifique internationale, c'est aussi les moments d'échange en anglais autour d'une pizza italienne partagée entre un Français, un Chinois et un Russe.

Merci à Quentin pour les tranches de rire, qui aurait cru qu'un cours sur les champignons puisse être aussi amusant. Un grand merci à Céline, pour son soutien envers et contre tout.

Mes derniers remerciements vont à ma famille, et plus particulièrement à mon père, à ma mère, et à mon frère. Je ne serais jamais arrivé jusqu'ici sans vous. Merci pour votre amour et votre patience inépuisable.

Paris, 2021

Abstract

Cosmic rays can power the exponential growth of a seed magnetic field by exciting instabilities that feed on the kinetic energy of the particles collective streaming motion. Of the different streaming instabilities, the non-resonant mode, also called Bell's mode, has received growing attention as it can amplify the magnetic field well beyond its initial intensity, and generate the necessary turbulence to help confine and accelerate cosmic rays in supernovae remnants and young stellar jets shocks via the first order Fermi mechanism. In general, it can develop in a large variety of environments, ranging from the cold and dense molecular clouds to the hot and diffuse intergalactic medium.

This work aims at elucidating the behaviour of the non-resonant cosmic rays streaming instability in such environments, where thermal and collisional effects can substantially modify its growth and saturation. In the first part of this thesis, we describe the instability within fluid theory by highlighting the basic physical mechanism leading to the exponential amplification of electromagnetic perturbations, and obtain analytical predictions for the growth rate for arbitrary ion elements. Owing to its non-resonant nature, a fluid description is a sufficiently accurate model of the instability only when the background plasma temperature is negligible. To study the instability in hot environments, where finite Larmor radius effects are important, we then resort to linear kinetic theory and extend the existing analytical results to the case of demagnetized ions. We find that the unstable wavelengths are not entirely suppressed, but are instead shifted toward larger scales with a strongly reduced growth rate.

The linear theory results are confirmed, and extended to the non-linear evolution in the second part of the thesis, by multi-dimensional hybrid-Particle-In-Cell simulations (kinetic ions and fluid electrons). The simulations highlight an important reduction of the level of magnetic field amplification in the hot regime [Marret et al. MNRAS 2021], indicating that it may be limited in hot astrophysical plasmas such as in superbubbles or the intergalactic medium. In colder and denser environments, such as H II regions and molecular clouds, particle collisions in the background plasma must be taken into account. We investigate numerically their impact by including Monte-Carlo Coulomb and neutral collisions in the simulations. We find that in poorly ionized plasmas, where proton-hydrogen collisions dominate, the instability is rapidly suppressed and our results from kinetic simulations confirm quantitatively existing, multi-fluid linear theory calculations. In contrast, we find that in fully ionized plasmas, Coulomb collisions unexpectedly favour the development of the instability by reducing self-generated pressure anisotropies that would otherwise oppose its growth.

Numerical simulations are currently the only means to investigate the non-linear evolution of the instability and to obtain quantitative estimates of the saturated magnetic field intensity. The final part of this thesis is devoted to answer the growing need for an experimental verification of the linear theory and simulations predictions. We describe the requirements on the plasma parameters to generate the instability in an experiment, and propose two possible setups based on existing high-power laser facilities, aiming at observing and characterizing the non-resonant mode for the first time in the laboratory.

Résumé

Les rayons cosmiques peuvent alimenter la croissance exponentielle d'un champ magnétique préexistant en déclenchant des instabilités qui grandissent grâce au mouvement de dérive collectif des particules. Parmi les différentes instabilités de dérive, le mode non-résonnant, aussi appelé mode de Bell, a fait l'objet d'une attention croissante car il peut amplifier le champ magnétique au-delà de son intensité initiale, et génère la turbulence nécessaire pour aider au confinement et à à accélération des rayons cosmiques. De manière générale, il peut se développer dans une grande variété d'environnements, allant des nuages moléculaires froids et denses au milieu intergalactique chaud et diffus.

Ce travail vise à élucider le comportement de l'instabilité non-résonante de dérives des rayons cosmiques dans de tels environnements, où les effets thermiques et collisionnels peuvent modifier considérablement sa croissance et sa saturation. Nous décrivons d'abord l'instabilité dans le cadre de la théorie fluide en mettant l'accent sur le mécanisme physique conduisant à l'amplification exponentielle des perturbations électromagnétiques, et obtenons des prédictions analytiques du taux de croissance pour des éléments ioniques arbitraires. En raison de sa nature non-résonante, une description fluide est suffisante pour saisir les principales caractéristiques de l'instabilité lorsque la température du plasma ambiant est négligeable. Pour étudier l'instabilité dans les environnements chauds, où les effets du rayon de Larmor fini sont importants, nous recourons à la théorie cinétique linéaire et étendons les résultats analytiques existants au cas d'ions découplés des perturbations magnétiques. Nous obtenons que les longueurs d'onde instables ne sont pas entièrement supprimées, mais sont plutôt déplacées vers des échelles plus grandes avec un taux de croissance fortement réduit.

Les résultats de la théorie linéaire sont confirmés, et étendus à l'évolution non-linéaire dans la deuxième partie de cette thèse, par des simulations multi-dimensionnelles hybrides de type "particle in cell" (ions cinétiques et électrons fluides). Les simulations mettent en évidence une réduction importante du niveau d'amplification du champ magnétique dans le régime chaud [Marret et al. MNRAS 2021], ce qui indique qu'il peut être limité dans les plasmas astrophysiques chauds tels que les superbulles ou le milieu intergalactique. Dans les environnements plus froids et plus denses, comme les régions H II et les nuages moléculaires, les collisions entre particules dans le plasma ambiant doivent être prises en compte. Nous étudions numériquement leur impact en incluant dans les simulations avec une méthode Monte-Carlo les collisions proton-proton et proton-hydrogène. Nous obtenons que l'instabilité est rapidement supprimée dans les plasmas faiblement ionisés, où les collisions proton-hydrogène dominent. Ces résultats de simulations cinétiques confirment quantitativement les calculs existants de la théorie linéaire multifluide. En revanche, nous constatons que les collisions coulombiennes favorisent de manière inattendue le développement de l'instabilité dans les plasmas entièrement ionisés, en réduisant des anisotropies de pression auto-générées qui autrement s'opposeraient à sa croissance.

Les simulations numériques sont actuellement le seul moyen d'étudier l'évolution non-linéaire de l'instabilité et d'obtenir des estimations quantitatives de l'intensité du champ magnétique après saturation. La dernière partie de cette thèse est consacrée à la conception d'expériences dédiées à la vérification des prédictions de la théorie linéaire et des simulations. Nous décrivons les conditions requises sur les paramètres du plasma pour générer l'instabilité dans une expérience, et proposons deux configurations possibles basées

sur les installations laser haute puissance existantes, en visant à observer et caractériser le mode non-résonant pour la première fois en laboratoire.

Table of contents

Chapter 1

Introduction

Contents

1.1 Context

This thesis constitutes a new contribution to the vast field of instabilities in plasma physics. Plasmas represent the majority of the matter visible in the Universe, from the auroras on Earth to the interstellar clouds illuminated by nearby stars. The charged particles that form the plasma state are characterised by collective motions mediated by the electromagnetic field, which lead to an extraordinary wealth of phenomena. Among these, plasma instabilities play an important role in numerous astrophysical environments as they can efficiently redistribute the energy between the fields and the ionized particles. This is of particular importance for the acceleration and transport of cosmic rays, in the Galaxy and beyond.

Cosmic rays are charged particles which propagate in space at velocities close to the speed of light. Despite the historical appellation of "rays", they are not electromagnetic radiation, but mainly constituted of protons with a small fraction of heavier elements, of positrons and of electrons. The first detection of cosmic rays dates back to balloon experiments led by Victor Hess in 1912, and significant progress have been made since in the detection techniques and instruments both on Earth and with satellites. The observations have unveiled that cosmic rays originating from outside the solar system cover a large range of energies, from tens of MeV up to ultra-high energies above 10^{11} GeV. The cosmic rays energy spectrum is shown in Fig. 1.1. It follows a power law, with varying index depending on the energy, as $E^{-2.7}$ from the GeV to the PeV (10^6 GeV, Hillas [1984]), and steepens at a few PeV corresponding to the so-called "knee" of the cosmic rays spectrum. It then flattens in the range of 10^{11} GeV, corresponding to the "ankle", and terminates at 10^{13} GeV (Cronin [2005]).

Understanding the acceleration and the transport of the cosmic rays is a central question in astrophysics, as they contain an important fraction of the energy released in supernovas (Helder et al. [2012]), and contribute as much as the magnetic field and

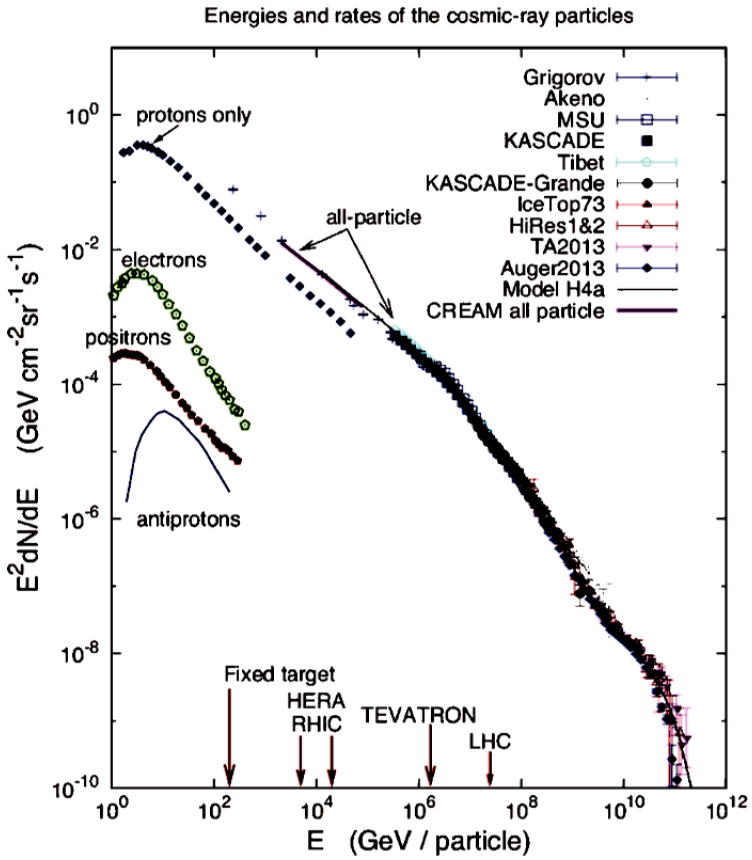

Figure 1.1: Observed cosmic rays spectrum as from Blasi [2014], compiled from different instruments. The arrows on the abscissa indicate energies reachable in various experimental devices.

the thermal gas pressure to the total energy density in our galaxy (Enßlin, T. A. et al. [2007]). They are also a source of ionization by collisions with the ambient medium in opaque molecular clouds where the electromagnetic radiations cannot penetrate, allowing a rich chemistry in the center of the clouds (Padovani et al. [2009], Aladro et al. [2013]). Cosmic rays can be of galactic or extra-galactic origin, depending on their Larmor radius, expressed as $r_L = E_{\mathrm{PeV}}/B_{\mu G}$ (in parsec) where E_{PeV} is the particle energy in PeV and $B_{\mu G}$ the magnetic field in μG. It is commonly assumed that the most energetic particles with energies well above 10^4 PeV must originate from extra-galactic sources (for a recent review see Drury [2012]). Indeed such high energy cosmic rays have a Larmor radius larger than 10^4 parsecs for a typical interstellar medium magnetic field of 1 μG, which is comparable to the size of the Milky Way, whose diameter is of the order of 3×10^4 parsec, and thus cannot be confined locally. In contrast lower energy particles, referred as galactic cosmic rays, are assumed to originate from local sources. Since they are confined by the galactic magnetic field, the particles below the knee propagate in the interstellar medium diffusively (Amato [2014]), such that their exact source cannot be inferred directly from their direction of propagation when arriving on Earth. The acceleration of particles can nevertheless be observed indirectly, by studying the gamma-rays emitted either by the decay of neutral pions created in collisions of cosmic ray protons with the ambient gas, or by inverse-Compton scattering of cosmic microwave background photons off the accelerated

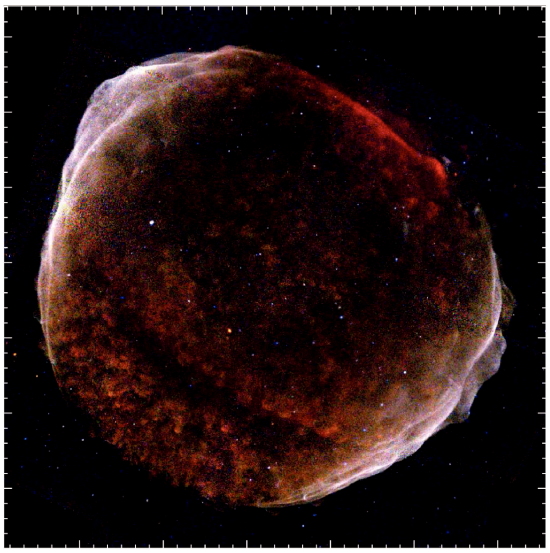

Figure 1.2: Image of SN 1006 seen in X-rays (Winkler et al. [2014]). Low ($0.5 - 1.2$ keV), medium ($1.2 - 2.0$ keV), and higher energy ($2.0 - 7.0$ keV) X-rays are colored red, green, and blue respectively.

electrons (Stage et al. [2006]). The accelerated electrons can also be detected indirectly via the X-rays synchrotron emission they produce (Koyama et al. [1995], Favata et al. [1997], Allen et al. [1997], Berezhko and Völk [2004]). As the electromagnetic radiations trajectory is not modified by the ambient magnetic field, their origin can be retraced and allows to identify possible sources of cosmic rays (Hona [2021]).

Among the observed sources of cosmic rays, the shocks of supernova remnants colliding with their surrounding ambient medium are believed to be very efficient galactic cosmic rays accelerators. A classical example of such supernova remnant is SN 1006. Located over 2 kiloparsecs from the Earth and aged of 1 kiloyear, it expands radially at velocities of the order of 3000 km.s^{-1}. An image of the remnant is shown in Fig. 1.2 in X-rays as seen by the Chandra space telescope (Winkler et al. [2014]). The emission of high energy X-rays follows a polar distribution (North West-South East), indicating the acceleration of electrons, and potentially of ions, in specific regions of the supernova remnant. The acceleration of particles at supernova shocks may be achieved through a process known as First Order Fermi acceleration, also called diffusive shock acceleration (e.g. Amato [2014]). Under this acceleration scheme, the particles are assumed to be confined by a turbulent magnetic field at the shock. As they bounce back and forth diffusively in the downstream and upstream regions, the particles gain energy at each crossing and eventually reach high energies from multiple re-accelerations. In addition, it was shown with large scale numerical simulations of shocks, that the acceleration of cosmic rays to high energies requires an ambient magnetic field parallel to the shock normal (Caprioli and Spitkovsky [2014]). This could explain the polar distribution of X-ray radiations observed in SN 1006, corresponding to an ambient magnetic field aligned with the North West-South East direction and allowing the acceleration of particles via diffusive shock acceleration in these regions (Schneiter et al. [2015]). An upper limit for the maximum energy reachable can be found by considering the rate at which cosmic rays cross a supernova shock and the acceleration time as a function of the shock precursor size and shock velocity (Bell [2013]),

which yields:

$$E_{\max} = 10^{14} \frac{r_g}{\lambda} B_{\mu G} \tau_{1000} u_7^2 \tag{1.1}$$

where $E_{\max}$ is in eV, r_L and λ are the Larmor radius and scattering mean free path of the cosmic ray respectively, u_7 is the shock velocity in units of 10^7 m.s^{-1} and τ_{1000} is the age of the supernova remnant in kiloyears. The most favorable assumption is to suppose $\lambda = r_g$, corresponding to the Bohm diffusion regime (Stage et al. [2006], Shalchi [2010]). Considering $u_7 = 0.3$, $B_{\mu G} = 1$ and $\tau_{1000} = 1$ as in the case of SN 1006 (Winkler et al. [2014]), one obtains a maximum energy $E_{\max} \sim 10^{13}$ eV, much smaller than the knee at 10^{15} eV. These, and similar estimates, show that if cosmic rays are to be accelerated to high energies via the First Order Fermi process, then the turbulent magnetic field at the shock front needs to be amplified, by more than one order of magnitude with respect to the typical interstellar magnetic field intensity $B \sim \mu G$.

In this direction, the ion streaming instabilities constitute a promising candidate to produce the necessary amplification of the magnetic field, by converting the drift kinetic energy of the cosmic rays crossing the shock front and leaking in the ambient medium into magnetic energy. These plasma instabilities develop when a population of energetic ions, such as cosmic rays, drifts at super-Alfvénic speeds in a background plasma permeated by a magnetic field (Kulsrud and Pearce [1969], Winske and Leroy [1984], Bell [2004], Amato and Blasi [2009]). The collective drifting motion of these energetic particles is thought to drive the exponential growth of electromagnetic perturbations in many space (Gary [1991]) and astrophysical (Völk et al. [2005], Cui et al. [2016]) plasmas. Depending on the plasma conditions, three different modes exist (Gary et al. [1984]): two of them rely on resonant particle-wave interactions, referred to as right-hand and left-hand resonant modes, while the third mode is instead non-resonant and its importance was recognized in early work on the Earth's ion-foreshock (Sentman et al. [1981], Onsager et al. [1991], Akimoto et al. [1993]). The non-resonant mode, also called Bell's mode in the astrophysics literature, has become central to the diffusive acceleration of cosmic rays in supernovae remnants shocks. This mode is thought to be able to amplify the magnetic field to values much larger than the ambient magnetic field, sufficiently to allow the acceleration of cosmic rays to PeV energies (Bell [2004], Amato and Blasi [2009]). This is in contrast to the two resonant modes which are limited to a magnetic field amplification lower than the ambient magnetic field (Bell [2013]). However, potentially important damping mechanisms may also need to be taken into account when considering the level of magnetic field amplification generated by the non-resonant mode. These are related to the conditions of the environment where the shock is propagating, such as the ambient plasma temperature (Zweibel and Everett [2010]) or the relative drift and collisions (ambipolar diffusion) between ambient ions and neutrals (Reville et al. [2008]).

Indeed, the non-resonant mode is expected to develop in a large variety of environments, ranging from the cold and dense molecular clouds to the hot and diffuse intergalactic medium. In this context, this thesis aims at expanding our knowledge on the behaviour of the instability in these environment, and in particular to study the importance of thermal effects in hot environments such as in superbubbles, and the effects of collisions in the ambient plasma, with neutrals but also among charged particles. Collisions can be important in many environments, such as H II regions, molecular clouds, as well as in laboratory plasmas. This latter case is of particular interest. Indeed numerical simulations

are currently the only means to investigate the non-linear evolution of the instability and to obtain quantitative estimates of the saturated magnetic field intensity. There is consequently a growing need for an experimental verification of the predictions made by linear theory and simulations. Work in this direction has begun with the right-hand mode which was investigated in recent experiments on the Large Plasma Device (Heuer et al. [2018]). The non-resonant streaming instability has never been observed in the laboratory. Although the parameters required are potentially within the reach of high intensity laser experiments with tens of Tesla externally applied magnetic fields (Albertazzi et al. [2013], Ivanov et al. [2021]), the large streaming population densities, drift velocities and ambient magnetic field required, together with the lack of theoretical knowledge on the effects of particle collisions on the development of the instability, have made its experimental investigations elusive. The final part of this thesis is devoted to tackle this problematic.

The manuscript is organized in six main chapters, with a natural progression from the theoretical study of the non-resonant streaming instability, complemented with numerical simulations of its non-linear evolution, and a final part dedicated to the design of laboratory experiments. In Chapter 2, the instability is described within fluid theory to highlight the basic physical mechanism leading to the exponential amplification of electromagnetic perturbations. In that chapter analytical predictions for the growth rate for arbitrary ion elements are obtained for the first time. Although the effects of heavier ions may be considered only as corrections (the cosmic rays are essentially made of protons), in the astrophysical context helium is also present and can modify the instability. In addition, it is necessary to take into account heavy ions accelerated in supernova remnants to explain the observed abundances in the cosmic rays spectrum (Tatischeff et al. [2021]). In the context of laboratory experiments, heavy ions effects can also become important as elements such as carbon and argon are frequently used. Owing to its non-resonant nature, a fluid description is a sufficiently accurate model of the instability only when the background plasma temperature is negligible. In order to study the instability in hot environments, where finite Larmor radius effects are important, linear kinetic theory is applied to extend the existing analytical results to the case of demagnetized ions. This is presented in Chapter 3, where it is found that the instability is not entirely suppressed, but the unstable wavelengths are instead shifted toward larger scales with a strongly reduced growth rate. The linear theory results are confirmed, and extended to the non-linear evolution by multi-dimensional hybrid-Particle-In-Cell simulations (kinetic ions and fluid electrons). The code used is presented in Chapter 4, together with the algorithms, the normalizations, as well as the numerical implementation of particle collisions. The simulations results are then presented in Chapter 5 and show a large amplification of the magnetic field in the cold regime, which is a key property of the instability in the context of cosmic rays acceleration at shocks. The simulations also highlight an important reduction of the level of magnetic field amplification in the hot regime, indicating that it may be limited in hot astrophysical plasmas such as the intergalactic medium. In colder and denser environments, such as H II regions and molecular clouds, particle collisions in the background plasma must be taken into account. This is investigated numerically in Chapter 6 by including Monte-Carlo Coulomb and neutral collisions in the simulations. It is found that in poorly ionized plasmas, where neutral collisions dominate, the instability is rapidly suppressed and our results from kinetic simulations confirm quantitatively existing multi-fluid linear theory calculations. In contrast, the simulations results show that Coulomb collisions in a

fully ionized plasma unexpectedly favour the development of the instability, by reducing self-generated pressure anisotropies that would otherwise oppose its growth. Finally, Chapter 7 is devoted to answer the growing need for an experimental verification of the linear theory and of the simulations predictions. The aim is to observe and characterize the non-resonant mode for the first time in the laboratory. In that respect, the stringent requirements placed on the laboratory plasma conditions to accommodate the instability are investigated and detailed. These requirements necessarily have to take into account the effects of finite temperature and particle collisions, studied and highlighted in the first part of this thesis. Finally, two possible setups which may be conducted on existing high-power laser facilities are proposed.

1.2 References

Akimoto, K., Winske, D., Gary, S. P., and Thomsen, M. F. (1993). Nonlinear evolution of electromagnetic ion beam instabilities. *Journal of Geophysical Research: Space Physics*, 98(A2):1419–1433.

Aladro, R., Viti, S., Bayet, E., and Riquelme, D. (2013). The influence of cosmic rays in the circumnuclear molecular gas of NGC 1068. *Astrophys. Space Sci. Proc.*, 34:21–27.

Albertazzi, B., Béard, J., Ciardi, A., Vinci, T., Albrecht, J., Billette, J., Burris-Mog, T., Chen, S. N., Da Silva, D., Dittrich, S., Herrmannsdörfer, T., Hirardin, B., Kroll, F., Nakatsutsumi, M., Nitsche, S., Riconda, C., Romagnagni, L., Schlenvoigt, H.-P., Simond, S., Veuillot, E., Cowan, T. E., Portugall, O., Pépin, H., and Fuchs, J. (2013). Production of large volume, strongly magnetized laser-produced plasmas by use of pulsed external magnetic fields. *Review of Scientific Instruments*, 84(4):043505.

Allen, G. E., Keohane, J. W., Gotthelf, E. V., Petre, R., Jahoda, K., Rothschild, R. E., Lingenfelter, R. E., Heindl, W. A., Marsden, D., Gruber, D. E., Pelling, M. R., and Blanco, P. R. (1997). Evidence of X-Ray Synchrotron Emission from Electrons Accelerated to 40 TeV in the Supernova Remnant Cassiopeia A. *ApJ*, 487(1):L97.

Amato, E. (2014). The origin of galactic cosmic rays. *International Journal of Modern Physics D*, 23(07):1430013.

Amato, E. and Blasi, P. (2009). A kinetic approach to cosmic-ray-induced streaming instability at supernova shocks. *Mon Not R Astron Soc*, 392(4):1591–1600.

Bell, A. R. (2004). Turbulent amplification of magnetic field and diffusive shock acceleration of cosmic rays. *Mon Not R Astron Soc*, 353(2):550–558.

Bell, A. R. (2013). Cosmic ray acceleration. *Astroparticle Physics*, 43:56–70.

Berezhko, E. G. and Völk, H. J. (2004). Direct evidence of efficient cosmic ray acceleration and magnetic field amplification in Cassiopeia A. *A&A*, 419(3):L27–L30.

Blasi, P. (2014). Recent developments in cosmic ray physics. *Nuclear Physics B - Proceedings Supplements*, 256–257:36–47.

Caprioli, D. and Spitkovsky, A. (2014). Simulations of ion acceleration at non-relativistic shocks. II. Magnetic field amplification. *The Astrophysical Journal*, 794(1):46.

Cronin, J. W. (2005). The highest-energy cosmic rays. *Nuclear Physics B - Proceedings Supplements*, 138:465–491.

Cui, Y., Pühlhofer, G., and Santangelo, A. (2016). A young supernova remnant illuminating nearby molecular clouds with cosmic rays. *A&A*, 591:A68.

Drury, L. O. (2012). Origin of cosmic rays. *Astroparticle Physics*, 39–40:52–60.

Enßlin, T. A., Pfrommer, C., Springel, V., and Jubelgas, M. (2007). Cosmic ray physics in calculations of cosmological structure formation. *antike und abendland*, 473(1):41–57.

Favata, F., Vink, J., dal Fiume, D., Parmar, A. N., Santangelo, A., Mineo, T., Preite-Martinez, A., Kaastra, J. S., and Bleeker, J. a. M. (1997). The broad-band X-ray spectrum of the CAS A supernova remnant as seen by the BeppoSAX observatory. *Astronomy and Astrophysics*, 324:L49–L52.

Gary, S. P. (1991). Electromagnetic Ion / Ion Instabilities and Their Consequences in Space Plasmas - a Review. *Space Science Reviews*, 56(3-4):373.

Gary, S. P., Smith, C. W., Lee, M. A., Goldstein, M. L., and Forslund, D. W. (1984). Electromagnetic ion beam instabilities. *The Physics of Fluids*, 27(7):1852–1862.

Helder, E., Vink, J., Bykov, A., Ohira, Y., Raymond, J., and Terrier, R. (2012). Observational signatures of particle acceleration in supernova remnants. *Space Science Reviews*, 173.

Heuer, P. V., Weidl, M. S., Dorst, R. S., Schaeffer, D. B., Bondarenko, A. S., Tripathi, S. K. P., Van Compernolle, B., Vincena, S., Constantin, C. G., Niemann, C., and Winske, D. (2018). Observations of a field-aligned ion/ion-beam instability in a magnetized laboratory plasma. *Physics of Plasmas*, 25:032104.

Hillas, A. M. (1984). The origin of ultra-high-energy cosmic rays. *Annual Review of Astronomy and Astrophysics*, 22(1):425–444.

Hona, B. (2021). Particle acceleration in the cygnus superbubble. *arXiv e-prints*, page arXiv:2108.09348.

Ivanov, V. V., Maximov, A. V., Betti, R., Leal, L. S., Moody, J. D., Swanson, K. J., and Huerta, N. A. (2021). Generation of strong magnetic fields for magnetized plasma experiments at the 1-MA pulsed power machine. *Matter and Radiation at Extremes*, 6(4):046901.

Koyama, K., Petre, R., Gotthelf, E. V., Hwang, U., Matsuura, M., Ozaki, M., and Holt, S. S. (1995). Evidence for shock acceleration of high-energy electrons in the supernova remnant SN1006. *Nature*, 378(6554):255–258.

Kulsrud, R. and Pearce, W. P. (1969). The Effect of Wave-Particle Interactions on the Propagation of Cosmic Rays. *ApJ*, 156:445.

Onsager, T. G., Winske, D., and Thomsen, M. F. (1991). Interaction of a finite-length ion beam with a background plasma: Reflected ions at the quasi-parallel bow shock. *Journal of Geophysical Research: Space Physics*, 96(A2):1775–1788.

Padovani, M., Galli, D., and Glassgold, A. E. (2009). Cosmic-ray ionization of molecular clouds. *A&A*, 501(2):619–631.

Reville, B., Kirk, J. G., Duffy, P., and O'Sullivan, S. (2008). Environmental limits on the nonresonant cosmic-ray current-driven instability. *International Journal of Modern Physics D*, 17(10):1795–1801.

Schneiter, E. M., Velázquez, P. F., Reynoso, E. M., Esquivel, A., and De Colle, F. (2015). 3D MHD simulation of polarized emission in SN 1006. 449(1):88–93.

Sentman, D. D., Edmiston, J. P., and Frank, L. A. (1981). Instabilities of low frequency, parallel propagating electromagnetic waves in the Earth's foreshock region. *Journal of Geophysical Research: Space Physics*, 86(A9):7487–7497.

Shalchi, A. (2010). Diffusive shock acceleration in supernova remnants: On the validity of the Bohm limit. *Astroparticle Physics*, 31(3):237.

Stage, M., Allen, G., Houck, J., and Davis, J. (2006). Cosmic ray diffusion near the Bohm limit in the Cassiopeia A supernova remnant. *Nature Physics*, 2.

Tatischeff, V., Raymond, J. C., Duprat, J., Gabici, S., and Recchia, S. (2021). The origin of galactic cosmic rays as revealed by their composition. *arXiv e-prints*, page arXiv:2106.15581.

Völk, H. J., Berezhko, E. G., and Ksenofontov, L. T. (2005). Magnetic field amplification in Tycho and other shell-type supernova remnants. *Astronomy & Astrophysics*, 433(1):229–240.

Winkler, P. F., Williams, B. J., Reynolds, S. P., Petre, R., Long, K. S., Katsuda, S., and Hwang, U. (2014). A high-resolution x-ray and optical study of SN 1006: Asymmetric expansion and small-scale structure in a type Ia supernova remnant. *ApJ*, 781(2):65.

Winske, D. and Leroy, M. M. (1984). Diffuse ions produced by electromagnetic ion beam instabilities. *Journal of Geophysical Research: Space Physics*, 89(A5):2673–2688.

Zweibel, E. G. and Everett, J. E. (2010). Environments for Magnetic Field Amplification by Cosmic Rays. *The Astrophysical Journal*, 709(2):1412–1419.

Chapter 2

Fluid description of the instability

Contents

2.1 Introduction

The streaming instabilities can develop when a background plasma is traversed by a population of energetic ions with a drift velocity aligned with an ambient magnetic field, leading to the exponential growth of magnetohydrodynamic-like waves, generated at the expense of the bulk kinetic energy of the streaming particles. Depending on their drift velocity and velocity dispersion, three distinct modes can be excited. In general they grow for streaming velocities larger than the Alfvén speed, have a growth time of the order of the ion cyclotron time, and can potentially coexist and compete in their growth. The right-hand resonant mode (Gary et al. [1984]) requires a small streaming and thermal velocity and is characterized by magnetic fluctuations with right-hand polarisation. The left-hand resonant mode requires low streaming velocity and large velocity dispersion, and is left-hand polarized. This mode can strongly modify the propagation of cosmic rays by producing magnetic turbulence on scales comparable to the particles Larmor radius, and resulting in an important scattering (Kulsrud and Pearce [1969]). Finally the non-resonant mode is right-hand polarized, requires a large drift velocity and its growth is not associated with cyclotron resonances as for the other two modes. This non-resonant mode will be the focus of this thesis. It was first investigated in the context of back-streaming ions from the Earth's bow shock to the foreshock region using a kinetic description (Sentman et al. [1981], Winske and Leroy [1984]), but was not further studied for twenty years after these pioneering publications. The instability was later rederived within a fluid framework

(Bell [2004]) and applied to the amplification of magnetic field at supernova shocks due to cosmic rays streaming in the interstellar medium.

This chapter is devoted to a theoretical study of the non-resonant streaming instability. The instability mechanism, as well as the growth rate and unstable wavelengths are calculated within the framework of fluid plasma theory, together with the energy exchange rates between the electromagnetic waves and the particles. These results are of particular importance as they constitute the fundamental characteristics of the unstable waves, and will be used as a basis in the following chapters to dimension and interpret the numerical simulations. The calculations will be performed while neglecting the gyro-radius of the particles, which is only valid when considering a cold and magnetized plasma. The effects of plasma temperature on the instability growth will be presented in Chapter 3.

2.2 Fluid model of the non-resonant mode

2.2.1 Equations of the fluid model

In the framework of fluid theory, each plasma components α can be described by the system of equations formed by the moments of the distribution function $f_\alpha(\mathbf{r}, \mathbf{v}, t)$, coupled to Maxwell's equations. The zeroth order moment equation may be calculated by multiplying the collisionless Vlasov equation by the mass of the population m_α and integrating over velocity space. This yields the equation of mass density conservation:

$$\frac{\partial \rho_\alpha}{\partial t} + \boldsymbol{\nabla} \cdot (\rho_\alpha \mathbf{u}_\alpha) = 0 \tag{2.1}$$

where $n_\alpha = \int_{-\infty}^{+\infty} f_\alpha \mathrm{d}\mathbf{v}$ is the plasma density, $\rho_\alpha = n_\alpha m_\alpha$ is the mass density and $\mathbf{u}_\alpha = \frac{1}{n_\alpha} \int_{-\infty}^{+\infty} \mathbf{v} f_\alpha \mathrm{d}\mathbf{v}$ is the fluid velocity. From this Eulerian equation, one finds that an explicit temporal variation of density is generated by spatial gradients of the mass flux. The first order moment equation can be calculated in a similar way by multiplying the Vlasov equation by $m_\alpha \mathbf{v}_\alpha$ and integrating over velocity space. One obtains the collisionless momentum density conservation equation as:

$$\frac{\partial \rho_\alpha \mathbf{u}_\alpha}{\partial t} + \mathbf{u}_\alpha \cdot \boldsymbol{\nabla}(\rho_\alpha \mathbf{u}_\alpha) = -\boldsymbol{\nabla} \cdot \mathbf{P}_\alpha + q_\alpha n_\alpha (\mathbf{E} + \mathbf{u}_\alpha \times \mathbf{B}) \tag{2.2}$$

where q_α is the charge of population α, and $\mathbf{P}_\alpha = m_\alpha \int_{-\infty}^{+\infty} (\mathbf{v} - \mathbf{u}_\alpha)(\mathbf{v} - \mathbf{u}_\alpha) f_\alpha \mathrm{d}\mathbf{v}$ is the pressure tensor. The third order moment may be obtained by multiplying the Vlasov equation by $m_\alpha \mathbf{v}\mathbf{v}$ and calculating the trace. This yields the total (kinetic and internal) energy conservation equation:

$$\frac{\partial}{\partial t}\left(\frac{\rho_\alpha u_\alpha^2}{2} + \rho_\alpha U_\alpha\right) + \boldsymbol{\nabla} \cdot \left(\left(\frac{\rho_\alpha u_\alpha^2}{2} + \rho_\alpha U_\alpha\right)\mathbf{u}_\alpha + \boldsymbol{\Phi}_\alpha\right) + \sum_k \sum_l \partial_k (P_{kl,\alpha} u_{l,\alpha}) - \mathbf{j}_\alpha \cdot \mathbf{E} = 0 \tag{2.3}$$

where $\rho_\alpha U_\alpha = \frac{3}{2} n_\alpha k_B T_\alpha$ with k_B the Boltzmann constant, $\boldsymbol{\Phi}_\alpha = \int_{-\infty}^{+\infty} f_\alpha \frac{m_\alpha v_\alpha^2}{2} \mathbf{v}_\alpha \mathrm{d}\mathbf{v}$ is the reduced heat flux, and $\mathbf{j}_\alpha = q_\alpha n_\alpha \mathbf{u}_\alpha$ is the current carried by the population α. These moments are exact equations, in the sense that they do not introduce additional approximations in the description of each plasma component with respect to the Vlasov

equation. Each equation depends on the next moment, forming an infinite hierarchy of equations. In order to obtain a finite system of equations one needs to introduce a closure relation. This is usually done for the second order moment by assuming a specific form of the pressure tensor. One simple approximation is the isothermal pressure assumption, where the plasma pressure is expressed as $P_\alpha = n_\alpha k_B T_0$ and T_0 is a constant and uniform temperature. This corresponds to the situation of a plasma population whose temperature is equilibrated with an external thermostat on time scales much shorter than the physics investigated, such that it is considered to remain constant during the plasma evolution. In the case of the solar wind for example, this is not a trivial assumption. Without any heating, the radial expansion of the solar wind should result in its cooling, in disagreement with satellites in-situ observations (Verscharen et al. [2019]). Another widely used approximation is the adiabatic assumption, corresponding to the opposite situation where no wave-particle energy exchange occur and the heat flux are supposed negligible on the time and spatial scales of interest. The pressure may then be expressed with the closure equation $\mathrm{d}(P_\alpha n_\alpha^{-\gamma})/\mathrm{d}t = 0$ where $\mathrm{d}/\mathrm{d}t$ is the material derivative and $\gamma = (N+2)/N$ with N the number of degrees of freedom of the system, i.e. $\gamma = 5/3$. More complex closure equations can be used, to take into account pressure anisotropies in the presence of a magnetic field (e.g. Hirabayashi et al. [2016]).

2.2.2 Modified single-fluid approach

Owing to it's non-resonant nature, the instability is not dependent at first order of the precise shape of the distribution functions of the electron and ion populations in the plasma (Gary et al. [1984]). In this case a fluid description of each population can prove sufficient to understand the instability mechanism, as well as obtain the growth rate and associated unstable wavenumbers. The fluid equations presented in Sec. 2.2.1 apply for each component of the plasma, which results in a complex system of equation, whose physics is not easily discerned. In order to simplify the problem, one may consider several populations as a single fluid by assuming that they follow the same dynamic. In this case the system of equations may be reduced, corresponding to the so-called single-fluid approach and which will be detailed in the following sections.

One can use a non-relativistic fluid approach to describe the non-resonant mode and calculate its characteristic spatial and temporal scale (Amato and Blasi [2009]). Several studies of the instability using fluid models exist in the literature (Bell [2004], Zirakashvili et al. [2008], Bai et al. [2015], Matthews et al. [2017], Mignone et al. [2018], van Marle et al. [2018]), and a similar approach will be adopted here, with a focus on the instability microphysics and mechanism. Consider the following situation: an initially uniform plasma made of main protons and electrons (noted with the subscripts "m" and "e" respectively) is embedded in a zeroth order magnetic field B_0, and traversed by a less dense population of super-Alfvénic streaming protons (noted with the subscript "cr" for cosmic rays) with a positive drift velocity in the main protons reference frame, parallel to the magnetic field. The calculation generalized to arbitrary elements is given in Appendix A, and has not been performed in the literature. Although the effects of heavier ions may be considered only as corrections (the cosmic rays are essentially made of protons), in the astrophysical context helium is also present and can modify the instability. In addition, it is necessary to take into account heavy ions accelerated in supernova remnants to explain the observed

abundances in the cosmic rays spectrum (see Tatischeff et al. [2021]). In the context of laboratory experiments, heavy ions effects can also become important as elements such as carbon and argon are frequently used. In the present section, this will be neglected for the clarity of the calculations, hence supposing a plasma made only of electrons and protons. In addition, the electrons will be supposed to follow closely the ion dynamic such that any effects due to charge separation and Hall effects are assumed negligible. The electron temperature will be assumed to be small, and the electron pressure gradients will be neglected. The plasma is supposed quasi-neutral:

$$-n_e + n_m = -n_{cr} \tag{2.4}$$

such that the background plasma (main protons and electrons) is electrically charged. The magnetic field evolution is calculated from Maxwell-Faraday's law:

$$\frac{\partial \mathbf{B}}{\partial t} = -\boldsymbol{\nabla} \times \mathbf{E} \tag{2.5}$$

and the total current from Maxwell-Ampère's law as:

$$\boldsymbol{\nabla} \times \mathbf{B} = \mu_0 e(-n_e \mathbf{u}_e + n_m \mathbf{u}_m + n_{cr} \mathbf{u}_{cr}) + \frac{1}{c^2} \frac{\partial \mathbf{E}}{\partial t} \tag{2.6}$$

where μ_0 is the magnetic permeability, e the elementary charge and c the speed of light. The ratio of the last term of the right-hand side, corresponding to the displacement current, to the curl of B while considering an Alfvénic fluctuation, yields a scaling as v_A^2/c^2 where v_A is the Alfvén speed. The transverse component of the displacement current will be neglected in the following calculations, hence considering a non-relativistic plasma with $v_A/c \ll 1$ and $\omega/k \ll 1$ where ω and k are the frequency and wavenumber respectively. This approximation is discussed in more details in Sec. 4.3.2. The total current is initially null: $\boldsymbol{\nabla} \times \mathbf{B}_0 = \mathbf{0}$, consistent with a homogeneous initial magnetic field. This is achieved by considering an initial drift velocity for the electron population relative to the main protons, in the same direction as the cosmic rays such that:

$$\mathbf{u}_e = \frac{n_{cr}}{n_m} \mathbf{u}_{cr} \tag{2.7}$$

A different way of compensating the current would be to distinguish two electrons populations: one with the same charge density as the main protons, and an additional population with the same charge density as the cosmic rays and drifting alongside them. Within the framework of kinetic theory, Amato and Blasi [2009] showed that the non-resonant mode can develop in both cases, and that the dispersion relation is only modified by a corrective term of the order $O(n_{cr}^2/n_m^2)$ depending on the choice to compensate the current. In this thesis only one population of electrons will be considered with a small density ratio n_{cr}/n_m such that the results may be applied to the case of two electron populations as well, similarly to previous studies (e.g. Winske and Leroy [1984], Reville et al. [2007]).

One may obtain the momentum density conservation equation for the background plasma by performing a summation of the main protons and electrons momentum conser-

vation equations (Eq. 2.2), and by using Ampère's law, which gives:

$$\rho\frac{\mathrm{d}\mathbf{u}}{\mathrm{d}t} = \frac{1}{\mu_0}(\nabla\times\mathbf{B})\times\mathbf{B} - \nabla\cdot\mathbf{P} - en_{cr}(\mathbf{E}+\mathbf{u}_{cr}\times\mathbf{B}) \tag{2.8}$$

where $\mathrm{d}/\mathrm{d}t = \partial/\partial t + \mathbf{u}\cdot\boldsymbol{\nabla}$ is the material derivative. The density, fluid velocity and total pressure tensor associated to the background plasma are defined as:

$$\mathbf{u} = \frac{\rho_e\mathbf{u}_e + \rho_m\mathbf{u}_m}{\rho_e+\rho_m} \tag{2.9}$$

$$\rho = \rho_e + \rho_m \tag{2.10}$$

$$P_{ij} = \sum_{\alpha=e,m} P_{ij,\alpha} \tag{2.11}$$

such that $\rho \approx \rho_m$. The first and second terms of the right hand side of Eq. 2.8 correspond to the Lorentz and pressure gradients forces classically obtained in the momentum conservation equation of an MHD fluid. The third term $-en_{cr}(\mathbf{E}+\mathbf{u}_{cr}\times\mathbf{B})$ expresses the interaction of the electrically charged background plasma with the electromagnetic field and with the cosmic rays population. The $-en_{cr}\mathbf{u}_{cr}\times\mathbf{B}$ term can be rewritten as a function of the electrons velocity using Eq. 2.7, such that the cosmic rays can be seen as interacting with the background plasma via the so-called electron return current they generate in the background plasma with the condition $\boldsymbol{\nabla}\times\mathbf{B}_0 = \mathbf{0}$. This interpretation however is valid only at early times, when the magnetic field perturbations are small such that the condition of a null total current is fulfilled. For late time evolution Eq. 2.7 does not hold, and the cosmic rays drift velocity is no longer directly correlated to the electrons drift velocity. The Lorentz force term $(\nabla\times\mathbf{B})\times\mathbf{B}/\mu_0$ which appears in Eq. 2.8 can be interpreted by decomposing the double cross product using vector calculus identities as follows:

$$\frac{1}{\mu_0}(\nabla\times\mathbf{B})\times\mathbf{B} = \frac{1}{\mu_0}\left[(\mathbf{B}\cdot\boldsymbol{\nabla})\mathbf{B} - (\boldsymbol{\nabla}\mathbf{B})\cdot\mathbf{B}\right] \tag{2.12}$$

where $(\boldsymbol{\nabla}\mathbf{B})_{ij} = \partial B_j/\partial x_i$. The first term of the right-hand side of Eq. 2.12 can be rewritten by considering the curvilinear coordinates s such that $\mathbf{n}/R = \mathrm{d}\mathbf{t}/\mathrm{d}s$, where $\mathbf{n}$ and $\mathbf{t}$ are the vector normal and tangent to the field line respectively, and R is the curvature radius, in the local plane where the curvature is defined.

$$\frac{1}{\mu_0}(\mathbf{B}\cdot\boldsymbol{\nabla})\mathbf{B} = \frac{1}{\mu_0}B\mathbf{t}\cdot\boldsymbol{\nabla}(B\mathbf{t}) \tag{2.13}$$

$$= \frac{B}{\mu_0}\left[\left(\frac{\partial B}{\partial s}\right)\mathbf{t} + \frac{\mathbf{n}}{R}B\right] \tag{2.14}$$

$$= \frac{1}{2\mu_0}\frac{\partial B^2}{\partial s}\mathbf{t} + \frac{B^2}{\mu_0}\frac{\mathbf{n}}{R} \tag{2.15}$$

The l component of the second term of the right-hand side of this equation can be written as:

$$\left(\frac{1}{\mu_0}(\boldsymbol{\nabla}\mathbf{B})\cdot\mathbf{B}\right)_l = \frac{1}{\mu_0}\sum_j \frac{\partial B_j}{\partial x_l}B_j \tag{2.16}$$

$$= \frac{1}{2\mu_0}\nabla_l B^2 \tag{2.17}$$

Using the gradient perpendicular to the magnetic field line $\boldsymbol{\nabla}_\perp = \boldsymbol{\nabla} - \mathbf{t}\,\partial/\partial s$, one obtains:

$$\frac{1}{\mu_0}(\nabla\times\mathbf{B})\times\mathbf{B} = -\boldsymbol{\nabla}_\perp\left(\frac{B^2}{2\mu_0}\right) + \frac{B^2}{\mu_0}\frac{\mathbf{n}}{R} \tag{2.18}$$

The first term corresponds to a gyrotropic magnetic pressure force perpendicular to the magnetic field line, the second one to a magnetic tension force which acts against the curvature of the magnetic field line, in the direction perpendicular to $\mathbf{B}$. This is of particular importance for the non-resonant mode, as small scales fluctuations can be stabilized by a strong magnetic field tension force.

Since the displacement current has been neglected, the electric field which appears in Eqs. 2.8 and 2.5 cannot be calculated from Maxwell-Ampère's equation. It cannot be obtained from Maxwell-Poisson's equation either, which only gives information on the electrostatic component. The electric field is instead obtained from Ohm's law, which can be derived as follows. Multiplying Eq. 2.2 by q_α/m_α, one obtains for the l component:

$$\frac{\partial j_{l,\alpha}}{\partial t} = n_\alpha\frac{q_\alpha^2}{m_\alpha}(\mathbf{E}+\mathbf{u}_\alpha\times\mathbf{B})_l - \sum_k \frac{q_\alpha}{m_\alpha}\frac{\partial P_{\alpha,kl}}{\partial x_k} - \sum_k \frac{\partial(n_\alpha q_\alpha u_{l,\alpha}u_{k,\alpha})}{\partial x_k} \tag{2.19}$$

Summing over the populations α and multiplying by $m_e/n_e e^2$:

$$\begin{aligned}\frac{m_e}{n_e e^2}\frac{\partial J_l}{\partial t} = &\left[1+\frac{m_e}{n_e e^2}\left(\frac{n_m q_m^2}{m_m}+\frac{n_{cr}q_{cr}^2}{m_{cr}}\right)\right]E_l \\ &+\left[\left(\mathbf{u}_e+\frac{m_e}{n_e e^2}\left(\frac{n_m q_m^2}{m_m}\mathbf{u}_m+\frac{n_{cr}q_{cr}^2}{m_{cr}}\mathbf{u}_{cr}\right)\right)\times\mathbf{B}\right]_l \\ &+\frac{1}{n_e e}\sum_k\frac{\partial P_{kl,e}}{\partial x_k} - \frac{m_e}{n_e e^2}\left[\frac{q_m}{m_m}\sum_k\frac{\partial P_{kl,m}}{\partial x_k}+\frac{q_{cr}}{m_{cr}}\sum_k\frac{\partial P_{kl,cr}}{\partial x_k}\right] \\ &-\frac{m_e}{n_e e^2}\sum_k\frac{\partial}{\partial x_k}\left(-n_e e u_{l,e}u_{k,e}+n_m q_m u_{l,m}u_{k,m}+n_{cr}q_{cr}u_{l,cr}u_{k,cr}\right)\end{aligned} \tag{2.20}$$

where $\mathbf{J} = n_m q_m\mathbf{u}_m + n_{cr}q_{cr}\mathbf{u}_{cr} + n_e e\mathbf{u}_e$ is the total current, $q_m = q_{cr} = e$ and $m_m = m_{cr} = m_p$. Considering $m_e/m_p \ll 1$ and neglecting the electron pressure gradients by supposing a negligible electron temperature, Ohm's law can be written as:

$$\mathbf{E} = \frac{\mathbf{J}\times\mathbf{B}}{en_e} - \mathbf{u}_m\times\mathbf{B} - \frac{n_{cr}}{n_m}\mathbf{u}_{cr}\times\mathbf{B} \tag{2.21}$$

Below the ion inertial length, the electron and ion dynamics can be partially decoupled, and the single fluid description becomes difficult to justify. If one supposes spatial scales above the inertial length, Ohm's law can be written while neglecting the Hall term $\mathbf{J}\times\mathbf{B}/en_e$.

Using $\mathbf{u}_m \times \mathbf{B} \approx \mathbf{u} \times \mathbf{B}$, one obtains:

$$\mathbf{E} = -\mathbf{u} \times \mathbf{B} - \frac{n_{cr}}{n_m}\mathbf{u}_{cr} \times \mathbf{B} \tag{2.22}$$

This equation corresponds to an ideal Ohm's law, augmented by an additional contribution due to the cosmic rays current, and has the interesting property that an induced electric field can exist in the reference frame of the background plasma. This is of particular importance in calculating the background plasma heating rate (see Sec. 2.2.4). Inserting Eq. 2.22 in Eqs. 2.8 and 2.5, and supposing an incompressible plasma such that $\boldsymbol{\nabla} \cdot \mathbf{u} = 0$ from Eq. 2.1, one obtains:

$$\frac{\mathrm{d}\mathbf{u}}{\mathrm{d}t} = \frac{1}{\mu_0 \rho}(\boldsymbol{\nabla} \times \mathbf{B}) \times \mathbf{B} - \frac{1}{\rho}\boldsymbol{\nabla} \cdot \mathbf{P} + \frac{n_{cr}}{n_m}\frac{e}{m_p}\mathbf{u} \times \mathbf{B} - \frac{1}{\rho}\mathbf{j}_{cr} \times \mathbf{B} \tag{2.23}$$

$$\frac{\partial \mathbf{B}}{\partial t} = [(\mathbf{B} \cdot \boldsymbol{\nabla})\mathbf{u} - (\mathbf{u} \cdot \boldsymbol{\nabla})\mathbf{B}] - \frac{1}{en_e}(\mathbf{j}_{cr} \cdot \boldsymbol{\nabla})\mathbf{B} \tag{2.24}$$

with $\mathbf{j}_{cr} = en_{cr}\mathbf{u}_{cr}$ the cosmic rays current, supposed constant. This assumption will be verified *a posteriori*. The assumption of an incompressible plasma is relevant to the study of electromagnetic perturbations, which verify the relation $\mathbf{k} \cdot \mathbf{E} = \mathbf{0}$ such that there is no electrostatic component and no density fluctuations. Although the background fluid pressure gradients do not appear in the calculation for transverse electromagnetic fluctuations, non-linear pressure gradients effects can nonetheless modify the growth of the non-resonant mode. This will be further investigated in Sec. 2.2.4. Eqs. 2.23 and 2.24 form a coupled non-linear system which describes the interaction between the electrically charged background plasma with the magnetic field, and will be the basis for the following analysis.

2.2.3 The mechanism of the non-resonant mode

A classical operation to study non-linear systems of equations is the linearization, where one expresses all the varying quantities as a sum of initial, zeroth order contributions, and first order, perturbed (or fluctuating) contributions. The second order terms are then neglected, allowing a clearer view of the early times evolution of the non-linear system. Linearizing Eqs. 2.23 and 2.24 yields:

$$\frac{\partial \mathbf{u}_1}{\partial t} = \frac{(\mathbf{B}_0 \cdot \boldsymbol{\nabla})\mathbf{B}_1}{\mu_0 \rho} + \frac{n_{cr}}{n_m}\Omega_0 \left(\mathbf{u}_1 \times \frac{\mathbf{B}_0}{B_0}\right) - \frac{1}{\rho}\mathbf{j}_{cr} \times \mathbf{B}_1 \tag{2.25}$$

$$\frac{\partial \mathbf{B}_1}{\partial t} + \frac{1}{en_e}(\mathbf{j}_{cr} \cdot \boldsymbol{\nabla})\mathbf{B}_1 = (\mathbf{B}_0 \cdot \boldsymbol{\nabla})\mathbf{u}_1 \tag{2.26}$$

where $\Omega_0 = eB_0/m_p$ is the proton cyclotron frequency, m_p is the proton mass and $\mathbf{j}_{cr}$ the constant, zeroth order proton cosmic rays current. The subscripts "0" and "1" refer to the order of the linearization. Many of the underlying features of the instability can be understood by inspecting these equations. The *first term* on the right hand-side of Eq. 2.25 is the magnetic tension force associated to the fluctuating magnetic field and dominates

	$v_\phi > 0$	$v_\phi < 0$
Positive helicity	Right polarization	Left polarization
Negative helicity	Left polarization	Right polarization

Table 2.1: Polarization and helicity of a circularly polarized electromagnetic wave as a function of the phase velocity $v_\phi = \omega_r/k$.

the background fluid dynamic at small enough scale. The *second term* is responsible for the cyclotron-like motion of the background fluid which occurs at a fraction of the cyclotron frequency. This motion is due to the ambient magnetic field, and to the background plasma excess of negative charge that compensates the cosmic rays charge. The *third term* is the source of the instability and drives growing background fluid velocity fluctuations via the interaction of the cosmic rays current with the fluctuating magnetic field. The linearized magnetic field induction equation (Eq. 2.26) has been rewritten to highlight its conservative character and the presence of a source term on the right-hand side, which is unchanged by the presence of cosmic rays and couples the background fluid velocity to the magnetic field fluctuations. The second term in the left-hand side of Eq. 2.26 can be rewritten as $-\boldsymbol{\nabla} \cdot (\mathbf{j}_{cr}\mathbf{B}_1/Q_e)$, corresponding to the advection of the magnetic field perturbation at a velocity $-j_{cr}/Q_e$, equal to the zeroth order electron drift velocity (Eq. 2.7).

The velocity perturbations will be taken of the form $\mathbf{u}_1 \mathrm{e}^{i(kx-\omega t)}$, and the magnetic field perturbations will be considered as propagating along the x direction aligned with the initial magnetic field such that $\mathbf{k} = k\mathbf{e}_x$ and $\mathbf{B} = B_0\mathbf{e}_x + \mathbf{B}_1\mathrm{e}^{i(kx-\omega t)}$. This corresponds to a circularly polarized, parallel propagating electromagnetic wave, which encompasses the non-resonant mode. The angular frequency is $\omega = \omega_r + i\gamma$ where ω_r is taken to be positive by convention, with γ the growth rate, and k the wave number which can be either positive or negative depending on the direction of propagation of the electromagnetic wave. The polarization of the wave is defined as the sense of rotation of the magnetic field in time, observed at a given position in space. The helicity is defined as the sense of rotation of the magnetic field in space, at a given time. Helicity and polarization are simply related in the case of plane wave through the direction of propagation $v_\phi = \omega/k$. Table 2.1 summarizes these properties of the circularly polarized waves.

One may pursue the analysis by noting that the fluid velocity and magnetic field perturbations in Eqs. 2.25 and 2.26 are coupled by only certain terms, which allows to distinguish coupling and non-coupling contributions. First, considering only the non-coupling terms (i.e. neglecting the first and third terms of Eq. 2.25 and the right-hand side of Eq. 2.26) one directly obtains a rotation of the background fluid at a frequency:

$$\omega_u = \frac{n_{cr}}{n_m}\Omega_0 \tag{2.27}$$

and a rotation of the magnetic field perturbation at a frequency:

$$\omega_r = -\frac{kj_{cr}}{en_e} \tag{2.28}$$

The wavenumber is negative to satisfy the convention $\omega_r \geq 0$, such that the mode is backward propagative. There is no instability, which is an expected result as the coupling terms have been neglected. Retaining only the coupling terms (i.e. neglecting the second term in the right-hand side of Eq. 2.25 and the second term in the left-hand side of Eq. 2.26) is equivalent to supposing fast growing modes, with a growth time much smaller than those associated to the perturbed magnetic field advection and to the background fluid cyclotron-like motion. In Fourier space the equations then become:

$$-i\omega\mathbf{u}_1 = i\frac{B_0 k}{\mu_0\rho}\mathbf{B}_1 - \frac{1}{\rho}\mathbf{j}_{cr}\times\mathbf{B}_1 \tag{2.29}$$

$$-i\omega\mathbf{B}_1 = iB_0 k\mathbf{u}_1 \tag{2.30}$$

Rewriting in terms of the components of the magnetic field perturbation yields:

$$i\frac{\omega^2}{B_0 k}B_{1y} = i\frac{B_0 k}{\mu_0\rho}B_{1y} + \frac{j_{cr}B_{1z}}{\rho} \tag{2.31}$$

$$i\frac{\omega^2}{B_0 k}B_{1z} = i\frac{B_0 k}{\mu_0\rho}B_{1z} - \frac{j_{cr}B_{1y}}{\rho} \tag{2.32}$$

By isolating ω one finds the dispersion relation of the non-resonant mode as:

$$\omega^2 = k^2 v_{A0}^2 \pm \frac{m_p}{e}\Omega_0\frac{k j_{cr}}{\rho} \tag{2.33}$$

with $v_{A0} = B_0/\sqrt{\mu_0\rho}$ where $\rho \approx n_m m_p$. The first term corresponds to the Alfvénic contribution, such that in the limit of zero cosmic rays current, one recovers the standard dispersion relation for Alfvén waves. This Alfvénic term can be seen as the effect of magnetic tension, which stabilizes the non-resonant mode at large wavenumbers when it is equal or greater to the magnetic force driving term. By considering a negative k, and choosing the negative sign solution in the second term (which corresponds to a left-hand polarized wave), one obtains a purely real angular frequency. In this case the only effect of the cosmic rays is to modify the dispersion relation of large wavelengths Alfvén waves. However choosing the positive sign solution (corresponding to a right-hand polarization), one obtains an instability for $|k| < k_{\max}$ with:

$$k_{\max} = \frac{n_{cr}}{n_m}\frac{u_{cr}}{v_{A0}^2}\Omega_0 \tag{2.34}$$

The growth rate $\gamma(k)$ may then be obtained in the form:

$$\gamma(k) = \sqrt{\alpha k + \beta k^2} \tag{2.35}$$

In the approximation of purely growing modes, i.e. $\gamma/\omega_r \gg 1$, an instability can also be obtained by considering k positive with a left-hand polarization such that the helicity remains negative. This is an important property of the non-resonant instability, which relies on the helical spatial structure of the electromagnetic and background fluid velocity fields to grow. Searching for an extremum of the growth rate yields the *fastest* growing

wavenumber:

$$k_{\text{fast}} = -\frac{\alpha}{2\beta} = -\frac{1}{2}\frac{n_{cr}}{n_m}\frac{u_{cr}}{v_{A0}^2}\Omega_0 \tag{2.36}$$

which is half of the *maximum* (largest) unstable wavenumber. This is the same result as those found in Winske and Leroy [1984] within kinetic theory and Bell [2004] within fluid theory. This expression shows that the wavenumber at which the instability grows depends linearly on the cosmic rays drift velocity. It also decreases linearly with the ambient magnetic field intensity, corresponding to the magnetic tension overcoming the cosmic rays magnetic force at larger scales when considering a stronger magnetic field. Inserting Eq. 2.36 in the growth rate expression, one obtains the growth rate for the fastest growing wavenumber as:

$$\gamma_{\text{fast}} = \frac{1}{2}\frac{n_{cr}}{n_m}\frac{u_{cr}}{v_{A0}}\Omega_0 \tag{2.37}$$

such that $\gamma_{\text{fast}} = k_{\text{fast}} v_{A0}$. Additionally, in the case of multiply charged ions with a low density ratio $n_{cr}/n_m \ll 1$, it can be shown (see Appendix A) that the fastest growth rate γ^i_{fast} and associated wavenumber k^i_{fast} are modified as:

$$\gamma^i_{\text{fast}} = \gamma_{\text{fast}}\frac{q_{cr}}{e}\left(\frac{m_p}{m_m}\right)^{1/2} \tag{2.38}$$

$$k^i_{\text{fast}} = k_{\text{fast}}\frac{q_{cr}}{e} \tag{2.39}$$

where q_{cr} and m_m are the cosmic rays charge and main ions mass respectively. In this case the growth rate increases linearly with the cosmic rays charge, and decreases with the square root of the main ions mass. It does not depend on the cosmic rays mass, nor on the main ions charge. One obtains the intuitive result that multiply charged drifting ions increase the effective magnetic force $-q_{cr}n_{cr}\mathbf{u}_{cr} \times \mathbf{B}$ driven by their current, which increases the growth rate and allows smaller scales to grow. Because of quasi-neutrality, the background ions charge does not play a role for the non-resonant mode growth rate, whereas the main ions mass introduces a larger inertia of the background fluid which opposes the growth of the instability. These results are not present in the literature, and may be important both for the acceleration of heavy elements at shocks (Tatischeff et al. [2021]), as well as for laboratory experiments. The effects of heavy ions will be further investigated in numerical simulations in Chapter 5.

The physical mechanism responsible for the instability can be better understood by considering large scales, in the range of wave numbers $|k| \ll k_{\max}$, where the contribution of the first term in the right-hand side of Eq. 2.25 corresponding to the magnetic tension can be neglected with respect to the cosmic rays magnetic force. The instability may then be described in the case of protons populations by the simplified system of equations:

$$\frac{\partial \mathbf{u}_1}{\partial t} = -\frac{1}{\rho}\mathbf{j}_{cr} \times \mathbf{B}_1 \tag{2.40}$$

$$\frac{\partial \mathbf{B}_1}{\partial t} = (\mathbf{B}_0 \cdot \boldsymbol{\nabla})\mathbf{u}_1 \tag{2.41}$$

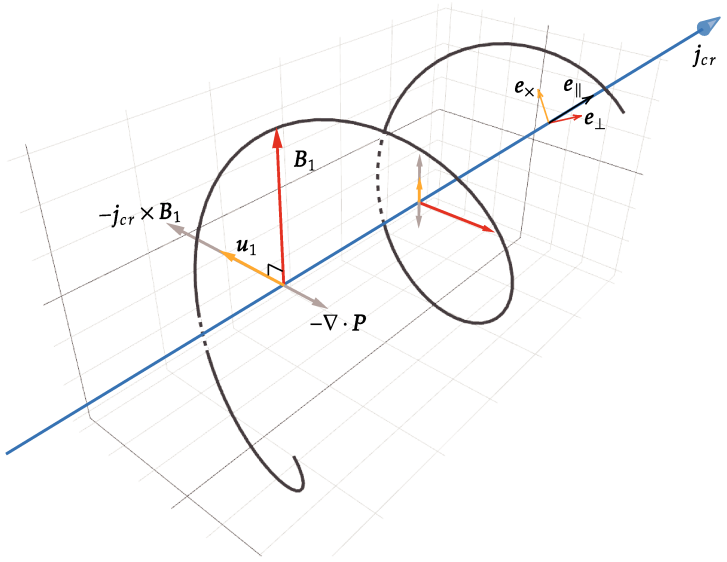

Figure 2.1: Schematic of the non-resonant instability. The initial magnetic field B_0 is parallel to the cosmic rays current j_{cr}. The black solid line illustrates the magnetic field spatial structure for a negative helicity wave. The instability is driven by the $-\mathbf{j}_{cr} \times \mathbf{B}_1$ force and is opposed by the background pressure gradients, which may be decomposed in a local magnetic field aligned basis $(\mathbf{e}_\parallel, \mathbf{e}_\times, \mathbf{e}_\perp)$ where $\mathbf{e}_\parallel \times \mathbf{B}_0 = \mathbf{0}$ and $\mathbf{e}_\perp \times \mathbf{B}_1 = \mathbf{0}$.

with $\rho \approx n_m m_p$ and $j_{cr} = e n_{cr} u_{cr}$. Eq. 2.40 does not include the magnetic tension which is the source of the Alfvén waves. As such, on large scales where the magnetic tension does not play a role, the non-resonant mode is a distinct wave mode and can no longer be considered as an alteration by cosmic rays of the classical Alfvén wave. The instability is driven by the protons cosmic ray current through the action of the magnetic force, $-\mathbf{j}_{cr} \times \mathbf{B}_1$ (Eq. 2.40), which produces fluid velocity fluctuations, $\mathbf{u}_1$, in the background plasma. The induced electric field, $-\mathbf{u}_1 \times \mathbf{B}_0$, feeds back and enhances the initial magnetic field perturbation B_1 via Faraday's law (Eq. 2.41). This increases the magnetic force, and closes the feedback loop of the instability. Solving Eqs. 2.40 and 2.41 in Fourier space, one obtains the growth rate $\gamma(k)$ varying as $k^{1/2}$:

$$\gamma(k) \approx \left(\frac{j_{cr}}{e n_m} |k| \Omega_0 \right)^{1/2} \tag{2.42}$$

By neglecting the magnetic tension, one finds from Eq. 2.40 that the field of velocity fluctuations grows in a direction perpendicular to the magnetic flucutation, i.e. with a phase shift of $-\pi/2$ with respect to the magnetic perturbation. This is shown in the schematic presented in Fig. 2.1. One obtains an helix spatial structure for both the velocity and the magnetic field along the initial magnetic field, aligned with the cosmic rays current. In the case where the Hall term $\mathbf{J} \times \mathbf{B}/e n_e$ in Eq. 2.21 is not negligible, then the electric field is induced by the electron fluid velocity which can be different from the background fluid velocity. In this case the induced magnetic field is not exactly perpendicular to the ion fluid velocity, and the instability growth is reduced, consistent with the results obtained in Zacharegkas et al. [2019]. Interestingly, this implies that one can expect a more efficient growth of the instability in pair plasmas, where the Hall effect

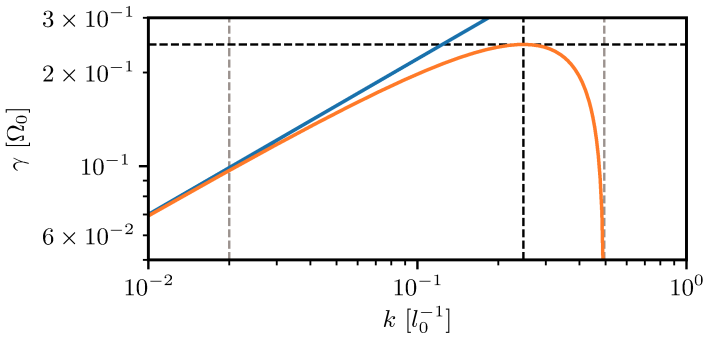

Figure 2.2: Growth rate $\gamma(k)$ (normalized to the proton cyclotron frequency Ω_0) as a function of the wavenumber k (normalized to the inverse proton inertial length $l_0^{-1} = (n_m e^2/\epsilon_0 m_p)^{-1/2}$ with ϵ_0 the dielectric permittivity) as from Eq. 2.33 (orange line) and in the long wavelength limit as from Eq. 2.42 (blue line), considering protons populations with a density ratio $n_{cr}/n_m = 0.01$ and a drift velocity $u_{cr}/v_{A0} = 50$. The right and left vertical dashed grey lines correspond to $k_{\max}$ and $k_{\min}$ respectively as from Eqs. 2.34 and 2.43. The vertical and horizontal dashed black lines correspond to the fastest growing k_{fast} and associated growth rate γ_{fast} respectively, as from Eqs. 2.36 and 2.37. For $k < k_{\min}$ the growth rate is not valid as the drift velocity perturbations should be taken into account in the dispersion relation.

is absent because of the equal positron and electron masses. This effect was confirmed by recent Particle in Cell numerical simulations of the instability (see Gupta et al. [2021]).

Given the important correlation between the magnetic field orientation and the local direction of acceleration of the plasma, a local magnetic field aligned basis $\mathbf{e}_{\parallel} = \frac{\mathbf{B}_0}{B_0}$ (parallel component), $\mathbf{e}_{\times} = \frac{\mathbf{B}_1}{B_1} \times \mathbf{e}_{\parallel}$ (normal component) and $\mathbf{e}_{\perp} = \mathbf{e}_{\parallel} \times \mathbf{e}_{\times}$ (perpendicular component, aligned with the perturbed magnetic field for an electromagnetic wave propagating along $\mathbf{B}_0$) can be used (see Fig. 2.1). This vector basis differs from the commonly used vector basis parallel and perpendicular to the *total* magnetic field. It is built to follow the local magnetic perturbation, such that the spatial average of any quantities on this frame of reference does not create any loss of information on the periodic space dependency of the wave. This basis will be used to analyse simulation results in the following chapters.

The growth rate of the non-resonant mode is shown in Fig. 2.2 as a function of the wavenumber k. One obtains a bell-shaped curve characteristic of the non-resonant mode such that small scales perturbations grow faster than large scales, with a sharp cut-off for $k > k_{\max}$. In addition to the upper limit on the unstable wavenumbers imposed by the magnetic tension force, the growth of the instability is also constrained at small wavenumbers. A lower limit for the unstable wavenumbers can be obtained by considering the time $(|k|u_{cr})^{-1}$ for cosmic rays to cross one wavelength (Bell [2004]), which has to be smaller than the cyclotron period Ω_0^{-1}. This corresponds to a magnetization condition stopping the exponential growth at scales comparable to the cosmic rays Larmor radius, as the cosmic rays start following the perturbed field lines, and gives the minimum k as:

$$k_{\min} = \frac{\Omega_0}{u_{cr}} \tag{2.43}$$

For wavenumbers below $k_{\min}$, the cosmic rays velocity perturbations cannot be neglected such that Eq. 2.24 is no longer valid, and the contribution of the $\mathbf{j}_{cr} \times \mathbf{B}_1$ term becomes

small with respect to the $\mathbf{j}_{cr1} \times \mathbf{B}_0$ term. For this reason, the growth rate presented in Fig. 2.2 is not valid below $k_{\min}$. A derivation including cosmic rays resonance was done in Bell [2004], showing that the driving term is too weak to drive the non-resonant instability for $k < k_{\min}$, such that the left-hand and right-hand resonant modes become dominant. In this case the cosmic rays cannot be considered as streaming with a constant velocity, and the precise distribution function of the cosmic rays must be taken into account as the population no longer interacts solely via its current with the unstable waves (Holcomb and Spitkovsky [2018]).

2.2.4 Energy conservation, plasma heating

In the previous section, only the first and second order moments of the Vlasov equation, namely the conservation of mass density and of momentum density have been exploited to study the non-resonant mode. Additional insights into the instability can be obtained by studying the energy transfers between the plasma and the electromagnetic field. In the following, the pressure and heat flux terms will be neglected with respect to the terms involving the electromagnetic field, in order to highlight the wave-particle energy exchanges. Summing the energy density conservation equation of the electrons and protons fluid (Eq. 2.3), the conservation of the kinetic and internal energies background plasma energies can be expressed as:

$$\rho \frac{\mathrm{d}}{\mathrm{d}t}\left(\frac{u^2}{2} + U\right) = \mathbf{j}_b \cdot \mathbf{E} \tag{2.44}$$

where $\rho U = 3p/2$ with p the isotropic part of the pressure tensor and $\mathbf{j}_b = en_m\mathbf{u}_m - en_e\mathbf{u}_e = \boldsymbol{\nabla} \times \mathbf{B}/\mu_0 - \mathbf{j}_{cr}$ is the background current. One may separate the internal and kinetic part of the energy conservation equation by calculating the kinetic energy conservation equation. This can be obtained from the conservation of momentum density of the background plasma:

$$\rho \frac{\mathrm{d}\mathbf{u}}{\mathrm{d}t} = -\boldsymbol{\nabla} \cdot \mathbf{P} - en_{cr}\mathbf{E} + \mathbf{j}_b \times \mathbf{B} \tag{2.45}$$

Taking the scalar product of this equation by $\mathbf{u}$ and neglecting the pressure term, one obtains the balance equation for the kinetic (directed) energy of the background as:

$$\rho \frac{\mathrm{d}}{\mathrm{d}t}\left(\frac{u^2}{2}\right) = -en_{cr}\mathbf{E} \cdot \mathbf{u} + (\mathbf{j}_b \times \mathbf{B}) \cdot \mathbf{u} \tag{2.46}$$

Substracting Eq. 2.46 from Eq. 2.44, one obtains the conservation equation for the internal energy of the background fluid:

$$\rho \frac{\mathrm{d}U}{\mathrm{d}t} = \mathbf{E} \cdot (\mathbf{j}_b + en_{cr}\mathbf{u}) - (\mathbf{j}_b \times \mathbf{B}) \cdot \mathbf{u} \tag{2.47}$$

The electromagnetic energy density conservation, neglecting the electric energy with respect to the magnetic energy, gives:

$$\frac{\partial}{\partial t}\left(\frac{B^2}{2\mu_0}\right) + \boldsymbol{\nabla} \cdot \left(\frac{\mathbf{E} \times \mathbf{B}}{\mu_0}\right) = -(\mathbf{j}_b + \mathbf{j}_{cr}) \cdot \mathbf{E} \tag{2.48}$$

The second term on the left-hand side corresponds to the Poynting flux. The right-hand side term expresses the interaction of the plasma with the electric field and allows energy exchanges between the fluid and the electromagnetic field. Finally the cosmic rays kinetic energy conservation equation reads:

$$\rho_{cr}\frac{\mathrm{d}}{\mathrm{d}t}\left(\frac{u_{cr}^2}{2}\right) = \mathbf{j}_{cr}\cdot\mathbf{E} \tag{2.49}$$

The sum of these conservation equations yields zero, which corresponds to the conservation of the total (kinetic, internal and electromagnetic) energy of the system.

These conservation equations can be further developed by specifying the form of the electric field $\mathbf{E}$ such that it can be eliminated from the expressions. Using Ohm's law one has $\mathbf{E} = -\mathbf{u}\times\mathbf{B} - \frac{n_{cr}}{n_m}\mathbf{u}_{cr}\times\mathbf{B}$ (Eq. 2.22), which gives the intermediary relations:

$$\mathbf{E}\cdot\mathbf{j}_b = \mathbf{u}\cdot\mathbf{F}_L + \frac{n_{cr}}{n_m}\mathbf{u}_{cr}\cdot\mathbf{F}_L + \mathbf{j}_{cr}\cdot(\mathbf{u}\times\mathbf{B}) \tag{2.50}$$

$$en_{cr}\mathbf{E}\cdot\mathbf{u} = -\frac{n_{cr}}{n_m}\mathbf{u}\cdot(\mathbf{j}_{cr}\times\mathbf{B}) \tag{2.51}$$

$$\mathbf{E}\cdot\mathbf{j}_{cr} = -\mathbf{j}_{cr}\cdot(\mathbf{u}\times\mathbf{B}) \tag{2.52}$$

$$(\mathbf{j}_b\times\mathbf{B})\cdot\mathbf{u} = \mathbf{u}\cdot\mathbf{F}_L - \mathbf{u}\cdot(\mathbf{j}_{cr}\times\mathbf{B}) \tag{2.53}$$

where $\mathbf{F}_L = (\boldsymbol{\nabla}\times\mathbf{B})\times\mathbf{B}/\mu_0$ is the Lorentz force. Inserting in the conservation equations gives:

$$\rho_{cr}\frac{\mathrm{d}}{\mathrm{d}t}\left(\frac{u_{cr}^2}{2}\right) = -\mathbf{j}_{cr}\cdot(\mathbf{u}\times\mathbf{B}) \tag{2.54}$$

$$\rho\frac{\mathrm{d}}{\mathrm{d}t}\left(\frac{u^2}{2}\right) = \mathbf{j}_{cr}\cdot(\mathbf{u}\times\mathbf{B}) + \mathbf{u}\cdot\mathbf{F}_L \tag{2.55}$$

$$\rho\frac{\mathrm{d}U}{\mathrm{d}t} = -\frac{n_{cr}}{n_m}\mathbf{F}_L\cdot[\mathbf{u}-\mathbf{u}_{cr}] \tag{2.56}$$

$$\frac{\partial}{\partial t}\left(\frac{B^2}{2\mu_0}\right) + \boldsymbol{\nabla}\cdot\left(\frac{\mathbf{E}\times\mathbf{B}}{\mu_0}\right) = -\mathbf{u}\cdot\mathbf{F}_L - \frac{n_{cr}}{n_m}\mathbf{u}_{cr}\cdot\mathbf{F}_L \tag{2.57}$$

The equations involve the spatial structure of the magnetic field via the Lorentz force term $\mathbf{F}_L$, which is not easily interpreted. Additional insight can be obtained by linearizing the equations, while neglecting first order cosmic rays drift velocity perturbations, corresponding to the non-resonant regime as presented in the previous sections. One obtains that the second order parallel electric field can be expressed as $\mathbf{E}_{\parallel} = -\mathbf{u}_1\times\mathbf{B}_1$. From Eq. 2.40, one obtains that the background fluid acceleration is oriented in the direction of $-\mathbf{j}_{cr}\times\mathbf{B}_1$. Given that the real frequency of the electromagnetic wave is negligible with respect to the instability growth rate for the non-resonant mode, and in the absence of external forces, one deduces that the velocity perturbations are aligned with the direction of the local magnetic force. Consequently, the second order induced parallel electric field slows down the cosmic rays, and accelerates the background plasma. The internal energy conservation equation can be better understood by considering the calculation in the reference frame of the background fluid. In this case the electric field and background fluid current can be written respectively as $\mathbf{E}' = \mathbf{E} + \mathbf{u}\times\mathbf{B}$ and $\mathbf{j}_b' = \mathbf{j}_b + Q_{cr}\mathbf{u}$, which allows to rewrite Eq.

2.47 as:

$$\rho \frac{\mathrm{d}U}{\mathrm{d}t} = \mathbf{j}_b' \cdot \mathbf{E}' \tag{2.58}$$

corresponding to the work of the electric force in the background fluid reference frame. Assuming $\mathbf{u}_m \approx \mathbf{u}$ and quasi-neutrality, the internal energy conservation equation can then be written as:

$$\rho \frac{\mathrm{d}U}{\mathrm{d}t} = e n_{cr} (\mathbf{u}_e - \mathbf{u}) \cdot [(\mathbf{u}_{cr} - \mathbf{u}) \times \mathbf{B}] \tag{2.59}$$

The inductive term due to the background plasma motion no longer appears, such that one obtains that the electric field induced by the cosmic rays drift velocity interacts with the current carried by the electrons, allowing important energy exchanges between the waves and the background plasma. This heating effect will be further investigated in numerical simulations in Chapters 5 and 6.

2.3 References

Amato, E. and Blasi, P. (2009). A kinetic approach to cosmic-ray-induced streaming instability at supernova shocks. *Mon Not R Astron Soc*, 392(4):1591–1600.

Bai, X.-N., Caprioli, D., Sironi, L., and Spitkovsky, A. (2015). Magnetohydrodynamic-Particle-in-Cell Method for Coupling Cosmic Rays with a Thermal Plasma: Application to Non-relativistic Shocks. *ApJ*, 809(1):55.

Bell, A. R. (2004). Turbulent amplification of magnetic field and diffusive shock acceleration of cosmic rays. *Mon Not R Astron Soc*, 353(2):550–558.

Gary, S. P., Smith, C. W., Lee, M. A., Goldstein, M. L., and Forslund, D. W. (1984). Electromagnetic ion beam instabilities. *The Physics of Fluids*, 27(7):1852–1862.

Gupta, S., Caprioli, D., and Haggerty, C. C. (2021). Lepton-driven Non-resonant Streaming Instability. *arXiv e-prints*, page arXiv:2106.07672.

Hirabayashi, K., Hoshino, M., and Amano, T. (2016). A new framework for magnetohydrodynamic simulations with anisotropic pressure. *Journal of Computational Physics*, 327:851–872.

Holcomb, C. and Spitkovsky, A. (2018). On the Growth and Saturation of the Gyroresonant Streaming Instabilities. *arXiv:1811.01951 [astro-ph]*.

Kulsrud, R. and Pearce, W. P. (1969). The Effect of Wave-Particle Interactions on the Propagation of Cosmic Rays. *ApJ*, 156:445.

Matthews, J. H., Bell, A. R., Blundell, K. M., and Araudo, A. T. (2017). Amplification of perpendicular and parallel magnetic fields by cosmic ray currents. *Mon Not R Astron Soc*, 469(2):1849–1860.

Mignone, A., Bodo, G., Vaidya, B., and Mattia, G. (2018). A Particle Module for the PLUTO Code. I. An Implementation of the MHD–PIC Equations. *ApJ*, 859(1):13.

Reville, B., Kirk, J. G., Duffy, P., and O'Sullivan, S. (2007). A cosmic ray current-driven instability in partially ionised media. *Astronomy & Astrophysics*, 475(2):435–439.

Sentman, D. D., Edmiston, J. P., and Frank, L. A. (1981). Instabilities of low frequency, parallel propagating electromagnetic waves in the Earth's foreshock region. *Journal of Geophysical Research: Space Physics*, 86(A9):7487–7497.

Tatischeff, V., Raymond, J. C., Duprat, J., Gabici, S., and Recchia, S. (2021). The origin of galactic cosmic rays as revealed by their composition. *arXiv e-prints*, page arXiv:2106.15581.

van Marle, A. J., Casse, F., and Marcowith, A. (2018). On magnetic field amplification and particle acceleration near non-relativistic astrophysical shocks: Particles in MHD cells simulations. *Monthly Notices of the Royal Astronomical Society*, 473:3394–3409.

Verscharen, D., Klein, K., and Maruca, B. (2019). The multi-scale nature of the solar wind.

Winske, D. and Leroy, M. M. (1984). Diffuse ions produced by electromagnetic ion beam instabilities. *Journal of Geophysical Research: Space Physics*, 89(A5):2673–2688.

Zacharegkas, G., Caprioli, D., and Haggerty, C. (2019). Modeling the Saturation of the Bell Instability Using Hybrid Simulations. *arXiv:1909.06481*.

Zirakashvili, V. N., Ptuskin, V. S., and Völk, H. J. (2008). Modeling bell's nonresonant cosmic-ray instability. *The Astrophysical Journal*, 678(1):255–261.

Chapter 3

Kinetic approach to the non-resonant mode

Contents

3.1 Introduction

Up to this point, the Larmor radius of the protons and electrons was considered negligible compared to the spatial scales relevant to the non-resonant instability, such that any kinetic effects due to a finite temperature were supposed negligible.

This chapter presents the derivation of the growth rate of the non-resonant mode while taking into account the background protons temperature. A wide range of parameters will be considered, starting from the zero and small temperature regimes (cold and warm plasma) up to the demagnetized regime (hot plasma) where the ion Larmor radius is larger than the unstable wavelengths. A kinetic description of the plasma components will be used in order to accurately describe finite Larmor radius effects, which do not appear in the fluid model, even by considering the background fluid pressure tensor. This work will focus on obtaining analytical results by expanding the full kinetic dispersion relation for

the non-resonant mode. The results are of particular importance to assess the spatial and temporal scales characteristic of the non-resonant mode in hot environments such as superbubbles and the intergalactic medium. In denser environments such as H II regions and molecular clouds, collisions can also become sufficiently frequent to modify the growth of the instability. This will be investigated in Chapter 6.

3.2 The linear dispersion relation

3.2.1 General relation

Waves propagating in a plasma can be studied by solving the Vlasov, Faraday and Ampère system of equations in Fourier space. The magnetic and electric field are linearized as:

$$\mathbf{B} = \mathbf{B}_0 + \mathbf{B}_1 \tag{3.1}$$

$$\mathbf{E} = \mathbf{E}_1 \tag{3.2}$$

where an ambient, homogeneous magnetic field is considered along the $\mathbf{e}_z$ direction $\mathbf{B}_0 = B_0\mathbf{e}_z$, such that $B_0 \gg B_1$. Ampère's law yields the relation:

$$i\mathbf{k} \times \mathbf{B}_1 = \mu_0\mathbf{J}_1 - \frac{i\omega}{c^2}\mathbf{E}_1 \tag{3.3}$$

where μ_0 is the magnetic permeability, c is the speed of light, $\mathbf{J}$ is the total conduction current, k is the wave number and ω is the angular frequency of the wave. The perturbed magnetic field B_1 may be expressed with Faraday's law as:

$$\mathbf{B}_1 = \frac{\mathbf{k} \times \mathbf{E}_1}{\omega} \tag{3.4}$$

from which one deduces:

$$\frac{c^2}{\omega^2}\mathbf{k} \times (\mathbf{k} \times \mathbf{E}_1) + \mathbf{E}_1 + \frac{i}{\omega\epsilon_0}\mathbf{J}_1 = \mathbf{0} \tag{3.5}$$

where $\epsilon_0 = 1/\mu_0 c^2$ is the dielectric permittivity of vacuum. Considering that the contributions from the plasma can be embedded in the conductivity tensor $\boldsymbol{\sigma}$, then the total conduction current writes:

$$\mathbf{J}_1 = \boldsymbol{\sigma} \cdot \mathbf{E}_1 \tag{3.6}$$

which gives the so-called dispersion relation:

$$\frac{c^2}{\omega^2}(\mathbf{kk} - k^2\mathbb{1}) \cdot \mathbf{E}_1 + \mathbf{E}_1 + \frac{i}{\omega\epsilon_0}\boldsymbol{\sigma} \cdot \mathbf{E}_1 = \mathbf{0} \tag{3.7}$$

where $\mathbb{1}$ is the identity matrix. Defining the ij element of the dispersion tensor:

$$R_{ij} = \frac{c^2}{\omega^2}(k_i k_j - k^2\delta_{ij}) + \delta_{ij} + \frac{i}{\omega\epsilon_0}\sigma_{ij} \tag{3.8}$$

with δ_{ij} the Kronecker delta, the dispersion relation can be rewritten in a compact form:

$$\mathbf{R} \cdot \mathbf{E}_1 = \mathbf{0} \tag{3.9}$$

It can then solved by calculating $\det |\mathbf{R}| = 0$, which allows to retrieve the frequency as a function of the wavenumber. Such analysis is central in the study of plasma instabilities, as it allows us to obtain the characteristic time and spatial scales associated to a given mode. In order to pursue the calculation, one needs the tensor $\boldsymbol{\sigma}$ which encompasses the specificity of the propagation medium and dictates the current resulting from an electric field perturbation. In the following $\boldsymbol{\sigma}$ will be obtained by calculating the perturbed distribution function, through the linearization of the Vlasov equation. This will allow us to obtain the current as a function of the perturbed electric field, and thus give access to the conductivity tensor. Only parallel propagating modes ($\mathbf{k} \times \mathbf{B}_0 = \mathbf{0}$) will be considered, which encompasses the non-resonant streaming instability.

3.2.2 Perturbed distribution function

The evolution of the distribution function $f(\mathbf{r}, \mathbf{v}, t)$ of each population α of the plasma is dictated by the Vlasov equation:

$$\frac{\partial f_\alpha}{\partial t} + \mathbf{v} \cdot \boldsymbol{\nabla} f_\alpha + \frac{q_\alpha}{m_\alpha}(\mathbf{E} + \mathbf{v} \times \mathbf{B}) \cdot \frac{\partial f_\alpha}{\partial \mathbf{v}} = 0 \tag{3.10}$$

where $\mathbf{E}(\mathbf{r}, t)$ and $\mathbf{B}(\mathbf{r}, t)$ are the macroscopic electric and magnetic field (see Sec. 4.4.2 for a discussion on the definition of "macroscopic"), q_α the charge and m_α the mass. In the following the subscript α will be omitted to simplify the notations. In order to obtain the total perturbed current $\mathbf{J}_1 = \sum_\alpha \mathbf{j}_{\alpha 1}$, a classical procedure is to use the methods of the characteristics (e.g. Gary and Feldman [1978], Gary [1992]). It consists in solving the Vlasov equation for each population as:

$$\frac{df_1}{dt} = -\frac{q}{m}\mathbf{E}_1 . \frac{\partial f_0}{\partial \mathbf{v}} - \frac{q}{m}(\mathbf{v} \times \mathbf{B}_1) . \frac{\partial f_0}{\partial \mathbf{v}} \tag{3.11}$$

with

$$\frac{df_1}{dt} = \frac{\partial f_1}{\partial t} + \mathbf{v} . \frac{\partial f_1}{\partial \mathbf{r}} + \frac{q}{m}(\mathbf{v} \times \mathbf{B}_0) . \frac{\partial f_1}{\partial \mathbf{v}} \tag{3.12}$$

the trajectory along a non-perturbed orbit, where the position and velocity correspond to the cyclotron motion of the particles in the unperturbed magnetic field:

$$\mathbf{v} = \frac{\mathrm{d}\mathbf{r}}{\mathrm{d}t} \tag{3.13}$$

$$\frac{\mathrm{d}\mathbf{v}}{\mathrm{d}t} = \frac{q}{m}\mathbf{v} \times \mathbf{B}_0 \tag{3.14}$$

One may integrate Eq. 3.11 directly in time along this non-perturbed orbit, which then allows to obtain the waves dispersion relation.

An alternate derivation is presented here, which takes advantage of the cylindrical symmetry of the problem. The calculation can be separated in four steps: first, obtaining the perturbed distribution function, then calculation of the plasma current, thirdly calculating

the conductivity tensor, and finally solving the dispersion relation. Linearizing Eq. 3.10 in Fourier space while neglecting second order terms, one obtains:

$$-i(\omega - \mathbf{k}\cdot\mathbf{v})f_1 + \frac{q}{m}(\mathbf{v}\times\mathbf{B}_0)\cdot\frac{\partial f_1}{\partial \mathbf{v}} = -\frac{q}{m}(\mathbf{E}_1 + \mathbf{v}\times\mathbf{B}_1)\cdot\frac{\partial f_0}{\partial \mathbf{v}} \tag{3.15}$$

Using cylindrical coordinates the velocity, wave vector and unperturbed magnetic field can be expressed as $\mathbf{v} = (v_\perp\cos\phi,\ v_\perp\sin\phi,\ v_\parallel)$, $\mathbf{k} = (0,\ 0,\ k)$ and $\mathbf{B}_0 = (0,\ 0,\ B_0)$ respectively, where $v_\perp$ and $v_\parallel$ refer to the velocity perpendicular and parallel to the initial magnetic field B_0, and ϕ refers to the azimuthal angle. The following relations hold:

$$\begin{aligned}
\mathrm{d}v_\perp &= \frac{\partial v_\perp}{\partial v_x}\mathrm{d}v_x + \frac{\partial v_\perp}{\partial v_y}\mathrm{d}v_y && (3.16)\\
&= \cos\phi\ \mathrm{d}v_x + \sin\phi\ \mathrm{d}v_y && (3.17)\\
\mathrm{d}\phi &= \frac{\partial \phi}{\partial v_x}\mathrm{d}v_x + \frac{\partial \phi}{\partial v_y}\mathrm{d}v_y && (3.18)\\
&= -\frac{\sin\phi}{v_\perp}\mathrm{d}v_x + \frac{\cos\phi}{v_\perp}\mathrm{d}v_y && (3.19)
\end{aligned}$$

The velocity derivatives can then be rewritten as :

$$\begin{aligned}
\frac{\partial f}{\partial v_x} &= \frac{\partial f}{\partial v_\perp}\frac{\partial v_\perp}{\partial v_x} + \frac{\partial f}{\partial \phi}\frac{\partial \phi}{\partial v_x} && (3.20)\\
&= \frac{\partial f}{\partial v_\perp}\cos\ \phi - \frac{1}{v_\perp}\frac{\partial f}{\partial \phi}\sin\ \phi && (3.21)\\
\frac{\partial f}{\partial v_y} &= \frac{\partial f}{\partial v_\perp}\frac{\partial v_\perp}{\partial v_y} + \frac{\partial f}{\partial \phi}\frac{\partial \phi}{\partial v_y} && (3.22)\\
&= \frac{\partial f}{\partial v_\perp}\sin\ \phi + \frac{1}{v_\perp}\frac{\partial f}{\partial \phi}\cos\ \phi && (3.23)
\end{aligned}$$

Defining the cyclotron frequency $\Omega_0 = qB_0/m$ and the shifted frequency $\psi = \omega - kv_\parallel$ one finds:

$$\frac{\partial f_1}{\partial \phi} + i\frac{\psi}{\Omega_0}f_1 = \frac{q}{m\Omega_0}(\mathbf{E}_1 + \mathbf{v}\times\mathbf{B}_1)\cdot\frac{\partial f_0}{\partial \mathbf{v}} \tag{3.24}$$

The terms coupling the zeroth order field to the perturbed distribution function no longer appear in the equation in cylindrical coordinates for the velocity, allowing a direction integration of the Vlasov equation. Using Eq. 3.4, one can write:

$$\mathbf{v}\times\mathbf{B}_1 = \frac{1}{\omega}\left[(\mathbf{v}\cdot\mathbf{E}_1)\mathbf{k} - (\mathbf{v}\cdot\mathbf{k})\mathbf{E}_1\right] \tag{3.25}$$

Replacing in the linearized Vlasov equation (Eq. 3.24):

$$\frac{\partial f_1}{\partial \phi} + i\frac{\psi}{\Omega_0}f_1 = \frac{q}{m\Omega_0}\mathbf{E}_1\cdot\left[\mathbb{1} - \mathbb{1}\frac{\mathbf{v}\cdot\mathbf{k}}{\omega} + \frac{\mathbf{v}\mathbf{k}}{\omega}\right]\cdot\frac{\partial f_0}{\partial \mathbf{v}} \tag{3.26}$$

The second term on the right hand side can be developed as:

$$\mathbf{E}_1\cdot\left[\mathbb{1} - \mathbb{1}\frac{\mathbf{v}\cdot\mathbf{k}}{\omega} + \frac{\mathbf{v}\mathbf{k}}{\omega}\right]\cdot\frac{\partial f_0}{\partial \mathbf{v}} = \mathbf{E}_1\cdot\mathbf{v}\frac{k}{\omega}\frac{\partial f_0}{\partial v_\parallel} + \left(1 - \frac{kv_\parallel}{\omega}\right)\mathbf{E}_1\cdot\frac{\partial f_0}{\partial \mathbf{v}} \tag{3.27}$$

Considering a drifting Maxwellian velocity distribution along the initial magnetic field B_0 with anisotropic temperatures $T_\parallel \neq T_\perp$, the initial distribution function f_0 can be expressed as:

$$f_0 = n_0 \sqrt{\frac{\alpha_\parallel}{\pi}} \left(\frac{\alpha_\perp}{\pi}\right) e^{-\alpha_\parallel (v_\parallel - u_0)^2} e^{-\alpha_\perp v_\perp^2} \tag{3.28}$$

with $\alpha_\parallel = m/2k_B T_\parallel$, $\alpha_\perp = m/2k_B T_\perp$, k_B the Boltzmann constant, u_0 the drift velocity and n_0 the initial density. The initial distribution function being gyrotropic ($\partial f_0/\partial\phi = 0$), one obtains:

$$\mathbf{E}_1 \cdot \frac{\partial f_0}{\partial \mathbf{v}} = \frac{\mathbf{E}_1 \cdot \mathbf{v}}{v_\perp} \frac{\partial f_0}{\partial v_\perp} \tag{3.29}$$

Calculating the distribution function velocity derivatives yields:

$$\frac{\partial f_0}{\partial v_\parallel} = -2 f_0 \, \alpha_\parallel (v_\parallel - u_0) \tag{3.30}$$

$$\frac{\partial f_0}{\partial v_\perp} = -2 f_0 \, \alpha_\perp v_\perp \tag{3.31}$$

Hence:

$$\frac{\partial f_1}{\partial \phi} + i\frac{\psi}{\Omega_0} f_1 = -2\frac{q}{m\Omega_0} \mathbf{E}_1 \cdot \mathbf{v} \left[\frac{k}{\omega}\alpha_\parallel (v_\parallel - u_0) + \alpha_\perp \frac{\psi}{\omega}\right] f_0 \tag{3.32}$$

By solving the associated first order linear homogeneous ordinary differential equation in f_1 one obtains:

$$f_1 = K e^{-i\frac{\psi}{\Omega_0}\phi} \tag{3.33}$$

The constant K can be obtained directly by considering the condition $f_1(\phi = 0) = f_1(\phi = 2\pi)$, which yields $K = 0$. Integrating Eq. 3.32 yields:

$$\hat{f}_1(\phi) = -\frac{1}{\Omega_0} e^{-i\frac{\psi}{\Omega_0}\phi} \int^\phi f_0 e^{i\frac{\psi}{\Omega_0}\phi'} 2\frac{q}{m} \mathbf{E}_1 \cdot \mathbf{v} \left[\frac{k}{\omega}\alpha_\parallel (v_\parallel - u_0) + \alpha_\perp \frac{\psi}{\omega}\right] \mathrm{d}\phi' \tag{3.34}$$

where the variation of the constant has been used to define:

$$f_1 = \hat{f}_1 e^{-i\frac{\psi}{\Omega_0}(\phi' - \phi)} \tag{3.35}$$

which has been inserted in Eq. 3.32. Defining $\psi^\pm = \psi \pm \Omega_0 = \omega - k v_\parallel \pm \Omega_0$, one finds:

$$e^{-i\frac{\psi}{\Omega_0}\phi} \int^\phi \cos\phi' e^{i\frac{\psi}{\Omega_0}\phi'} \mathrm{d}\phi' = \frac{\Omega_0}{2} \left[\frac{e^{i\phi}}{i\psi^+} + \frac{e^{-i\phi}}{i\psi^-}\right] \tag{3.36}$$

$$e^{-i\frac{\psi}{\Omega_0}\phi} \int^\phi \sin\phi' e^{i\frac{\psi}{\Omega_0}\phi'} \mathrm{d}\phi' = \frac{\Omega_0}{2i} \left[\frac{e^{i\phi}}{i\psi^+} - \frac{e^{-i\phi}}{i\psi^-}\right] \tag{3.37}$$

The perturbed distribution function is then obtained as:

$$\hat{f}_1 = i\frac{q}{m} f_0 \left[\frac{k}{\omega}\alpha_\parallel (v_\parallel - u_0) + \alpha_\perp \frac{\psi}{\omega}\right] \mathbf{E}_1 \cdot \boldsymbol{\eta} \tag{3.38}$$

where the vector $\boldsymbol{\eta}$ is defined as:

$$\boldsymbol{\eta} = iv_\perp \left(\frac{e^{i\phi}}{\psi^+} + \frac{e^{-i\phi}}{\psi^-}\right)\mathbf{e}_x + v_\perp \left(\frac{e^{i\phi}}{\psi^+} - \frac{e^{-i\phi}}{\psi^-}\right)\mathbf{e}_y + 2\frac{v_\parallel}{\psi}\mathbf{e}_z \tag{3.39}$$

3.2.3 Perturbed current

The perturbed current carried by a given population, defined as $\mathbf{j}_1 = q\int_{-\infty}^{+\infty} \hat{f}_1 \mathbf{v} \mathrm{d}\mathbf{v}$, can now be calculated as:

$$\mathbf{j}_1 = i\frac{q^2}{m}\int_{-\infty}^{+\infty} \boldsymbol{\eta}\mathbf{v} f_0 \left[\frac{k}{\omega}\alpha_\parallel(v_\parallel - u_0) + \alpha_\perp \frac{\psi}{\omega}\right]\cdot \mathbf{E}_1 \mathrm{d}\mathbf{v} \tag{3.40}$$

First, the integral in the first term of Eq. 3.40 is evaluated. The dyadic product $\boldsymbol{\eta}\mathbf{v}$ can be expressed as:

$$\boldsymbol{\eta}\mathbf{v} = \begin{pmatrix} iv_\perp^2 \cos\phi\left(\frac{e^{i\phi}}{\psi^+} + \frac{e^{-i\phi}}{\psi^-}\right) & iv_\perp^2 \sin\phi\left(\frac{e^{i\phi}}{\psi^+} + \frac{e^{-i\phi}}{\psi^-}\right) & iv_\perp v_\parallel\left(\frac{e^{i\phi}}{\psi^+} + \frac{e^{-i\phi}}{\psi^-}\right) \\ v_\perp^2 \cos\phi\left(\frac{e^{i\phi}}{\psi^+} - \frac{e^{-i\phi}}{\psi^-}\right) & v_\perp^2 \sin\phi\left(\frac{e^{i\phi}}{\psi^+} - \frac{e^{-i\phi}}{\psi^-}\right) & v_\perp v_\parallel\left(\frac{e^{i\phi}}{\psi^+} - \frac{e^{-i\phi}}{\psi^-}\right) \\ 2\frac{v_\parallel}{\psi}v_\perp\cos\phi & 2\frac{v_\parallel}{\psi}v_\perp\sin\phi & 2\frac{v_\parallel^2}{\psi} \end{pmatrix} \tag{3.41}$$

The velocity integral can be rewritten in cylindrical coordinates as:

$$\int_{-\infty}^{+\infty}\mathrm{d}\mathbf{v} = \int_0^{2\pi}\mathrm{d}\phi\int_0^{+\infty} v_\perp \mathrm{d}v_\perp \int_{-\infty}^{+\infty}\mathrm{d}v_\parallel \tag{3.42}$$

The terms of the form $\sin\phi$, $\cos\phi$, $e^{i\phi}$ and $e^{-i\phi}$ yield 0 when integrating over the angle ϕ. The other terms can be integrated in ϕ and $v_\perp$ as follows:

$$i\int_{-\infty}^{+\infty} f_0 v_\perp^2 \cos\phi\left(\frac{e^{i\phi}}{\psi^+} + \frac{e^{-i\phi}}{\psi^-}\right)\mathrm{d}\mathbf{v}_\perp = i\pi\int_0^{+\infty} f_0 v_\perp^3 \mathrm{d}v_\perp \left(\frac{1}{\psi^+} + \frac{1}{\psi^-}\right)\mathrm{d}v_\perp \tag{3.43}$$

$$i\int_{-\infty}^{+\infty} f_0 v_\perp^2 \sin\phi\left(\frac{e^{i\phi}}{\psi^+} + \frac{e^{-i\phi}}{\psi^-}\right)\mathrm{d}\mathbf{v}_\perp = -\pi\int_0^{+\infty} f_0 v_\perp^3 \mathrm{d}v_\perp \left(\frac{1}{\psi^+} - \frac{1}{\psi^-}\right)\mathrm{d}v_\perp \tag{3.44}$$

$$\int_{-\infty}^{+\infty} f_0 v_\perp^2 \cos\phi\left(\frac{e^{i\phi}}{\psi^+} - \frac{e^{-i\phi}}{\psi^-}\right)\mathrm{d}\mathbf{v}_\perp = \pi\int_0^{+\infty} f_0 v_\perp^3 \mathrm{d}v_\perp \left(\frac{1}{\psi^+} - \frac{1}{\psi^-}\right)\mathrm{d}v_\perp \tag{3.45}$$

$$\int_{-\infty}^{+\infty} f_0 v_\perp^2 \sin\phi\left(\frac{e^{i\phi}}{\psi^+} - \frac{e^{-i\phi}}{\psi^-}\right)\mathrm{d}\mathbf{v}_\perp = i\pi\int_0^{+\infty} f_0 v_\perp^3 \mathrm{d}v_\perp \left(\frac{1}{\psi^+} + \frac{1}{\psi^-}\right)\mathrm{d}v_\perp \tag{3.46}$$

$$\int_{-\infty}^{+\infty} 2\frac{f_0}{\psi}\mathrm{d}\mathbf{v}_\perp = \frac{4\pi}{\psi}\int_0^{+\infty} f_0 v_\perp \mathrm{d}v_\perp \tag{3.47}$$

The perpendicular velocity integrals can be found by using the following property:

$$G_n = \int_0^{+\infty} v_\perp^n e^{-\alpha_\perp v_\perp^2}\mathrm{d}v_\perp = \frac{n-1}{2\alpha_\perp}G_{n-2} \tag{3.48}$$

$$G_1 = \frac{1}{2\alpha_\perp} \tag{3.49}$$

Hence the integral:

$$G_3 = \frac{1}{2\alpha_\perp^2} \tag{3.50}$$

The integrals on the parallel velocity component need to be calculated for the terms $ij = (11, 12, 21, 22)$ of the tensor $\boldsymbol{\eta}\mathbf{v}$. Defining:

$$I^\pm = i\frac{n_0 q^2}{2m\omega}\int_{-\infty}^{+\infty}\left[kv_\parallel(\alpha_\parallel - \alpha_\perp) - ku_0\alpha_\parallel - \omega\alpha_\perp\right]\frac{1}{\alpha_\perp}\left(\frac{\alpha_\parallel}{\pi}\right)^{1/2}\frac{e^{-\alpha_\parallel(v_\parallel - u_0)^2}}{\omega - kv_\parallel \pm \Omega_0}\mathrm{d}v_\parallel \tag{3.51}$$

and the quantity:

$$u^2 = \alpha_\parallel(v_\parallel - u_0)^2 \tag{3.52}$$

such that $v_\parallel = u/\sqrt{\alpha_\parallel} + u_0$ and $\mathrm{d}v_\parallel = \mathrm{d}u/\sqrt{\alpha_\parallel}$, the expression becomes:

$$I^\pm = i\frac{n_0 q^2}{2m\omega}\int_{-\infty}^{+\infty}\left[\frac{u}{\sqrt{\alpha_\parallel}}(\alpha_\perp - \alpha_\parallel) + \alpha_\perp\left(u_0 - \frac{\omega}{k}\right)\right]\frac{1}{\alpha_\perp}\left(\frac{\alpha_\parallel}{\pi}\right)^{1/2} \times \frac{e^{-u^2}}{u - \frac{\sqrt{\alpha_\parallel}}{k}(\omega - ku_0 \pm \Omega_0)}\mathrm{d}u \tag{3.53}$$

$I^\pm$ can be expressed as a function of the Fried and Conte integral (Fried and Conte [1961]):

$$Z(\zeta) = \frac{1}{\sqrt{\pi}}\int_{-\infty}^{+\infty}\frac{e^{-u^2}}{u - \zeta}\mathrm{d}u \tag{3.54}$$

by defining $\zeta^\pm = \frac{\sqrt{\alpha_\parallel}}{k}(\omega - ku_0 \pm \Omega_0)$. Using the following properties (Callen [2006]) for $\mathrm{Im}(\zeta) > 0$ and $n \geq 0$:

$$Z_n(\zeta) = \frac{1}{\sqrt{\pi}}\int_{-\infty}^{+\infty}\frac{u^n e^{-u^2}}{u - \zeta}\mathrm{d}u \tag{3.55}$$

$$Z_1 = -\frac{Z'}{2} = 1 + \zeta Z \tag{3.56}$$

$$Z_2 = -\zeta\frac{Z'}{2} = \zeta + \zeta^2 Z \tag{3.57}$$

$$Z_3 = \frac{1}{2}\left[1 + 2\zeta^2(1 + \zeta Z)\right] \tag{3.58}$$

where the prime notation corresponds to the derivative with respect to ζ, one finds:

$$I^\pm = i\frac{n_0 q^2}{2m\omega}\left[\frac{\alpha_\parallel - \alpha_\perp}{2\alpha_\perp}Z'(\zeta^\pm) + \sqrt{\alpha_\parallel}\left(u_0 - \frac{\omega}{k}\right)Z(\zeta^\pm)\right] \tag{3.59}$$

The velocity integral for the $ij = 33$ term of the $\boldsymbol{\eta}\mathbf{v}$ tensor will now be calculated. Defining:

$$I = 2i\frac{n_0 q^2}{m}\int_{-\infty}^{+\infty}\left[\frac{k}{\omega}\alpha_\parallel(v_\parallel - u_0) + \alpha_\perp\left(1 - \frac{kv_\parallel}{\omega}\right)\right]\frac{\alpha_\perp}{\pi}\left(\frac{\alpha_\parallel}{\pi}\right)^{1/2} \times v_\parallel^2\frac{e^{-\alpha_\perp v_\perp - \alpha_\parallel(v_\parallel - u_0)^2}}{\omega - kv_\parallel}\mathrm{d}\mathbf{v} \tag{3.60}$$

Using Eqs. 3.47 and 3.49:

$$I = 2i\frac{n_0 q^2}{m}\int_{-\infty}^{+\infty}\left[\frac{k}{\omega}\alpha_\parallel(v_\parallel - u_0) + \alpha_\perp\left(1 - \frac{kv_\parallel}{\omega}\right)\right]\left(\frac{\alpha_\parallel}{\pi}\right)^{1/2} v_\parallel^2\frac{e^{-\alpha_\parallel(v_\parallel - u_0)^2}}{\omega - kv_\parallel}\mathrm{d}v_\parallel \tag{3.61}$$

Using the previously defined u yields:

$$I = 2i\frac{n_0 q^2}{m\omega}\int_{-\infty}^{+\infty}\left(\frac{\alpha_\parallel}{\pi}\right)^{1/2}\left[\frac{u}{\sqrt{\alpha_\parallel}}(\alpha_\perp - \alpha_\parallel) + u_0\alpha_\perp - \frac{\omega}{k}\alpha_\perp\right]\left[\frac{u^2}{\alpha_\parallel} + u_0^2 + 2\frac{uu_0}{\sqrt{\alpha_\parallel}}\right] \times \frac{e^{-u^2}}{\dfrac{\omega}{k} - \dfrac{u}{\sqrt{\alpha_\parallel} - u_0}}\frac{\mathrm{d}u}{\sqrt{\alpha_\parallel}} \tag{3.62}$$

Defining $\zeta = \dfrac{\sqrt{\alpha_\parallel}}{k}(\omega - ku_0)$ and Γ as:

$$\Gamma = u^3\frac{\alpha_\perp - \alpha_\parallel}{\alpha_\parallel^{3/2}} + u^2\left[\frac{\alpha_\perp}{\alpha_\parallel}\left(3u_0 - \frac{\omega}{k}\right) - 2u_0\right] + u\left[\frac{1}{\sqrt{\alpha_\parallel}}\left(u_0^2(3\alpha_\perp - \alpha_\parallel) - 2u_0\alpha_\perp\frac{\omega}{k}\right)\right] + \alpha_\perp\left[u_0^3 - \frac{\omega}{k}u_0^2\right] \tag{3.63}$$

In a more compact form:

$$\Gamma = au^3 + bu^2 + cu + d \tag{3.64}$$

This allows to express I as:

$$I = -2i\frac{n_0 q^2}{m\omega}\int_{-\infty}^{+\infty}\left(\frac{\alpha_\parallel}{\pi}\right)^{1/2}\frac{e^{-u^2}}{u - \zeta}\Gamma\ \mathrm{d}u \tag{3.65}$$

Using Eqs. 3.56 to 3.58, one finds:

$$I = -2i\frac{n_0 q^2}{m\omega}\sqrt{\alpha_\parallel}\left[Z_3 a + Z_2 b + Z_1 c + Zd\right] \tag{3.66}$$

One can now write the elements of the conductivity tensor $\boldsymbol{\sigma}$ for each species.

3.2.4 Conductivity tensor

Combining Eq. 3.40, Eqs. 3.43 to 3.46, and Eqs. 3.59, 3.66 yields:

$$\sigma_{11} = i\frac{\epsilon_0}{2}\frac{\omega_p^2}{\omega}\left[\frac{T_\perp - T_\parallel}{2T_\parallel}(Z'(\zeta^+) + Z'(\zeta^-)) + \frac{1}{\sqrt{2}v_{T\parallel}}\left(u_0 - \frac{\omega}{k}\right)(Z(\zeta^+) + Z(\zeta^-))\right] \tag{3.67}$$

$$\sigma_{12} = \frac{\epsilon_0}{2}\frac{\omega_p^2}{\omega}\left[\frac{T_\perp - T_\parallel}{2T_\parallel}(Z'(\zeta^-) - Z'(\zeta^+)) + \frac{1}{\sqrt{2}v_{T\parallel}}\left(u_0 - \frac{\omega}{k}\right)(Z(\zeta^-) - Z(\zeta^+))\right] \tag{3.68}$$

$$\sigma_{21} = -\sigma_{12} \tag{3.69}$$

$$\sigma_{22} = \sigma_{11} \tag{3.70}$$

$$\sigma_{13} = \sigma_{23} = \sigma_{31} = \sigma_{32} = 0 \tag{3.71}$$

$$\sigma_{33} = 2i\epsilon_0\frac{\omega_p^2}{\omega}\sqrt{\alpha_\parallel}\left[Z_3(\zeta)a + Z_2(\zeta)b + Z_1(\zeta)c + Z(\zeta)d\right] \tag{3.72}$$

where $\omega_p^2 = n_0q^2/\epsilon_0 m$ is the plasma frequency. The conductivity tensor, defined by the relation $\mathbf{J}_1 = \boldsymbol{\sigma}\cdot\mathbf{E}_1$, can now be written explicitly as a sum over each of the plasma components:

$$\sum_\alpha \mathbf{j}_{1\alpha} = \sum_\alpha \boldsymbol{\sigma}_\alpha \cdot \mathbf{E}_1 \tag{3.73}$$

The kinetic dispersion relation can now be solved, by calculating the determinant of the tensor defined in Eq. 3.8. The components can be written as:

$$R_{11} = 1 - \frac{k^2c^2}{\omega^2} + \frac{i\sigma_{11}}{\omega\epsilon_0} \tag{3.74}$$

$$R_{12} = \frac{i\sigma_{12}}{\omega\epsilon_0} \tag{3.75}$$

$$R_{21} = -R_{12} \tag{3.76}$$

$$R_{22} = R_{11} \tag{3.77}$$

$$R_{33} = 1 + \frac{i\sigma_{33}}{\omega\epsilon_0} \tag{3.78}$$

$$R_{13} = R_{23} = R_{31} = R_{32} = 0 \tag{3.79}$$

where the conductivity tensor $\boldsymbol{\sigma}$ is the sum over each plasma components. Calculating $\det|\mathbf{R}| = 0$:

$$\left(1 + \frac{i\sigma_{33}}{\omega\epsilon_0}\right)\left[\left(1 - \frac{k^2c^2}{\omega^2} + \frac{i\sigma_{11}}{\omega\epsilon_0}\right)^2 - \frac{\sigma_{12}^2}{\omega^2\epsilon_0^2}\right] = 0 \tag{3.80}$$

One obtains that the electrostatic modes are decoupled from the electromagnetic modes. For electrostatic modes (left bracket, corresponding to $\mathbf{k}\times\mathbf{E}_1 = \mathbf{0}$):

$$1 + \frac{i\sigma_{33}}{\omega\epsilon_0} = 0 \tag{3.81}$$

And for electromagnetic modes (right bracket, corresponding to $\mathbf{k} \cdot \mathbf{E}_1 = 0$):

$$1 - \frac{k^2 c^2}{\omega^2} + \frac{i\sigma_{11} \pm \sigma_{12}}{\omega \epsilon_0} = 0 \tag{3.82}$$

where the upper sign (plus) is for right-hand polarized modes, and the lower sign (minus) is for left-hand polarized modes. The latter equation will be investigated as the non-resonant mode is electromagnetic. Inserting Eqs. 3.67 and 3.68 in Eq. 3.82, one finally obtains:

$$1 - \frac{k^2 c^2}{\omega^2} - \sum_\alpha \frac{\omega_{p\alpha}^2}{\omega^2} \left[\frac{T_{\perp\alpha} - T_{\parallel\alpha}}{2T_{\parallel\alpha}} Z'(\zeta_\alpha^\pm) + \frac{1}{\sqrt{2} v_{T\parallel\alpha}} \left(u_\alpha - \frac{\omega}{k} \right) Z(\zeta_\alpha^\pm) \right] = 0 \tag{3.83}$$

with $v_{T\parallel\alpha} = \sqrt{k_B T_{\parallel\alpha}/m_\alpha}$ and $\zeta_\alpha^\pm$ the argument of the Fried and Conte functions:

$$\zeta_\alpha^\pm = \frac{1}{\sqrt{2} v_{T\parallel\alpha} k} (\omega - k u_\alpha \pm \Omega_\alpha) \tag{3.84}$$

where the subscript "0" for the drift velocity has been discarded to simplify the notation. This equation is the dispersion relation of electromagnetic waves propagating along an ambient magnetic field, and will be used to calculate the growth rate and unstable wavenumbers associated to the non-resonant mode. The first term in the right-hand side of Eq. 3.83 contains the effects of the temperature anisotropy, and the second term contains the effects of the zeroth order drift velocity. Since this equation encompasses all the parallel propagating electromagnetic modes, it is rather complex and needs further simplification to obtain analytical results. This is the purpose of the following sections.

3.3 Analytical solutions in various environments

3.3.1 Interaction regimes

In the following, the initial temperature will be supposed isotropic, such that $T_{\parallel\alpha} = T_{\perp\alpha} = T_\alpha$. In addition, it can be shown (Amato and Blasi [2009], Zacharegkas et al. [2019]) that the linear properties of the non-resonant mode are not modified by relativistic effects, such that $1 \ll k^2 c^2/\omega^2$. The dispersion relation can then be written as:

$$-k^2 c^2 - \frac{1}{\sqrt{2}} \sum_\alpha \left[\frac{\omega_{p\alpha}^2}{v_{T\alpha}} \left(u_\alpha - \frac{\omega}{k} \right) Z(\zeta_\alpha^\pm) \right] = 0 \tag{3.85}$$

This complex equation can only be solved numerically using dispersion codes, where the roots of the equation are found using dedicated numerical methods while considering a set of initial plasma parameters on a predefined range of wavenumbers or angular frequencies. Useful analytical results can however be obtained by simplifying the Fried and Conte functions using Taylor and asymptotic expansions.

The argument of the Fried and Conte functions is a key parameter that characterizes the interaction of the population α with the electromagnetic waves of angular frequency ω and wave number k. Depending on the value of $\zeta_\alpha^\pm$ (Eq. 3.84), three regimes of interaction can be distinguished (Gary and Feldman [1978]). The first one corresponds to $|\zeta_\alpha^\pm| > 1$,

where the bulk of the velocity distribution function of the population α is far from the cyclotron resonance condition $\omega - ku_\alpha \pm \Omega_\alpha = 0$. This so-called *cold regime* is non-resonant and may be correctly described using both a kinetic or a fluid approach, where the details of the distribution function are unimportant. The other case $|\zeta_\alpha^\pm| < 1$ can be defined as the *hot and demagnetized regime*, as the thermal Larmor radius is larger than the wavelengths of the mode. In such a case the particles respond weakly to the electromagnetic field perturbations. The intermediary regime, $|\zeta_\alpha^\pm| \sim 1$, corresponds to the situation where the bulk of the velocity distribution function lies near the cyclotron resonant velocity with the electromagnetic waves and, depending on the polarization and direction of propagation, important cyclotron resonant interactions can occur. This regime is particularly relevant to the case of the right-hand resonant and left-hand resonant streaming instabilities (Kulsrud and Pearce [1969]). The case $|\zeta_\alpha^\pm| \gtrsim 1$ can also be considered, where finite Larmor radius appear as small corrective terms in the dispersion relation, and will be referred as the *warm regime*. The three regimes of cold, warm and hot regimes will be considered successively in Sec. 3.3.2, 3.3.3 and 3.3.4. A particular emphasis will be made on the hot regime, for which no analytical theory has been developed in the literature.

3.3.2 Cold regime

The non-resonant streaming instability has first been investigated in the work of Sentman et al. [1981], where the authors studied reflected ions in the Earth bow shock and their propagation in the upstream solar wind. They found a "non-resonant fire-hose like" mode by solving numerically the kinetic dispersion relation of parallel propagating electromagnetic waves. The instability has been further investigated in Winske and Leroy [1984], where it was found that the instability may be described by neglecting the background protons, electrons and streaming population temperature, relativistic effects, and by supposing low frequency modes $\omega < \Omega_\alpha$ and a small density ratio $n_{cr}/n_m \ll 1$. Under such assumptions, the $\zeta_\alpha^\pm$ parameter in Eq. 3.85 can be simplified in order to obtain analytical results, using the approximation:

$$\zeta_\alpha^\pm \approx \frac{1}{\sqrt{2}} \left(-\frac{u_\alpha}{v_{T\alpha}} \pm \frac{1}{k r_{L\alpha}} \right) \tag{3.86}$$

where $r_{L\alpha} = v_{T\alpha}/\Omega_\alpha$ is the thermal Larmor radius of the population α. In the case of small thermal velocities, i.e. the drift velocity is larger than the thermal velocity and the thermal Larmor radius is smaller than the electromagnetic perturbation wavenumber, one obtains $|\zeta_\alpha^\pm| \gg 1$. In this limit the Fried and Conte functions can be approximated by a Taylor expansion at first order as:

$$Z(\zeta_\alpha^\pm) = -\frac{1}{\zeta_\alpha^\pm} \tag{3.87}$$

After simplification (Winske and Leroy [1984]), the fastest growing mode growth rate $\gamma_{\rm cold}$, wavenumber $k_{\rm cold}$ and real angular frequency $\omega_{\rm r,cold}$ may be calculated analytically as:

$$\gamma_{\rm cold} = \frac{1}{2} \frac{n_{cr}}{n_m} \frac{u_{cr}}{v_{A0}} \Omega_0 \tag{3.88}$$

$$k_{\rm cold} = \frac{1}{2}\frac{n_{cr}}{n_m}\frac{u_{cr}}{v_{A0}^2}\Omega_0 \tag{3.89}$$

$$\omega_{\rm r,cold} = \frac{1}{2}\frac{n_{cr}^2}{n_m^2}\frac{u_{cr}^2}{v_{A0}^2}\Omega_0 \tag{3.90}$$

One recovers the exact same results as the fluid model presented in Sec. 2.2.3. In the cold case the growth rate is independent of the ambient magnetic field and of the main protons temperature, which corresponds to the Larmor radius being much smaller than the instability wavelength, such that it does not modify the instability. This regime of interaction is particularly relevant in the context of supernova shocks in the cold and tenuous interstellar medium (Bell [2004]) and of back streaming populations from the earth bow shock region (Onsager et al. [1991], Akimoto et al. [1993]), where thermal effects are expected to be small.

3.3.3 Warm regime

In the same way as in the cold regime, the Fried and Conte function can be simplified using Taylor expansions while retaining additional terms to account for thermal corrections (Zweibel and Everett [2010]) as:

$$Z(\zeta_\alpha^\pm) = -\frac{1}{\zeta_\alpha^\pm} - \frac{1}{2(\zeta_\alpha^\pm)^3} + i\pi^{1/2}e^{-(\zeta_\alpha^\pm)^2} \tag{3.91}$$

The $-1/2(\zeta_\alpha^\pm)^3$ term represents the partial decoupling between the magnetic field and the particles due to their finite Larmor radius, whereas the imaginary term (not present at first order in the cold limit) encompasses the effects of particles interacting resonantly with the wave. The dispersion relation may then be written in the form :

$$\omega^2 - \omega\left(\frac{k^2 v_{Tm}^2}{2\Omega_0} + \Omega_0\frac{n_{cr}}{n_m} - i\sqrt{\pi}\frac{\Omega_0^2}{k v_{Tm}}e^{-\frac{\Omega_0^2}{k^2 v_{Tm}^2}}\right) - k^2 v_{A0}^2 + \Omega_0\frac{n_{cr}}{n_m}k u_{cr} = 0 \tag{3.92}$$

Supposing that the electrons remain cold, while retaining thermal effects for the background protons, the fastest growing mode $\gamma_{\rm warm}$ and associated wavenumber $k_{\rm warm}$ in the warm regime (also called WICE, Warm Ions Cold Electrons) are then found as:

$$\gamma_{\rm warm} = \left(\frac{n_{cr}}{n_m}\frac{u_{cr}}{v_{Tm}}\right)^{2/3}\Omega_0 \tag{3.93}$$

$$k_{\rm warm} = \left(\frac{n_{cr}}{n_m}\frac{u_{cr}}{v_{Tm}}\right)^{1/3}\frac{\Omega_0}{v_{Tm}} \tag{3.94}$$

The growth rate in this regime depends linearly on the initial magnetic field, and as $T_m^{-1/3}$ on the background protons temperature. Finite Larmor radius effects tend to reduce the non-resonant mode growth rate and shift the unstable wavelengths toward larger scales. A threshold for this regime can be calculated as $v_{A0}/v_{Tm} < (n_{cr}u_{cr}/n_m v_{Tm})^{1/3}$. This warm regime of interaction is of interest in low density, high temperature medium such as superbubbles and galaxy cluster shocks, where the non-resonant mode may be affected by the finite background protons temperature.

3.3.4 Hot and demagnetized regime

In the case of hot protons in a plasma permeated by a weak magnetic field, the background protons thermal Larmor radius can be larger than the instability wavelength. In this case, the Fried and Conte function can be expressed with its asymptotic approximation similarly to the cold and warm regimes, and allowing an analytical treatment of the dispersion relation (Marret et al. [2021]). By making the assumption of cold electrons and of cosmic rays with a large drift over thermal velocity ratio, the arguments of the Fried and Conte functions follow the limits: $|\zeta_{cr}^{\pm}| \gg 1$, $|\zeta_{e}^{\pm}| \gg 1$ and $|\zeta_{m}^{\pm}| < 1$. Using the appropriate asymptotic expansions, the Fried and Conte functions can then be rewritten (Fried and Conte [1961]) as:

$$Z(\zeta_{cr}^{\pm}) = -\sqrt{2}\left(\pm\frac{1}{kr_{Lcr}} - \frac{u_{cr}}{v_{Tcr}}\right)^{-1} + O(\zeta_{cr}^{\pm})^3 \tag{3.95}$$

$$Z(\zeta_{e}^{\pm}) = -\sqrt{2}\left(\pm\frac{1}{kr_{Le}} - \frac{u_{e}}{v_{Te}}\right)^{-1} + O(\zeta_{e}^{\pm})^3 \tag{3.96}$$

$$Z(\zeta_{m}^{\pm}) = -\sqrt{2}\left(\pm\frac{1}{kr_{Lm}}\right) + i\pi^{1/2} \quad + O(\zeta_{m}^{\pm})^3 \tag{3.97}$$

The exponential terms have been simplified and the contributions of order $O(\zeta_{\alpha}^{\pm})^3$ have been neglected. In the following, the real part of the expansions for each populations α will be noted R_α:

$$R_{cr} = -\sqrt{2}\left(\pm\frac{1}{kr_{Lcr}} - \frac{u_{cr}}{v_{Tcr}}\right)^{-1} \tag{3.98}$$

$$R_{e} = -\sqrt{2}\left(\pm\frac{1}{kr_{Le}} - \frac{u_{e}}{v_{Te}}\right)^{-1} \tag{3.99}$$

$$R_{m} = -\sqrt{2}\left(\pm\frac{1}{kr_{Lm}}\right) \tag{3.100}$$

Inserting the Fried and Conte expansions in the dispersion relation gives:

$$\sqrt{2}k^2\frac{v_{A0}^2}{\Omega_0^2} = \frac{1}{v_{Tm}}\left[\frac{\omega}{k}(R_m + i\pi^{1/2})\right] + \frac{R_e}{v_{Te}}\frac{\omega_{pe}^2}{\omega_{pm}^2}\left[\frac{\omega}{k} - u_e\right] + \frac{R_{cr}}{v_{Tcr}}\frac{\omega_{pcr}^2}{\omega_{pm}^2}\left[\frac{\omega}{k} - u_{cr}\right] \tag{3.101}$$

Separating the real and imaginary parts of the frequency $\omega = \omega_r + i\gamma$, one obtains:

$$\gamma(k) = -k\frac{\left[\sqrt{2}k^2\frac{v_{A0}^2}{\Omega_0^2} + \frac{u_e}{v_{Te}}\frac{\omega_{pe}^2}{\omega_{pm}^2}R_e + \frac{u_{cr}}{v_{Tcr}}\frac{\omega_{pcr}^2}{\omega_{pm}^2}R_{cr}\right]\frac{\pi^{1/2}}{v_{Tm}}}{\left[\frac{R_m}{v_{Tm}} + \frac{R_e}{v_{Te}}\frac{\omega_{pe}^2}{\omega_{pm}^2} + \frac{R_{cr}}{v_{Tcr}}\frac{\omega_{pcr}^2}{\omega_{pm}^2}\right]^2 + \frac{\pi}{v_{Tm}^2}} \tag{3.102}$$

$$\omega_r(k) = k\frac{\left[\sqrt{2}k^2\frac{v_{A0}^2}{\Omega_0^2} + \frac{u_e}{v_{Te}}\frac{\omega_{pe}^2}{\omega_{pm}^2}R_e + \frac{u_{cr}}{v_{Tcr}}\frac{\omega_{pcr}^2}{\omega_{pm}^2}R_{cr}\right]\left[\frac{R_m}{v_{Tm}} + \frac{R_e}{v_{Te}}\frac{\omega_{pe}^2}{\omega_{pm}^2} + \frac{R_{cr}}{v_{Tcr}}\frac{\omega_{pcr}^2}{\omega_{pm}^2}\right]}{\left[\frac{R_m}{v_{Tm}} + \frac{R_e}{v_{Te}}\frac{\omega_{pe}^2}{\omega_{pm}^2} + \frac{R_{cr}}{v_{Tcr}}\frac{\omega_{pcr}^2}{\omega_{pm}^2}\right]^2 + \frac{\pi}{v_{Tm}^2}} \tag{3.103}$$

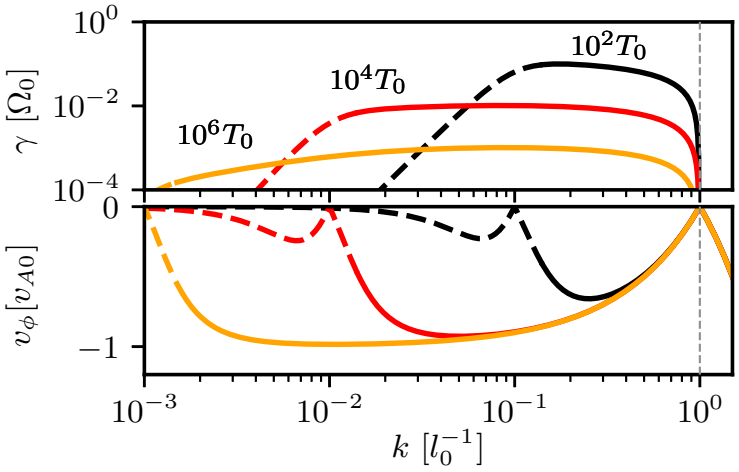

Figure 3.1: Growth rate $\gamma_{\rm hot}$ (upper panel) and phase velocity $v_\phi = \omega_{\rm r,hot}/k$ (lower panel) as a function of the wave number k, obtained from Eqs. 3.104 and 3.105. Parameters used are, in normalized units: $n_{cr}/n_m = 0.01$, $u_{cr} = 100\ v_{A0}$. The black, red and orange curves corresponds to $T_m = 10^2,\ 10^4,\ 10^6\ T_0$ respectively. The dotted portion of each curve corresponds to wave numbers where the demagnetized main protons assumption is not fulfilled. The grey vertical dashed line corresponds to $k = k_{\rm max}$ from Eq. 2.34.

Considering protons populations with a small density ratio n_{cr}/n_m, neglecting electron inertia and using the initial null current condition (Eq. 2.7), one obtains after some algebra the growth rate and real angular frequency in the hot, demagnetized regime of interaction:

$$\gamma_{\rm hot}(k) = \frac{(2\pi)^{1/2}}{r_{Lm}\xi} \frac{\dfrac{k}{\Omega_0}\left(v_{A0}^2 - \dfrac{n_{cr}}{n_m}u_{cr}^2\right) \mp \left(\dfrac{k^2}{\Omega_0^2}v_{A0}^2 + \dfrac{n_{cr}^2}{n_m^2}\right)u_{cr}}{\dfrac{\pi}{k^2 r_{Lm}^2} + 2\left(\dfrac{1}{k^2 r_{Lm}^2} - \dfrac{n_{cr}}{n_m}\dfrac{1}{\xi} - 1\right)^2} \tag{3.104}$$

$$\omega_{\rm hot}(k) = \frac{k^3 r_{Lm}^2\left(k^2 r_{Lm}^2 - 1\right)\left(\dfrac{n_{cr}}{n_m}u_{cr} \pm \dfrac{k}{\Omega_0}v_{A0}^2\right)}{k^4 r_{Lm}^4 + k^2 r_{Lm}^2\left(\dfrac{\pi}{2} - 2\right) + 1} \tag{3.105}$$

with $\xi = \pm k u_{cr}/\Omega_0 - 1$. Eqs. 3.104 and 3.105 are plotted in Fig. 3.1 as a function of the wavenumber k. The growth rate is strongly reduced with increasing temperature. The fastest growing mode is also modified, and shifts towards smaller wave numbers compared to the cold regime. In the warm regime, finite Larmor radius effects of the main protons play a role in determining the largest unstable wave number (Zweibel and Everett [2010]). In the hot regime however, the competition between the magnetic tension and the cosmic rays current driving term is the only determining factor of the largest unstable wave number, and one obtains good agreement with the fluid estimate $k_{\rm max} = \frac{n_{cr}}{n_m}\frac{u_{cr}}{v_{A0}^2}\Omega_0$. This property can be understood by considering the fluid model presented in Sec. 2.2 while retaining the Hall effect in Ohm's law to account for the decoupling between electrons and background protons in the demagnetized and collisionless regime. In that case, if one neglects the background pseudo-cyclotron motion, the resulting linearized background fluid

momentum conservation equation (eq. 2.25) is not modified. Consequently the maximum unstable wavenumber $k_{\max}$ is still solely determined by the balance between the cosmic rays magnetic force and the magnetic tension, hence the identical results in the cold and hot regimes.

Eqs. 3.104 and 3.105 may be further reduced to obtain information on the fastest growing mode. Considering $kr_{Lm} \gg 1$ and $ku_{cr}/\Omega_0 \gg 1$, which corresponds to the hypothesis of demagnetized main protons, and to the non-resonant instability requirement $k > k_{\min}$, one finds:

$$\gamma_{\text{hot}}(k) = \left(\frac{\pi}{2}\right)^{1/2} \frac{1}{r_{Lm} u_{cr}} \left[\pm \left(v_{A0}^2 - \frac{n_{cr}}{n_m} u_{cr}^2 \right) - \left(k \frac{v_{A0}^2}{\Omega_0^2} + \frac{1}{k} \frac{n_{cr}^2}{n_m^2} \right) u_{cr} \Omega_0 \right] \tag{3.106}$$

$$\omega_{\text{hot}}(k) = k \left(\frac{n_{cr}}{n_m} u_{cr} \pm \frac{k}{\Omega_0} v_{A0}^2 \right) \tag{3.107}$$

Calculating the growth rate derivative over k and searching for an extremum yields:

$$k_{\text{hot}} = \frac{n_{cr}}{n_m} \frac{\Omega_0}{v_{A0}} \tag{3.108}$$

Inserting in the expressions of $\gamma_{\text{hot}}(k)$ and $\omega_{\text{hot}}(k)$, one obtains the growth rate, real angular frequency and phase velocity $v_{\phi,\text{hot}} = \omega_{\text{hot}}/k_{\text{hot}}$ for the *fastest* growing unstable mode:

$$\gamma_{\text{hot}} = \left(\frac{\pi}{2}\right)^{1/2} \frac{n_{cr}}{n_m} \frac{u_{cr}}{v_{Tm}} \Omega_0 \tag{3.109}$$

$$\omega_{\text{r,hot}} = \frac{n_{cr}^2}{n_m^2} \frac{u_{cr}}{v_{A0}} \Omega_0 \tag{3.110}$$

$$v_{\phi,\text{hot}} = -\frac{n_{cr}}{n_m} u_{cr} \tag{3.111}$$

Eqs. 3.108 to 3.111 hold for $k_{\text{cold}} r_{Lm} \gtrsim 2$ This threshold for the hot regime originates from the first order asymptotic expansion of the main protons Fried and Conte function (Eq. 3.97), which cannot accurately describe the complete function for $\zeta_m^{\pm} \gtrsim 1/2$. One finds that the growth rate decreases as $T^{-1/2}$ with temperature, more rapidly than the $T^{-1/3}$ dependency in the warm protons regime. This result may be of importance in high temperature plasmas with small ambient magnetic field, where the instability growth may be strongly reduced. The real angular frequency and the fastest growing wave number are independent of the main protons temperature. In addition, the fastest growing wave number is also independent of the cosmic rays velocity. The phase velocity $v_{\phi,\text{hot}} = \omega_{\text{r,hot}}/k_{\text{hot}}$ is equal and opposed to the electron drift velocity compensating the cosmic rays current, which is the same result as in the cold regime.

These analytical results can be used to estimate the characteristic time and spatial scales associated to the non-resonant instability in various environments. Using a density ratio $n_{cr}/n_m = 10^{-5}$ and a shock velocity $u_{cr} = 2.10^3$ km.s^{-1} encountered in supernova and galaxy clusters shocks, one immediately finds that very large plasma β_m are required to reach the hot regime. Considering typical parameters of a cold and tenuous interstellar medium, $n_m = 1$ cm^{-3}, $T_m = 10^4$ K and $B = 10^{-6}$ G the demagnetized regime is not

relevant even by considering locally smaller magnetic field, and larger temperatures such as those found in superbubbles (Mac Low and McCray [1988]). The picture may change however when considering leakage of cosmic rays in the intergalactic medium. Taking parameters $n_m = 10^{-6}$ cm^{-3}, $n_{cr} = 10^{-9}$ cm^{-3}, $T_m = 10^6$ K, $u_{cr} = 10^2$ km.s^{-1}, and a magnetic field $B = 10^{-11}$ G (Kulsrud and Zweibel [2008]), one obtains demagnetized main protons. The growth rate $\gamma_{\rm hot} = 6.6 \times 10^{-10}$ s^{-1} corresponds to a growth time of the order of $2\pi\gamma_{\rm hot}^{-1} = 300$ years, which is strongly reduced by temperature by a factor $(2\pi)^{1/2} v_{A0}/v_{Tm} = 3 \times 10^{-3}$ compared to the cold prediction. The instability is not suppressed however, indicating that it may still develop in such environment and modify the propagation and transport of cosmic rays.

3.4 References

Akimoto, K., Winske, D., Gary, S. P., and Thomsen, M. F. (1993). Nonlinear evolution of electromagnetic ion beam instabilities. *Journal of Geophysical Research: Space Physics*, 98(A2):1419–1433.

Amato, E. and Blasi, P. (2009). A kinetic approach to cosmic-ray-induced streaming instability at supernova shocks. *Mon Not R Astron Soc*, 392(4):1591–1600.

Bell, A. R. (2004). Turbulent amplification of magnetic field and diffusive shock acceleration of cosmic rays. *Mon Not R Astron Soc*, 353(2):550–558.

Callen, J. D. (2006). Coulomb Collisions. In *Fundamentals of Plasma Physics*. University of Wisconsin, Madison, Wisconsin, draft edition.

Fried, B. D. and Conte, S. D. (1961). *The Plasma Dispersion Function*. Elsevier.

Gary, S. P. (1992). The mirror and ion cyclotron anisotropy instabilities. *Journal of Geophysical Research: Space Physics*, 97(A6):8519–8529.

Gary, S. P. and Feldman, W. C. (1978). A second-order theory for k B0 electromagnetic instabilities. *Physics of Fluids*, 21(1):72.

Kulsrud, R. and Pearce, W. P. (1969). The Effect of Wave-Particle Interactions on the Propagation of Cosmic Rays. *ApJ*, 156:445.

Kulsrud, R. M. and Zweibel, E. G. (2008). On the origin of cosmic magnetic fields. *Reports on Progress in Physics*, 71(4):046901.

Mac Low, M.-M. and McCray, R. (1988). Superbubbles in disk galaxies. *The Astrophysical Journal*, 324:776.

Marret, A., Ciardi, A., Smets, R., and Fuchs, J. (2021). On the growth of the thermally modified non-resonant streaming instability. *Monthly Notices of the Royal Astronomical Society*, 500(2):2302–2315.

Onsager, T. G., Winske, D., and Thomsen, M. F. (1991). Interaction of a finite-length ion beam with a background plasma: Reflected ions at the quasi-parallel bow shock. *Journal of Geophysical Research: Space Physics*, 96(A2):1775–1788.

Sentman, D. D., Edmiston, J. P., and Frank, L. A. (1981). Instabilities of low frequency, parallel propagating electromagnetic waves in the Earth's foreshock region. *Journal of Geophysical Research: Space Physics*, 86(A9):7487–7497.

Winske, D. and Leroy, M. M. (1984). Diffuse ions produced by electromagnetic ion beam instabilities. *Journal of Geophysical Research: Space Physics*, 89(A5):2673–2688.

Zacharegkas, G., Caprioli, D., and Haggerty, C. (2019). Modeling the Saturation of the Bell Instability Using Hybrid Simulations. *arXiv:1909.06481*.

Zweibel, E. G. and Everett, J. E. (2010). Environments for Magnetic Field Amplification by Cosmic Rays. *The Astrophysical Journal*, 709(2):1412–1419.

Chapter 4

Hybrid-PIC algorithm and numerical setup

Contents

4.1 Introduction

While linear theory is useful to establish the stability conditions and growth rates, it gives no quantitative information on the non-linear evolution of the modes as well as on the saturation of the instability. This difficulty can be overcome by performing computer simulations, where the integro-differential equations which govern the evolution of the plasma are solved numerically for a given set of initial parameters. The plasma being

constituted of charged particles, one needs to self-consistently compute their dynamic together with the electric and magnetic field evolution. The interactions between fields and particles occur via the source terms in Maxwell equations, which depend on the density of each of the plasma component, and on the total current. Such macroscopic quantities can be obtained in two ways: either by studying the evolution of the distribution function of each plasma component using Vlasov equation, and calculating the associated moments to retrieve the density and current; or calculate directly the evolution of the moments of the distribution function. The first method corresponds to the kinetic approach, the second method to the fluid approach. In both cases, depending on the size and duration of the plasma considered, the numerical resolution is very expensive in computation time and it is generally performed using massively parallelized codes running on hundreds (thousands) of CPUs or GPUs cores.

This chapter presents the numerical model used for the simulations presented in this thesis, the equations solved, as well as the physical hypothesis and limitations of the code. It also presents an overview of the physics of particle collisions, as well as their implementation in the simulations. The simulation results will be shown in the following Chapters 5 and 6.

4.2 Simulation models

4.2.1 Kinetic and fluid approaches

The coupled system of the Vlasov and Maxwell equations may be solved using various numerical methods, referred in the literature as Vlasov codes and Particle in Cell (PIC) codes. In Vlasov codes, the Vlasov equation is solved directly for each population of the plasma by discretizing the distribution functions in phase space, and by solving the resulting seven-dimensional system of equations (3D space, 3D velocity, and time) coupled with Maxwell's equations. This allows an accurate description of the linear and non-linear evolution of the plasma while retaining all kinetic effects. A disadvantage of this method is that the calculations require large amounts of computer memory, often restricting calculations to 1D or 2D geometry.

The PIC method aims to solve the Vlasov equation in an alternate manner, by discretizing the distribution function of each populations in space and in velocity using macroparticles, usually $10^5 - 10^{12}$ (Le et al. [2019]) depending on the dimensionality of the simulations, each macroparticle representing a fraction of the total distribution function. Note that the term "particle" in the PIC acronym can be misleading, as it is rather macroparticles which are themselves a discretization of the distribution function, and in no way real particles. Newton's motion equation is computed together with Maxwell equations for each macroparticle, which captures the same physics as solving Vlasov equation. Such calculation may be parallelized efficiently by computing individually the motion of each macroparticles while splitting the task among several processors by domain decomposition, leading to a consequent reduction of the real calculation time. However, the distribution function discretization leads to important numerical noise and to poor description of the the tails of the distribution functions. This can be partially mitigated by using more macroparticles, and by resorting to numerical adjustments such as high

order shape functions and numerical smoothing terms added in the equations, at the cost of additional computational time and deteriorated physical accuracy. As a consequence, numerical simulations are always a trade-off between size, resolution, physical accuracy and computational time.

In MagnetoHydroDynamic (MHD) codes the plasma is described by its zero order (density), first order (fluid velocity) and second order (pressure) moments, which are coupled to Maxwell's equations. The electrons and ions are supposed to be tied together by the magnetic field and evolve as a single quasi-neutral fluid. MHD models do not include kinetic effects such as resonances and finite Larmor radius effects, and are used to study the evolution of plasmas on large spatial and temporal scales, usually inaccessible to PIC codes.

4.2.2 The hybrid approach

The dynamic of a plasma is dictated by the interaction between multiple populations with various charges and masses, coupled with the electromagnetic field. For full-PIC simulations, where both the electrons and ions are modelled by macroparticles, the time step and mesh size must be adapted to follow the small electrons time and spatial scales. This requires prohibitive computational resources when studying plasmas at the ion scales because of the small electron to proton mass ratio $m_e/m_p \approx 5 \times 10^{-4}$, and results in overly small time steps and fine spatial resolution which are not always absolutely required to study the ion dynamic. When studying plasmas on ion scales, a common approximation in full-PIC simulations is to artificially increase the mass ratio to bring the electrons scales closer to the ions', i.e. $m_e/m_i \to 1$, at the cost of a degraded physical accuracy. The asymptotic limit of such approach is pair plasmas, where electrons and positrons are considered, and it is important for many astrophysical applications such as pulsar winds (Wada and Shibata [2007], Pétri [2016], Spitkovsky [2017]) and extra-galactic jets (Marcowith et al. [1995]).

The hybrid-PIC approach aims to alleviate the separation of scales issue in ion-electron plasma. It mixes fluid and PIC models by considering the electrons as a massless neutralising fluid, whereas the ion populations are treated kinetically. The massless assumption comes from the fact that the electrons are supposed to adapt to the ion dynamic at each time step to satisfy the quasi-neutrality hypothesis, which requires infinitely large accelerations, or equivalently infinitely small mass, i.e $m_e/m_i \to 0$. Alternatively, this can be understood as an approximation of infinitely large scale separation between the ions and electrons, such that the electrons dynamic is supposed instantaneous with respect to the ions'. This allows to relax the stringent constraints on the time step and spatial resolution imposed by the electron small mass, and permits long time scale studies while retaining the ions' kinetic effects. The non-resonant streaming instability is characterized by large time and spatial scales, of the order of the ions' inverse cyclotron frequency and inertial length. As such, a kinetic description of those of the electrons is unnecessary. In fact, a kinetic treatment of the ions is also not mandatory to capture the essential physics of the instability, in the limit of a small ion temperature. It becomes important in the situation where the ion Larmor radius is comparable or larger than the unstable wavelengths, as detailed in Sec. 3.2. The simulations presented in this thesis were performed with

the hybrid-PIC computer code Heckle (Smets, R. and Aunai [2011]), developed at the Laboratoire de Physique des Plasmas in France. The ions are described as macroparticles, and the electrons as a massless fluid. This hybrid approach is well suited to study the kinetic, non-linear evolution of systems at the ions temporal and spatial scale while avoiding prohibitive computational time. It can also be employed to calculate theoretically the dispersion relation of plasma waves, and reproduces the ion physics contained in a fully kinetic description while discarding electron kinetic effects such as electron Landau damping and electron cyclotron resonance (Told et al. [2016]).

A similar approach called MHD-PIC has been the subject of a growing interest in the astroparticle community for the acceleration of cosmic rays at shocks. The idea is to mix the particle and fluid approaches in order to be able to simulate plasmas on large time and spatial scales. Following a similar philosophy to the hybrid-PIC model, the electrons and background ions are treated as an MHD fluid, while a kinetic treatment is retained only for the cosmic rays which then contribute to the source terms in Maxwell's equation. This is particularly adequate to simulate the acceleration of cosmic rays at shocks, where the individual motion of the accelerated particles must be computed, whereas the kinetic effects in the background plasma may be neglected in some cases. Such approach however does not resolve the intermediary regime, i.e. the injection of cosmic rays, initially part of the background plasma and the expanding supernova remnant at the shock boundary. Current state-of-the-art MHD-PIC simulations circumvent this issue by injecting cosmic rays following prescriptions obtained from smaller scales PIC simulations of shocks (Bai et al. [2015], Casse et al. [2018], Mignone et al. [2018]).

4.3 The Heckle code

4.3.1 System of equations and normalizations

This section presents the basic set of equations solved by the code, the numerical scheme, and discuss the approximations and limitations of the code. The motion for each ion macroparticle k is obtained from Newton's equation while considering the electric and magnetic forces:

$$\frac{\mathrm{d}\mathbf{x}_k}{\mathrm{d}t} = \mathbf{v}_k \tag{4.1}$$

$$\frac{\mathrm{d}\mathbf{v}_k}{\mathrm{d}t} = \frac{q_k}{m_k}(\mathbf{E} + \mathbf{v}_k \times \mathbf{B}) \tag{4.2}$$

where q_k and m_k are the charge and mass respectively. The electromagnetic force is calculated using the electric and magnetic fields which are discretized on a Cartesian grid, and linearly interpolated from the grid to the macroparticle position. The magnetic field evolution is obtained from Maxwell-Faraday's equation:

$$\frac{\partial \mathbf{B}}{\partial t} = -\boldsymbol{\nabla} \times \mathbf{E} \tag{4.3}$$

As the electrons are not treated kinetically, the electric field must be obtained from the electron momentum density conservation equation, which gives in the case of negligible

electron inertia ($m_e = 0$) the generalized Ohm's law:

$$\mathbf{E} = -\mathbf{u}_i \times \mathbf{B} + \frac{1}{en_e}(\mathbf{J} \times \mathbf{B} - \boldsymbol{\nabla} \cdot \mathbf{P}_e) + \eta \mathbf{J} - \eta' \Delta \mathbf{J} \tag{4.4}$$

The first term on the right-hand side corresponds to the electric field produced by the ions fluid motion, the second and third terms are the Hall and electron pressure gradients contribution respectively. The fourth term corresponds to the electric field generated in the plasma because of the finite resistivity η, and the last term is a numerical dissipative term, with η' the hyperviscosity. In the simulations presented in this work, the electron pressure is calculated by supposing an isothermal, isotropic behavior:

$$P_e = n_e k_B T_e \tag{4.5}$$

where k_B is the Boltzmann constant, and T_e the uniform electron temperature fixed at the beginning of the simulation. In this case the pressure is a scalar, such that the pressure gradient forces due to the electrons can be computed directly as $\boldsymbol{\nabla} P_e = k_B T_e \boldsymbol{\nabla} n_e$.

The numerical drawback of using Ohm's law to calculate the electric field is the n_e^{-1} dependency in the Hall and electron pressure gradients terms. In PIC simulations, the number of macroparticles per cell results from the dynamic of the simulated plasma. As such, if the dynamic leads to the generation of a strong electric field in some regions of space, the macroparticles can be swept away from a given cell, decreasing the density and amplifying an electric field which will bring back the macroparticles via the pressure gradient term in Ohm's law. However if this electric field is too large, the macroparticles will "miss" the density hole. This can ultimately lead to a numerical singularity with a null density and a very large or undefined electric field. The most direct way of dealing with such issue is to inject new macroparticles in the simulation in under-dense regions, which is not always physically accurate and has a high computational cost. The density holes can also be avoided by reducing electric field fluctuations artificially. This can be done by introducing numerical resistivity terms at small scales in Ohm's law, allowing to dissipate electric fluctuations in regions of sharp gradients of the plasma current. This is the method employed in Heckle with the hyperviscosity term in Eq. 4.4. This hyperviscosity term has the interesting property of conserving large scale current structures, which may play an important role in hybrid-PIC simulations of magnetic reconnection (Aunai et al. [2013]).

4.3.2 The plasma current

Maxwell-Ampère's equation allows to calculate the total conduction current J in the plasma as a function of the electromagnetic field, and may be separated into the longitudinal and transverse components to the wave propagation direction $\mathbf{k}/k$ (noted with the subscripts "L" and "T" respectively). The longitudinal and transverse electric fields and currents can then be written as $\mathbf{J}_L = \mathbf{J} \cdot \mathbf{kk}/k^2$, $\mathbf{J}_T = \mathbf{J} - \mathbf{J}_L$, $\mathbf{E}_L = \mathbf{E} \cdot \mathbf{kk}/k^2$ and $\mathbf{E}_T = \mathbf{E} - \mathbf{E}_L$, such

that Maxwell-Ampère's equation becomes:

$$\mathbf{0} = \mu_0 \mathbf{J}_L + \frac{1}{c^2}\frac{\partial \mathbf{E}_L}{\partial t} \tag{4.6}$$

$$\boldsymbol{\nabla} \times \mathbf{B} = \mu_0 \mathbf{J}_T + \frac{1}{c^2}\frac{\partial \mathbf{E}_T}{\partial t} \tag{4.7}$$

In the non-relativistic limit, one may neglect the transverse component of the displacement current, corresponding to the second term in the right-hand side of Eq. 4.7. The transverse current $\mathbf{J}_T$ can then be obtained directly from the curl of B, and is used to calculate the Hall, resistive and hyperviscosity terms in Ohm's law. As a consequence the current involved in Ohm's law is only the transverse one in the hybrid-PIC non-relativistic model, which is an approximation of the exact equation where the total current (longitudinal and transverse) appears. A direct consequence of such simplification is that the speed of light, or alternatively the dielectric permittivity of vaccum, is not defined in the simulations. This leads to numerical complications when modeling plasma effects below the Debye length, such as Coulomb collisions. This will be further discussed in Sec. 4.4. The longitudinal current $\mathbf{J}_L$ is involved in the charge conservation equation:

$$\frac{\partial}{\partial t}\sum_\alpha Q_\alpha + \boldsymbol{\nabla} \cdot \mathbf{J}_L = 0 \tag{4.8}$$

The first term in the left-hand side is associated to the hypothesis of quasi-neutrality, but cannot be neglected *a priori* with respect to the longitudinal current gradient. Hence, despite the quasi-neutrality hypothesis, a longitudinal (electrostatic) component of the electric field can still exist. As a result, the acoustic ionic and ion Bernstein modes can develop in the hybrid-PIC model despite the longitudinal current not being explicitly part of the solved system of equations.

4.3.3 Normalizations and numerical scheme

The Hybrid-PIC code Heckle uses normalized quantities in order to manipulate numbers of the order unity to avoid numerical precision issues. Masses and charges are normalized to the proton mass m_p and elementary charge e respectively. The densities and magnetic field are normalized to a uniform reference value $n_0 = n_m(t=0)$ where n_m is the main ions density, and $B_0 = B(t=0)$. Frequencies, lengths and velocities are normalized to the initial proton cyclotron angular frequency $\Omega_0 = eB_0/m_p$, initial proton inertial length $l_0 = v_{A0}/\Omega_0 = c/\omega_{pm}$ where c is the speed of light, $\omega_{pm} = (n_0 e^2/\varepsilon_0 m_p)^{1/2}$ is the protons plasma frequency and $v_{A0} = B_0/(\mu_0 n_0 m_p)^{1/2}$ is the initial Alfvén velocity with μ_0 the magnetic permeability. Temperatures are expressed in terms of energy as $k_B T_0 = m_p v_{A0}^2$. Finally the electric field is normalized to $E_0 = v_{A0} B_0$.

The code solves the Vlasov-Maxwell system of equations using a predictor-corrector explicit scheme for the electromagnetic field, defined on a Cartesian grid. The numerical scheme used can be described as follows (Smets, R. and Aunai [2011]). First, the predictor step:

- $\mathbf{v}_{n+1/2} = \mathbf{v}_{n-1/2} + \dfrac{q\Delta t}{m}\left[\mathbf{E}_n + \dfrac{\mathbf{v}_{n+1/2} + \mathbf{v}_{n-1/2}}{2} \times \mathbf{B}_n\right]$

- $\mathbf{x}_{n+1} = \mathbf{x}_n + \Delta t \mathbf{v}_{n+1/2}$
- $\mathbf{N}_{n+1/2} = \Sigma_s q_s (S_n + S_{n+1})/2$
- $\mathbf{V}_{n+1/2} = \Sigma_s (S_n + S_{n+1}) \mathbf{v}_{n+1/2} / 2\mathbf{N}_{n+1/2}$
- $\mathbf{B}_{n+1/2} = \mathbf{B}_n - \dfrac{\Delta t}{2} \boldsymbol{\nabla} \times \mathbf{E}_n$
- $\mathbf{J}_{n+1/2} = \boldsymbol{\nabla} \times \mathbf{B}_{n+1/2}$
- $\mathbf{P}_{n+1/2} = N_{n+1/2} T_0$
- $\mathbf{E}_{n+1/2} = -\mathbf{V}_{n+1/2} \times \mathbf{B}_{n+1/2} + \dfrac{1}{N_{n+1/2}} \left(\mathbf{J}_{n+1/2} \times \mathbf{B}_{n+1/2} - \boldsymbol{\nabla} P_{n+1/2} \right) + \eta \mathbf{J}_{n+1/2}$
- $\mathbf{E}_{n+1} = -\mathbf{E}_n + 2\mathbf{E}_{n+1/2}$
- $\mathbf{B}_{n+1} = \mathbf{B}_{n+1/2} - \dfrac{\Delta t}{2} \boldsymbol{\nabla} \times \mathbf{E}_{n+1}$
- $\mathbf{J}_{n+1} = \boldsymbol{\nabla} \times \mathbf{B}_{n+1}$

Then, the corrector step:

- $\mathbf{v}_{n+3/2} = \mathbf{v}_{n+1/2} + \dfrac{q \Delta t}{m} \left[\mathbf{E}_{n+1} + \dfrac{\mathbf{v}_{n+3/2} + \mathbf{v}_{n+1/2}}{2} \times \mathbf{B}_{n+1} \right]$
- $\mathbf{x}_{n+2} = \mathbf{x}_{n+1} + \Delta t \mathbf{v}_{n+3/2}$
- $\mathbf{N}_{n+3/2} = \Sigma_s q_s (S_{n+1} + S_{n+2})/2$
- $\mathbf{V}_{n+3/2} = \Sigma_s (S_{n+1} + S_{n+2}) \mathbf{v}_{n+3/2} / 2\mathbf{N}_{n+3/2}$
- $\mathbf{B}_{n+3/2} = \mathbf{B}_{n+1} - \dfrac{\Delta t}{2} \boldsymbol{\nabla} \times \mathbf{E}_{n+1}$
- $\mathbf{J}_{n+3/2} = \boldsymbol{\nabla} \times \mathbf{B}_{n+3/2}$
- $\mathbf{P}_{n+3/2} = N_{n+3/2} T_0$
- $\mathbf{E}_{n+3/2} = -\mathbf{V}_{n+3/2} \times \mathbf{B}_{n+3/2} + \dfrac{1}{N_{n+3/2}} \left(\mathbf{J}_{n+3/2} \times \mathbf{B}_{n+3/2} - \boldsymbol{\nabla} P_{n+3/2} \right) + \eta \mathbf{J}_{n+3/2}$
- $\mathbf{E}_{n+1} = \dfrac{1}{2} (\mathbf{E}_{n+1/2} + \mathbf{E}_{n+3/2})$
- $\mathbf{B}_{n+1} = \mathbf{B}_{n+1/2} - \dfrac{\Delta t}{2} \boldsymbol{\nabla} \times \mathbf{E}_{n+1}$
- $\mathbf{J}_{n+1} = \boldsymbol{\nabla} \times \mathbf{B}_{n+1}$

with q the charge, m the mass and Δt the numerical time step. The motion of a macroparticle is computed using a non-relativistic Boris pusher (Boris [1970]), which algorithm is presented here for completeness. The equation which needs to be solved at the predictor step is:

$$\frac{\mathbf{v}_{n+1/2} - \mathbf{v}_{n-1/2}}{\Delta t} = \frac{q}{m} \left[\mathbf{E}_n + \left(\frac{\mathbf{v}_{n+1/2} + \mathbf{v}_{n-1/2}}{2} \right) \times \mathbf{B}_n \right] \tag{4.9}$$

Defining the variables:

$$\mathbf{v}_{n-1/2} = \mathbf{v}^- - \frac{q \mathbf{E}_n}{m} \frac{\Delta t}{2} \tag{4.10}$$

and

$$\mathbf{v}_{n+1/2} = \mathbf{v}^+ + \frac{q \mathbf{E}_n}{m} \frac{\Delta t}{2} \tag{4.11}$$

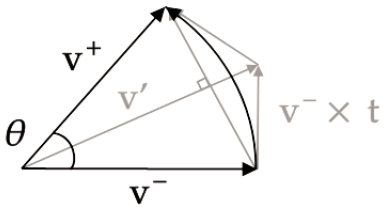

Figure 4.1: Illustration of the Boris pusher algorithm.

the equation of motion for a given macroparticle can be rewritten as:

$$\frac{\mathbf{v}^+ - \mathbf{v}^-}{\Delta t} = \frac{q}{2m}(\mathbf{v}^+ + \mathbf{v}^-) \times \mathbf{B}_n \tag{4.12}$$

Θ is the rotation angle between $\mathbf{v}^+$ and $\mathbf{v}^-$:

$$\left|\tan\frac{\Theta}{2}\right| = \frac{|\mathbf{v}^+ - \mathbf{v}^-|}{|\mathbf{v}^+ + \mathbf{v}^-|} = t = \frac{qB_n}{m}\frac{\Delta t}{2} \tag{4.13}$$

Defining the quantity v' as:

$$\mathbf{v}' = \mathbf{v}^- + \mathbf{v}^- \times \mathbf{t} \tag{4.14}$$

$$\mathbf{v}^+ = \mathbf{v}^- + \mathbf{v}' \times \mathbf{s} \tag{4.15}$$

To get $|\mathbf{v}^+| = |\mathbf{v}^-|$, one needs $s = 2/(1+t^2)$. Defining $F = q\Delta t/2m$ and $G = 2/(1+B_n^2F^2)$, one may solve the macroparticle motion as:

$$\mathbf{s} = \mathbf{v} + F\mathbf{E}_n \tag{4.16}$$

$$\mathbf{u} = \mathbf{s} + F(\mathbf{s} \times \mathbf{B}_n) \tag{4.17}$$

$$\mathbf{v} = \mathbf{s} + G(\mathbf{u} \times \mathbf{B}_n) + F\mathbf{E}_n \tag{4.18}$$

The algorithm is illustrated in Fig. 4.1 This operation is equivalent to performing half the acceleration by the electric field, then the rotation due to the magnetic field, and finally the other half acceleration by the electric field. The calculation is then repeated at the corrector step.

In PIC and hybrid-PIC simulations the particle pusher is the most expensive step, as it requires to repeat the calculation for each individual macroparticle. The computational time on a CPU for a modern computer is of the order of 1 μs per macroparticle and per time step. Considering a simulation with 10^7 macroparticles for a duration of 10^5 time steps, and neglecting the fields calculation on the grid, one obtains a computation time of approximately 12 days. This long duration can be reduced by parallelizing the calculation over several CPUs. By performing the simulation on a super computer and splitting the task between 100 CPU cores, one obtains a much more reasonable time of 3 hours. This rough estimation supposes a perfect scaling of the code performance with the number of cores. In practice this is not the case, as the parallelization process requires communication between the CPU cores which introduces overhead in the calculation. No study has been done on the scalability of the Heckle code, but it was observed to be approximately linear up to 1000 cores.

4.3.4 Macroparticle initialization

The background ions are initialized with a Maxwellian distribution:

$$f(\mathbf{v}) = n_0 \left(\frac{\alpha}{\pi}\right)^{3/2} e^{-\alpha(\mathbf{v}-\mathbf{u}_0)^2} \tag{4.19}$$

with $\alpha = m/2k_BT$, k_B the Boltzmann constant, $\mathbf{u}_0$ the drift velocity and n_0 the initial density. Such distribution can be obtained numerically by sampling macroparticles using the Box-Muller method (Box and Muller [1958]). Considering two uniformly distributed random numbers $(R_1, R_2) \in]0, 1]$, the velocity component v_j of a given macroparticle is calculated as:

$$v_j = \sqrt{-\frac{2\ln(R_1)k_BT_j}{m}}\cos(2\pi R_2) \tag{4.20}$$

where T_j is the temperature of the ion population in the j direction. This method corresponds to the calculation of the cumulative distribution function, which is then inverted in polar coordinates to obtain the velocity following a Maxwellian distribution.

It is known that the cosmic rays at supernova shocks and propagating in the galaxy follow a power law (Arbutina and Zekovic [2021]), usually defined in the cosmic rays research community as a function of momentum. In this calculation however the distribution will be defined as a function of velocity for numerical convenience. Such distribution can be obtained similarly to the Maxwellian case by inverting the cumulative distribution function. Considering velocities in a given direction between the minimum and maximum $v_{\min}$ and $v_{\max}$ and with a power index α, one may define the power law velocity distribution function as:

$$f(v) = Av^\alpha \tag{4.21}$$

where A is a normalization factor such that:

$$\int_{v_{\min}}^{v_{\max}} Aw^\alpha \mathrm{d}w = \frac{A}{\alpha+1}(v_{\max}^{\alpha+1} - v_{\min}^{\alpha+1}) = 1 \tag{4.22}$$

which gives $A = (\alpha+1)/(v_{\max}^{\alpha+1} - v_{\min}^{\alpha+1})$ with $\alpha \neq -1$. Integrating this expression between $v_{\min}$ and a random finite number v gives:

$$\int_{v_{\min}}^{v} Aw^\alpha \mathrm{d}w = \frac{A}{\alpha+1}(v^{\alpha+1} - v_{\min}^{\alpha+1}) = R \tag{4.23}$$

If the distribution is normalized, then R is a uniformly distributed random number between 0 and 1, which can be obtained numerically using a random number generator. Hence:

$$v = \left(\frac{\alpha+1}{A}R + v_{\min}^{\alpha+1}\right)^{1/(\alpha+1)} \tag{4.24}$$

Inserting the normalization factor, one finally obtains:

$$v = \left[(v_{\max}^{\alpha+1} - v_{\min}^{\alpha+1})\ R + v_{\min}^{\alpha+1}\right]^{1/(\alpha+1)} \tag{4.25}$$

The random velocity v follows a power law distribution between $v_{\min}$ and $v_{\max}$ with a power value α. The mean velocity u can be calculated directly as:

$$u = \int_{v_{min}}^{v_{max}} A w^{\alpha+1} \mathrm{d}w \tag{4.26}$$

$$= \frac{\alpha+1}{\alpha+2} \frac{v_{\max}^{\alpha+2} - v_{\min}^{\alpha+2}}{v_{\max}^{\alpha+1} - v_{\min}^{\alpha+1}} \tag{4.27}$$

with $\alpha \neq (-1, -2)$. However, for the case of the non-resonant mode, the exact shape of the distribution function does not play a role in the growth of the unstable wavelengths. More precisely, only the zeroth and first order moments are involved, namely the density and fluid velocity as presented in Sec. 2.2.3. As such, the cosmic rays drifting population will be modelled in the simulations using a Maxwellian distribution, without any loss of physical accuracy. This model cannot be used when studying the left-hand and right-hand resonant modes, where details of the cosmic rays streaming population are important in determining the growth of the electromagnetic perturbations (e.g. Holcomb and Spitkovsky [2018]). In this case the distribution function cannot be assumed to be Maxwellian, and a realistic distribution function must be considered.

4.3.5 Coupling the macroparticles to the fields

The coupling between fields and particles is accomplished via the moments (density, fluid velocity) of the distribution which appear in Ohm's and Ampère's laws. The fields being defined on a discrete, Cartesian grid, the moments must also be calculated on this grid. This operation is called moments deposition. The electron charge density is obtained from the quasi-neutrality hypothesis, $en_e \approx \sum_l q_l n_l$, and the ion fluid velocity $\mathbf{u}_i$ is obtained by a sum over the ion populations ℓ such that:

$$en_e(\mathbf{x}) = q_i n_i(\mathbf{x}) = \sum_{k,\ell} q_\ell S(\mathbf{x} - \mathbf{x}_{\ell,k}) \tag{4.28}$$

$$\mathbf{u}_i(\mathbf{x}) = \sum_{\ell,k} \mathbf{v}_{\ell,k} S(\mathbf{x} - \mathbf{x}_{\ell,k}) / \sum_{\ell,k} S(\mathbf{x} - \mathbf{x}_{\ell,k}) \tag{4.29}$$

In these expressions, $\mathbf{x}$ is the grid point position, $\mathbf{x}_{k,\ell}$ the position of a macro-particle k from population ℓ, and:

$$S(\mathbf{x} - \mathbf{x}_{\ell,k}) = W_\ell \prod_j S_j \tag{4.30}$$

is the first order shape function where:

$$S_j = \begin{cases} 0 & |(\mathbf{x} - \mathbf{x}_{\ell,k}) \cdot \mathbf{e}_j| \geq \Delta x_j \\ |(\mathbf{x} - \mathbf{x}_{\ell,k}) \cdot \mathbf{e}_j| / \Delta x_j & |(\mathbf{x} - \mathbf{x}_{\ell,k}) \cdot \mathbf{e}_j| < \Delta x_j \end{cases} \tag{4.31}$$

with $j = x$ for simulations in 1D aligned along the $\mathbf{e}_x$ direction. For 2D simulations in the $\mathbf{e}_x$ and $\mathbf{e}_y$ directions, $j = x, y$ and $j = x, y, z$ for 3D simulations. Δx_j is the grid size in the j direction. The shape function corresponds to the spatial extent of a macroparticle. An illustration is given in Fig. 4.2. The ion species have different numerical weights W_ℓ

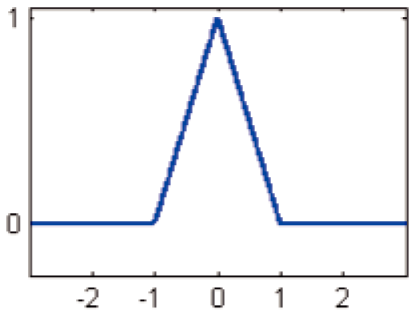

Figure 4.2: Illustration of S_j (ordinate) as a function of $|(\mathbf{x}-\mathbf{x}_{\ell,k})\cdot\mathbf{e}_j|/\Delta x_j$ (abscissa) considering a first order shape function.

for fluid quantities calculation, defined as:

$$W_\ell = \frac{n_\ell}{N_\ell} \tag{4.32}$$

with n_ℓ the density and N_ℓ the number of macroparticles per cell at the beginning of the simulation. The numerical weight allows the simulation of very different densities while keeping the same number of macroparticles for each species. The pressure tensor, defined as $\mathbf{P}_\ell = m_\ell \int_{-\infty}^{+\infty}(\mathbf{v}-\mathbf{u}_\ell)(\mathbf{v}-\mathbf{u}_\ell)f_\ell(\mathbf{v})\mathrm{d}\mathbf{v}$, can be calculated in the same manner for the interpretation of simulations. The expression used for numerical calculation of the integral for the component ij for a population ℓ is then:

$$P_{ij,\ell} = m_\ell \sum_k S(\mathbf{x}-\mathbf{x}_{\ell,k})(v_{i,\ell k}-u_{i,\ell})(v_{j,\ell k}-u_{j,\ell}) \tag{4.33}$$

The pressure is a centered moment, and consequently needs to be recalculated if one needs to project its components in a different vector basis, such as the local magnetic field aligned basis $\mathbf{e}_\parallel = \frac{\mathbf{B}_0}{B_0} = \mathbf{e}_x$ (parallel component), $\mathbf{e}_\times = \frac{\mathbf{B}_1}{B_1} \times \mathbf{e}_\parallel$ (normal component) and $\mathbf{e}_\perp = \mathbf{e}_\parallel \times \mathbf{e}_\times$ (perpendicular component) defined in Sec. 2.2.3.

In Heckle, a first order shape function is used, allowing a given macroparticle to contribute to the calculation of fluid moments in a maximum of two cells (in 1D geometry). This permits a precise description of gradients in the simulations, as the spatial extent of a macroparticle is of the order of the grid size. The cost of this accuracy is an increased numerical noise for a given number of particle per cells. The motion of a macroparticle from one cell to the adjacent one makes its shape function vanish, generating high frequency electric fluctuations on scales of the order of the grid size. This can lead to numerical instability and is inherent to the PIC approach. The most direct way of reducing these fluctuations is to increase the number of macroparticles per cell, at the cost of a larger computational time. Alternatively, higher order shape functions can be used, corresponding to a given macroparticle contributing to a larger number of cells. High order shape functions are commonly used in PIC codes to avoid resorting to a large number of macroparticles per cell, at the expense of a poorer description of spatial gradients and of an increased numerical complexity in the moment deposition calculation.

4.4 Including particle collisions in the simulations

4.4.1 Coulomb collision operator

The Coulomb collisions refer to interactions between charged particles via electric fields on small scales, as opposed to interactions via the electric field generated by collective effects such as the induction and the Hall electric field obtained in fluid theory. The evolution of the distribution function of a population α in a plasma including collisions is described by the Boltzmann equation:

$$\frac{\partial f_\alpha}{\partial t} + \mathbf{v}\cdot\boldsymbol{\nabla} f_\alpha + \frac{q_\alpha}{m_\alpha}(\mathbf{E}+\mathbf{v}\times\mathbf{B})\cdot\frac{\partial f_\alpha}{\partial \mathbf{v}} = \left(\frac{\partial f_\alpha}{\partial t}\right)_C \tag{4.34}$$

The electric field $\mathbf{E}$ in Eq. 4.34 is the large scale electric field, and does not include the fluctuating component on scales below a certain characteristic small scale, which will be characterized in the following. Collisions are taken into account via the term on the right-hand side of Eq. 4.34, which corresponds to the variation of the number of particles of the population α per unit of time and of phase space because of collisions. Under this generic name is hidden the complexity of interactions between the particles themselves, and it also includes close range interactions such as charged-neutral particle collisions. The collision operator can be decomposed as:

$$\left(\frac{\partial f_\alpha}{\partial t}\right)_C = \sum_\beta C_{\alpha\beta} \tag{4.35}$$

where $C_{\alpha\beta}$ is the contribution of the collisions between the populations α and β. It can be written in the general form:

$$C_{\alpha\beta} = \int u \frac{\mathrm{d}\sigma}{\mathrm{d}\Omega}(f'_\alpha f'_\beta - f_\alpha f_\beta)\mathrm{d}^3\mathbf{v}_\beta \mathrm{d}\Omega \tag{4.36}$$

where $f_{\alpha,\beta}$ and $f'_{\alpha,\beta}$ are the distribution functions before and after the collision respectively, u is the relative velocity before collision, and $\mathrm{d}\sigma/\mathrm{d}\Omega$ is the differential collision cross-section with Ω the scattering angle. Because of its complexity, it is rarely used in this form in analytical or numerical studies and requires simplifications to make calculations tractable. The Bhatnagar-Gross-Krook (BGK) operator (Bhatnagar et al. [1954]) is the simplest approximation of the collision operator and consists in a relaxation term of the form:

$$\left(\frac{\partial f_\alpha}{\partial t}\right)_C = -\nu(f_\alpha - f_{\alpha 0}) \tag{4.37}$$

with $f_{\alpha 0}$ an equilibrium distribution (usually a Maxwellian distribution) and ν a characteristic frequency, often assimilated to the collision frequency. It is a phenomenological operator, which characterizes the tendency of collisions to reduce anisotropies and drive the distribution toward a Maxwellian. Its main advantage is its relative simplicity in analytical calculations. A more precise approximation of the Boltzmann operator can be obtained by taking into account the fact that small angle scattering collisions are much more frequent that large angle scattering collisions in a plasma. One may then obtain

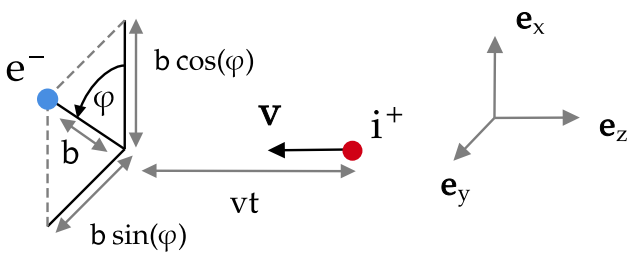

Figure 4.3: Schematic view of a Coulomb collision between an electron (noted e^-) and an ion (noted i^+) in the Lorentz model. The two particles are separated by a distance vt in the $\mathbf{e}_z$ direction, and by the distance b called impact parameter, in the plane $(\mathbf{e}_x, \mathbf{e}_y)$.

after a lengthy derivation the Landau collisions operator (Landau [1965]):

$$C_{\alpha\beta} = -\frac{1}{8\pi\epsilon_0^2}\frac{q_\alpha^2 q_\beta^2}{m_\alpha}\ln\Lambda_{\alpha\beta}\frac{\partial}{\partial\mathbf{v}_\alpha}\cdot\int\frac{u^2\mathbb{1}-\mathbf{uu}}{u^3}\cdot\left(\frac{f_\alpha}{m_\beta}\frac{\partial f_\beta}{\partial\mathbf{v}_\beta}-\frac{f_\beta}{m_\alpha}\frac{\partial f_\alpha}{\partial\mathbf{v}_\alpha}\right)\mathrm{d}^3\mathbf{v}_\beta \tag{4.38}$$

While still difficult to handle in analytical calculations, this operator can be solved numerically in PIC simulations.

4.4.2 Theoretical elements of Coulomb collisions

The effects of Coulomb collision can be illustrated by considering the Lorentz model, where a test particle electron collides with an immobile ion. The derivation can be found in textbooks such as Trubnikov [1965] and Callen [2006]. A brief summary of the calculation is presented here. In the reference frame of the electron, the ion is assumed to move with a velocity $-v\mathbf{e}_z$ in a straight line trajectory. The electron position can then be written as a function of the impact parameter b, time t and angle φ:

$$\mathbf{x} = b\cos(\varphi)\ \mathbf{e}_x + b\sin(\varphi)\ \mathbf{e}_y + vt\ \mathbf{e}_z \tag{4.39}$$

$$|\mathbf{x}| = \sqrt{b^2+v^2t^2} \tag{4.40}$$

A schematic of the situation is shown in Fig. 4.3. The electron interacts with the ion via the electric force $\mathbf{F}(\mathbf{x}) = -Ze^2\mathbf{x}/4\pi\epsilon_0|\mathbf{x}|^3$ with Z the ion atomic number. The change of velocity can then be obtained by integrating Newton's equation in the direction perpendicular to the initial velocity as:

$$m_e\Delta\mathbf{v}_\perp = -\frac{Ze^2 b}{4\pi\epsilon_0}(\cos(\varphi)\mathbf{e}_x+\sin(\varphi)\mathbf{e}_y)\int_{-\infty}^{+\infty}\frac{\mathrm{d}t}{(b^2+v^2t^2)^{3/2}} \tag{4.41}$$

$$= -\frac{Ze^2}{2\pi\epsilon_0 bv}(\cos(\varphi)\mathbf{e}_x+\sin(\varphi)\mathbf{e}_y) \tag{4.42}$$

with $t=0$ for $|\mathbf{x}|=b$. Their is no parallel component as $t/(b^2+v^2t^2)^{3/2}$ is an odd function of t and consequently vanishes when integrated in time. Considering $b\sim n_e^{-1/3}$ and $v\sim v_{Te}$, one obtains $\Delta v_\perp/v \sim (n_e\lambda_D^3)^{-2/3} \ll 1$ such that the typical angle of deflection by a single encounter between the electron and an ion is small. For elastic collisions, the total electron

energy is conserved such that:

$$\frac{1}{2}m_e|\mathbf{v}|^2 = \frac{1}{2}m_e|\mathbf{v}+\Delta\mathbf{v}|^2 \tag{4.43}$$

which yields:

$$\mathbf{v}\cdot\Delta\mathbf{v} = v\Delta v_\parallel \approx -\frac{1}{2}\Delta\mathbf{v}_\perp\cdot\Delta\mathbf{v}_\perp \tag{4.44}$$

Hence:

$$\Delta v_\parallel = -\frac{2Z^2e^4}{(4\pi\epsilon_0)^2b^2v^3m_e} \tag{4.45}$$

By integrating over angles, impact parameters and number of ions passed by the electron: $n_i\int \mathrm{d}^3x dt = n_i\frac{\mathrm{d}z}{\mathrm{d}t}\int \mathrm{d}x\mathrm{d}y = n_i v\int_0^{2\pi} d\varphi\int_0^{+\infty} b\ \mathrm{d}b$, the averaged parallel force can be calculated as:

$$\langle F_\parallel\rangle = m_e\frac{\Delta v_\parallel}{\Delta t} = m_e n_i v\int_0^{2\pi}\mathrm{d}\varphi\int_0^{+\infty}\Delta v_\parallel b\ \mathrm{d}b \tag{4.46}$$

$$= -4\pi\frac{Z^2e^4}{(4\pi\epsilon_0)^2v^2m_e}n_i\int_0^{+\infty}\frac{\mathrm{d}b}{b} \tag{4.47}$$

This integral diverges in both limits, but can be reduced by physical considerations. The lower limit $b_{\min}$ can be estimated as the classical distance of closest approach between the electron and the ion, which can be defined as the distance for which $|\Delta v_\parallel| = |\Delta v_\perp|$ corresponding to a $\pi/2$ deflection (often referred as the Landau length), and yields $b_{\min} = Ze^2/12\pi\epsilon_0 k_b T_e$. The electron kinetic energy is supposed to be of the order $m_e v^2 \approx 3k_bT_e$ while considering electrons with a Maxwellian distribution. The upper limit $b_{\max}$ can be estimated as the maximum impact parameter for which the interaction between the electron and the immobile ion alters significantly the electron trajectory. In this case the Debye length, corresponding to the distance above which the ion Coulomb potential is screened by the electrons, can be used such that $b_{\max} = \lambda_D = (\epsilon_0 k_B T_e/n_e e^2)^{1/2}$. The averaged parallel force then becomes:

$$\langle F_\parallel\rangle = -4\pi\frac{Z^2e^4}{(4\pi\epsilon_0)^2v^2m_e}n_i\int_{b_{\min}}^{b_{\max}}\frac{\mathrm{d}b}{b} = -4\pi\frac{Z^2e^4}{(4\pi\epsilon_0)^2v^2m_e}n_i\ln\Lambda \tag{4.48}$$

where $\ln\Lambda$ is the Coulomb logarithm with:

$$\Lambda = \frac{b_{\max}}{b_{\min}} \tag{4.49}$$

The Debye length constitutes the minimum spatial scale of the electric field fluctuations in Eq. 4.34. The Coulomb logarithm is of the order $\ln\Lambda \sim 10-30$ depending on the plasma parameters. It can be considered to remain constant as a first order approximation. Using quasi-neutrality the equality $Zn_i = n_e$ holds, hence:

$$m_e\frac{\mathrm{d}v_\parallel}{\mathrm{d}t} = -\nu_{ei}^L m_e v_\parallel \tag{4.50}$$

where ν_{ei}^{L} is the Coulomb collision frequency in the Lorentz model of a single test electron in a population of immobile field ions:

$$\nu_{ei}^{\mathrm{L}} = \frac{1}{4\pi\epsilon_0^2}\frac{Ze^4}{m_e^2}\frac{n_e}{v^3}\ln\Lambda \tag{4.51}$$

This rate depends strongly on the relative velocity v and linearly with the density, such that high temperature, low density plasma tend to be collisionless. The collision being elastic, the slowing down in the parallel direction (to the initial velocity) leads to a scattering in the perpendicular direction. In the case of a Maxwellian distribution of slowly drifting test particle electrons population (relative to their thermal velocity), it can be shown that the collision frequency is modified by a factor $4/3\sqrt{\pi} \approx 0.75$. From this expression, one may calculate the plasma conductivity which appears in Ohm's law $\mathbf{J} = \sigma\mathbf{E}$ as $\sigma = n_e e^2/m_e\nu_{ei}^{L}$.

The calculation for collisions between two moving particles, being electrons or ions, is more complicated than in the Lorentz model, as the field particle cannot be considered immobile, and involves the Rosenbluth potentials (Rosenbluth et al. [1957]). It can be shown that the situation of a test particle α colliding with a background population β following a Maxwellian velocity distribution leads to several Coulomb collision processes: momentum loss, parallel and perpendicular diffusion, and energy loss, expressed respectively as:

$$\frac{\mathrm{d}}{\mathrm{d}t}(m_\alpha\mathbf{v}) = -\nu_S^{\alpha/\beta} m_\alpha\mathbf{v} \tag{4.52}$$

$$\frac{\mathrm{d}}{\mathrm{d}t}|\mathbf{v}-\mathbf{u}|_\perp^2 = -\nu_\perp^{\alpha/\beta} v^2 \tag{4.53}$$

$$\frac{\mathrm{d}}{\mathrm{d}t}|\mathbf{v}-\mathbf{u}|_\parallel^2 = -\nu_\parallel^{\alpha/\beta} v^2 \tag{4.54}$$

$$\frac{\mathrm{d}}{\mathrm{d}t}\varepsilon_\alpha = -\nu_\varepsilon^{\alpha/\beta}\varepsilon_\alpha \tag{4.55}$$

with v the velocity of the test particle in the background reference frame, and $\varepsilon_\alpha = m_\alpha v^2/2$. To each process is associated a characteristic rate:

$$\nu_S^{\alpha/\beta} = -\left[\left(1+\frac{m_\alpha}{m_\beta}\right)\psi\right]\nu_0^{\alpha/\beta} \tag{4.56}$$

$$\nu_\perp^{\alpha/\beta} = -\left[\psi+\psi'-\frac{\psi}{2x}\right]\nu_0^{\alpha/\beta} \tag{4.57}$$

$$\nu_\parallel^{\alpha/\beta} = -\left[\frac{\psi}{x}\right]\nu_0^{\alpha/\beta} \tag{4.58}$$

$$\nu_\varepsilon^{\alpha/\beta} = -\left[2\nu_S^{\alpha/\beta}-\nu_\perp^{\alpha/\beta}-\nu_\parallel^{\alpha/\beta}\right]\nu_0^{\alpha/\beta} \tag{4.59}$$

In these expressions, $x = v_\alpha^2/v_{T\beta}^2$ with $v_{T\beta}^2$ the thermal velocity of the background particles β, and ψ is the Maxwell integral:

$$\psi(x) = \frac{2}{\sqrt{x}}\int_0^x \mathrm{d}t\sqrt{t}e^{-t} \tag{4.60}$$

The fundamental collision frequency $\nu_0^{\alpha/\beta}$ is defined by:

$$\nu_0^{\alpha/\beta} = \frac{1}{4\pi\epsilon_0^2}\frac{q_\alpha^2 q_\beta^2}{m_\alpha^2}\frac{n_\beta}{v^3}\ln\Lambda_{\alpha\beta} \tag{4.61}$$

where the Coulomb logarithm $\ln\Lambda_{\alpha\beta}$ is calculated as:

$$\ln\Lambda_{\alpha\beta} = \ln\left(4\pi\epsilon_0\lambda_D\frac{m_{\alpha\beta}}{m_\beta}\frac{k_B T_\beta}{q_\alpha q_\beta}\right) \tag{4.62}$$

with $m_{\alpha\beta} = m_\alpha m_\beta/(m_\alpha + m_\beta)$ the reduced mass. As each collision event produces a small scattering, the Coulomb collision frequency does not represent the actual frequency at which each individual interactions occur. It quantifies instead a characteristic time for which numerous interactions lead to an overall significant change in velocity. The Coulomb collisions can be separated in intra-species and inter-species collisions, depending on whether the collisions occur among particles of a given population, or between two different populations. The intra-species collisions produce the effect of reducing temperature anisotropies and drive the distribution toward an isotropic Maxwellian. Inter-species collisions reduce the relative drift velocity between the colliding populations, and equalize temperatures between the populations (Trubnikov [1965]).

Supposing that the colliding populations have a characteristic relative velocity equal to their thermal velocity $v = v_{T\alpha}$, the Maxwell integral can be simplified asymptotically, allowing the slowing down rates to be ordered with respect to the electron-ion collision fundamental collision frequency as:

$$\nu_S^{e/e} = \frac{0.86}{Z_i}\nu_0^{e/i}, \quad \nu_S^{i/i} = 0.86 Z_i^2\sqrt{\frac{m_e}{m_i}}\nu_0^{e/i}, \quad \nu_S^{i/e} = 0.75 Z_i\frac{m_e}{m_i}\nu_0^{e/i} \tag{4.63}$$

with $Z_i = q_i/e$. A similar scaling can be found for the diffusion and energy loss rates (Callen [2006]). In the simulations presented in this thesis, the electron-electron collisions are not explicitly computed, but are implicitly assumed to occur on time scales much shorter than those associated to other components of the plasma, consistent with the isothermal fluid assumption used for the electron population. The electron-ion collisions are taken into account via a fixed resistivity in Ohm's law (see Sec. 4.5). The ion-electron momentum loss is much less efficient than electron-ion momentum loss, because of the large difference in mass. For this reason ion-electron collisions will be neglected in the simulations presented in this work. Only the ion-ion collisions are directly computed in the simulations.

4.4.3 Numerical implementation

The numerical resolution of the ion-ion Coulomb collisions was implemented in the hybrid-PIC code Heckle by Loïc Nicolas during its PhD thesis at the LERMA laboratory (Nicolas [2017]). The Landau collisions operator is numerically solved using the method proposed in Takizuka and Abe [1977]. The algorithm is corrected to take into account different numerical weights between populations following the prescription of Miller and Combi

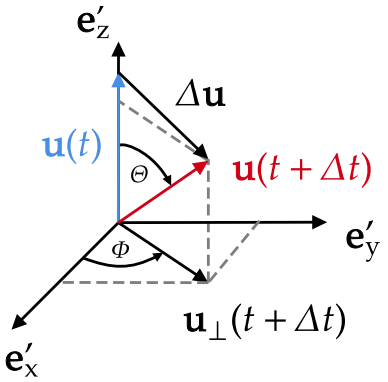

Figure 4.4: Schematic view of the spherical coordinates used to calculate the post collision velocity $\mathbf{u}(t+\Delta t)$ of a pair of macroparticles, as a function of the relative velocity $\mathbf{u}(t)$ before the collision.

[1994] and Nanbu and Yonemura [1998]. This section gives a brief overview of the numerical method employed.

The algorithm relies on the pairing of macroparticles within a given cell in the simulation at each time step, which then allows to compute a scattering angle. Although the collisions are binary in the simulations, this does not contradict the physical process of Coulomb collision, as the average total effect of randomly paired macroparticle collisions over many time step is equivalent to solving the Landau operator (Takizuka and Abe [1977]). Once the random pairing of macroparticles is performed, the scattering angle is computed from the relative velocity using a Monte Carlo algorithm. The calculation is done in the reference frame $(\mathbf{e}'_x, \mathbf{e}'_y, \mathbf{e}'_z)$, where the relative velocity between a pair of macroparticles is aligned with the $\mathbf{e}'_z$ direction as illustrated in Fig. 4.4. The change in velocity $\Delta\mathbf{u} = \mathbf{u}(t+\Delta t) - \mathbf{u}(t)$ with Δt the numerical time step is then obtained in the simulation reference frame $(\mathbf{e}_x, \mathbf{e}_y, \mathbf{e}_z)$ as:

$$\Delta u_x = \frac{u_x}{u_\perp} u_z \sin\Theta\cos\Phi - \frac{u_y}{u_\perp} u \sin\Theta\sin\Phi - u_x(1-\cos\Theta) \tag{4.64}$$

$$\Delta u_y = \frac{u_y}{u_\perp} u_z \sin\Theta\cos\Phi + \frac{u_x}{u_\perp} u \sin\Theta\sin\Phi - u_y(1-\cos\Theta) \tag{4.65}$$

$$\Delta u_z = -u_\perp \sin\Theta\cos\Phi - u_z(1-\cos\Theta) \tag{4.66}$$

where $u_\perp = \sqrt{u_x^2 + u_y^2}$ is the velocity in the $(\mathbf{e}_x, \mathbf{e}_y)$ plane, and $u = |\mathbf{u}(t)|$. Using these expressions, the post collision velocities of the two colliding macroparticles α and β are then calculated as:

$$\mathbf{v}_\alpha(t+\Delta t) = \mathbf{v}_\alpha(t) + \frac{m_{\alpha\beta}}{m_\alpha}\Delta\mathbf{u} \tag{4.67}$$

$$\mathbf{v}_\beta(t+\Delta t) = \mathbf{v}_\beta(t) + \frac{m_{\alpha\beta}}{m_\beta}\Delta\mathbf{u} \tag{4.68}$$

The angle Φ is calculated by sampling a uniformly distributed angle such that $0 < \Phi < 2\pi$. The scattering angle Θ is obtained from the relations:

$$\sin\Theta = \frac{2\delta}{1+\delta^2} \tag{4.69}$$

$$1 - \cos\Theta = \frac{2\delta^2}{1+\delta^2} \tag{4.70}$$

where δ is a random variable which characterizes a collision frequency in the simulations. It follows a Gaussian distribution of variance:

$$\langle\delta^2\rangle = \frac{1}{8\pi\epsilon_0^2}\frac{q_\alpha^2 q_\beta^2}{m_{\alpha\beta}^2}\frac{n_L}{u^3}\Delta t \ln\Lambda \tag{4.71}$$

with $n_L = \min(n_\alpha, n_\beta)$. The scattering occurs at each time step, and is stronger for larger δ. In order to account for different numerical weights in inter-species collisions, the δ parameter must be corrected (Miller and Combi [1994], Nanbu and Yonemura [1998]) as:

$$\delta' = \begin{cases} \delta \times \dfrac{\max(W_\alpha, W_\beta)}{W_\beta} & N_\alpha > N_\beta \\ \delta \times \dfrac{\max(W_\alpha, W_\beta)}{W_\alpha} & N_\alpha < N_\beta \end{cases} \tag{4.72}$$

where $N_{\alpha,\beta}$ is the number of macroparticles of species α and β in a given numerical cell, where the macroparticle pairing is done. The calculation of the δ parameter and of the Coulomb logarithm involves the dielectric permittivity ϵ_0, which is not defined in the system of equations solved in the code. As a consequence the values of δ and $\ln\Lambda$ are normalized via the two parameters σ_0 and Ψ_0 defined as:

$$\sigma_0 = \frac{1}{8\pi\epsilon_0^2}\frac{e^4}{m_p^2}\frac{n_0}{v_{A0}^3}\Omega_0 \tag{4.73}$$

and:

$$\Psi_0 = \ln\left(4\pi\frac{(k_B T_0\epsilon_0)^{3/2}}{e^3\sqrt{n_0}}\right) \tag{4.74}$$

which are given as input to the simulations. Fixing these parameters is equivalent to defining the reference density n_0 and magnetic field B_0, such that they verify the parameters σ_0 and Ψ_0 while being constrained by the elementary charge e, proton mass m_p, speed of light c and dielectric permittivity ϵ_0.

4.4.4 Ion-neutral collisions

The ion-neutral collisions differ significantly from the Coulomb collisions, as they result from close range interaction between the neutral and the ion. The Coulomb collisional scattering is the result of multiple interactions, as opposed to the "classical" binary collisions occurring for neutral collisions. A schematic is shown in Fig. 4.5. The resulting scattering angle for each individual encounter can be large and depends on the atomic properties of the colliding particles. In this study, only proton-hydrogen collisions are considered. Such collisions are characterized by a collision frequency $\nu_{in} = n_n\sigma_{in}\Delta u$, where

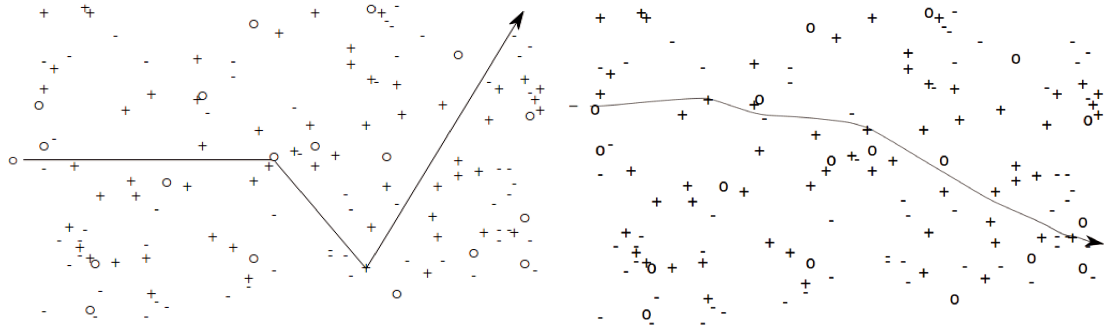

Figure 4.5: Schematic view of neutral (left panel) and Coulomb (right panel) collisions scattering as from Callen [2006].

n_n is the neutral density, σ_{in} is the collision cross-section, which is a function of Δu, and $\Delta u = |\mathbf{u}_i - \mathbf{u}_n|$ is the relative velocity between the proton "i" and the neutral "n". The probability $P(\Delta t)$ to undergo a collision during a time $\Delta t \ll \nu_{in}^{-1}$ is then:

$$P(\Delta t) = 1 - e^{-\nu_{in}\Delta t} \approx \nu_{in}\Delta t \tag{4.75}$$

The numerical calculation of the effects of proton-hydrogen collisions on the ion dynamics was implemented during this thesis. It is performed following a Monte Carlo method proposed in Vahedi and Surendra [1995], Nanbu and Kitatani [1995] and Sukhinin et al. [2018]. Only elastic collisions are considered. The ionisation fraction is supposed to be small, such that the effect of proton-hydrogen collisions on the neutral population is small. In this case the density, fluid velocity and temperature of the neutrals can be assumed to remain constant. The neutral dynamic is not calculated, hence energy is not conserved in the simulations: the hydrogen population acts as a sink for the momentum and energy of the colliding proton population. The algorithm can be described as follows.

1. First, for each macroparticle of a given population, the velocity of a neutral particle, $\mathbf{u}_n$, is sampled from a Maxwellian distribution with a density and temperature specified as input of the simulation.

2. The relative velocity Δu (in units of v_{A0}) is then computed, together with the collision energy E, expressed in eV and calculated as $E = \frac{1}{2}\frac{m_p}{e}(\Delta u)^2 E_\sigma$, where E_σ is a reference energy, and m_p and e are the proton mass and elementary charge respectively, in code units.

3. The proton-hydrogen elastic collision cross-section is obtained from Krstic and Schultz [1999] (see Fig. 4.6) using the numerical fit provided in the publication, which is valid for collisions energies between 0.1 and 100 eV, as:

$$\sigma_{in} = 591.039 - 87.7354\ln(E) + 2.56830\ln(E)^2 \tag{4.76}$$

4. The collision probability is then calculated as $P = \alpha\nu_{in}\Delta t$, where α is a multiplying factor which allows to scale the cross section.

5. A uniformly distributed random number R between 0 and 1 is drawn. A collision occurs if $R < P$.

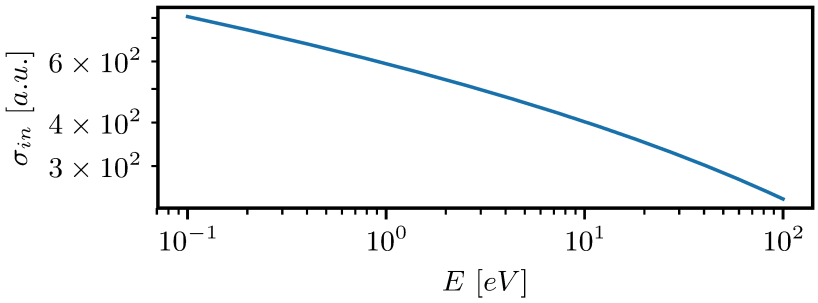

Figure 4.6: Proton-hydrogen elastic collision cross-section σ_{in} in a.u. (1 a.u. $= 2.8 \times 10^{-17}\text{cm}^2$) as a function of the collision energy E(eV).

6. The proton with a pre collision velocity $\mathbf{u}_{\text{old}}$ is given a new velocity $\mathbf{u}_{new}$ after the collision with the neutral as:

$$\mathbf{u}_{\text{cm}} = \frac{1}{2}(\mathbf{u}_{\text{old}} + \mathbf{u}_n) \tag{4.77}$$

$$\mathbf{u}_{\text{old,cm}} = \mathbf{u}_{\text{old}} - \mathbf{u}_{\text{cm}} \tag{4.78}$$

$$\mathbf{u}_{\text{new,cm}} = u_{\text{old,cm}}\mathbf{e}_{\text{rand}} \tag{4.79}$$

$$\mathbf{u}_{\text{new}} = \mathbf{u}_{\text{new,cm}} + \mathbf{u}_{\text{cm}} \tag{4.80}$$

where $\mathbf{e}_{\text{rand}} = \sin\theta\cos\phi\ \mathbf{e}_x + \sin\theta\sin\phi\ \mathbf{e}_y + \cos\theta\ \mathbf{e}_z$ is a unit vector of random orientation with $\theta \in [0;\pi[$ and $\phi \in [0;2\pi[$. The subscript "cm" denotes the center of mass reference frame. Hence the post collision velocity in the simulation reference frame is:

$$\mathbf{u}_{\text{new}} = \frac{1}{2}\left[\mathbf{u}_{\text{old}} + \mathbf{u}_n + \Delta u\ \mathbf{e}_{\text{rand}}\right] \tag{4.81}$$

These steps are repeated at each time step for each macroparticle, at the predictor and corrector steps of the hybrid-PIC solver.

4.5 Numerical setup and run parameters

The simulations are performed in 1D and 2D space. The macroparticles velocity and the fields components are defined in the three directions. It was shown in Winske and Quest [1986] that 1D simulations are sufficient to capture the essential physics of the instability. 2D simulations can nonetheless bring additional information on the spatial structure of the magnetic field amplification regions. Two populations of protons, the *main* (noted with the subscript "m") and the *cosmic rays* (noted with the subscript "cr"), were considered both with an initial Maxwellian velocity distribution function. The ambient magnetic field is initially homogeneous and oriented in the $\mathbf{e}_x$ direction, aligned with the simulation domain. The cosmic rays population of density $n_{cr} = 0.01\ n_0$ is given a positive drift velocity parallel to the ambient magnetic field u_{cr}, in the reference frame of the main protons. In this configuration, the unstable electromagnetic fluctuations are expected to propagate with a negative phase velocity, right-hand polarization and negative helicity.

	dim	n_{cr}/n_m	u_{cr}	β_m	T_m	T_{cr}	T_e	L_x/L_y	$\Delta x/\Delta y$	Δt	$N_{cr}/\ N_m$
1DTH	1D	0.01	100	0.2 - 400	0.1 - 200	1	1	1000/	1/	10^{-4}	500/500
2DTH	2D	0.01	100	20, 50, 100	10, 25, 50	1	1	1000/200	1/1	10^{-4}	75/75

Table 4.1: Normalized parameters used in the simulations for the thermally modified non-resonant mode, noted "TH" for thermal, with $\beta_m = 2(v_{Tm}/v_{A0})^2$. Δx and Δy are the mesh size in the x and y directions, N_{cr} and N_m are the initial number of macroparticles per cell for the cosmic rays and main protons populations respectively.

	dim	n_{cr}/n_m	u_{cr}	ν_0	T_m	T_{cr}	T_e	L_x/L_y	$\Delta x/\Delta y$	Δt	$N_{cr}/\ N_m$
1DCC	1D	0.01	50	0.01 - 100	1	1	1	1000/	1/	10^{-5}	100/100
1DCN	1D	0.01	50	0.01 - 30	1	1	1	1000/	1/	10^{-5}	100/100
2DCC	2D	0.01	50	27	1	1	1	1000/200	1/1	10^{-4}	100/100

Table 4.2: Normalized parameters used in the simulations including particle collisions, noted "CC" for Coulomb collisions and "CN" for collisions with neutrals with ν_0 the collision frequency between the main protons, and with the hydrogen population.

The main reason to choose a large density ratio is to maximize the growth rate in the simulations and reduce the computational cost. This approximation is quite common in PIC numerical studies of the non-resonant mode (Winske and Leroy [1984], Riquelme and Spitkovsky [2009], Gargate et al. [2010], Zacharegkas et al. [2019]. As stated in Sec. 2.2, there is no physics added to the problem by artificially increasing the density ratio, as long as the background charge compensating the cosmic rays charge is sufficiently small. This was studied in the work of Amato and Blasi [2009] who showed that the linear dispersion relation can be modified by a term of the order $O(n_{cr}^2/n_m^2)$ depending on if the cosmic rays current was compensated by the background electrons, or by a population of low density electrons streaming along the cosmic rays. There is no clear consensus on which of these possibilities occur in supernova and jets shocks (Zweibel and Everett [2010]), however as long as the density ratio is not close to unity the simulations may still be relevant to both scenarios. The electron density and initial velocity are calculated to ensure quasi-neutrality and satisfy the initial current condition $\mathbf{j}_{cr} = -\mathbf{j}_e$ (Eq. 2.7). A summary of the simulation parameters used can be found in Tables 4.1 and 4.2.

The simulation domain is of length $L_x = 1000\ l_0$ and discretized with 1000 cells for one-dimensional simulations, corresponding to a possible range of wavenumbers $2\pi L_x^{-1} \leq k \leq \pi l_0^{-1}$. These dimensions are sufficient to accommodate the expected range of unstable wavenumbers $k_{\max} = l_0^{-1}$ and $k_{\min} = 0.01\ l_0^{-1}$ for the "TH" runs (Eqs. 2.34 and 2.43). The plasma and field quantities are initially homogeneous, and periodic boundary conditions are used in all directions. The numerical scheme being explicit, the time step Δt must be chosen to satisfy the Courant–Friedrichs–Lewy condition on the whistler waves and the most energetic macroparticles. It also needs to satisfy the condition on the particle collisions $\nu_0^{-1} \ll \Delta t$ with ν_0 the collision frequency. This latter condition restricted the range of collisions frequencies investigated, as large values $\nu_0 \gg 100$ would require prohibitively small numerical time steps to resolve low energy collisions. Each cell is initially filled with a large number of macroparticles per cell (500 for each proton populations in the TH runs) to properly describe high temperature Maxwellian distributions, as well as the large density fluctuations that occur during the instability growth. For two-dimensional

simulations, a domain length $L_y = 200\ l_0$ was used in the y-direction, discretized with 200 cells. Simulations with $L_y = 400\ l_0$ discretized with 400 cells were also performed, without any noticeable changes in the results. In 2D runs the number of macroparticles per cell is reduced to lower the high numerical cost of multidimensional simulations. The simulations setup is an initial value problem as the cosmic rays population is not injected over time during the simulation. The importance of this assumption compared to the case of a continuous injection of streaming particles will be discussed in Sec. 5.4.2. In the case of particle acceleration at shocks, the simulation setup can be visualized as a line (1D) or rectangle (2D) of plasma downstream of the shock front. The largest dimension ($\mathbf{e}_x$ direction) is aligned with the ambient magnetic field, parallel to the shock surface normal. The remaining directions are supposed invariant and homogenous because of the periodic boundary conditions, i.e. there is no spatial gradients in those directions. The actual shock is not simulated. Only the suprathermal particles leaking from the shock and propagating in the surrounding ambient medium are considered, and constitute the cosmic rays drifting population.

The cosmic rays and electrons temperatures T_{cr} and T_e are chosen to be equal to the reference temperature T_0 to avoid important pressure effects due to the electrons, and to exclude the resonant streaming instabilities from competing with the non-resonant mode. For simulations including protons-hydrogen collisions, the hydrogen population temperature is taken to be T_0. The simulations noted "TH" are focused on studying the effects of the initial main protons temperatures, ranging from $T_m = 0.1$ to $200\ T_0$. In the simulations noted "CC" are investigated the effect of Coulomb collisions on the non-resonant mode, while considering a wide range of collision frequencies, from $\nu_0 = 0.01\ \Omega_0$ to $\nu_0 = 1000\ \Omega_0$. Similarly the simulations noted "CN" focus on the effect of proton-hydrogen collisions, with a range of frequencies $\nu_0 = 0.01\ \Omega_0$ to $\nu_0 = 30\ \Omega_0$. The reference energy is taken as $E_\sigma = 1$ eV, and the neutral temperature is chosen equal to the main protons temperature $T_n = T_m = T_0$, such that the collision energy is of the order of 1 eV. In this case the typical collision cross-section of a thermal proton with an hydrogen is $\sigma_{in} = 600$ a.u. as per Eq. 4.76. The simulations noted "TH" will be investigated in the following Chapter 5, and the simulations noted "CC" and "CN" will be investigated in Chapter 6.

The resistivity η and hyperviscosity η' in Ohm's law (Eq. 4.4) are fixed as $\eta = 10^{-3} B_0/en_0$ and $\eta' = 10^{-3} B_0 l_0^2/en_0$ in order to reduce small scale fluctuations without introducing important dissipative effects. The resitivity is an effect of electron-proton collisions, as shown in Sec. 4.4.2. Hence choosing a constant resistivity is equivalent to supposing a constant electron-proton Coulomb collision frequency. However the actual electron-proton collision frequency is related to the proton-proton frequency via the relation $\nu_{e/i} = \sqrt{m_p/m_e}\ \nu_{i/i}$ with $\nu_{i/i} \equiv \nu_0$. The resistive effects can be compared to the induction term, and is quantified with the magnetic Reynolds number as $R_m = LV\mu_0\sigma$, where L and V are a characteristic length and velocity respectively, and $\sigma = n_e e^2/m_e\nu_{e/i}$ is the conductivity. One has $L \sim 2\pi/k_{\max}$, and $V \sim j_{cr}B/\rho\gamma$ where γ is the growth rate, as from Eq. 2.40. This yields the scaling:

$$R_m \sim \pi \frac{j_{cr} v_{A0}}{\gamma^2} \frac{\mu_0 e}{\sqrt{m_e m_p}} \frac{\Omega_0}{\nu_0} \sim 10^3 \frac{\Omega_0}{\nu_0} \tag{4.82}$$

for the "CC" simulations including Coulomb collisions. The resistivity effects are thus expected to become important on the smallest wavelength of the instability for proton-proton collision frequencies which were not investigated in this work, above $10^3\Omega_0$. As such, the small and constant resistivity used in the simulations is solely numerical to reduce small scale electric fluctuations.

4.6 References

Amato, E. and Blasi, P. (2009). A kinetic approach to cosmic-ray-induced streaming instability at supernova shocks. *Mon Not R Astron Soc*, 392(4):1591–1600.

Arbutina, B. and Zekovic, V. (2021). On the distribution function of suprathermal particles at collisionless shocks. *arXiv e-prints*, page arXiv:2108.09085.

Aunai, N., Hesse, M., Black, C., Evans, R., and Kuznetsova, M. M. (2013). Influence of the dissipation mechanism on collisionless magnetic reconnection in symmetric and asymmetric current layers. *Physics of Plasmas*, 20:2901.

Bai, X.-N., Caprioli, D., Sironi, L., and Spitkovsky, A. (2015). Magnetohydrodynamic-Particle-in-Cell Method for Coupling Cosmic Rays with a Thermal Plasma: Application to Non-relativistic Shocks. *ApJ*, 809(1):55.

Bhatnagar, P. L., Gross, E. P., and Krook, M. (1954). A Model for Collision Processes in Gases. I. Small Amplitude Processes in Charged and Neutral One-Component Systems. *Physical Review*, 94(3):511–525.

Boris, J. P. (1970). Acceleration calculation from a scalar potential. *Proceedings of the fourth conference on numerical simulation of plasmas*.

Box, G. and Muller, M. E. (1958). A note on the generation of random normal deviates. *Annals of Mathematical Statistics*, 29:610–611.

Callen, J. D. (2006). Coulomb Collisions. In *Fundamentals of Plasma Physics*. University of Wisconsin, Madison, Wisconsin, draft edition.

Casse, F., van Marle, A. J., and Marcowith, A. (2018). On magnetic field amplification and particle acceleration near non-relativistic collisionless shocks: Particles in MHD Cells simulations. *Plasma Physics and Controlled Fusion*, 60:014017.

Gargate, L., Fonseca, R. A., Niemiec, J., Pohl, M., Bingham, R., and Silva, L. O. (2010). The nonlinear saturation of the non-resonant kinetically driven streaming instability. *ApJL*, 711(2):L127–L132.

Holcomb, C. and Spitkovsky, A. (2018). On the Growth and Saturation of the Gyroresonant Streaming Instabilities. *arXiv:1811.01951 [astro-ph]*.

Krstic, P. S. and Schultz, D. R. (1999). Atomic and plasma-material interaction data for fusion. V. 8. Elastic and related transport cross sections for collisions among isotopomers. *Atom. And Plasma-Material Inter. Data Fusion (Sup. Nuclear Fusion)*, 8(1):0–699.

Landau, L. (1965). The transport equation in the case of Coulomb interactions. In Ter Haar, D., editor, *Collected Papers of L.D. Landau*, pages 163–170. Pergamon.

Le, A., Stanier, A., Daughton, W., Ng, J., Egedal, J., Nystrom, W. D., and Bird, R. (2019). Three-dimensional stability of current sheets supported by electron pressure anisotropy. *Physics of Plasmas*, 26(10):102114.

Marcowith, A., Henri, G., and Pelletier, G. (1995). Gamma-ray emission of blazars by a relativistic electron–positron beam. *Monthly Notices of the Royal Astronomical Society*, 277(2):681–699.

Mignone, A., Bodo, G., Vaidya, B., and Mattia, G. (2018). A Particle Module for the PLUTO Code. I. An Implementation of the MHD–PIC Equations. *ApJ*, 859(1):13.

Miller, R. H. and Combi, M. R. (1994). A Coulomb collision algorithm for weighted particle simulations. *Geophysical Research Letters*, 21(16):1735–1738.

Nanbu, K. and Kitatani, Y. (1995). An ion-neutral species collision model for particle simulation of glow discharge. *J. Phys. D: Appl. Phys.*, 28(2):324–330.

Nanbu, K. and Yonemura, S. (1998). Weighted particles in coulomb collision simulations based on the theory of a cumulative scattering angle. *Journal of Computational Physics*, 145(2):639–654.

Nicolas, L. (2017). *Effects of Collisions on the Magnetic Streaming Instability*. Theses, Université Pierre et Marie Curie - Paris VI.

Pétri, J. (2016). Theory of pulsar magnetosphere and wind. *Journal of Plasma Physics*, 82(5):635820502.

Riquelme, M. A. and Spitkovsky, A. (2009). Nonlinear study of Bell's cosmic ray current-driven instability. *The Astrophysical Journal*, 694(1):626–642.

Rosenbluth, M. N., MacDonald, W. M., and Judd, D. L. (1957). Fokker-planck equation for an inverse-square force. *Phys. Rev.*, 107(1):1–6.

Smets, R. and Aunai, N. (2011). Heckle, https://github.com/rochSmets/heckle.

Spitkovsky, A. (2017). Kinetic modeling of pulsar magnetospheres and winds. pages 17–ATP17–119.

Sukhinin, G. I., Salnikov, M. V., and Fedoseev, A. V. (2018). The effect of the type of ion–neutral collisions on ion cloud formation. In *Proceedings of the 5th International Conference for Science Educators and Teachers (ISET) 2017*, page 020029, Phuket, Thailand.

Takizuka, T. and Abe, H. (1977). A binary collision model for plasma simulation with a particle code. *Journal of Computational Physics*, 25(3):205–219.

Told, D., Cookmeyer, J., Astfalk, P., and Jenko, F. (2016). A linear dispersion relation for the hybrid kinetic-ion/fluid-electron model of plasma physics. *New Journal of Physics*, 18(7):075001.

Trubnikov, B. A. (1965). Particle interactions in a fully ionized plasma. *Reviews of Plasma Physics*, 1:105.

Vahedi, V. and Surendra, M. (1995). A Monte Carlo collision model for the particle-in-cell method: Applications to argon and oxygen discharges. *Computer Physics Communications*, 87(1):179–198.

Wada, T. and Shibata, S. (2007). A particle simulation for the global pulsar magnetosphere: The pulsar wind linked to the outer gaps. *Monthly Notices of the Royal Astronomical Society*, 376(4):1460–1464.

Winske, D. and Leroy, M. M. (1984). Diffuse ions produced by electromagnetic ion beam instabilities. *Journal of Geophysical Research: Space Physics*, 89(A5):2673–2688.

Winske, D. and Quest, K. B. (1986). Electromagnetic ion beam instabilities: Comparison of one- and two-dimensional simulations. *Journal of Geophysical Research: Space Physics*, 91(A8):8789–8797.

Zacharegkas, G., Caprioli, D., and Haggerty, C. (2019). Modeling the Saturation of the Bell Instability Using Hybrid Simulations. *arXiv:1909.06481*.

Zweibel, E. G. and Everett, J. E. (2010). Environments for Magnetic Field Amplification by Cosmic Rays. *The Astrophysical Journal*, 709(2):1412–1419.

Chapter 5

Simulations results for the non-resonant mode

Contents

5.1 Introduction

The linear theory relies on the fundamental assumption of small perturbations, such that perturbations of a given quantity are small compared to the initial equilibrium value. The growth rate of the non-resonant instability can then be found by solving the linearized equations, which gives an unbounded exponential growth of the instability. However such growth cannot be infinite, as the principle of conservation of the system total energy prevents any growth beyond the amount of free energy available. When perturbations become comparable to the initial state values, the linear theory breaks

down, and the complex system of the Vlasov and Maxwell equations must be solved in its full non-linear form. This can be achieved with numerical simulations, which allows to study the fundamental mechanism of the non-resonant mode, late time evolution, saturation mechanism and saturated magnetic field intensity. The instability has been extensively studied numerically using modified magneto-hydrodynamics (MHD) (Bell [2004], Zirakashvili et al. [2008]), hybrid-Particle-In-Cell (PIC ions and massless fluid electrons)(Winske and Leroy [1984], Akimoto et al. [1993], Haggerty and Caprioli [2019], Marret et al. [2021]), full-PIC (Riquelme and Spitkovsky [2009], Ohira et al. [2009], Crumley et al. [2019]) and MHD-PIC (Bai et al. [2015], Casse et al. [2018], Mignone et al. [2018]) simulations. The MHD-PIC method in particular has received growing attention as it combines the kinetic treatment of the cosmic rays while retaining the advantage of modelling the background plasma as a magnetofluid, over large spatial and temporal scales. Neglecting kinetic effects in the background plasma however is not always justified. For example, in the hot plasmas of superbubbles or in the intergalactic medium, the background's ions thermal Larmor gyro-radius can become comparable to or larger than the unstable wavelengths and a kinetic treatment of the background plasma is necessary. In addition, even in relatively cold plasmas, collisionless hybrid-PIC simulation have shown the non-linear development of significant ion pressure anisotropies in the background plasma (Marret et al. [2021]), suggesting that the assumption of an isotropic scalar pressure, often employed in fluid models, may not always be justified.

This chapter is devoted to hybrid-PIC numerical simulations of the non-resonant streaming instability. The instability mechanism, growth rate, saturation level, spatial structure, density fluctuations, background plasma heating and cosmic rays scattering are investigated, and compared to theoretical expectations while considering a wide range of main protons temperature. In the following, unless stated otherwise the simulation parameters are those corresponding to the "TH" runs (thermal) presented in Table 4.1.

5.2 Growth of the instability

5.2.1 Magnetic field amplification

One of the main feature of the non-resonant streaming instability is the generation of large amplitude magnetic fluctuations. Contrary to the right-hand and left-hand resonant mode, amplification beyond the initial magnetic field intensity is possible because of the large drift velocity required to drive the instability, which keeps the cosmic rays demagnetized (Bell [2013]). The evolution of the perturbed magnetic field intensity $B_1 = |\mathbf{B} - \mathbf{B}_0|$ is presented in Fig. 5.1 for two different main protons temperatures $T_m = T_0$ (cold regime) and $T_m = 25\ T_0$ (hot regime). The magnetic field intensity is averaged over space, hence encompassing perturbations at all the scales permitted by the size and resolution of the simulation domain. Considering for a start the cold case, with $T_m = T_0$, one can distinguish four phases. The first one (from $t = 0$ to $2\ \Omega_0^{-1}$) and corresponds to micro-adjustments of the plasma quantities from the random initialization to its eigenmode values. The second phase (from $t = 2$ to $18.5\ \Omega_0^{-1}$) is characterized by the exponential amplification of the perturbed magnetic field intensity, and continues even for perturbations larger than the initial magnetic field intensity. It will be refereed to as the linear phase or exponential

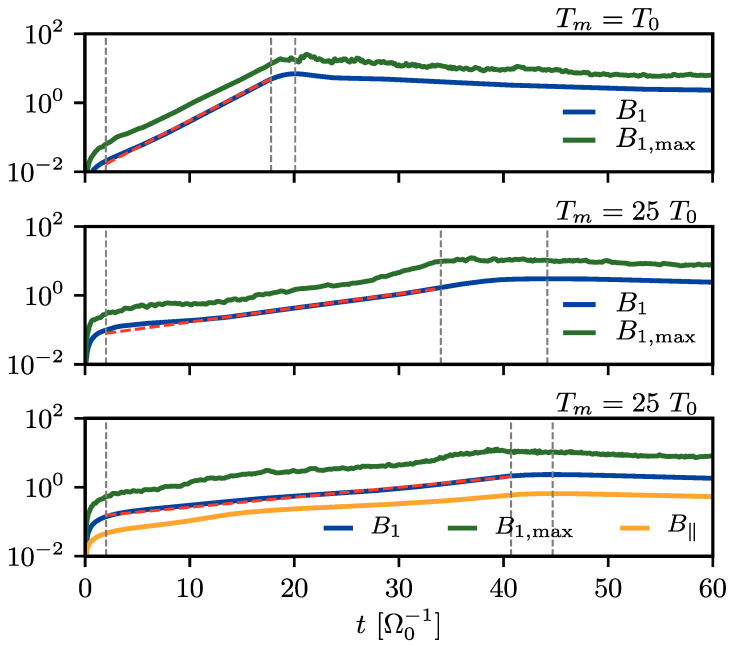

Figure 5.1: Perturbed magnetic field intensity $B_1 = |\mathbf{B} - \mathbf{B}_0|$ evolution over time (normalized to B_0) and integrated over space (blue solid line), and maximum value in simulation domain $B_{1,\max}/B_0$ (green solid line), for 1D simulations with a main protons temperature $T_m = T_0$ (upper panel) and $T_m = 25\ T_0$ (middle panel). The result of a 2D simulation with $T_m = 25\ T_0$ is presented in the lower panel. The red dashed line corresponds to an exponential fit in the linear phase. The orange line in the lower panel correspond to the perturbed magnetic field parallel component $B_\parallel = \mathbf{B}_1 \cdot \mathbf{e}_x$. The vertical dashed lines corresponds, from left to right, to the beginning of the linear regime, transition to the non-linear regime and to magnetic saturation, which is reached typically after 6 e-foldings of growth.

phase of growth interchangeably. A non-linear phase occurs after $t_{\mathrm{NLT}} = 18.5\ \Omega_0^{-1}$ (Non-Linear Transition), further amplifying the magnetic field until the saturation is reached at $t = 21\ \Omega_0^{-1}$ and leading to a large amplification of the magnetic field, reaching peak values 10 times the ambient magnetic field. Finally, the fourth phase corresponds to a slow relaxation of the system with enhanced wave activity.

In 1D simulations, the magnetic field perturbations cannot be oriented along the simulation domain ($\mathbf{e}_x$ direction). This is imposed by Faraday's law in Fourier space:

$$\mathbf{B} = \frac{i}{\omega}\mathbf{k} \times \mathbf{E} \tag{5.1}$$

with $\mathbf{k} = k\mathbf{e}_x$, together with the condition given by the Maxwell-Thomson equation $\mathbf{k} \cdot \mathbf{B} = 0$ which forbid any longitudinal component $\mathbf{B} \cdot \mathbf{k}\mathbf{k}/k^2$, hence imposing transverse perturbations. In addition, the unstable waves are circularly polarized, implying that using a local magnetic field aligned basis $\mathbf{e}_\parallel = \frac{\mathbf{B}_0}{B_0} = \mathbf{e}_x$ (parallel component), $\mathbf{e}_\times = \frac{\mathbf{B}_1}{B_1} \times \mathbf{e}_\parallel$ (normal component, aligned with the cosmic rays magnetic force $-\mathbf{j}_{cr} \times \mathbf{B}_1$) and $\mathbf{e}_\perp = \mathbf{e}_\parallel \times \mathbf{e}_\times$ (perpendicular component) can provide meaningful information on the spatial structure of the unstable waves in 1D simulations, as the unit vector $\mathbf{e}_\perp$ is exactly aligned with the perturbed magnetic field $\mathbf{B}_1$ and rotates together with it. In 2D simulations oblique and perpendicular propagating modes can exist, and consequently magnetic field amplification

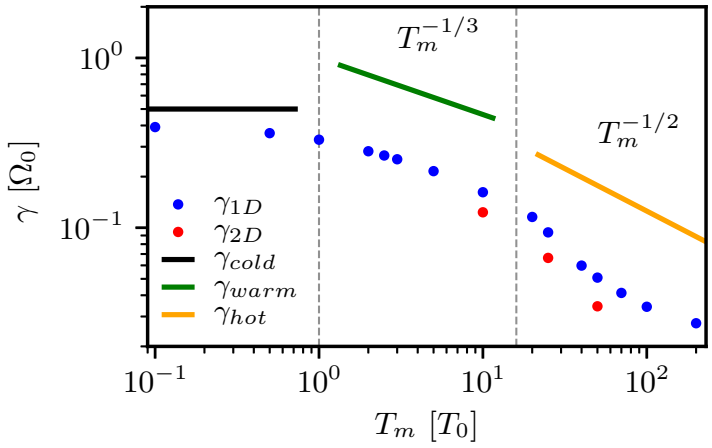

Figure 5.2: 1D and 2D simulations growth rate $\gamma_{\rm 1D,2D}$ (blue and red dots), Winske and Leroy [1984] prediction $\gamma_{\rm cold}$ (Eq. 5.2), Reville et al. [2008] prediction $\gamma_{\rm warm}$ (Eq. 5.3) and growth rate prediction of this work $\gamma_{\rm hot}$ (Eq. 5.4, solid orange line) as a function of the main protons temperature T_m. The vertical dashed lines indicates the transition to the warm regime $v_{A0}/v_{Tm} < (n_{cr}u_{cr}/n_m v_{Tm})^{1/3}$ (Zweibel and Everett [2010], left line at $T_m = T_0$), and to the hot regime $k_{\rm cold} r_{Lm} > 2$ (right line at $T_m = 16\ T_0$).

in the $\mathbf{e}_x$ direction is possible. This is shown in the lower panel of Fig. 5.1 for the simulation parameters $n_{cr}/n_m = 0.01$, $u_{cr}/v_{A0} = 100$ and $T_m/T_0 = 25$, where a small component of the amplified magnetic field is oriented parallel to the initial magnetic field. It is however much smaller compared to the perpendicular component by an order of magnitude, such that even in 2D simulations the $\mathbf{e}_\perp$ unit vector can be considered as approximately aligned with the total $\mathbf{B}_1$.

5.2.2 Instability growth rate and temperature dependency

One important parameter characterizing the linear phase of an instability is its growth rate. As presented in Sec. 3.2, the growth rate of the non-resonant mode depends on the temperature of the main protons and can be strongly reduced when finite proton Larmor radius effects become important. Fig. 5.2 shows the predictions of the *fastest* growing mode in the three regimes of cold (Eq. 5.2), warm (Eq. 5.3) and hot (Eq. 5.4) main protons:

$$\gamma_{\rm cold} = \frac{1}{2}\frac{n_{cr}}{n_m}\frac{u_{cr}}{v_{A0}}\Omega_0 \tag{5.2}$$

$$\gamma_{\rm warm} = \left(\frac{n_{cr}}{n_m}\frac{u_{cr}}{v_{Tm}}\right)^{2/3}\Omega_0 \tag{5.3}$$

$$\gamma_{\rm hot} = \left(\frac{\pi}{2}\right)^{1/2}\frac{n_{cr}}{n_m}\frac{u_{cr}}{v_{Tm}}\Omega_0 \tag{5.4}$$

together with the growth rates extracted from 1D and 2D simulations $\gamma_{\rm 1D,2D}$, as a function of the main protons temperature. The warm and hot regimes thresholds are defined by the conditions $v_{A0}/v_{Tm} < (n_{cr}u_{cr}/n_m v_{Tm})^{1/3}$ and $k_{\rm cold} r_{Lm} \gtrsim 2$ respectively, with $r_{Lm} = v_{Tm}/\Omega_0$ and $k_{\rm cold} = \frac{1}{2}\frac{n_{cr}}{n_m}\frac{u_{cr}}{v_{A0}^2}\Omega_0$. The growth rate in the hot regime is found to

decrease with the temperature as $T_m^{-1/2}$ as expected from the linear theory calculation of this work. In the low temperature limit, the cold prediction from Winske and Leroy [1984] is very accurate, but becomes rapidly invalid for temperatures $T_m > T_0$. The intermediate warm regime from T_0 to 16 T_0 is well reproduced by the prediction from Reville et al. [2008] and Zweibel and Everett [2010] with a decrease of the growth rate with temperature as $T_m^{-1/3}$. The overestimates in the warm and hot regimes by a factor ~ 2 may be linked to the fact that the theoretical values correspond to the fastest growing mode. The magnetic field intensity measured in the simulations is integrated over the whole k spectrum, which gives an overall smaller growth rate than if only the fastest growing mode was observed (see Appendix B for a discussion on the growth rate measurements in the simulations).

5.2.3 Growth rate for arbitrary mass and charge

The non-resonant streaming instability can be excited in various space and astrophysical environments such as at the Earth bow shock, as well as in jet and supernova shocks. In those situations the plasma is essentially made of protons, which may be one of the reasons why the existing literature does not consider heavier elements. However such assumption cannot be made when considering the acceleration of heavier elements at shocks, as well as in laboratory experiments, where the plasmas are often constituted of elements such as carbon or argon. The instability growth rate can be calculated for arbitrary charge and mass of the main and cosmic rays populations. The derivation is given in Appendix A. Considering a small density ratio $n_{cr}/n_m \ll 1$, the growth rate expression may be simplified to obtain:

$$\gamma_{\text{cold}} = \frac{1}{2}\frac{n_{cr}}{n_m}\frac{u_{cr}}{v_{A0}}\Omega_0\frac{q_{cr}}{e}\left(\frac{m_p}{m_m}\right)^{1/2} \tag{5.5}$$

where Ω_0 and v_{A0} are the proton cyclotron frequency and proton Aflvén speed. The growth rate increases linearly with the cosmic rays charge, and decreases with the square root of the main ions mass. It does not depend on the cosmic rays mass, nor on the main ions charge. The maximum wavenumber can be calculated in a similar way:

$$k_{\text{max}} = \frac{n_{cr}}{n_m}\frac{u_{cr}}{v_{A0}^2}\Omega_0\frac{q_{cr}}{e} \tag{5.6}$$

and the minimum wavenumber:

$$k_{\text{min}} = \frac{\Omega_0}{u_{cr}}\frac{m_p}{m_{cr}}\frac{q_{cr}}{e} \tag{5.7}$$

The cosmic rays charge shifts the range of unstable wavenumbers toward smaller scale. This has been observed in MHD-PIC simulations of the instability (see Crumley et al. [2019]). The maximum unstable wavelength increase with cosmic rays mass can be understood in terms of the cyclotron resonance condition, as heavier elements allow the growth of larger scale electromagnetic perturbations without resonant interaction occurring with the streaming particles. The dependencies on mass and charges can be understood by examining the linearized background plasma momentum density conservation (Eq. 2.25) and induction (Eq. 2.26) equations. Neglecting the pseudo-cyclotron acceleration term

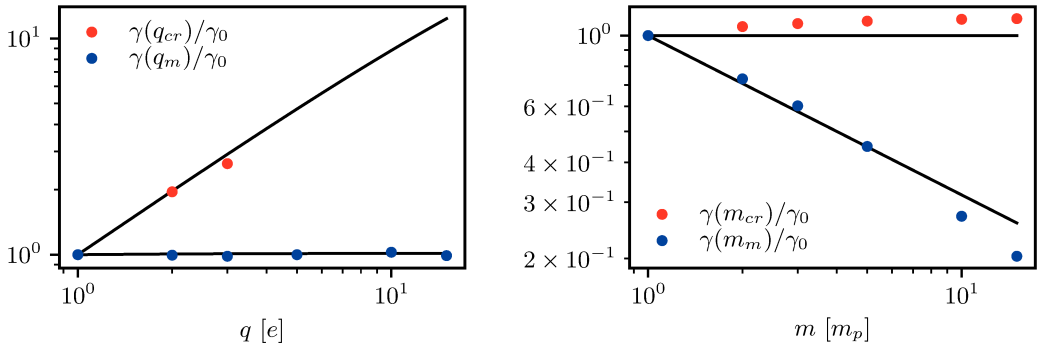

Figure 5.3: Growth rate of the non-resonant mode obtained in 1D simulations with $u_{cr}/v_{A0} = 50$, $n_{cr}/n_m = 0.01$, as a function of the charge (left panel) and mass (right panel) of the cosmic rays (red dots) and main ions (blue dots). The growth rates are normalized to the value obtained in simulations with protons only $\gamma_0 = 0.25\ \Omega_0$. The solid black lines indicates the theoretical prediction as from Eq. 5.5.

and the magnetic field advection, one obtains:

$$\frac{\partial \mathbf{u}_1}{\partial t} = \frac{(\mathbf{B}_0 \cdot \boldsymbol{\nabla})\mathbf{B}_1}{\mu_0 n_m m_m} - \frac{n_{cr}}{n_m}\frac{q_{cr}}{m_m}\mathbf{u}_{cr} \times \mathbf{B}_1 \tag{5.8}$$

$$\frac{\partial \mathbf{B}_1}{\partial t} = (\mathbf{B}_0 \cdot \boldsymbol{\nabla})\mathbf{u}_1 \tag{5.9}$$

Because of quasi-neutrality, the main ions charge density does not come into play as it is approximately equal to the electrons charge density in the low density ratio limit. The cosmic rays driving term, corresponding to the second term in the right-hand side of Eq. 5.8, is proportional to the cosmic rays current and consequently generates larger velocity perturbations for multiply charged elements. Both the magnetic tension and cosmic rays magnetic force terms are inversely proportional to the main ions mass, corresponding to the effect of the background plasma inertia opposing the growth of velocity perturbations.

These results are well recovered in the simulations. Fig. 5.3 presents the numerically obtained growth rate as a function of the mass and charge of the cosmic rays and of the main ions, normalized to the growth rate in the case of protons populations. For simulations with varying cosmic rays charge, values above $q_{cr}/e = 3$ are not shown as the fastest growing wavelengths shifts below the ion inertial length, rapidly preventing any substantial growth of the non-resonant mode (Zacharegkas et al. [2019]). Indeed for the parameters used in the simulations with varying mass and charge, $u_{cr}/v_{A0} = 50$, $n_{cr}/n_m = 0.01$, one obtains the largest growing wavelength as $\lambda_{\max} = \pi \frac{e}{q_{cr}} l_0$, which is smaller than the inertial length l_0 for $q_{cr}/e > \pi$. The simulations yield a slowly increasing growth rate with varying cosmic rays mass. This dependency, which does not appear in the expression of the fastest growing mode (Eq. 5.5), can be understood as an effect of the increased maximum unstable wavelength (Eq. 5.7). As the growth rate is measured by studying the magnetic field intensity evolution integrated over all scales, one obtains an overall faster amplification when a wider range of spatial scales turns to be unstable. This result is of interest in the case of cosmic rays acceleration at shocks. Indeed heavy elements can destabilize the non-resonant mode on larger spatial scales, which may help better confine lighter elements with a smaller Larmor radius and ease the diffusive shock

acceleration process to high energies. This effects will however be limited, since the $q_{cr}m_p/em_{cr}$ ratio is smaller than unity but of the same order of magnitude for all elements of interest.

5.2.4 Magnetic field spectrum

In the context of cosmic rays acceleration in supernova remnants shocks, the confinement of energetic particles at shock boundary requires strong magnetic amplification, at wavelengths comparable to the gyroradius of the accelerated particles. As such, the scale at which the instability generates magnetic field fluctuations is a fundamental parameter. The non-resonant mode growth rate is a function of the wavenumber, and it is larger for small scales fluctuations, i.e. for large wavenumbers (Eq. 2.42). As the instability develops, the magnetic field intensity increases exponentially, and the largest unstable wavenumber $k_{\max} = \frac{n_{cr}}{n_m}\frac{u_{cr}}{v_{A0}^2}\Omega_0$, which is inversely proportional to the magnetic field, decreases. This leads to a progressive reduction of the range of unstable wavelength as the instability saturates at small scales first, followed by larger scales. This is an important property of the non-resonant mode, whose range of unstable wavenumbers strongly vary over the course of the unstable waves growth.

In order to study the evolution of the magnetic field perturbations as a function of the wavelength, one may investigate their spectrum in Fourier space in the simulations. Furthermore, the circularly polarized electromagnetic waves produced by the non-resonant mode possess a definite negative helicity, corresponding to the sense of rotation in space at a given time, which can be observed in the simulations and separated from the positive helicity component. The helical field lines with a positive helicity follow the space curve $\mathbf{s}_+$ defined as (Weidl et al. [2016]):

$$\mathbf{s}_+ = x\ \mathbf{e}_x + r\cos(|k|x)\mathbf{e}_y - r\sin(|k|x)\mathbf{e}_z \tag{5.10}$$

with $x \in \mathbb{R}$ and $r > 0$, and similarly for negative helicity:

$$\mathbf{s}_- = x\ \mathbf{e}_x + r\cos(|k|x)\mathbf{e}_y + r\sin(|k|x)\mathbf{e}_z \tag{5.11}$$

The positive $\widetilde{B}_+$ and negative helicity $\widetilde{B}_-$ components in Fourier space can be separated using the following relations (Terasawa et al. [1986]):

$$\widetilde{B}_+(|k|) = \frac{\widetilde{B}_y(|k|) + i\widetilde{B}_z(|k|)}{2} \tag{5.12}$$

$$\widetilde{B}_-(|k|) = \frac{\widetilde{B}_y(|k|) - i\widetilde{B}_z(|k|)}{2} \tag{5.13}$$

with $\widetilde{B}$ the Fourier transformed component. This corresponds to the operation of shifting the relative phases of the signals, then superimposing them in Fourier space. In the case of a negative wavenumber as for the non-resonant mode, the positive and negative helicity components are then given by the complex conjugate of the helicity components for $k > 0$, i.e. for $k < 0$ one has $\widetilde{B}_+(k) = \widetilde{B}_-(|k|)$ and $\widetilde{B}_-(k) = \widetilde{B}_+(|k|)$. The helicity decomposition does not allow us to distinguish right-hand polarized backward propagating waves from left-hand polarized forward propagating waves, or right-hand polarized forward

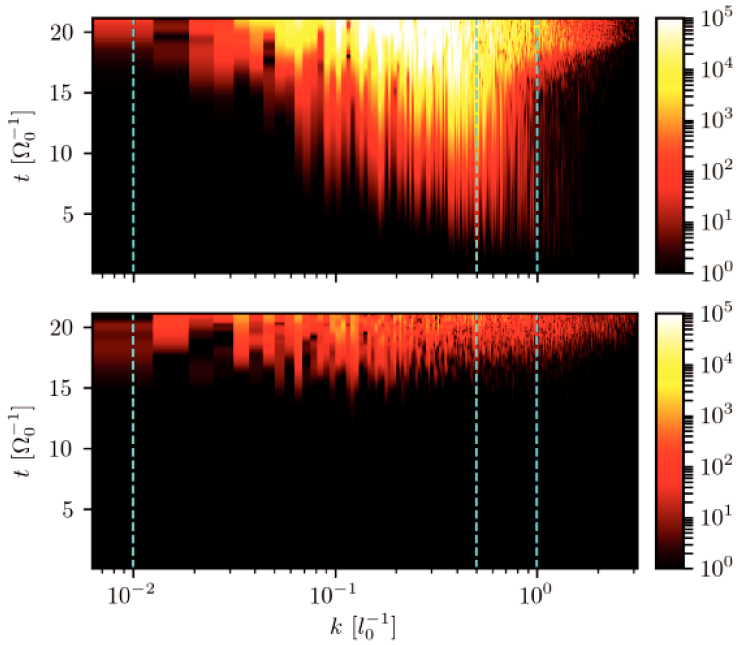

Figure 5.4: Magnetic field power spectral density evolution between $t = 0\ \Omega_0^{-1}$ and saturation at $t = 21\ \Omega_0^{-1}$ as a function of the wavenumber, in a 1D simulation with $T_m = T_0$. *Upper panel*: negative helicity component $|\widetilde{B}_-(k)|^2$. *Lower panel*: positive helicity component $|\widetilde{B}_+(k)|^2$. The cyan dashed vertical lines indicate, from left to right, the initial smallest unstable wavenumber $k_{\rm min} = 10^{-2} l_0^{-1}$, fastest growing wavenumber $k_{\rm fast} = 0.5\ l_0^{-1}$ and maximum unstable wavenumber $k_{\rm max} = l_0^{-1}$.

propagating waves from left-hand polarized backward propagating waves, as they share the same helicity. This degeneracy is not an issue in the simulations presented in this work however, as the large density ratio, large drift velocities and small cosmic rays temperature used ensure that the non-resonant mode is dominant over the resonant modes. As such the negative helicity component can be assumed to be mainly the result of the non-resonant mode contribution, allowing to filter magnetic perturbations unrelated to the instability.

The magnetic field power spectral density of the positive $|\widetilde{B}_+(k)|^2$ and negative $|\widetilde{B}_-(k)|^2$ helicity components of the perturbed magnetic field are presented in Fig. 5.4 as a function of time. One can clearly observe that the negative helicity component is dominant, with a progressive shift toward larger scales well-constrained by the minimum and maximum wavenumber $k_{\rm min}$ and $k_{\rm max}$. The growth is initially maximum for the wavenumber $k_{\rm fast} = \frac{1}{2}\frac{n_{cr}}{n_m}\frac{u_{cr}}{v_{A0}^2}\Omega_0 = 0.5\ l_0^{-1}$ in agreement with linear theory results. The positive helicity components starts growing when the magnetic field perturbations become non-linear $B_1/B_0 > 1$, after $t = 15\ \Omega_0^{-1}$. Because of the cyclotron resonance condition with the cosmic rays, the non-resonant mode cannot grow on scales larger than the cosmic rays Larmor radius. This constitutes an important limitation in the case of diffusive shock acceleration of particles at jet and supernova shocks, and an inverse cascade effect must be invoked if it were to be able to confine high energy particles (Bell [2013]), as the first order Fermi acceleration process requires a strong magnetic field on scales comparable to the cosmic rays Larmor radius to confine the particles near the shock boundary.

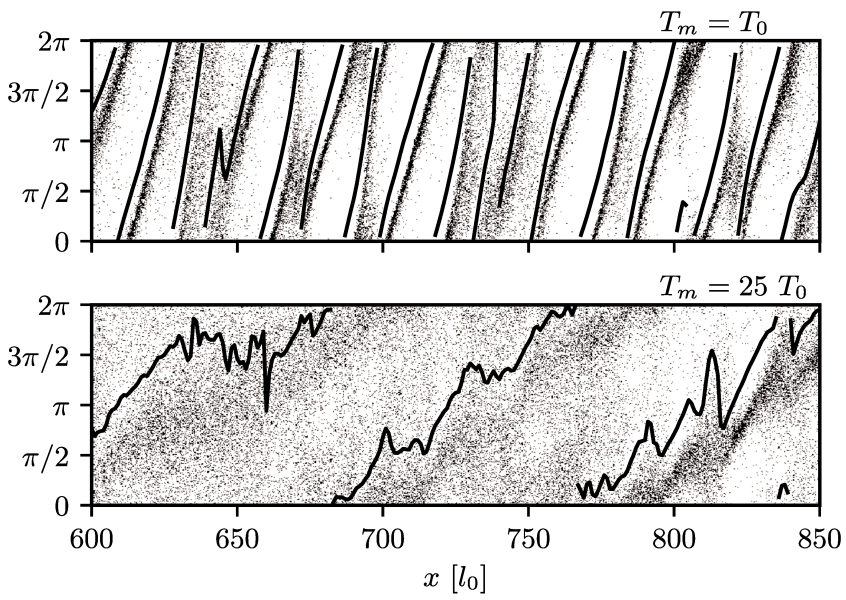

Figure 5.5: Perturbed magnetic field phase $\phi_B = \tan^{-1}(B_z/B_y)$ (black solid line) and main protons particle velocity phase $\phi_v = \tan^{-1}(v_z/v_y)$ (black dots) as a function of space (from 600 to 800 x/l_0) for 1D simulations, during the linear growth phase phase. *Upper panel*: $T_m = T_0$. *Lower panel*: $T_m = 25\ T_0$.

5.2.5 Magnetic field and velocity correlation

As discussed in Sec. 2.2.3, the instability relies on the helicity of the perturbed magnetic field and background fluid velocity field. Both interact via the induced electric field and generate a positive feedback with one another, destabilizing the electromagnetic wave. The resulting main protons velocity field (or streamlines) is a helix with negative helicity, left-hand polarization, positive direction of propagation and with a norm increasing exponentially over time, whereas the perturbed magnetic field forms expanding field lines with negative helicity, right-hand polarization and negative direction of propagation. This spatial structure is illustrated in Fig. 2.1, and is well observed in the simulations. The interlaced magnetic and velocity fields structure is shown in Fig. 5.5, where the main protons particle velocity phase $\phi_v = \tan^{-1}(v_z/v_y)$ is plotted along with the perturbed magnetic field phase $\phi_B = \tan^{-1}(B_z/B_y)$ at the beginning of the non-linear growth phase, for low temperature $T_m = T_0$ and high temperature $T_m = 25\ T_0$ simulations.

The positive slope of the perturbed magnetic field phase ϕ_B illustrates the negative helicity of the wave. In the cold case (Fig. 5.5 upper panel) it is clear that the velocity phase ϕ_v also develops a coherent structure that closely follows that of the magnetic field. At a given position x, the velocity phase of all the particles bunches around a well defined value in the cold case, for example at $x = 625 l_0$ the velocity phase is $\phi_v \approx \pi$. The phase shift between the magnetic field and the velocity field at a given position, $\Delta\phi = \phi_B - \phi_v$, is close to $\pi/2$, which is expected from the background plasma momentum density conservation equation (Eq. 5.8). Neglecting the magnetic tension force, one finds that the cosmic rays driving term $-\mathbf{j}_{cr} \times \mathbf{B}_1/\rho$ accelerates the background fluid in a direction perpendicular to both the ambient and local perturbed magnetic field. The phase shift $\Delta\phi$ is observed to remain constant during the linear evolution of the instability,

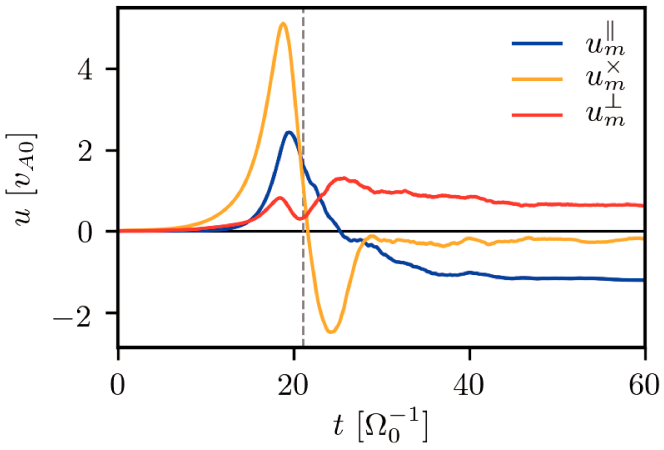

Figure 5.6: Main protons fluid velocity in a local magnetic field aligned basis. The blue, orange and red solid lines correspond to the $\mathbf{e}_{\parallel}$, $\mathbf{e}_{\times}$ and $\mathbf{e}_{\perp}$ components respectively. The grey dashed vertical line indicates the instability saturation at $t = 21\ \Omega_0^{-1}$.

corresponding to a coherent motion of the main protons with respect to the electromagnetic wave. Increasing the temperature does not modify the helicity of the perturbation (Fig. 5.5 lower panel), and one obtains an increase in wavelength which was predicted by linear theory, as small scales fluctuations do not grow efficiently because of the protons finite Larmor radius. In addition, the phase bunching of the main protons velocity is less clearly defined compared to the cold regime. This may indicate a possible physical interpretation to the monotonously decreasing growth rate with thermal velocity found in the hot regime (Eq. 5.4): the main protons high mobility in the demagnetized regime allows them to migrate quickly along the ambient magnetic field, mixing up the phase shift between the background velocity and the magnetic field fluctuations. As a result, the induced electric field is weakened and the instability grows less efficiently.

The main protons dynamic can be studied in a complementary manner by projecting the fluid velocity components in the local magnetic field aligned basis $(\mathbf{e}_{\parallel}, \mathbf{e}_{\times}, \mathbf{e}_{\perp})$ (see Fig. 2.1), and averaging the result over the simulation domain. Since this basis follows the local magnetic field helical structure, no information is lost on the velocity components after the averaging operation. The result is presented in Fig. 5.6 for a 1D simulation in the cold case, $T_m = T_0$. One obtains a clear acceleration in the direction of the cosmic rays magnetic force $(\mathbf{e}_{\times})$ during the exponential growth phase, which confirms the result obtained by studying the phase shift between the magnetic field and main protons fluid velocity field. The main protons are also accelerated in the direction parallel to the initial magnetic field $(\mathbf{e}_{\parallel})$. This is in agreement with the theoretical results obtained in Sec. 2.2.4, where it was found that the slowing down of the cosmic rays drifting population is associated to an acceleration of the background fluid.

These effects can also be observed and quantified in 2D simulations. Fig. 5.7 presents the phase difference between the fluid velocity phase and magnetic field phase $\Delta\phi = \phi_B - \phi_v$ for three different times: $t = 15\ \Omega_0^{-1}$, $t = 35\ \Omega_0^{-1}$ and $t = 45\ \Omega_0^{-1}$, corresponding to the beginning and end of the linear growth phase, and after magnetic saturation. The main protons temperature is $T_m = 25\ T_0$. During the early times of growth (upper panel), the magnetic field and background velocity field are essentially uncorrelated and the growth is

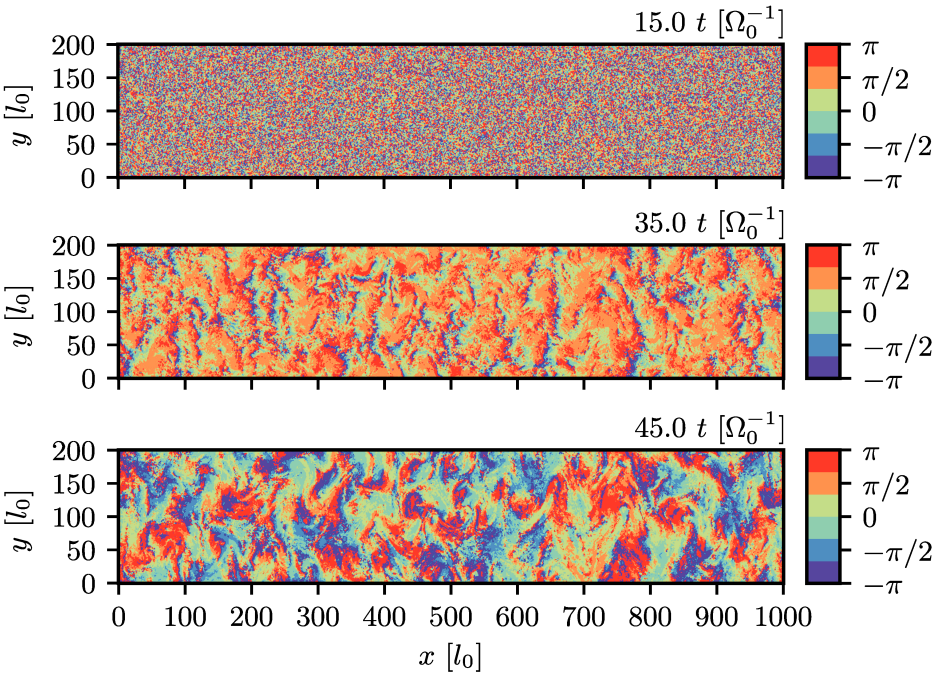

Figure 5.7: Magnetic field and main protons velocity phase difference $\Delta\phi$ map at three different times: beginning of the linear growth phase ($t = 15\ \Omega_0^{-1}$), during the linear growth phase ($t = 35\ \Omega_0^{-1}$), after saturation ($t = 45\ \Omega_0^{-1}$). The difference is calculated locally as $\Delta\phi = \tan^{-1}(\sin(\phi_B - \phi_v)/\cos(\phi_B - \phi_v))$. Obtained from a 2D simulations with $T_m = 25\ T_0$. The theoretical prediction from the fluid model yields a uniform phase shift $\Delta\phi = \pi/2$, which is recovered in the simulations, with modulations due to the high temperature of the main protons.

slow. By the end of the linear phase (middle panel), the phase shift tends to the expected value $\Delta\phi = \phi_B - \phi_v = \pi/2$ and allows the growth of the perturbation, although perturbed by thermal effects. After the magnetic field saturation (lower panel), it randomizes as the cosmic rays magnetic force no longer imposes the magnetic field spatial structure to the background fluid velocity.

5.3 Late time evolution

5.3.1 Non-linear phase

To study the instability evolution and understand how the instability saturates, one may investigate the time evolution of the maximum and minimum unstable wave numbers $k_{\max} = \frac{n_{cr}}{n_m}\frac{u_{cr}}{v_{A0}^2}\Omega_0$ and $k_{\min} = \Omega_0/u_{cr}$, which are expected to play a central role in determining the maximum reachable magnetic field. The results are presented in Fig. 5.8 upper panel. As the magnetic field increases, $k_{\max}$ decreases whereas $k_{\min}$ increases. The moment these wave numbers become equal corresponds to the magnetic field saturation proposed in Bell [2004]: the instability condition $k_{\min} < |k| < k_{\max}$ cannot be satisfied at any scale, leading to saturation.

Fig. 5.8 middle panel presents the time derivative of the main protons fluid velocity in the $\mathbf{e}_\times$ direction $\partial u_m^\times/\partial t$, which corresponds to the direction of the magnetic force in

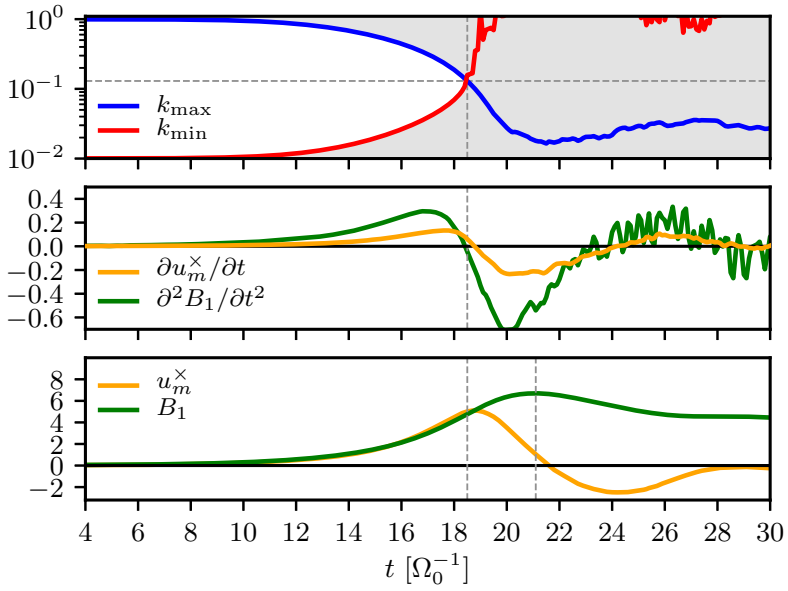

Figure 5.8: *Upper panel*: maximum (blue solid line) and minimum (red solid line) unstable k (in unit of l_0^{-1}), as a function of time between $t = 4\ \Omega_0^{-1}$ and $t = 30\ \Omega_0^{-1}$. The condition $k_{\max} = k_{\min}$ is indicated with the vertical dashed line at $t_{\rm NLT} = 18.5\ \Omega_0^{-1}$, and reported in other panels. Greyed regions correspond to stable wave numbers. *Middle panel*: first order time derivative of the main protons normal velocity $u_m^{\times}$ (in unit of v_{A0}, orange solid line) and perturbed magnetic field intensity second order time derivative (in unit of B_0 and multiplied by a factor 100, green solid line). *Lower panel*: perturbed magnetic field intensity B_1 (green solid line) and main protons normal fluid velocity component (orange solid line). The magnetic field saturation is indicated with the vertical dashed line at $t_{\rm sat} = 21\ \Omega_0^{-1}$. Values are taken from 1D simulation with a main protons temperature $T_m = T_0$.

the local magnetic field basis (also shown in Fig. 5.6). The acceleration is increasing exponentially during the linear phase, starts to decrease after $t = 17\ \Omega_0^{-1}$, and then becomes negative at $t \sim 21\ \Omega_0^{-1}$, corresponding to a slowing down of the main protons rotation. The fluctuating magnetic field second order time derivative is expected to be closely related to the velocity field via the Faraday's equation (Eq. 2.26) while neglecting the magnetic field advection:

$$\frac{\partial^2 \mathbf{B}_1}{\partial t^2} = (\mathbf{B}_0 \cdot \boldsymbol{\nabla}) \frac{\partial \mathbf{u}_1}{\partial t} \tag{5.14}$$

and is also shown in the figure. It exhibits the same behaviour as the velocity derivative, confirming the correlation between the main protons fluid motion and the growth of the magnetic perturbation. One obtains an excellent match between the $k_{\max} = k_{\min}$ condition discussed previously and the deceleration of the main protons velocity. This suggests that this condition is correlated to the transition toward a non-linear phase of growth, and not to magnetic saturation as the magnetic field is seen to keep growing, although at a slower rate. The same correlation is recovered in all the simulations, indicating that the $k_{\max} = k_{\min}$ condition may be a robust criteria to identify quantitatively the end of the exponential growth. Note that the exponential growth continues even for large magnetic perturbation: the non-linear transition occurs when the perturbed magnetic field intensity is already greater than the initial ambient magnetic field.

The non-linear phase which follows the linear phase of the instability is characterized by a decrease of the main protons fluid rotation velocity and a reduced magnetic field growth. Fig. 5.8 lower panel presents the main protons normal velocity and perturbed magnetic field intensity evolution over time. The transition toward non-linear growth, correlated to the maximum in normal velocity $u_m^{\times}$ is shown with the vertical dashed black line at $t_{\rm NLT} = 18.5\ \Omega_0^{-1}$, and the magnetic field saturation by the second vertical dashed black line at $t_{sat} = 21\ \Omega_0^{-1}$ corresponding to the maximum in magnetic field intensity. The magnetic field keeps growing during the non-linear phase until the normal velocity component becomes negative, corresponding in the magnetic field aligned basis to a loss of the $-\pi/2$ phase shift with respect to the magnetic perturbation necessary to the growth of the non-resonant mode. The parallel induced electric field changes sign and no longer slows down the cosmic rays drift velocity (Eq. 2.54), leading to the magnetic field saturation. This saturation mechanism is well observed in all the simulations. The normal velocity component decrease during the non-linear phase is due both to the conversion of the remaining rotational kinetic energy accumulated during the linear phase into magnetic energy via the induced electric field, and to the loss of the coupling between the magnetic perturbation and the main protons fluid rotation. The magnetic force driving term no longer operates, leading to a decrease of the normal velocity component (which is being projected in the $\mathbf{e}_\perp$ direction) in the local magnetic field aligned basis.

5.3.2 Magnetic field intensity at saturation

The saturated magnetic field intensity is a key parameter of the instability in the context of supernova shocks, as it dictates whether cosmic rays can be confined and accelerated via first order Fermi acceleration. An estimate of the saturated magnetic field intensity can be found by studying the time evolution of the two limiting wave numbers $k_{\rm min}$ and $k_{\rm max}$. During the instability growth, B increases with time and so does the minimum unstable wave number, whereas the maximum wave number decreases. The magnetic field saturation is expected to occur when $k_{\rm max} = k_{\rm min}$ (Bell [2004]). The corresponding magnetic field is then estimated by considering the protons cosmic rays drift velocity to be constant such that the drift kinetic energy density $W_{cr} = n_{cr} m_p u_{cr}^2/2$ is also constant (Bell [2004]). The saturated magnetic field energy density $W_{B,\rm sat} = B_{\rm sat}^2/2\mu_0$ can then be written as:

$$W_{B,\rm sat} \sim W_{cr,0} \tag{5.15}$$

The condition $k_{\rm min} = k_{\rm max}$ does not depend on the cosmic rays charge, indicating that the saturated magnetic field is also insensitive to the charge. This is in agreement with the results obtained in recent PIC simulations by Gupta et al. [2021]. For relativistic cosmic rays drift velocities, the $k_{\rm min}$ limit is expressed as $k_{\rm min} = \Omega_0/u_{cr}\gamma_{cr}$ where $\gamma_{cr} = 1/\sqrt{1 - u_{cr}^2/c^2}$ is the cosmic rays Lorentz factor (Amato and Blasi [2009], Zacharegkas et al. [2019]). In this case Bell's saturation criterion is written as $B^2/2\mu_0 = \rho_{cr}\gamma_{cr}u_{cr}^2/2$. In general, depending on the cosmic rays drift kinetic energy, a large magnetic field amplification $B_1/B_0 > 1$ can be obtained. This is an important feature of the non-resonant instability, as the left-hand and right-hand resonant modes are restricted to fluctuations amplification $B_1/B_0 \sim 1$ because of the resonance condition on the cosmic rays (Bell [2013]).

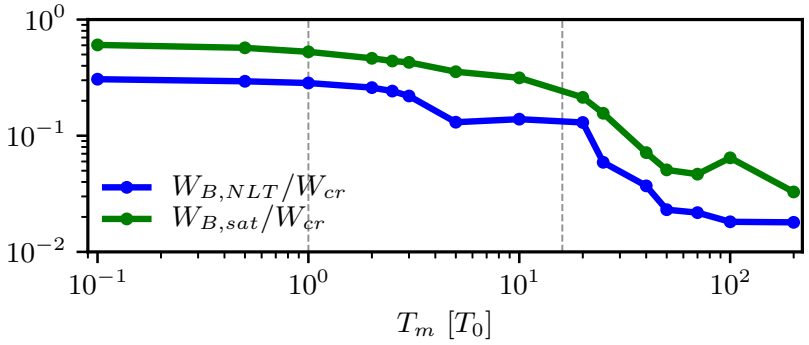

Figure 5.9: Magnetic field energy density $W_B = B^2/2\mu_0$ normalized to the initial cosmic rays drift kinetic energy density $W_{cr} = n_{cr} m_p u_{cr}^2/2$ $(t_0) = 50\ l_0^{-3} m_p v_{A0}^2$, as a function of the main protons temperature for 1D simulations. Blue curve corresponds to the ratio at non-linear transition (noted NLT) and green curve to the ratio at magnetic saturation (noted sat). The non-linear transition time is found numerically by equating $k_{\max} = k_{\min}$ averaged in the simulation box. The two dashed vertical lines corresponds to the limits of the warm and hot regimes of interaction as in Fig. 5.8.

A different estimate can be obtained by considering energy exchange rates within quasi-linear theory calculations (Winske and Leroy [1984]), which yield that the rate of energy gained by the magnetic field is half of the rate of loss of the protons cosmic rays drift kinetic energy. Extrapolating this result to saturation and supposing that the cosmic rays drift velocity is null at saturation, one obtains for the magnetic energy density:

$$W_{B,\mathrm{sat}} \sim \frac{1}{2} W_{cr,0} \tag{5.16}$$

which is half of the fluid prediction obtained from the condition $k_{\min} = k_{\max}$. However, kinetic theory calculations show that for the instability to exist, the cosmic rays drift velocity must be larger than the Alfvén speed in the amplified field (Gary et al. [1984]). In some regimes, this condition is violated and the growth of the instability is halted before the $k_{\min} = k_{\max}$ limit is reached (Riquelme and Spitkovsky [2009]). All the difficulty lies in assessing the highly non-linear evolution of the cosmic rays drift velocity, which would then determine whether the conditions $k_{\min} = k_{\max}$ or $u_{cr} \sim v_A$ gives the most accurate saturation mechanism, and whether the assumption of constant or completely depleted drift kinetic energy is relevant to estimate the saturated magnetic field. As such, only numerical simulations can provide a precise answer on the saturation mechanism and saturated magnetic field, for a given set of initial conditions.

Fig. 5.9 presents the ratio between the magnetic field energy density $W_B = B^2/2\mu_0$ and the initial cosmic rays kinetic energy density $W_{cr} = n_{cr} m_p u_{cr}^2/2$, at non-linear transition (noted "NLT", blue solid line) and at saturation (noted "sat", green solid line), as a function of the main protons temperature. In the cold regime, the simulations yield a conversion efficiency of 30 per cent at the transition from linear to non-linear growth (determined by the condition $k_{\min} = k_{\max}$ measured in the simulations), and about 60 per cent at saturation which is close to the quasi-linear theory prediction. The intermediate, warm regime of interaction shows a quick decrease of the conversion efficiency with temperature. For temperatures corresponding to the hot, demagnetized regime of interaction, the magnetic

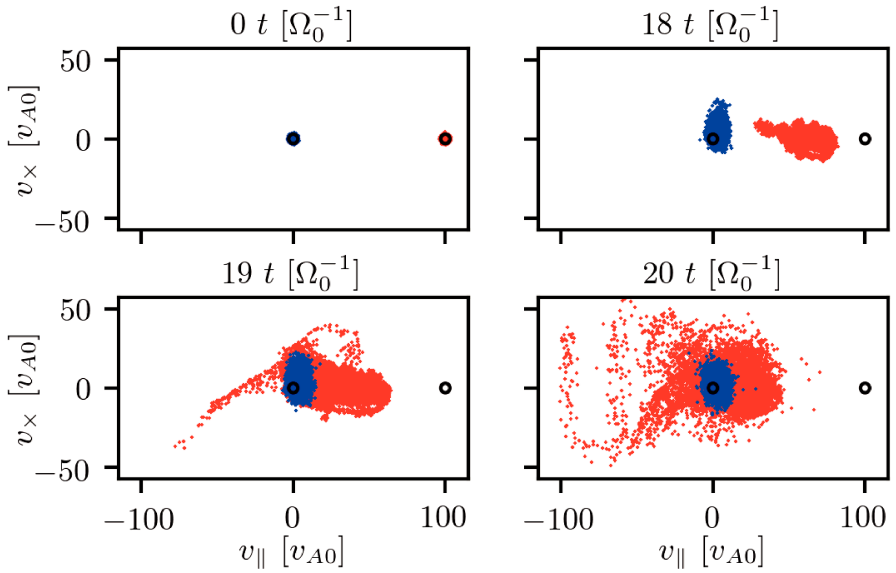

Figure 5.10: Distribution of the main protons (blue dots) and cosmic rays (red dots) in $(v_\parallel, v_\times)$ space, during the instability non-linear phase. Obtained from a 1D simulation with a main protons temperature $T_m = T_0$. The black circles indicate the initial velocity dispersion.

energy shows low amplification of the order of 5 per cent of the initial drift kinetic energy. The amplification during the non-linear phase brings a factor two in amplification compared to the linear phase, with a peak value at $B_1/B_0 \approx 7.8$ for the cold case.

5.4 Wave-particle interactions

5.4.1 Pressure anisotropies

The non-resonant streaming instability fundamental mechanism relies on the fluid motion of the background plasma, driven by the magnetic force generated by the current carried by the cosmic rays. This induces magnetic perturbations which enhance the magnetic force, leading to an instability, as presented in Sec. 2.2.3. This process does not involve resonance between the waves and individual particles in the plasma. However, kinetic effects can nevertheless modify the instability growth. The simulations show that the instability leads to the development of important anisotropies in the protons velocity distributions for both the main and the cosmic rays populations, which cannot be described by fluid simulations with isotropic closures.

Fig. 5.10 shows the distributions of the proton populations in $(v_\parallel, v_\times)$ space during the non-linear phase of the instability growth in a 1D simulation with cold main protons, in the local magnetic field aligned basis $(\mathbf{e}_\parallel, \mathbf{e}_\times, \mathbf{e}_\perp)$. The upper left panel presents the initial velocity distribution for reference. The other panels illustrate the particle distribution during the non-linear phase of growth. The parallel electric field induced by the main protons rotating motion $\mathbf{E}_\parallel = -\mathbf{u}_1 \times \mathbf{B}_1$ decelerates the cosmic rays (upper right panel), leading to particles acquiring a velocity in the opposite direction to their original one (in the reference frame of the initially immobile main protons, lower left panel), in agreement with

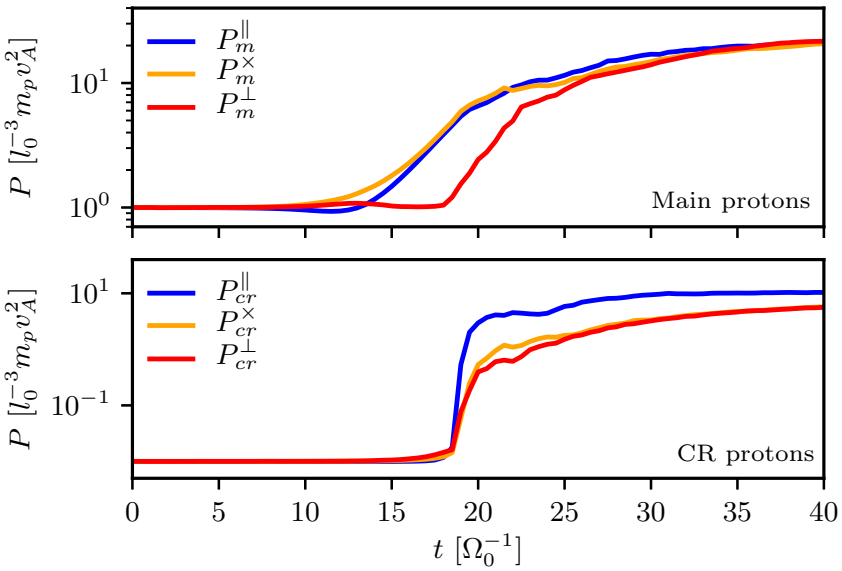

Figure 5.11: Diagonal terms of the pressure tensor in the local magnetic field aligned basis for the main protons (upper panel) and cosmic rays (lower panel), as a function of time between $t = 0\ \Omega_0^{-1}$ and $t = 40\ \Omega_0^{-1}$, for a main protons temperature $T_m = T_0$. The blue, orange and red curves corresponds to the parallel $P^{\parallel}$, normal $P^{\times}$ and perpendicular $P^{\perp}$ components respectively. The values are calculated locally, then averaged over the simulation domain. Obtained from a 1D simulation with a main protons temperature $T_m = T_0$.

results found in full-PIC numerical simulations including the cosmic rays back-reaction on the instability (Riquelme and Spitkovsky [2009]). The cosmic rays are then able to interact resonantly when the resonance condition $\omega - k v_{\parallel cr} \pm \Omega_{cr} = 0$ is fulfilled for right-hand polarized (plus sign) backward propagating ($\omega > 0, k < 0$) waves, with $v_{\parallel cr}$ the cosmic ray velocity along $\mathbf{B}_0$. One obtains $v_{\parallel cr} = -(\omega + \Omega_{cr})/|k| < 0$, which may explain the strong cosmic rays scattering in the $(\mathbf{e}_y, \mathbf{e}_z)$ plane observed in the simulations (lower right panel). This effect is highly non-linear: the cosmic rays destabilize electromagnetic waves in a non-resonant way, and interact later on with the large amplitude waves they have generated. The cosmic rays velocity distribution, which was initially Maxwellian, is greatly altered during the linear and non-linear evolution, and returns to the Maxwellian only during the relaxation phase. The main protons acceleration in the normal direction $\mathbf{e}_{\times}$ is well observed (upper right panel), and it is correlated to the slowing down of the cosmic rays.

The heating and scattering of the proton populations can be quantified by investigating the time evolution of the diagonal terms of the protons pressure tensor over time. Fig. 5.11 shows the diagonal components in the magnetic field aligned basis for the main protons (upper panel) and the cosmic rays (lower panel) in the low temperature case $T_m = T_0$. The main protons pressure starts increasing in the parallel and normal direction first, as magnetic perturbations become of the same order as the initial magnetic field. There is no heating in the perpendicular direction. The main protons are then isotropized after saturation, and are slowly heated during the relaxation phase. By supposing a perfect gas behaviour, the temperature can be estimated as $k_b T_m \sim P_m / n_m$, hence obtaining values which correspond to a one order of magnitude increase with respect to the initial

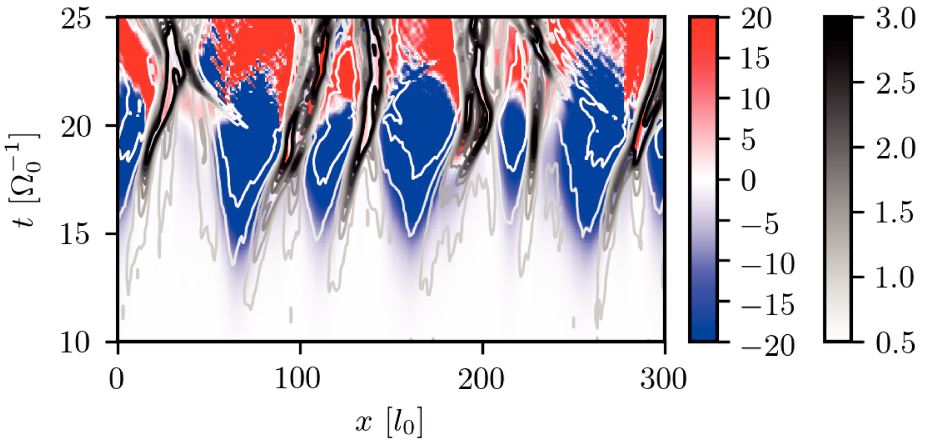

Figure 5.12: Parallel electric field component $E_{\parallel}$ (in unit of $v_{A0}B_0$, blue to red color scale) and main protons density n_m (white to black contours) as a function of space (from 0 to 300 x/l_0, abscissa) and time (from 10 to 25 $t\Omega_0$, ordinate), for a 1D simulation with a cold main protons temperature $T_m = T_0$. The magnetic field saturation is reached at $t = 21\ \Omega_0^{-1}$.

one. Simulations with larger initial main protons temperatures show less heating as the instability develops less efficiently. The same pressure anisotropies are obtained in 2D simulations. The pressure gradient generated between the normal and perpendicular components may act as a self-stabilizing force which opposes the main protons rotation, thus reducing the growth rate of the instability as well as the saturation level. As a consequence, introducing collisions between main protons at frequencies comparable to the non-resonant mode growth rate can favour the growth of the non-resonant mode, by isotropizing the pressure components and reducing the pressure gradient counter force. The origin of those pressure anisotropies, together with the interplay of the anisotropic heating and the isotropization by collisions, will be further investigated in Chapter 6.

The cosmic rays pressure increase in the $(\mathbf{e}_\times, \mathbf{e}_\perp)$ plane takes place when a fraction of the streaming particles acquire a negative parallel velocity component. This corresponds to the sudden increase in pressure, in agreement with the previous discussion. The cosmic rays velocity dispersion during the linear growth phase seen in $(v_\parallel, v_\times)$ space (Fig. 5.10 upper right panel) is an effect of the velocity space representation, which does not take into account the position of the macro-particles. The cosmic rays follow an organized motion as no pressure increase occurs, becoming stochastic after resonant interactions begin settling in during the non-linear phase (Fig. 5.10 lower left panel).

5.4.2 Parallel electric field and density fluctuations

The heating in the parallel direction has a different origin, and can be linked to the electric field induced by the rotating motion of the main protons. A study of the relative intensities of the longitudinal $\mathbf{k} \cdot \mathbf{E}/k$ and transverse $\mathbf{k} \times \mathbf{E}/k$ electric field reveals an important electrostatic component developing during the non-linear phase. The longitudinal electric field (corresponding to the component parallel to the initial magnetic field B_0 in 1D simulations) spatial and temporal evolution is presented in Fig. 5.12 alongside with the main protons density. Regions of fast growing mode appear well delimited in space. Large

electric field gradients are generated, leading to an important heating of both protons populations. The background fluid is accelerated in the same direction as the cosmic rays initial velocity (Eq. 2.55). Because of the continuity equation, the background plasma accumulates density toward the positive $\mathbf{e}_{\parallel}$ direction, on the right of the growing electric field regions in Fig. 5.12. Large density fluctuations are generated with cavities of low density, correlated with regions of fast growing modes and important heating of both protons populations. The reversal of the electric field occurs after saturation ($t_{sat} = 21\ \Omega_0^{-1}$), corresponding to the main protons normal velocity $u_m^{\times}$ changing sign in the magnetic field aligned basis (Fig. 5.8, lower panel) and inducing a positive electric field $\mathbf{E} \cdot \mathbf{e}_{\parallel} = -(\mathbf{u}_1 \times \mathbf{B}_1) \cdot \mathbf{e}_{\parallel} > 0$. As a consequence the cosmic rays are no longer slowed down, and their drift kinetic energy cannot be converted into magnetic energy anymore. This leads to the non-resonant mode saturation as discussed previously.

The 2D simulations bring additional information on the main protons density spatial structures. The simulations results are presented in Fig. 5.14. Density fluctuations are found to increase in scale from tenth to hundredth of l_0 over time, as small scale density holes along the initial magnetic field direction (observed in 1D simulations) merge together to generate large scale fluctuations during the non-linear evolution of the instability. The density holes expand in the perpendicular plane because of the increasing magnetic pressure, generating density fluctuations up to $n_m/n_0 \sim 2$ in the background plasma at the same spatial scales as the magnetic fluctuations, on the order of a hundredth of the proton inertial length for the parameters investigated. This result agrees with previous studies using a fluid description (Bell [2013], Bai et al. [2015]), consistent with the fact that the density perturbations are not the results of individual wave-particles interactions. In this case the hybrid-PIC simulations yield the same result as fluid simulations. The density fluctuations may play a role in allowing further magnetic field amplification, by allowing potentially important dynamo effects to take place at supernova shocks (del Valle et al. [2016]). This also constitutes a marker of the development of the instability, and may be used as an observable in laboratory experiments (see Chapter 7).

As in previous studies (e.g. Winske and Leroy [1984], Riquelme and Spitkovsky [2009]), the simulations were performed without a continuous injection of streaming particles, corresponding to an initial value problem as stated in Chapter 4. The immediate consequence is that the cosmic rays current is self-consistently decreasing through time as the cosmic rays drift kinetic energy is being converted into magnetic fluctuations. An alternative approach is to maintain the driving current, either by re-accelerating the cosmic rays artificially (Lucek and Bell [2000]), or by injecting new ones in the simulation domain over time (Bai et al. [2015], Mignone et al. [2018], Casse et al. [2018]) which was used to directly simulate particles acceleration at supernova shocks. A comparison between these approaches shows that the development of the non-resonant instability is not significantly altered. In particular the magnetic field intensity at saturation and the density fluctuations are quantitatively similar, with magnetic field amplifications of the order of ten times the ambient magnetic field and large density fluctuation of the order of the initial plasma density. These results however apply to the cold regime, and the ambient medium temperature remains an important factor in determining whether the non-resonant streaming instability can efficiently generate magnetic field fluctuations, and should be taken into account to model accurately cosmic rays acceleration with “non-ideal” plasma conditions.

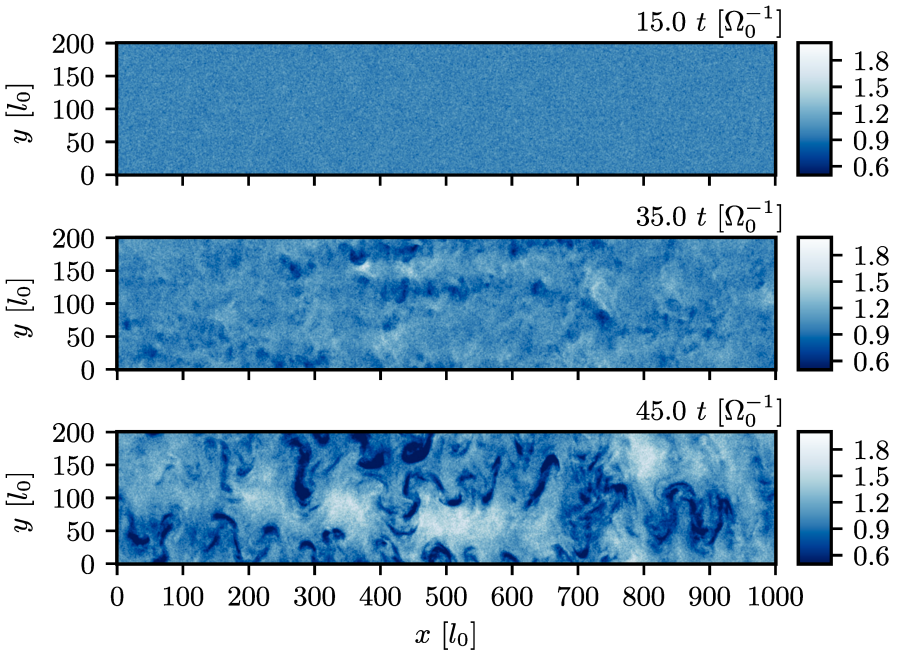

Figure 5.13: Main protons density n_m/n_0 map at three different times: beginning of the linear growth phase ($t = 15\ \Omega_0^{-1}$), during the linear growth phase ($t = 35\ \Omega_0^{-1}$), after saturation ($t = 45\ \Omega_0^{-1}$). Obtained from a 2D simulation with $T_m = 25\ T_0$.

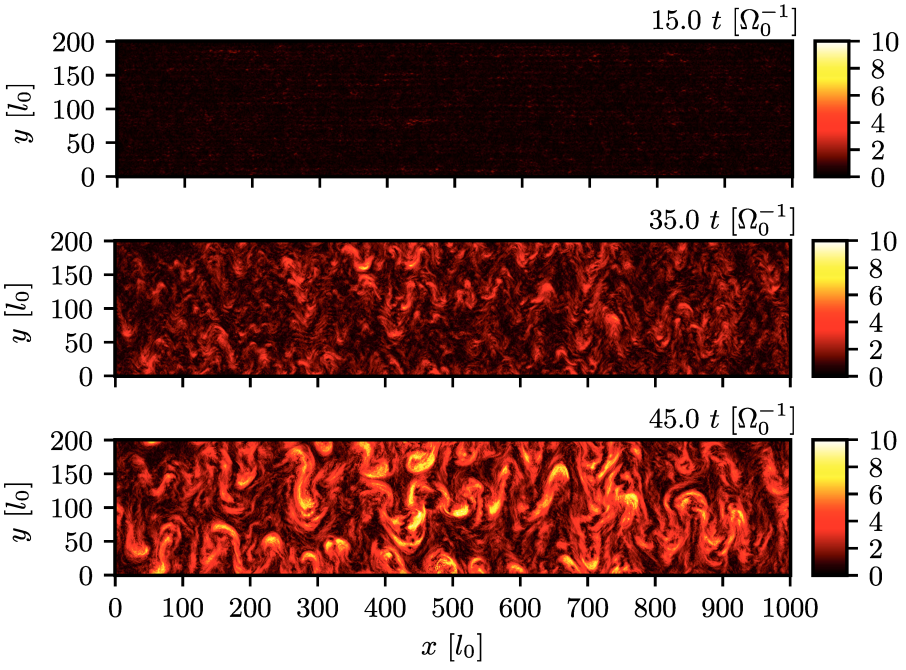

Figure 5.14: Perturbed magnetic field intensity $B_1 = ||\mathbf{B} - \mathbf{B}_0||/B_0$ map at three different times: beginning of the linear growth phase ($t = 15\ \Omega_0^{-1}$), during the linear growth phase ($t = 35\ \Omega_0^{-1}$), after saturation ($t = 45\ \Omega_0^{-1}$). Obtained from a 2D simulation with $T_m = 25\ T_0$.

5.5 Summary

Multidimensional hybrid-PIC simulations of the non-resonant streaming stability have been performed, while considering a wide range of background plasma temperatures, as well as varying mass and charges for the ion populations. The results may be summarized as follows.

- The non-resonant streaming instability generates exponentially growing electromagnetic fluctuations, propagating parallel to the ambient magnetic field. The simulations show that the instability growth rate and saturated magnetic field can be strongly reduced when increasing the background protons temperature, in agreement with linear theory predictions. The finite Larmor radius of the background ions weakens the coherent motion with the magnetic perturbation required to grow the instability, thus producing a damping of the unstable waves.

- Theoretical predictions on the growth rate as a function of mass and charge of the main and streaming populations agree with simulation results. Multiply charged streaming ions favour the instability by increasing the driving current for a given density and drift velocity, whereas heavy main ions increase the background plasma inertia and slow down the instability development.

- The instability mechanism described in Sec. 2.2.3 is well observed in the simulations. In particular, the strong correlation between the background plasma fluid motion and the electromagnetic wave, which possesses a negative helicity with a clearly defined helical structure in space, is retrieved both in 1D and 2D runs. This correlation plays a fundamental role in the saturation of the instability.

- A non-linear phase of growth of the magnetic field perturbations has been described. The condition $k_{\min} = k_{\max}$ can be used as a robust criteria for the beginning of this phase, characterized by a slowing down of the background plasma fluid motion and a progressive loss of correlation between the fluid velocity magnetic fields until saturation is reached.

- The streaming population drift kinetic energy is converted into magnetic field fluctuations, eventually leading to particles propagating in a direction opposite to their initial drift velocity. Owing to the negative helicity and right-hand polarization of the waves, strong cyclotron resonance occurs, as the streaming particles can interact resonantly with the large amplitude waves that they have themselves generated in a non-resonant way during the early times of growth. This produces a strong scattering of the streaming particles in the plane perpendicular to the initial magnetic field.

- The instability is found to generate important pressure anisotropies in the background plasma, as well as important density fluctuations during the late time evolution of the unstable waves. The density fluctuations are a product of the development of an important electrostatic component of the electric field fluctuations, together with the large magnetic pressure generated by the non-linear magnetic field amplification.

- The magnetic field energy density at saturation obtained in the simulations is in reasonable agreement with theoretical estimates obtained by energy conservation

arguments, in the case of a cold background plasma. In the hot regime, the instability saturated magnetic field energy density is strongly reduced. It is not totally suppressed however, indicating that the instability may still amplify the magnetic field and modify the transport of cosmic rays in hot and low magnetic field environments such as the intergalactic medium.

In addition to the effects of a finite background plasma temperature, the instability may also be modified if one takes into account particle collisions, between charged particles or with a population of neutrals. In the MHD framework, particles collisions are often implicitly assumed to occur on time scales much shorter than the scales of interest, such that the pressure tensor may be considered as isotropic. In addition, the electron and ion temperature are commonly assumed equal, which can be justified by a strong collisionality between the populations. In the particular case of the non-resonant mode, the simulations showed that the instability can self-generate pressure anisotropies, invalidating the isotropic assumption. The interplay between anisotropic pressure generation, and isotropization by collisions is a strongly non-linear process, which may be investigated with numerical simulations. This is the subject of the following chapter, which tackles the question of the effects of particle collisions on the non-resonant mode.

5.6 References

Akimoto, K., Winske, D., Gary, S. P., and Thomsen, M. F. (1993). Nonlinear evolution of electromagnetic ion beam instabilities. *Journal of Geophysical Research: Space Physics*, 98(A2):1419–1433.

Amato, E. and Blasi, P. (2009). A kinetic approach to cosmic-ray-induced streaming instability at supernova shocks. *Mon Not R Astron Soc*, 392(4):1591–1600.

Bai, X.-N., Caprioli, D., Sironi, L., and Spitkovsky, A. (2015). Magnetohydrodynamic-Particle-in-Cell Method for Coupling Cosmic Rays with a Thermal Plasma: Application to Non-relativistic Shocks. *ApJ*, 809(1):55.

Bell, A. R. (2004). Turbulent amplification of magnetic field and diffusive shock acceleration of cosmic rays. *Mon Not R Astron Soc*, 353(2):550–558.

Bell, A. R. (2013). Cosmic ray acceleration. *Astroparticle Physics*, 43:56–70.

Casse, F., van Marle, A. J., and Marcowith, A. (2018). On magnetic field amplification and particle acceleration near non-relativistic collisionless shocks: Particles in MHD Cells simulations. *Plasma Physics and Controlled Fusion*, 60:014017.

Crumley, P., Caprioli, D., Markoff, S., and Spitkovsky, A. (2019). Kinetic simulations of mildly relativistic shocks – I. Particle acceleration in high Mach number shocks. *Mon Not R Astron Soc*, 485(4):5105–5119.

del Valle, M. V., Lazarian, A., and Santos-Lima, R. (2016). Turbulence-induced magnetic fields in shock precursors. *Mon Not R Astron Soc*, 458(2):1645–1659.

Gary, S. P., Smith, C. W., Lee, M. A., Goldstein, M. L., and Forslund, D. W. (1984). Electromagnetic ion beam instabilities. *The Physics of Fluids*, 27(7):1852–1862.

Gupta, S., Caprioli, D., and Haggerty, C. C. (2021). Lepton-driven Non-resonant Streaming Instability. *arXiv e-prints*, page arXiv:2106.07672.

Haggerty, C. C. and Caprioli, D. (2019). dHybridR: A Hybrid–Particle-in-Cell Code Including Relativistic Ion Dynamics. *ApJ*, 887(2):165.

Lucek, S. G. and Bell, A. R. (2000). Non-linear amplification of a magnetic field driven by cosmic ray streaming. *Monthly Notices of the Royal Astronomical Society*, 314(1):65–74.

Marret, A., Ciardi, A., Smets, R., and Fuchs, J. (2021). On the growth of the thermally modified non-resonant streaming instability. *Monthly Notices of the Royal Astronomical Society*, 500(2):2302–2315.

Mignone, A., Bodo, G., Vaidya, B., and Mattia, G. (2018). A Particle Module for the PLUTO Code. I. An Implementation of the MHD–PIC Equations. *ApJ*, 859(1):13.

Ohira, Y., Reville, B., Kirk, J. G., and Takahara, F. (2009). Two-dimensional particle-in-cell simulations of the nonresonant, cosmic-ray-driven instability in supernova remnant shocks. *The Astrophysical Journal*, 698(1):445–450.

Reville, B., Kirk, J. G., Duffy, P., and O'Sullivan, S. (2008). Environmental limits on the nonresonant cosmic-ray current-driven instability. *International Journal of Modern Physics D*, 17(10):1795–1801.

Riquelme, M. A. and Spitkovsky, A. (2009). Nonlinear study of Bell's cosmic ray current-driven instability. *The Astrophysical Journal*, 694(1):626–642.

Terasawa, T., Hoshino, M., Sakai, J.-I., and Hada, T. (1986). Decay instability of finite-amplitude circularly polarized Alfven waves: A numerical simulation of stimulated Brillouin scattering. *Journal of Geophysical Research: Space Physics*, 91(A4):4171–4187.

Weidl, M. S., Winske, D., Jenko, F., and Niemann, C. (2016). Hybrid simulations of a parallel collisionless shock in the large plasma device. *Physics of Plasmas*, 23:122102.

Winske, D. and Leroy, M. M. (1984). Diffuse ions produced by electromagnetic ion beam instabilities. *Journal of Geophysical Research: Space Physics*, 89(A5):2673–2688.

Zacharegkas, G., Caprioli, D., and Haggerty, C. (2019). Modeling the Saturation of the Bell Instability Using Hybrid Simulations. *arXiv:1909.06481*.

Zirakashvili, V. N., Ptuskin, V. S., and Völk, H. J. (2008). Modeling bell's nonresonant cosmic-ray instability. *The Astrophysical Journal*, 678(1):255–261.

Zweibel, E. G. and Everett, J. E. (2010). Environments for Magnetic Field Amplification by Cosmic Rays. *The Astrophysical Journal*, 709(2):1412–1419.

Chapter 6

Collisional non-resonant mode

Contents

6.1 Introduction

As presented in Sec. 5.4, even in relatively cold plasmas, collisionless hybrid-PIC simulation have shown the non-linear development of significant ion pressure anisotropies in the background plasma (Marret et al. [2021]), suggesting that the assumption of an isotropic scalar pressure, often employed in fluid models, may not always be justified. Pressure anisotropies may be suppressed by particle collisions, among other isotropization mechanisms. The Coulomb collisions, as well as the neutral collisions, are usually neglected in studies of space and astrophysical plasmas which are very tenuous (of the order of 1 cm^{-3} in the cold interstellar medium and in the solar wind) such that particle collisions occur on time scales much longer than the plasma processes of interest. In the case of the non-resonant mode, considering a supernova shock which propagates at a velocity $u_{cr} = 10^3$ $\mathrm{km.s}^{-1}$ in an cold and tenuous interstellar medium with a density $n_m = 1$ cm^{-3}, an ambient magnetic field $B = 5$ μG, a low temperature $T_m = 10^4$ K and a cosmic rays flux $n_{cr}u_{cr} = 10^4$ $\mathrm{cm}^{-2}s^{-1}$ (Zweibel and Everett [2010]), one obtains a protons Coulomb frequency (Eq. 4.61) and instability growth rate (Eq. 2.37) as $\nu_0/\gamma_{\mathrm{cold}} \approx 3 \times 10^{-2}$. In this case Coulomb collisions can be considered negligible *a priori*, which is the assumption commonly made in the literature. However, increasing the plasma density to $n_m = 90$ cm^{-3}

encountered in ionized H II regions (Galarza et al. [1999]) such as in the case of SN 1987A (Orlando, S. et al. [2019]), while keeping the other parameters, one obtains a proton Coulomb frequency and non-resonant mode growth rate as $\nu_0/\gamma_{\rm cold} \sim 24$, large enough to expect collisions to occur on time scales comparable to the non-resonant mode growth time. More precisely, large enough for the rate of change of the particles velocity resulting from numerous Coulomb interactions to occur on time scales comparable to the growth rate. While ion-neutral collisions have been shown to damp the non-resonant mode (Reville et al. [2007]), no studies have been done while considering Coulomb collisions.

The simulations presented in this chapter aim to investigate these problematic, by studying the effects of particle collisions on the growth of the non-resonant mode using hybrid-PIC simulations with Monte Carlo Collisions (MCC). A particular emphasis is made on the pressure anisotropies generated by the instability, and the isotropizing effect of collisions. In the following, the simulation parameters used will be those corresponding to the "CC" (Coulomb collisions) and "CN" (collisions with neutrals) runs presented in Table 4.2.

6.2 Growth rate dependency with collision frequency

6.2.1 Neutral collisions

Given that the instability relies on the interaction of large scale fluid motions with the electromagnetic wave, and that intra-species Coulomb collisions conserve momentum and energy (Trubnikov [1965]), one may expect that Coulomb collisions will have no effects on the instability, at least in its linear phase of growth. Proton-neutral collisions on the contrary, differ significantly from the Coulomb collisions as both momentum and energy of the background proton population are not conserved. This leads to important damping of the electromagnetic waves, including the non-resonant mode (Khodachenko, M. L. et al. [2004], Forteza et al. [2007], Reville et al. [2007]). This may occur in supernova remnants expanding near molecular clouds, which are the subject of active research (e.g. Chevalier [1999], Feinstein et al. [2009]). In this situation collisions with neutrals are expected to be important because of the low temperature and ionization fraction. Following the analysis of Reville et al. [2007] and adopting the values $T_m = 10^2$ K, $n_m = 23$ cm^{-3}, a low ionization fraction $x = 0.01$ and a drift velocity $u_{cr} = 10^8$ cm.s^{-1} (Malkov et al. [2005]), while considering that the ion-neutral collision frequency follows the approximate expression (Kulsrud and Pearce [1969]):

$$\nu_0 \approx 8.9 \times 10^{-9} n_n \left(\frac{T_m}{10^4 \text{ K}}\right)^{0.4} \text{s}^{-1} \tag{6.1}$$

then the growth rate is smaller than the collision frequency, such that neutral collisions cannot be neglected.

The effect of ion-neutral collisions on the non-resonant mode has been calculated in Reville et al. [2007], by using a MHD model while including a collisional friction term in

the background plasma momentum conservation equation (Tagger et al. [1995]) such that:

$$\frac{\mathrm{d}\mathbf{u}}{\mathrm{d}t} = \frac{\mathbf{J}\times\mathbf{B}}{\rho} - \nu_{in}(\mathbf{u}-\mathbf{u}_n) \tag{6.2}$$

with ν_{in} a characteristic slowing down time by ion-neutral collisions. The neutral fluid velocity $\mathbf{u}_n$ is computed by considering only the friction force:

$$\frac{\mathrm{d}\mathbf{u}_n}{\mathrm{d}t} = -\nu_{ni}(\mathbf{u}_n-\mathbf{u}) \tag{6.3}$$

with $\nu_{ni} = \nu_{in} n_n/n_i$ is a characteristic neutral slowing down time by neutral-ion collisions where n_n and n_i are the neutral and ion densities respectively. The dispersion relation can then be obtained as:

$$\omega\left(\omega^2 + \frac{n_{cr}}{n_m}\frac{u_{cr}^2}{r_{Lcr}}k\right) + i\nu_0\left[(1+Z)\omega^2 + Z\frac{n_{cr}}{n_m}\frac{u_{cr}^2}{r_{Lcr}}k\right] = 0 \tag{6.4}$$

with $r_{Lcr} = u_{cr}/\Omega_0$ and $Z = n_m/n_n$ the density ratio between the ions and the neutrals. In the case of a low ionization fraction, the growth rate can be reduced analytically with the simplifying assumption $Z \ll 1$ as:

$$\gamma_{in}(k) = -\frac{\nu_0}{2} + \frac{1}{2}\left(\nu_0^2 + 4\Omega_0\frac{n_{cr}}{n_m}u_{cr}k\right)^{1/2} \tag{6.5}$$

with $\nu_0 \equiv \nu_{in}$. This is plotted in Fig. 6.1 considering $k = k_{\max}/4 = \frac{1}{4}\frac{n_{cr}}{n_m}\frac{u_{cr}}{v_{A0}^2}\Omega_0$, such that $\gamma_{in}(k = k_{\max}/4, \nu_0 = 0) = \gamma_{\mathrm{cold}}$ with $\gamma_{\mathrm{cold}} = \frac{1}{2}\frac{n_{cr}}{n_m}\frac{u_{cr}}{v_{A0}}\Omega_0$ the fastest growing mode in the collisionless cold case (Winske and Leroy [1984]), together with the growth rate obtained in 1D simulations including proton-neutral collisions ("CN" runs). One obtains that the non-resonant streaming instability is rapidly damped with increasing neutral collisions frequency. The growth rate dependency with collision frequency is well recovered in the simulations. The neutral collisions reduce the background fluid velocity perturbations, leading to a weaker induced electric field and consequently smaller growth rate and magnetic field amplification. The observed offset may be explained by the fact that the magnetic field intensity in the simulations is integrated over the whole k spectrum, which gives an overall smaller growth rate than if only the fastest growing mode was observed (see Appendix B).

6.2.2 Coulomb collisions

For the case of a fully ionized collisional background where neutral collisions are negligible, and proton-proton Coulomb collisions are dominant ("CC" runs), the simulations show that the growth rate is enhanced for $\nu_0 \gtrsim \gamma_0$, where $\gamma_0 = 0.15\ \Omega_0$ is the growth rate in the collisionless case. The increase is maximum for a collision frequency $\nu_0 = 27\ \Omega_0$ two orders of magnitude larger than γ_0, yielding a growth rate $\gamma = 0.17\ \Omega_0$ (rightmost vertical dashed line in the figure). The saturated magnetic field energy density, $W_{B,\mathrm{sat}}$ is displayed in Fig. 6.1 middle panel, and shows an increase from $W_B^{cl} = 6.84$ (in units of $l_0^{-3} m_p v_{A0}^2$) in the collisionless case up to $W_{B,\mathrm{sat}} = 1.21\ W_{B,\mathrm{sat}}^{cl}$ for $\nu_0 = 27\ \Omega_0$. Because of its relatively large density in the simulations, the cosmic rays population becomes collisional with the

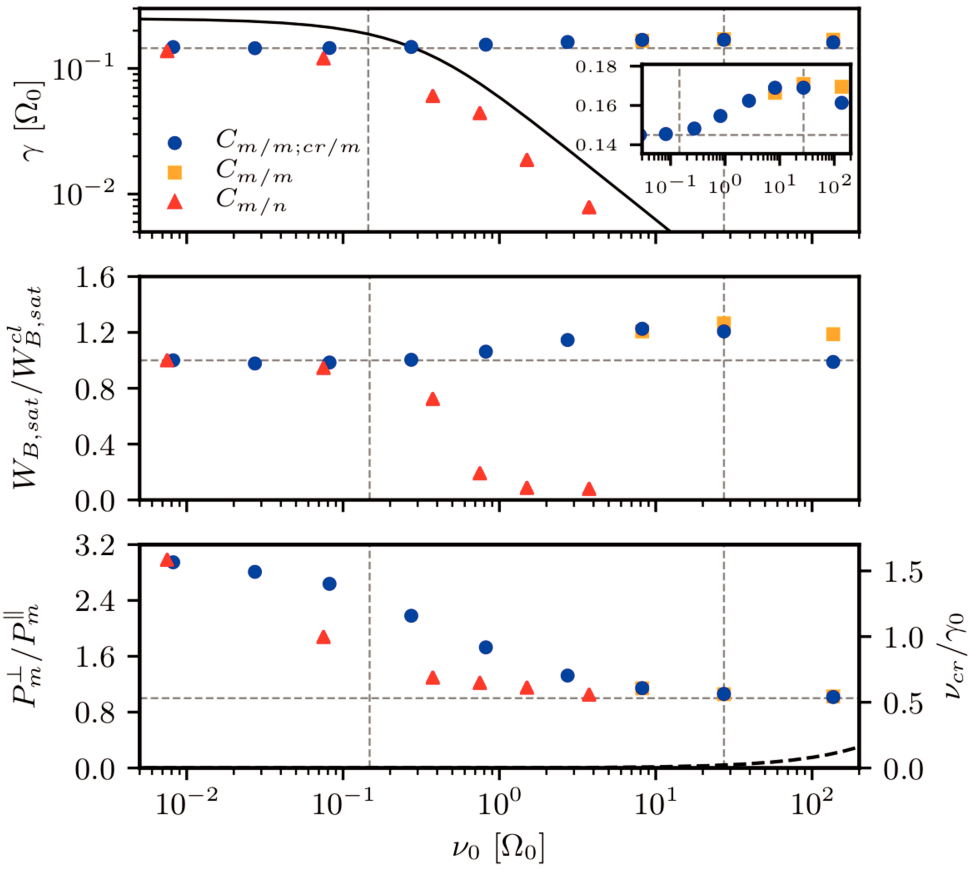

Figure 6.1: *Upper panel*: Magnetic field growth rate $\gamma(\nu_0)$, in 1D runs with Coulomb collisions between all protons populations ($C_{m/m;cr/m}$, blue dots) and with Coulomb collisions between main protons only ($C_{m/m}$, orange squares) where $\nu_0 = e^4 n_m \ln\Lambda / 4\pi m_p^2 \epsilon_0^2 v_{T0}^3$ is the collision frequency among the main proton, $\ln\Lambda$ is the Coulomb logarithm, and $v_{T0} = (k_B T_0/m_p)^{1/2}$ the thermal velocity. The red triangles indicates simulations with main proton-neutral collisions ($C_{m/n}$), where $\nu_0 = n_n \sigma_n v_{T0}$ is the main proton-neutral collision frequency, n_n is the neutral density and σ_n is the neutral collision cross-section. The solid black line corresponds to the theoretical growth rate γ_{in} considering $k = k_{\max}/4$. The magnetic field growth rate in the collisionless case $\gamma_0 = 0.15\ \Omega_0$ is indicated with the horizontal dashed line and by the first horizontal dashed line. The maximum growth rate for simulations with Coulomb collisions is indicated with the second vertical dashed line at $\nu_0 = 27\ \Omega_0$. The growth rates are obtained by a numerical fit on the spatially averaged perturbed magnetic field intensity. *Middle panel*: Magnetic field energy density $W_{B,\mathrm{sat}} = B^2_{\mathrm{sat}}/2\mu_0$ at saturation, normalized to the value in collisionless simulations $W^{cl}_{B,\mathrm{sat}} = 6.84\ l_0^{-3} m_p v_{A0}^2$. *Lower panel*: Mean value of the anisotropy parameter $P_\perp/P_\parallel$ averaged over the exponential phase of growth. The dashed black line (bottom right) corresponds to the initial cosmic ray-main proton collision frequency ν_{cr}, normalized to γ_0.

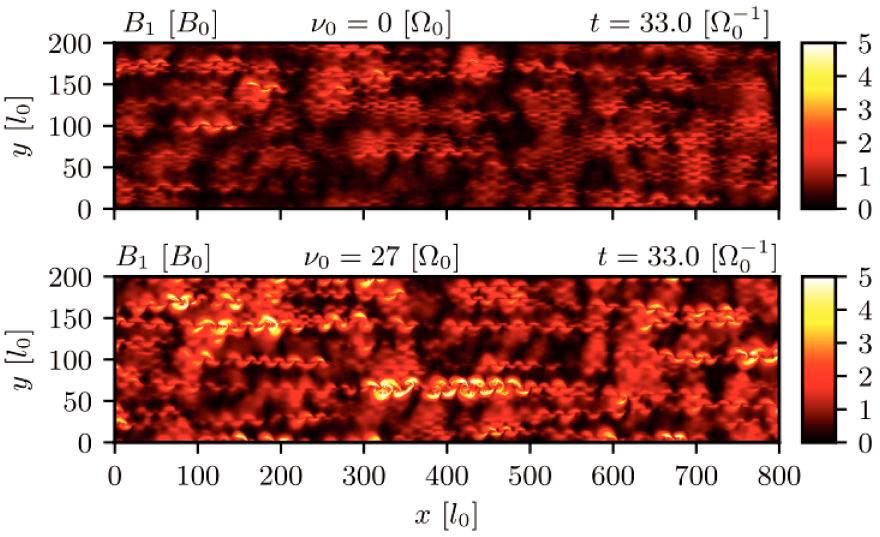

Figure 6.2: Map of the perturbed magnetic field intensity B_1, in units of B_0, during the exponential phase of growth in 2D simulations between $x = 0$ and $x = 800\ l_0$. *Upper panel*: Collisionless simulation. *Lower panel*: Including Coulomb collisions with a collision frequency $\nu_0 = 27\ \Omega_0$.

background protons for a reference Coulomb collision frequency larger than $\nu_0 = 27\ \Omega_0$, as shown in the lower panel of Fig. 6.1. The relative drift velocity is reduced by collisions on time scales comparable with the instability growth time, leading to a smaller growth rate as well as lower magnetic field amplification. In order to overcome this numerical limitation, and be closer to the case of cosmic rays propagating in the interstellar medium, simulations where cosmic rays-main protons collisions were artificially ignored have been performed, and yield that the non-resonant mode magnetic field energy at saturation is maintained in the case of collisionless cosmic rays.

In 2D simulations, the growth rate of the magnetic field intensity averaged over space during the linear phase is marginally larger ($\sim 1\%$) in the collisional case. The magnetic field is amplified similarly to 1D simulations, with an average magnetic field energy density ratio between the collisional and collisionless simulations of ~ 1.3 over the growth of the instability. This is illustrated in Fig. 6.2, which displays maps of the perturbed magnetic field intensity for 2D collisionless and collisional ($\nu_0 = 27\ \Omega_0$) simulations. The most unstable wavenumbers are found to be insensitive to the collision frequency, with unstable waves growing on scales of the order $\lambda \sim 2\pi k_{cold}^{-1} \sim 25\ l_0$ where $k_{cold} = \frac{1}{2}\frac{n_{cr}}{n_m}\frac{u_{cr}}{v_{A0}^2}\Omega_0$ is the fastest growing unstable wavenumber obtained from linear kinetic theory calculations for negligible background plasma temperature (Winske and Leroy [1984]).

The increased amplification of the magnetic field in the collisional case is linked to the suppression of the pressure anisotropies. The lower panel of Fig. 6.1 shows the anisotropy parameter $P_\times/P_\perp$ as a function of the collision frequency, calculated in the local magnetic field aligned basis $\mathbf{e}_\parallel = \frac{\mathbf{B}_0}{B_0} = \mathbf{e}_x$ (parallel component), $\mathbf{e}_\times = \frac{\mathbf{B}_1}{B_1} \times \mathbf{e}_\parallel$ (normal component) and $\mathbf{e}_\perp = \mathbf{e}_\parallel \times \mathbf{e}_\times$ (perpendicular component, aligned with the perturbed magnetic field $\mathbf{B}_1$). The anisotropy parameter is averaged over the exponential phase of growth of the instability and over the simulation domain. One obtains that the growth rate and magnetic field energy density are at a maximum when anisotropies are entirely

suppressed. The simulations show that the collision frequency must be larger than the instability growth rate, up to two orders of magnitude for the simulation parameters considered, to effectively suppress the anisotropies produced by the non-resonant mode. This corresponds to a competition between the instability tendency to generate pressure anisotropies in the background plasma, and the isotropization effect of collisions. This competition is overtaken by collisions during the whole instability growth for $\nu_0 > 10\ \Omega_0$ for the simulation parameters considered.

6.3 Full pressure tensor effects

6.3.1 Pressure anisotropies in the amplified magnetic field

In order to describe the anisotropic heating of the background protons observed in the simulations presented in Chapter 5, one must distinguish the evolution of the energy densities in the directions parallel and perpendicular to the *total* magnetic field. This can be done within the framework of the double adiabatic Chew-Goldberger-Low (CGL) theory (Chew et al. [1956]). Assuming cold electrons, and neglecting heat fluxes and non-gyrotropic (i.e. non-diagonal) pressure components, one may write the two equations for the main protons pressure in the directions parallel and perpendicular to the *total* magnetic field as:

$$\frac{\mathrm{d}}{\mathrm{d}t}\left(\frac{P_m^{\parallel} B^2}{\rho^3}\right) = 0 \tag{6.6}$$

$$\frac{\mathrm{d}}{\mathrm{d}t}\left(\frac{P_m^{\perp}}{\rho B}\right) = 0 \tag{6.7}$$

where $\mathrm{d}/\mathrm{d}t = \partial/\partial t + \mathbf{u}\cdot\boldsymbol{\nabla}$ denotes the material derivative and ρ the main protons density. The advective term may be written as:

$$\mathbf{u}\cdot\boldsymbol{\nabla}\left(\frac{P_m^{\parallel} B^2}{\rho^3}\right) = \boldsymbol{\nabla}\cdot\left(\mathbf{u}\frac{P_m^{\parallel} B^2}{\rho^3}\right) - \frac{P_m^{\parallel} B^2}{\rho^3}\boldsymbol{\nabla}\cdot\mathbf{u} \tag{6.8}$$

Supposing no density fluctuations such that $\boldsymbol{\nabla}\cdot\mathbf{u} = 0$ (Eq. 2.1), and averaging over space in the periodic simulation domain such that the flux term cancels out, one may neglect the advective component of the material derivative. The integrated CGL equations then read:

$$\frac{\partial}{\partial t}\left\langle\frac{P_m^{\parallel} B^2}{\rho^3}\right\rangle = 0 \tag{6.9}$$

$$\frac{\partial}{\partial t}\left\langle\frac{P_m^{\perp}}{\rho B}\right\rangle = 0 \tag{6.10}$$

where the brackets denote the spatial average. Those equation can be directly integrated, and yield that in the incompressible case, an increase in magnetic field implies a decrease of the parallel pressure component, and an increase of the perpendicular component. This result is a consequence of the conservation of the first and second adiabatic invariants (Kulsrud [1983]) in an amplified magnetic field, and is well recovered in the simulations, as is shown in Fig. 6.3. This figure highlights the correlation between the growth of the

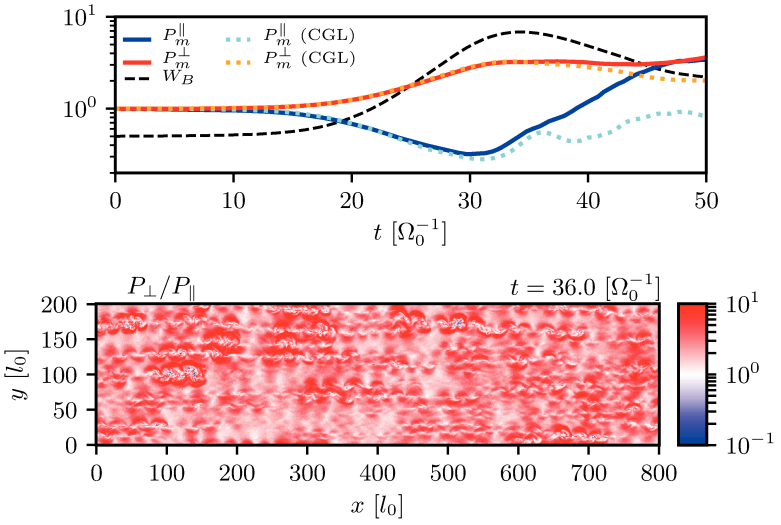

Figure 6.3: *Upper panel*: evolution of the spatial average of the perpendicular and parallel components $P_m^{\perp}$ and $P_m^{\parallel}$ (to the *total* magnetic field) of the main protons pressure tensor calculated from the local macroparticles distribution (solid lines) and magnetic field energy density $W_B = B^2/2\mu_0$ (dashed black line) in units of $l_0^{-3} m_p v_{A0}^2$, obtained from a 1D collisionless simulation. The dotted orange and cyan lines show the CGL prediction as from Eqs. 6.9 and 6.10 obtained from the simulations. *Lower panel*: map of the anisotropy parameter $P_\perp/P_\parallel$ at the end of the exponential phase of growth in a 2D collisionless simulation between $x = 0$ and $x = 800\ l_0$.

non-resonant mode and the generation of pressure anisotropies. The exponential growth of the magnetic perturbations between $t \sim 20$ and $t \sim 30\ \Omega_0^{-1}$ is associated with important anisotropies. Defining the anisotropy parameter as $P_m^{\perp}/P_m^{\parallel}$, one obtains a maximum spatially averaged value $P_m^{\perp}/P_m^{\parallel} = 9.1$ at $t = 31.5\ \Omega_0^{-1}$ before the magnetic field saturation is reached at $t = 34\ \Omega_0^{-1}$. Eqs. 6.9 and 6.10 describe accurately the observed anisotropies, up to saturation where non-gyrotropic pressure terms (which were verified to be important only after saturation, not shown here) must be taken into account and invalidate the simplified CGL equations (Hunana et al. [2019]). Similar pressure anisotropy values are obtained in 2D simulations, as shown in the lower panel of Fig. 6.3 where a map of the anisotropy parameter at the end of the exponential phase of growth is displayed. Pressure anisotropies are present over the whole simulation domain on the same spatial scales as the unstable wavelengths, and are correlated to regions of fast growth of the electromagnetic perturbations.

6.3.2 The role of micro-instabilities

Pressure anisotropies $P_m^{\perp}/P_m^{\parallel} > 1$ are usually associated with the growth of the ion-cyclotron and mirror micro-instabilities which tend to reduce them (Gary et al. [1976]). Fig. 6.4 displays the distribution (cell count) of the anisotropy parameter $P_m^{\perp}/P_m^{\parallel}$ as a function of $\beta_m^{\parallel} = P_m^{\parallel}/W_B$, together with the thresholds for different growth rates of the ion-cyclotron and mirror instabilities, obtained by solving the linear kinetic dispersion relation (Hellinger et al. [2006]). The maximum anisotropy is constrained by the mirror mode, for a growth rate $\gamma_{mi} > 10^{-2}\ \Omega_0$ comparable with the non-resonant mode growth

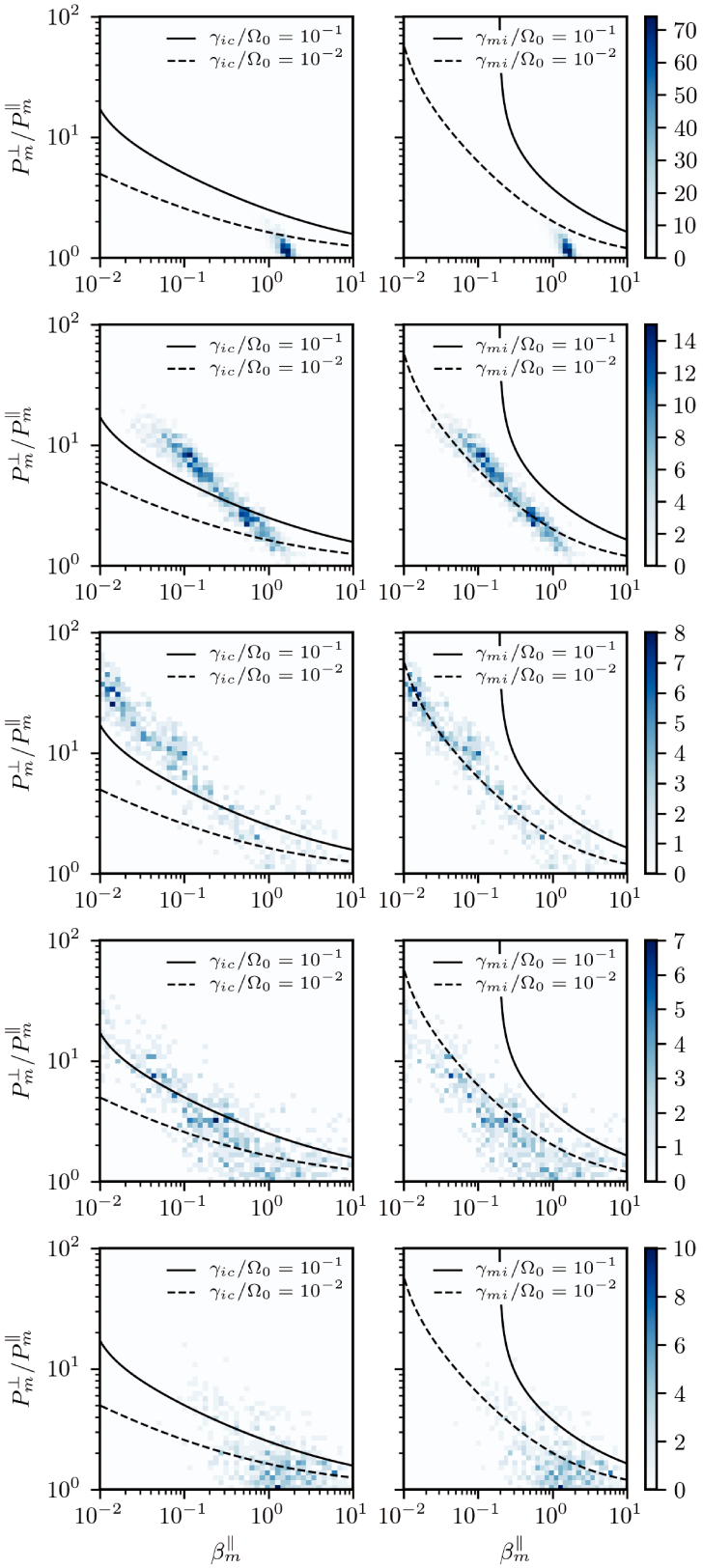

Figure 6.4: Distribution (cell count) of the pressure anisotropy $P_m^\perp/P_m^\parallel$ as a function of $\beta_m^\parallel = 2\mu_0 P_m^\parallel/B^2$, obtained in a 1D simulations without collisions at different times. From top to bottom: $t = 15, 25, 35, 45, 55\ \Omega_0^{-1}$. Note the different color scales. The solid and dashed black lines indicate the threshold for the ion-cyclotron γ_{ci} (left panels) and mirror γ_{mi} (right panels) modes obtained from linear kinetic theory assuming a homogeneous plasma with bi-Maxwellian populations (Hellinger et al. [2006]).

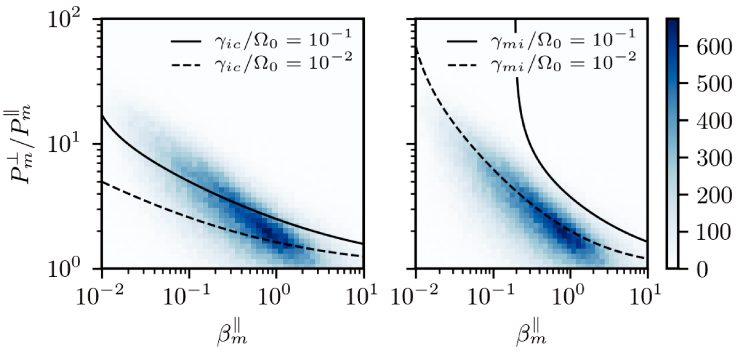

Figure 6.5: Same as Fig. 6.4 in a 2D collisionless simulation, during the exponential phase of growth. The larger cell count due to the higher dimensionality (2×10^5 cells) yield better statistics than in 1D simulations (10^3 cells).

rate $\gamma \sim 10^{-1}\ \Omega_0$. The combination of the parallel cooling down, and of the magnetic field amplification driven by the non-resonant instability, tends to reduce the parallel plasma beta $\beta_m^\parallel = P_m^\parallel/W_B$ and to slow the growth of the mirror mode. This allows large anisotropies $P_m^\perp/P_m^\parallel > 10$ to develop. The ion-cyclotron instability, predicted to be dominant in the low $\beta_m^\parallel$ regime, does not constrain the anisotropy. This may be explained by the spatial inhomogeneity of the magnetic field amplification, in the present case due to the non-resonant mode, which impairs the growth of the ion-cyclotron mode (Southwood and Kivelson [1993]), as also observed in the solar wind (Hellinger et al. [2006]). The same results are obtained in 2D simulations, as shown in Fig. 6.5.

6.3.3 The effects of anisotropies on the non-resonant mode

In the Cartesian basis aligned with the simulation domain, the pressure anisotropies are described by the off-diagonal components of the pressure tensor. Because of the electromagnetic wave helical structure in space, one obtains gradients of the off-diagonal terms of the full pressure tensor along B_0 (refer to Fig. 2.1 for an illustration). These gradients affect the background plasma dynamic in the plane perpendicular to B_0, and must be taken into account in the momentum conservation equation (Eq. 2.25) via a pressure gradient force which was neglected in the linear analysis of the instability. The competition between the magnetic and the pressure gradient forces is presented in the left panel of Fig. 6.6 for 1D simulations during the end of the linear phase of growth (the right panels will be discussed in the following section). It is clear that the force driving the instability, $-\mathbf{j}_{cr} \times \mathbf{B}$, is opposed by the background protons pressure gradients $-\boldsymbol{\nabla} \cdot \mathbf{P}_m$. This leads to a less efficient acceleration of the background fluid, and consequently to smaller magnetic field fluctuations (Eq. 2.41). This behaviour is strongly non-linear: the instability generates important non-linear heating, which retro-acts on the growth rate and reduces it.

An interesting result is that the kinetic linear dispersion of the non-resonant mode (Winske and Leroy [1984], Amato and Blasi [2009]) already includes anisotropic heating effects, which can be quantitatively estimated from quasi-linear theory (Winske and Leroy [1984]). The kinetic theory nevertheless gives the same results (growth rate, wavenumber) as MHD calculations which do not include the pressure tensor (Bell [2004]). This can be

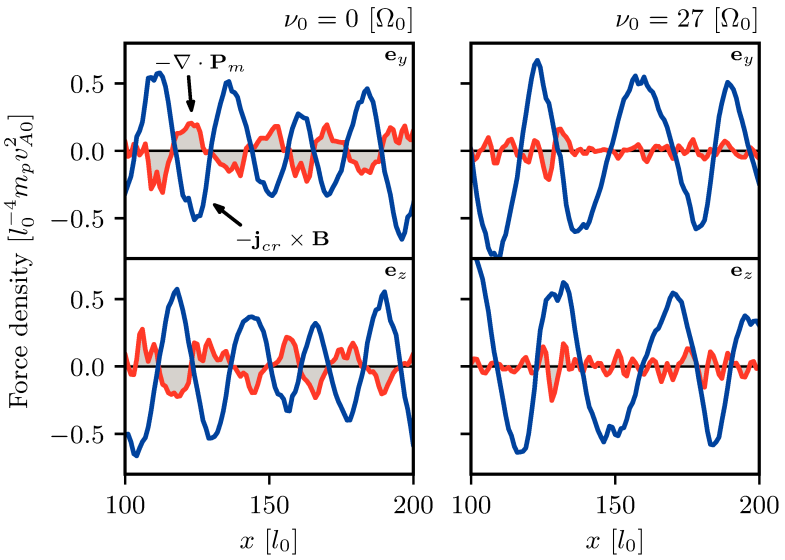

Figure 6.6: *Upper and lower left panels*: Cosmic rays induced magnetic force $-\mathbf{j}_{cr} \times \mathbf{B}$ (blue solid line) and main protons pressure gradients $-\boldsymbol{\nabla} \cdot \mathbf{P}_m$ (red solid line) components in the plane perpendicular to B_0 ($\mathbf{e}_y, \mathbf{e}_z$), as a function of space between $x = 100$ and $x = 200$ l_0. Data is taken during the exponential growth phase at $t = 30$ Ω_0^{-1} in a 1D collisionless simulation. *Upper and lower right panels*: with Coulomb collisions at a frequency $\nu_0 = 27$ Ω_0. The grey regions highlight the pressure gradients contribution, convoluted with a Gaussian to reduce fluctuations at the mesh size scale l_0 in the figure.

understood by examining the fluid momentum density conservation equation for a given population of the plasma:

$$\frac{\partial \mathbf{u}_\alpha}{\partial t} + (\mathbf{u}_\alpha \cdot \boldsymbol{\nabla})\mathbf{u}_\alpha + \frac{1}{\rho_\alpha}\boldsymbol{\nabla} \cdot \mathbf{P}_\alpha - \frac{q_\alpha}{m_\alpha}(\mathbf{E} + \mathbf{u}_\alpha \times \mathbf{B}) = \mathbf{0} \tag{6.11}$$

where $\mathbf{P}_\alpha = P_\alpha^{\parallel}\mathbf{bb} + P_\alpha^{\perp}(\mathbf{I} - \mathbf{bb}) + \boldsymbol{\Pi}_\alpha$ with $\mathbf{I}$ the identity matrix and $\mathbf{b} = \mathbf{B}/B$. In the CGL limit, the non-gyrotropic components $\boldsymbol{\Pi}_\alpha$ are assumed negligible (Hunana et al. [2019]). Ommiting the Lorentz force in order to focus on the effects of the pressure tensor and linearizing the momentum density conservation equation gives

$$\frac{\partial u_x}{\partial t} + \frac{1}{\rho_0}\partial_x p_\perp = 0 \tag{6.12}$$

$$\frac{\partial u_y}{\partial t} + \frac{1}{\rho_0}\partial_y p_\perp = 0 \tag{6.13}$$

$$\frac{\partial u_z}{\partial t} + \frac{1}{\rho_0}\partial_z p_\parallel = 0 \tag{6.14}$$

where ρ_0 is the unperturbed mass density. In the case of transverse fluctuations propagating along $\mathbf{e}_z$, one has $\partial_x = 0$ and $\partial_y = 0$. It appears immediately that the pressure anisotropy does not modify the plasma motion in the plane perpendicular to the propagation direction, and does not oppose the cosmic rays magnetic force $\mathbf{j}_{cr} \times \mathbf{B}$ which acts in this plane. As a result, the inclusion of the pressure tensor in the linearized equations does not modify the instability, as also noted in Bell [2004]. As such, the study of the partial stabilization of the

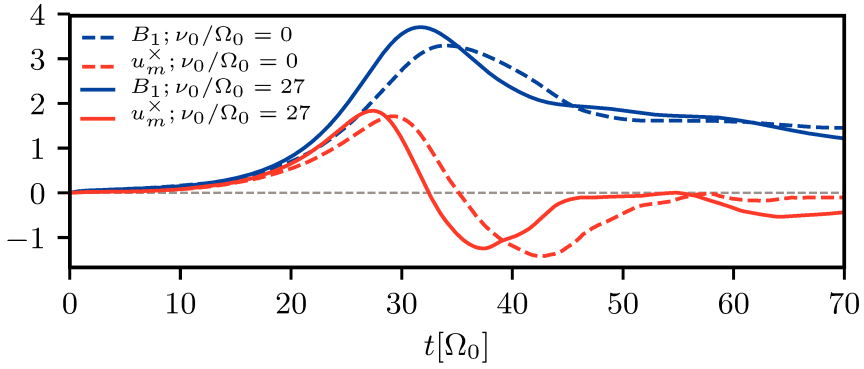

Figure 6.7: Perturbed magnetic field intensity $B_1 = ||\mathbf{B} - \mathbf{B}_0||$ (in units of B_0, blue lines) and normal main protons fluid velocity $u_m^\times$ (in units of v_{A0}, red lines) as a function of time, for the collisionless case (dashed line) and collisional case (solid line, $\nu_0 = 27\ \Omega_0$).

non-resonant mode driven by pressure anisotropies requires fully non-linear simulations, and can not be done with fluid simulations using an isotropic closure.

6.3.4 Destabilization by Coulomb collisions

Pressure anisotropies may be mitigated by introducing Coulomb collisions between protons. This is confirmed by simulations, which yield an important reduction of the anisotropies, as shown in the lower panel of Fig. 6.1. The pressure components are essentially equal during the whole instability growth, reducing the pressure gradients and ultimately promoting the growth of the non-resonant mode. In other words, the Coulomb collisions impair the self-stabilizing tendency of the non-resonant mode, further destabilizing the growing electromagnetic waves. This explains the increase in magnetic field growth rate and energy density at saturation with increasing Coulomb collision frequency. This is illustrated in the right panel of Fig. 6.6, where the pressure gradients no longer oppose the cosmic rays magnetic force, allowing a faster growth of the velocity perturbations. The time evolution of the magnetic field fluctuations is presented in Fig. 6.7 together with the background protons fluid velocity normal component $u_m^\times$ as a function of time, in the collisionless and collisional cases. Such a dual display emphasizes the close connection between the fluctuating magnetic field B_1 and fluid velocity u_1 raised in Eqs. 2.40 and 2.41. One obtains a larger acceleration of the background protons and consequently a larger magnetic field amplification in the collisional case, confirming the destabilizing effect of Coulomb collisions on the non-resonant mode. The magnetic field saturation occurs when the main protons normal fluid velocity becomes negative, resulting in the reversal of the induced second order parallel electric field $\mathbf{E}_\parallel = -\mathbf{u}_1 \times \mathbf{B}_1$ which prevents the cosmic rays from being further slowed down and to transfer their kinetic energy into magnetic energy. This saturation mechanism, presented in Sec. 5.3, is well recovered in both the collisionless and collisional cases.

For the set of initial parameters considered (see Table 4.2), the simulations yield $|\mathbf{j}_{cr} \times \mathbf{B}|/|\boldsymbol{\nabla} \cdot \mathbf{P}_m| \sim 3$ during the exponential phase of growth in the collisionless case. This leads to a reduction of $\sim 14\%$ of the maximum fluid velocity u reached at a given position by the background plasma before saturation. The resulting magnetic amplification

may be estimated via Ohm's law and Faraday's law (Eq. 2 of the manuscript) which gives:

$$B \sim \frac{kB_0 u}{\gamma} \tag{6.15}$$

with k the wavenumber and γ the growth rate. This yields a proportionality between the fluid and magnetic field perturbations, compatible with the simulation results, where $B/B_0 = 3.9$ in the collisional case and $B/B_0 = 3.3$ in the collisionless case corresponding to a 18% increase. A larger enhancement ($> 100\%$) is not expected to be reachable, since it would require that the pressure gradients overcome the cosmic rays magnetic force, and thus preventing the growth of the instability entirely.

These results indicate that despite its non-resonant character, kinetic effects induced in the background plasma play an important role in the growth of the instability. The isotropic pressure closures often used in fluid models cannot capture the microphysics of the background heating and the self-stabilizing effect of the resulting spatial gradients of the non-diagonal terms of the pressure tensor. This may lead to an overestimate of the magnetic field amplification when applied to collisionless or poorly collisional plasmas where the instability growth time is smaller than the collision time. On the contrary, in collisional environments such as in laboratory plasmas and in H II regions for astrophysical plasmas, the mitigation of the pressure anisotropies by Coulomb collisions may enhance the accuracy of a fluid description, and favor the growth of the non-resonant mode.

In the case of a weaker cosmic rays flux, the reduction of the growth rate γ will in turn reduce the instability driven anisotropic heating rate. Consequently, one may expect that the anisotropic heating will be overcome by the isotropization mediated by ion-ion Coulomb collisions for a smaller collision frequency ν_0. An order of magnitude estimate of the collision frequency necessary to mitigate the self-generated anisotropies can be found by comparing the anisotropic heating rate, obtained from quasi-linear theory (Winske and Leroy [1984]):

$$\left(\frac{\partial T_\perp}{\partial t}\right)_{NR} = 4\gamma_{\rm cold}\frac{W_B}{n_m} \tag{6.16}$$

to the isotropization of temperatures by Coulomb collisions:

$$\left(\frac{\partial T_\perp}{\partial t}\right)_{c} = -\nu_0 T_0 \kappa \tag{6.17}$$

where $T_\perp$ is the temperature perpendicular to the *total* magnetic field in units of energy and:

$$\kappa = \frac{1}{2\pi^{1/2}A}\left(-3 + (A+3)\left[\frac{\tan^{-1}(A^{1/2})}{A^{1/2}}\right]\right) \tag{6.18}$$

is a decreasing function of $A = T_\perp/T_\parallel - 1 \sim T_\perp/T_0 - 1$. Because heating is dominant in the perpendicular direction one may approximate $T_\parallel \sim T_0$ with T_0 the initial isotropic ion temperature. Using the prediction from quasi-linear theory for the saturated magnetic field $W_B \sim W_{cr}/2$, the condition for collisions to become effective in suppressing the pressure anisotropies can then be written as:

$$\frac{\nu_0}{\gamma_{\rm max}} \gtrsim 2\frac{W_{cr}}{n_m T_0 \kappa} \tag{6.19}$$

In addition, whether these pressure anisotropies affect the instability can be estimated by a scaling between the pressure gradients and the magnetic force driving the instability as:

$$k_{\rm fast} n_m A T_0 \gtrsim j_{cr} B \tag{6.20}$$

with $k_{\rm fast} = k_{\rm max}/2$ the fastest growing wavenumber (Eq. 2.36). This yields the condition that the anisotropy parameter A should be $\gtrsim 2v_{A0}^2/v_{T0}^2$ with $v_{T0}^2 = k_B T_0/m_p$, for pressure gradients to influence the instability. For the parameters considered $W_{cr}/n_m T_0 = 12.5$ and $v_{A0}/v_{T0} = 1$. For the collisionless simulations $A \sim 4$ (see Fig. 6.3), and pressure gradients are expected to modify the growth of the instability, which is indeed what is observed in the simulations. In addition, the collision frequency required for anisotropies to be suppressed by Coulomb collisions gives $2W_{cr}/n_m T_0 \kappa \sim 400$, in good agreement with the values obtained from the simulations, $\nu_0/\gamma_0 \sim 300$.

In general, the level of pressure anisotropy produced by the non-resonant streaming instability may be estimated from quasi-linear theory using the scaling $T_\perp \sim 2W_B/n_m + T_0$, such that $A \sim W_{cr}/n_m T_0$. Using this estimate, the criterion for pressure gradients to impact the growth of the instability becomes:

$$\frac{1}{4}\frac{n_{cr} u_{cr}^2}{n_m v_{A0}^2} \gtrsim 1 \tag{6.21}$$

which is the ratio of the cosmic rays to the *initial* magnetic field energy densities, and it is independent of the background plasma density. Considering a supernova shock which propagates at a velocity $u_{cr} = 10^3$ km.s^{-1} in a cold interstellar medium with $n_m = 1$ cm^{-3}, $B = 5$ μG, $T_0 = 10^4$ K and with a cosmic rays flux $n_{cr} u_{cr} = 10^4$ cm$^{-2} s^{-1}$ (Zweibel and Everett [2010]), one obtains $n_{cr} u_{cr}^2/4 n_m v_{A0}^2 = 0.2$ and a protons Coulomb collision frequency of $\nu_0/\gamma_{max} = 3 \times 10^{-2}$ (Trubnikov [1965]), much smaller than the criterion $2W_{cr}/n_m T_0 \kappa = 41$. Under such collisionless conditions, one may expect pressure anisotropies to develop and reduce the growth rate and saturated magnetic field with respect to the theoretical predictions. Increasing the main protons density to $n_m = 90$ cm^{-3}, as encountered in H II regions (Galarza et al. [1999], Orlando, S. et al. [2019]), while keeping the other parameters the same one obtains a collision frequency $\nu_0/\gamma_{max} = 24$. This is of the same order as the criterion $2W_{cr}/n_m T_0 \kappa = 27$, indicating that Coulomb collisions should reduce the anisotropies spontaneously generated by the instability and enhance its growth.

6.4 References

Amato, E. and Blasi, P. (2009). A kinetic approach to cosmic-ray-induced streaming instability at supernova shocks. *Mon Not R Astron Soc*, 392(4):1591–1600.

Bell, A. R. (2004). Turbulent amplification of magnetic field and diffusive shock acceleration of cosmic rays. *Mon Not R Astron Soc*, 353(2):550–558.

Chevalier, R. A. (1999). Supernova remnants in molecular clouds. *The Astrophysical Journal*, 511(2):798–811.

Chew, G. F., Goldberger, M. L., Low, F. E., and Chandrasekhar, S. (1956). The Boltzmann equation an d the one-fluid hydromagnetic equations in the absence of particle collisions. *Proceedings of the Royal Society of London. Series A. Mathematical and Physical Sciences*, 236(1204):112–118.

Feinstein, F., Fiasson, A., Gallant, Y., Chaves, R. C. G., Marandon, V., de Naurois, M., Kosack, K., Rowell, G., and Collaboration, H. E. S. S. (2009). What do supernova remnants interacting with molecular clouds reveal? *AIP Conference Proceedings*, 1112(1):54.

Forteza, P., Oliver, R., Ballester, J. L., and Khodachenko, M. L. (2007). Damping of oscillations by ion-neutral collisions in a prominence plasma. *Astronomy & Astrophysics*, 461(2):731–739.

Galarza, V. C., Walterbos, R. A. M., and Braun, R. (1999). Spectrophotometry of H II Regions, Diffuse Ionized Gas, and Supernova Remnants in M31: The Transition from Photoionization to Shock Ionization. *The Astronomical Journal*, 118:2775–2796.

Gary, S. P., Montgomery, M. D., Feldman, W. C., and Forslund, D. W. (1976). Proton temperature anisotropy instabilities in the solar wind. *Journal of Geophysical Research*, 81:1241–1246.

Hellinger, P., Trávníček, P., Kasper, J. C., and Lazarus, A. J. (2006). Solar wind proton temperature anisotropy: Linear theory and WIND/SWE observations. *Geophysical Research Letters*, 33(9).

Hunana, P., Tenerani, A., Zank, G. P., Khomenko, E., Goldstein, M. L., Webb, G. M., Cally, P. S., Collados, M., Velli, M., and Adhikari, L. (2019). An introductory guide to fluid models with anisotropic temperatures. Part 1. CGL description and collisionless fluid hierarchy. *J. Plasma Phys.*, 85(6):205850602.

Khodachenko, M. L., Arber, T. D., Rucker, H. O., and Hanslmeier, A. (2004). Collisional and viscous damping of MHD waves in partially ionized plasmas of the solar atmosphere. *Antike und Abendland: Beiträge zum Verständnis der Griechen und Römer und ihre Nachlebens*, 422(3):1073–1084.

Kulsrud, R. and Pearce, W. P. (1969). The Effect of Wave-Particle Interactions on the Propagation of Cosmic Rays. *ApJ*, 156:445.

Kulsrud, R. M. (1983). MHD description of plasma. In *Basic Plasma Physics: Selected Chapters, Handbook of Plasma Physics, Volume 1*, page 1.

Malkov, M. A., Diamond, P. H., and Sagdeev, R. Z. (2005). On the gamma-ray spectra radiated by protons accelerated in supernova remnant shocks near molecular clouds: The case of supernova remnant RX J1713.7-3946. *The Astrophysical Journal*, 624(1):L37–L40.

Marret, A., Ciardi, A., Smets, R., and Fuchs, J. (2021). On the growth of the thermally modified non-resonant streaming instability. *Monthly Notices of the Royal Astronomical Society*, 500(2):2302–2315.

Orlando, S., Miceli, M., Petruk, O., Ono, M., Nagataki, S., Aloy, M. A., Mimica, P., Lee, S.-H., Bocchino, F., Peres, G., and Guarrasi, M. (2019). 3D MHD modeling of the expanding remnant of SN 1987A - Role of magnetic field and non-thermal radio emission. *Antike und Abendland: Beiträge zum Verständnis der Griechen und Römer und ihre Nachlebens*, 622:A73.

Reville, B., Kirk, J. G., Duffy, P., and O'Sullivan, S. (2007). A cosmic ray current-driven instability in partially ionised media. *Astronomy & Astrophysics*, 475(2):435–439.

Southwood, D. J. and Kivelson, M. G. (1993). Mirror instability: 1. Physical mechanism of linear instability. *Journal of Geophysical Research*, 98(A6):9181.

Tagger, M., Falgarone, E., and Shukurov, A. (1995). Ambipolar filamentation of turbulent magnetic fields. 299:940.

Trubnikov, B. A. (1965). Particle interactions in a fully ionized plasma. *Reviews of Plasma Physics*, 1:105.

Winske, D. and Leroy, M. M. (1984). Diffuse ions produced by electromagnetic ion beam instabilities. *Journal of Geophysical Research: Space Physics*, 89(A5):2673–2688.

Zweibel, E. G. and Everett, J. E. (2010). Environments for Magnetic Field Amplification by Cosmic Rays. *The Astrophysical Journal*, 709(2):1412–1419.

Chapter 7

Toward laboratory experiments

Contents

7.1 Introduction

The theory and numerical simulations of plasmas constitute two invaluable tools in understanding the physics of the non-resonant streaming instability, as well as its role in the amplification of the magnetic field and in the acceleration of cosmic rays in astrophysical shocks. However, theoretical investigations such as the one presented in this thesis are restricted to the linear phase of the instability, and give few information on the late evolution of the plasma. Numerical simulations allow us to overcome this limitation, but are by nature limited to the system of equation which is numerically solved. In addition, the computational cost becomes prohibitive for "realistic" plasma parameters observed in astrophysical systems, and restricts most numerical investigations to idealized situations.

The third way to approach the problem is by studying actual astrophysical plasmas, which can be observed from the Earth via the radiations they emit. As presented in Sec.

2.1, the acceleration of cosmic rays at shocks can be studied by analysing the gamma rays emitted by the energetic particles. Their interaction with the Earth's atmosphere initiates a cascade of interactions, leading to the formation of a shower of secondary charged particles. Those with velocities faster than the local speed of light in the atmosphere can resonate with the electromagnetic radiations and produce flashes of Cerenkov emission, which gives information on the primary gamma rays. This approach was applied to SNR RX J1713.7−3946 and Cassiopeia A (Aharonian et al. [2001, 2004]), highlighting the possible role of supernova remnants as efficient cosmic rays accelerators. However this observational approach is also limited by the spatial resolution of the telescopes, which need to be compared with the spatial scales involved in the microphysics of the non-resonant instability. In the case of the HESS system of telescopes (Hinton [2004]), the angular resolution is of a few arc minutes. For Cassiopeia A, which is located at 3.4 kiloparsecs from the Earth, this corresponds to a spatial resolution of the images of the order of the parsec. Considering the plasma parameters of the supernova remnants propagating at a velocity $u_{cr} = 10^3$ km.s^{-1} in an interstellar medium with density $n_m = 1$ cm^{-3}, and with an ambient magnetic field $B = 5$ μG, one finds the maximum non-resonant mode wavelength as $\lambda_{\max} = 2\pi k_{\min}^{-1} = 1.3 \times 10^5$ km, much shorter than the telescope spatial resolution and out of reach for direct *in situ* observations.

One may circumvent this difficulty by bringing the plasmas closer to us. Experimental investigations of plasmas under extreme conditions have drawn increasing attention in the astrophysics community. Plasma phenomenon such as the streaming instabilities may be observed in experiments which can fit in a laboratory, using a combination of state of the art lasers together with sources of large intensity magnetic field. The right-hand resonant streaming instability has been investigated using the Large Plasma Device at the University of California where plasmas up to 18 meters long with a 300 G axial magnetic field can be obtained (Leneman et al. [2006]). The streaming population was created by irradiating a solid target made of high density polyethylene C_2H_4 and graphite with a high intensity laser, generating an expanding plasma with velocities up to hundreds of kilometers per second. Such combination of large scale ambient plasma, ambient magnetic field and relatively large streaming velocities allowed to observe the right-hand resonant mode in a recent experimental campaign (Heuer et al. [2018]). Electromagnetic field fluctuations were observed with a polarization and a frequency compatible with the theoretical expectations, constituting the first experimental demonstration of the right-hand resonant streaming instability. The non-resonant streaming instability has however not yet been observed in the laboratory. This chapter is devoted to possible designs of future experimental investigations on the non-resonant streaming instability. It describes the conditions which must be satisfied to observe the non-resonant mode in the laboratory, as well as theoretical predictions on the expected time and spatial scales involved. Several considerations which need to be taken into account when attempting to observe the instability in laboratory conditions are presented, from the effects of temperature and collisionality to the modification of the non-resonant mode behaviour for ion species with various mass and charge. Two possible setups are proposed, together with the relevant diagnostics which may allow us to analyse and understand the results.

7.2 Experimental constraints

Three fundamental elements must gathered to recreate the non-resonant mode in the laboratory: a background plasma, a super-Alfvénic streaming population and an ambient magnetic field aligned with the stream velocity. Although the parameters required are potentially within the reach of high intensity laser experiments with tens of Tesla externally applied magnetic fields (Albertazzi et al. [2013], Ivanov et al. [2021]), the large streaming population densities, drift velocities and ambient magnetic field required, together with the lack of theoretical knowledge on the effects of particle collisions and of ion charge and mass on the development of the instability, have made its experimental investigations elusive. The main constraints on the experiments can be summarized as follows:

- The instability must grow on time scales compatible with the plasma lifespan, and on spatial scales compatible with the size of the plasma and of the magnetized regions.
- The density ratio between the streaming population and the background plasma must be less than unity, whereas the relative velocity normalized to the Alfvén velocity must be larger than unity.
- The particle flux must not be too large to avoid the demagnetization of the background plasma, nor too small to avoid damping by ion finite Larmor radius effects, as well as the growth of the resonant modes.
- The e-folding reached at the end of the experiment, that is the integrated growth rate over the experiment duration, must be larger than unity in order to observe a substantial growth of the perturbations.

During the growth of the instability, the streaming population drift kinetic energy is converted in large amplitude magnetic field perturbations. This leads to a reduction of the streaming velocity and to a scattering of the particles in the plane perpendicular to the ambient magnetic field. The resulting changes in the streaming population energy spectrum could be measured using a Thomson parabola, together with the magnetic field amplification (obtainable by Faraday rotation). This would allow the verification of the theoretical prediction on the saturated magnetic field intensity, which is a central parameter of the non-resonant instability in the context of acceleration of particles at supernova shocks. In addition to magnetic field perturbations, the instability is characterized by large density fluctuations of the order of the initial background plasma density, produced by the increasing magnetic pressure on the same spatial scales as the electromagnetic waves, and which may be observed in laboratory experiments by laser interferometry.

7.2.1 Ambient magnetic field and instability regimes

Intense magnetic fields may be obtained in the laboratory using Helmholtz coils to generate uniform magnetic fields for a duration of a few μs, with intensities up to tens of Teslas on scales of the order of the centimeter (Albertazzi et al. [2013]). The instability is modified by finite Larmor radius effects, hence requiring strong magnetic fields to keep the Larmor radius smaller than the unstable wavelengths in order to prevent unwanted

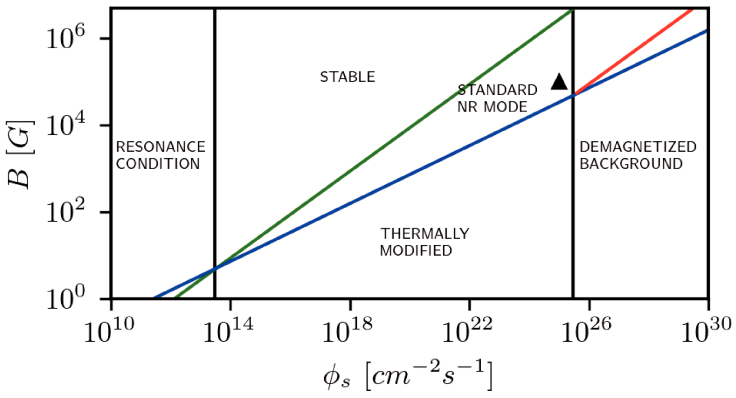

Figure 7.1: Parameter space reproduced as from Zweibel and Everett [2010] and considering $n_m = 10^{19}$ cm^{-3} and $T_m = 10^5$ K. The black triangle corresponds to the parameters $\phi_s = 10^{25}$ cm^{-2}s^{-1} and $B = 10$ T $(0.1MG)$, which may be obtained in current experimental facilities, and lies in the "standard", cold non-resonant mode unstable region. The green line corresponds to the streaming population non-resonant condition, the blue line to the transition to the thermally modified regime, the two vertical black lines to the resonance condition on the streaming population (left) and demagnetization of the background ions in the thermally modified regime (right), and the red line to the background ions demagnetization in the standard regime.

wave damping in the experiments. The magnetic field intensity cannot be arbitrarily large however, in order to be compatible with current technical limits, and to accommodate for unwanted physical effects. First, to avoid important magnetic tension effects which have been shown to halt the instability growth at sufficiently small scales. Second, to prevent the magnetization of the streaming population at large scales, and third, to satisfy the ion streaming instabilities requirement of super-Alfvénic flows $u_s > v_A$. These constraints can be visualized in Fig. 7.1, which presents the instability regimes as a function of the ambient magnetic field intensity and of the streaming population flux, while considering the background plasma parameters $n_m = 10^{19}$ cm^{-3} and $T_m = 10^5$ K typical of laser produced plasmas. The non-resonant mode may be observed for a wide range of parameters, but only a restricted regions in parameter space is unmodified by the background ions temperature. The constraints on the background ions magnetization, on the magnetic tension, as well as the Larmor radius constraint, may be summarized by conditions on the streaming population flux $\phi_s(\mathbf{r}, t) = n_s(\mathbf{r}, t)u_s(\mathbf{r}, t)$ and ambient magnetic field strength B (Zweibel and Everett [2010]), for a fixed background plasma density n_m and temperature T_m. The instability regimes are obtained with the expressions given in the following Eqs. 7.1 to 7.4, expressed in CGS units, which are valid for protons and electrons plasmas. These may be modified by a factor of the order unity when considering heavier elements. Such corrections will be neglected for determining order of magnitudes estimates on the instability regimes. First, the condition that the instability is non-resonant, obtained by considering $kr_{Ls} > 1$, where $r_{Ls} = u_s/\Omega_0$ is the streaming population Larmor radius, can be expressed as:

$$B < 8.7 \times 10^{-7} \phi_s^{1/2} \tag{7.1}$$

For larger magnetic field, the streaming ions are significantly affected by the ambient magnetic field and their velocity perturbations cannot be neglected. In such a case the resonant streaming instabilities (right-hand and left-hand) become dominant over the

non-resonant mode. The condition that the background ions are magnetized, $kr_{Lm} < 1$, where $r_{Lm} = v_{Tm}/\Omega_0$ is the main ions Larmor radius, yields:

$$B > 5 \times 10^{-10} T^{1/4} \phi_s^{1/2} \tag{7.2}$$

Below this limit the thermal ions Larmor radius becomes larger than the unstable wavelength, and the instability growth rate and saturation are strongly reduced. The condition that the instability is not modified by thermal effects, corresponding to the warm regime of the instability, is given by:

$$B > 2.3 \times 10^{-9} T^{1/3} n_m^{1/6} \phi_s^{1/3} \tag{7.3}$$

If this condition is violated the unstable wavelengths are modified, and consequently the requirements on the streaming population demagnetization, and magnetization of the background ions, are also modified. This imposes constraints on the streaming particle flux in the thermally modified regime:

$$3 \times 10^{-16} n_m T_m^2 < \phi_s < 10^4 n_m T_m^{1/2} \tag{7.4}$$

In addition to the constraints on temperature, particle flux and ambient magnetic field, the unstable wavelengths must also be taken into account, namely the condition:

$$\frac{k_{\min} L}{2\pi} > 1 \tag{7.5}$$

imposing that the largest unstable wavelength should be smaller than the size of the experiments, which is itself constrained by the size of the background plasma and by the size of the region where the Helmholtz coils can maintain a strong and uniform magnetic field.

7.2.2 Stream-background Coulomb collisions

The density and mass of the background plasma are critical parameters of the experiments as they modify the growth rate of the instability, as well as the collisionality with the streaming particles via Coulomb collisions. The background plasma may be obtained by ionizing a preexisting gas jet, typically made of hydrogen or argon, with a nanosecond laser. Such jets are generated by ejecting low density ($\sim 10^{18}$ cm^{-3}), high pressure (~ 10 bar) neutral gas from a gas nozzle, generating axisymmetric density profiles around the direction of propagation. The radial density profile of such gas jet follows a Gaussian, exponentially decreasing law with the distance to the axis, and is known experimentally (Malka et al. [2000]). The high velocities acquired by the plasma from the laser pulse should not be lost to collisions with the background (Thaury et al. [2009]), which imposes conditions on the relative velocity, mass and charge of the background and streaming ions. As presented in Sec. 4.4.2, the characteristic time scale $(\nu_S^{\alpha/\beta})^{-1}$ associated to the slowing down of test particles α by a population of field particles β may be calculated as (Trubnikov [1965], Callen [2006]):

$$\nu_S^{\alpha/\beta} = -\nu_0^{\alpha/\beta} \left(1 + \frac{m_\alpha}{m_\beta}\right) \psi(x) \tag{7.6}$$

where

$$\nu_0^{\alpha/\beta} = \frac{1}{4\pi\epsilon_0^2}\frac{q_\alpha^2 q_\beta^2}{m_\alpha^2}\frac{n_\beta}{u_\alpha^3}\ln\Lambda_{\alpha\beta} \tag{7.7}$$

is the fundamental Coulomb collision frequency and $\psi(x)$ is the Maxwell integral, with $x = u_\alpha/v_{T\beta}$ the relative speed parameters and u_α the velocity of the test particle in the reference frame of the population β. In the case of a particle of population α propagating in a background plasma made of electrons and a single species of ions, the slowing down time scale is calculated as:

$$\nu_S^{\alpha/i,e} = \nu_S^{\alpha/i} + \nu_S^{\alpha/e} \tag{7.8}$$

One may deduce the associated collision mean free path $\lambda_S = u_\alpha/\nu_S^{\alpha/i,e}$, which corresponds to the average distance traveled by a particle with velocity u_α before suffering a significant reduction of its drift velocity by Coulomb collisions. One may define a collisionality parameter as λ_S/L where L is the characteristic size of the experiment, which should be larger than unity in order to avoid any substantial loss of momentum before the instability may develop in the experiments:

$$\frac{\lambda_S}{L} > 1 \tag{7.9}$$

This parameter can be maximized by considering large relative velocities, together with small stream and background populations charge.

7.2.3 Background ion-neutral collisions

In addition to the ionization degree, the ionization fraction of the background plasma, i.e. the fraction of ionized particles, also plays an important role in the non-resonant mode growth. Ion-neutral collisions differ significantly from the Coulomb collisions as both the momentum and the energy of the background ion population are not conserved, leading to an important damping of the instability as seen in Sec 6.2.1. Similarly to temperature effects, the damping by neutral collisions should be avoided in experimental investigations, hence requiring the background plasma to be fully ionized to minimize the ion-neutral collision frequency. The ionization state of a gas in local thermodynamic equilibrium may be calculated using Saha's law as a function of the gas temperature:

$$\frac{N_{j+1}}{N_j} = 2\frac{Z_{j+1}}{n_e Z_j}\left(\frac{2\pi m_e k_B T}{h^2}\right)^{3/2} e^{-\Delta\epsilon_j/k_B T} \tag{7.10}$$

where N_j is the number of particles in the state of ionization j, Z_j is the degeneracy of states for the ions i, h is the Planck constant and $\Delta\epsilon_j = \epsilon_{j+1} - \epsilon_j$ is the energy required to remove the $i+1$ electron. In the case of a pure hydrogen gas this system of equation can be solved analytically. Assuming that most of the neutral hydrogen are in the ground state, then $g_1 = 2$, and $g_2 = 1$ since the ionized state is a proton. One can rewrite Saha's equation as:

$$\frac{N_2}{N_1} = \frac{1}{2}\left(\frac{2\pi m_e k_B T}{h^2}\right)^{3/2} e^{-\Delta\epsilon_1/k_B T} \tag{7.11}$$

By conservation of the charge, on may define $x = n_e/n = N_1/(N_1 + N_2)$ where x is the ionization fraction with n the total density of hydrogen and protons. Inserting in Eq. 7.11

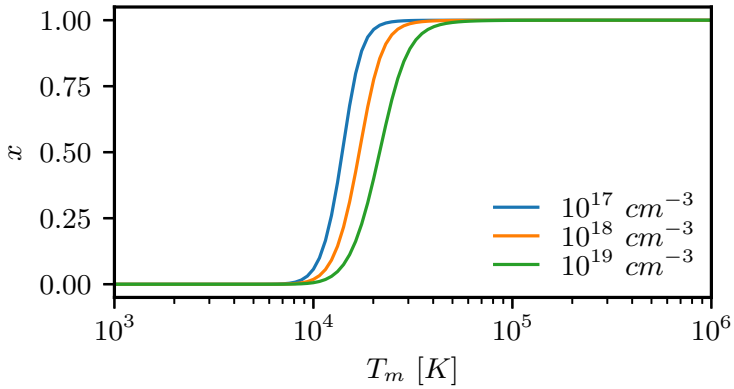

Figure 7.2: Ionization fraction x calculated with Eqs. 7.12 and 7.13 as a function of the hydrogen gas temperature T_m for various gaz densities n.

and solving the resulting second order equation in x, one obtains:

$$x = \frac{-K + \sqrt{K^2 + 4K}}{2} \tag{7.12}$$

where

$$K = \frac{e^{-13.6eV/k_BT}}{n} \left(\frac{2\pi m_e k_B T}{h^2} \right)^{3/2} \tag{7.13}$$

The ionization fraction x is showed in Fig. 7.2 as a function of the hydrogen gas temperature T for various densities n. Considering typical parameters encountered in laser-plasma laboratory experiments, $n_m = 10^{19}$ cm^{-3} and $T = 10^5$ K, one obtains a fully ionized hydrogen gas such that the damping effect of ion-neutral collision may be neglected. Experiments with lower background ions temperature can also be conducted, and in this case the ion-neutral damping effect should be taken into account.

7.3 Target Normal Sheath Acceleration setup

7.3.1 Acceleration mechanism and energy spectrum

Plasmas with large drift velocities can be obtained in the laboratory by the use of short pulse lasers. The Target Normal Sheet Acceleration (TNSA) method consists in irradiating a solid target, ionizing the atoms of the front side and accelerating electrons inside the target, which propagate in the solid and escape by the rear side. The large charge separation created generates a strong electric field parallel to the surface normal, accelerating the ions to high energies, up to tens of MeV, with a low angle of dispersion. The ions then propagate following a ballistic trajectory if no external force is applied. A schematic of the TNSA acceleration process is shown in Fig. 7.3. The protons are the most efficiently accelerated particles, because of their higher charge to mass ratio. This acceleration mechanism generates highly energetic protons beams for a duration ranging from the picosecond to hundreds of picoseconds, depending on the laser pulse duration. The energy spectrum of the accelerated ions can be calculated using a two-fluid model for the electrons

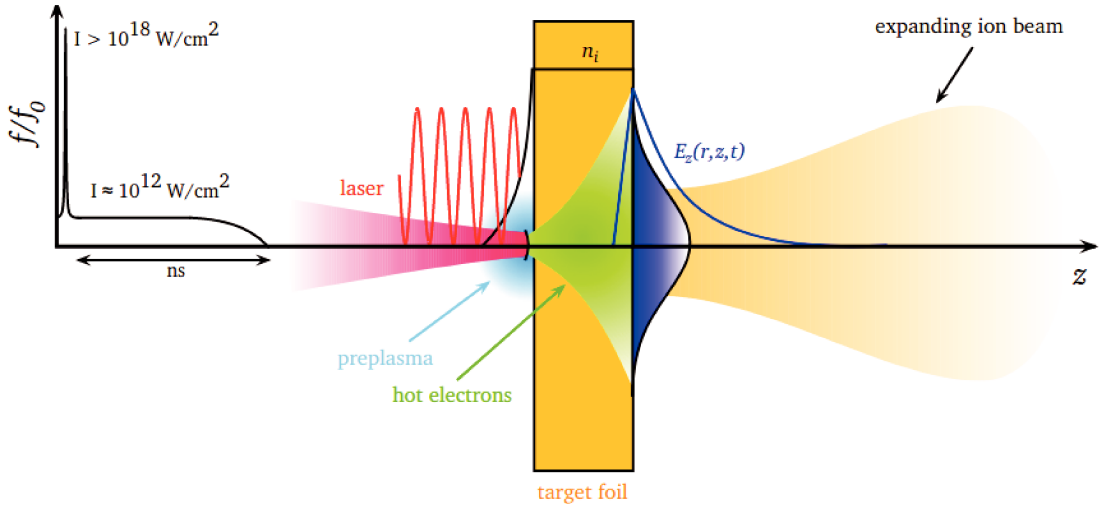

Figure 7.3: Schematic view of the TNSA acceleration mechanism, as from Roth and Schollmeier [2016]. The laser pulse irradiates the target on the front side (left), which accelerates electrons along the z direction and creates a charge space on the rear side (right). This produces a strong electric field leading to the acceleration of the ions from the solid target.

and ions, while supposing an isothermal expansion with no particles collisions and purely electrostatic acceleration. The predicted energy spectrum of the accelerated particles then follows an exponentially decreasing law with kinetic energy $E_{kin} = m_i v^2/2$ given by Mora [2003]:

$$\frac{\mathrm{d}N}{\mathrm{d}E_{\mathrm{kin}}} = \frac{n_e c_s t}{\sqrt{2Zk_B T_{\mathrm{hot}} E_{\mathrm{kin}}}} \exp\left(-\sqrt{\frac{2E_{\mathrm{kin}}}{Zk_B T_{\mathrm{hot}}}}\right) \tag{7.14}$$

where N is the ion number, $c_s = \sqrt{Zk_B T_e/m_i}$ is the sound speed, Z the ion charge and t is the expansion time. This can be rewritten in terms of velocity as:

$$\frac{\mathrm{d}N}{\mathrm{d}v} = \frac{n_e c_s t}{v_{T,\mathrm{hot}}} \sqrt{\frac{m_i}{Zm_e}} \exp\left(-\frac{v}{v_{T,\mathrm{hot}}} \sqrt{\frac{m_i}{Zm_e}}\right) \tag{7.15}$$

with $v_{T,\mathrm{hot}} = \sqrt{k_B T_{\mathrm{hot}}/m_e}$ the thermal velocity of the hot electrons population heated by the laser pulse. The final distribution function of the accelerated protons, integrated over the acceleration time can be expressed as:

$$f(v) = n_0 \frac{\alpha \mathrm{e}^{\alpha v}}{e^{\alpha v_{\mathrm{max}}} - e^{\alpha v_{\mathrm{min}}}} \tag{7.16}$$

where v_{max} and v_{min} are the minimum and maximum velocity of the accelerated protons, n_0 the proton density at the source, and α is a function of the hot electrons temperature at the target surface, which can be inferred from experimental measurements of the protons energy spectrum.

7.3.2 Beam divergence, density and flux

An example of experimental TNSA protons spectrum is given in Fig. 7.4. The data was obtained on the LULI/ELFIE installation (Zou et al. [2008]) by the experimental team

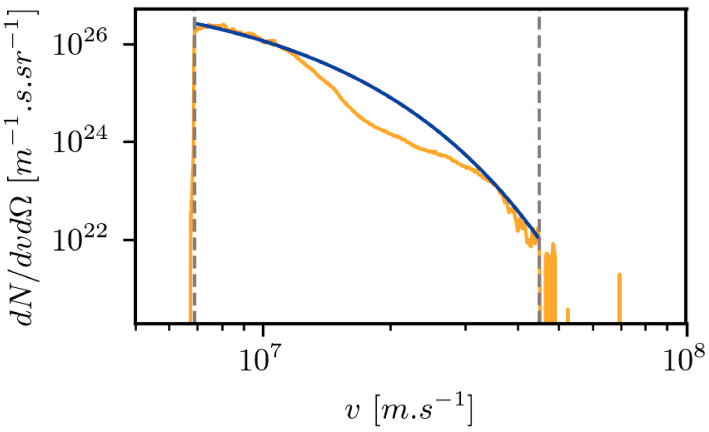

Figure 7.4: Number of protons per units of velocity and solid angle. Orange line: experimental data. Blue line: numerical fit following an exponential law as Eq. 7.16. The dashed grey vertical lines correspond to the minimum and maximum velocities considered in the calculations to normalize the distribution function.

directed by Julien Fuchs, using a laser pulse with a duration of 300 fs, a focal spot of 10 μm and an intensity $I = 1 \times 10^{19}$ W.cm^{-2}. The deviation from the exponential dependency at $v \sim 2 \times 10^7$ m.s^{-1} may be caused by the divergence of the proton beam, as the measured spectrum was obtained by observing particles propagating parallel to the target surface normal. Consequently, because of their velocity perpendicular to the bulk drift velocity, a small fraction of the accelerated particles do not reach the detector. The TNSA accelerated protons maximum angle of divergence at a given velocity is well constrained experimentally (Mancic et al. [2010]), and follows a universal law when scaled to the maximum energy reached by the accelerated protons (Bolton et al. [2014]). The angle $\theta(v)$ can be obtained empirically by a polynomial fit of several experimental observations as a function of the kinetic energy E_{kin} and maximum kinetic energy $E_{\max}$ as:

$$\theta(v) = M_0 + M_1 \left(\frac{E_{kin}}{E_{\max}}\right) + M_2 \left(\frac{E_{kin}}{E_{\max}}\right)^2 + M_3 \left(\frac{E_{kin}}{E_{\max}}\right)^3 + M_4 \left(\frac{E_{kin}}{E_{\max}}\right)^4 \tag{7.17}$$

where $(M_0; M_1; M_2; M_3; M_4) = (6.9675; 114.61; -324; 370.61; -166.56)$, and is shown in Fig. 7.5 for a maximum energy $E_{\max} = 11$ MeV. The maximum divergence is found for velocities $v = 2.5 \times 10^7$ m.s^{-1}, with an angle $\theta_{\max} = 20°$. The divergence will be neglected in the following calculations of the accelerated protons density and flux, as the bulk of the protons spectrum is characterized by a low divergence ($\theta \sim 10°$) which does not modify significantly the results. In this section, the streaming population will be noted with the subscript "s". The density of particles $n_s(v)$ with a velocity between v_i and v_{i+1} may be calculated analytically by integrating Eq. 7.16 over velocity, which directly gives:

$$n_s(v) = \int_{v_i}^{v_{i+1}} f(v')\mathrm{d}v' \tag{7.18}$$

$$= \frac{n_0}{e^{\alpha v_{\max}} - e^{\alpha v_{\min}}}(e^{\alpha v_{i+1}} - e^{\alpha v_i}) \tag{7.19}$$

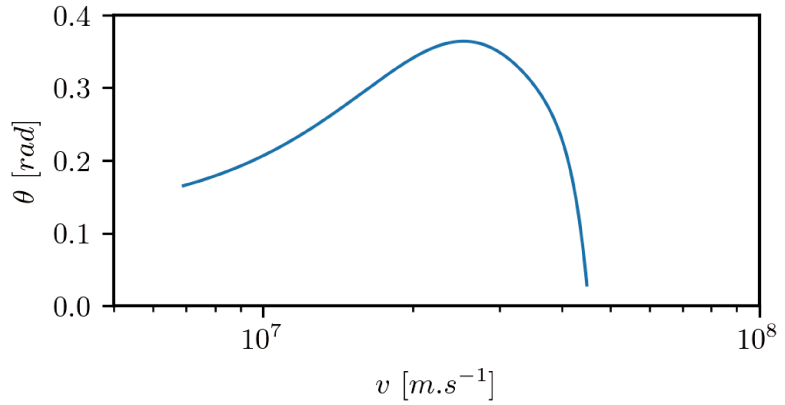

Figure 7.5: Angular divergence as a function of velocity, obtained from Eq. 7.17 for a maximum energy $E_{\max} = 11$ MeV.

The particle flux $\phi_s(v)$ may also be obtained analytically as:

$$\phi_s(v) = \int_{v_i}^{v_{i+1}} v' f(v') \mathrm{d}v' \tag{7.20}$$

$$= \frac{n_0}{e^{\alpha v_{\max}} - e^{\alpha v_{\min}}} \left[e^{\alpha v_{i+1}} \left(v_{i+1} - \frac{1}{\alpha} \right) - e^{\alpha v_i} \left(v_i - \frac{1}{\alpha} \right) \right] \tag{7.21}$$

The growth rate of the non-resonant streaming instability may then be obtained from the protons particle flux and as a function of the background plasma parameters:

$$\gamma = \frac{1}{2} \frac{\phi_s}{n_m} \frac{\Omega_0}{v_A} \sqrt{\frac{m_p}{m_m}} \tag{7.22}$$

where the flux ϕ_s is integrated over the velocity spectrum. In order to determine whether such growth rate may allow us to observe the non-resonant instability, one may calculate the e-folding, defined as the integral of the growth rate in the standard, cold non-resonant mode regime over the duration of the interaction $\int_{t_0}^{t_{end}} \gamma \mathrm{d}t$ where t_0 is the beginning and t_{end} the end time of the stream-background interaction. The e-folding reached at the end of the experiment should be larger or of the order unity in order to observe a substantial growth of the instability.

A schematic of a TNSA experimental design is given in Fig. 7.6. The background plasma is generated by ionizing a pre-existing neutral gas jet with a nanosecond duration laser. Considering the spectrum obtained experimentally as in Fig. 7.4 propagating in a uniform background plasma made of argon with density $n_m = 10^{19}$ cm^{-3} embedded in an ambient magnetic field $B = 20$ T, for an acceleration duration of 1 ps and a stream density at the source $n_0 = 10^{19}$ cm^{-3}, one obtains an e-folding of 7.4×10^{-2} insufficient to observe the non-resonant mode.

Future experiments could be modified by extending the duration of the TNSA acceleration, reducing the streaming population flux, and increasing the ambient magnetic field intensity. Considering an acceleration time of 10^2 ps, which could potentially be reached with current laser installations (Zou et al. [2008]), and a streaming population flux 10 times lower with a magnetic field intensity $B = 60$ T, one obtains an e-folding of 0.7, which may be sufficient to observe the beginning of the linear phase of growth of the

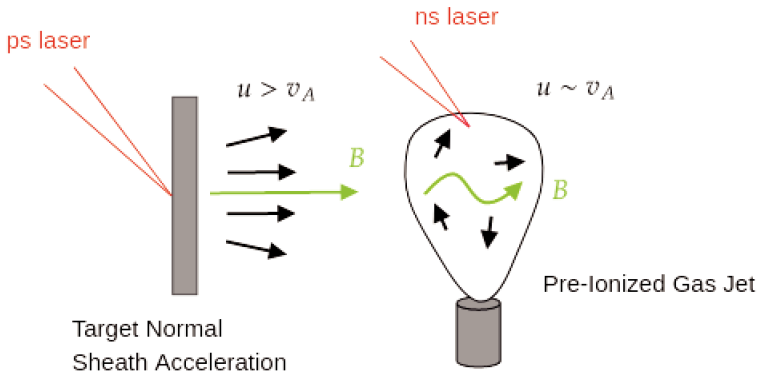

Figure 7.6: Schematic of the TNSA accelerated protons beam penetrating a pre-ionized gas jet escaping from a nozzle.

non-resonant instability in its standard, cold regime. This experiment was designed by the team led by Julien Fuchs. New experiments will be conducted at the VULCAN laser facility next year using high power lasers and intense magnetic field sources, aiming at improving the diagnostics with adjusted laser intensities and pulse duration. The following sections will present an alternative setup, aiming at improving the maximum reachable e-folding in the experiments.

7.4 Counter-propagating plasma plumes setup

7.4.1 Plasma collimation

The main weakness of the TNSA driven experimental setup is the duration of the streaming protons population acceleration, typically of the order of tens of picosecond. In order to overcome this limitation, the background and streaming populations may also be obtained by irradiating a target with a lower intensity but longer pulse duration laser on the front side, vaporizing the solid and generating an expanding plasma plume with large densities, temperature and expansion velocity. Such plasmas have a typical lifespan of the order of tens to hundreds of nanoseconds and expand in all directions from the source.

In order to obtain a focused, large flux of particles, a strong magnetic field can be applied parallel to the surface normal. The resulting magnetically confined plasma expansion can then be considered as a one-dimensional collimated flow (Ciardi et al. [2013]). The process of plasma collimation by a magnetic field is well described in Albertazzi et al. [2014], Higginson et al. [2017] and Revet et al. [2021]. After the irradiation of the target by the laser pulse, the plasma plume expands in the ambient magnetic field, generating a curvature of the field lines. The resulting magnetic field tension force opposes the expansion, which leads to the formation of an oblique shock, and redirects the flow toward the direction parallel to the initial magnetic field. The collimation radius, i.e the radial distance that the plasma plume can propagate before being redirected, may be estimated from the condition of equilibrium between the kinetic pressure and the magnetic field

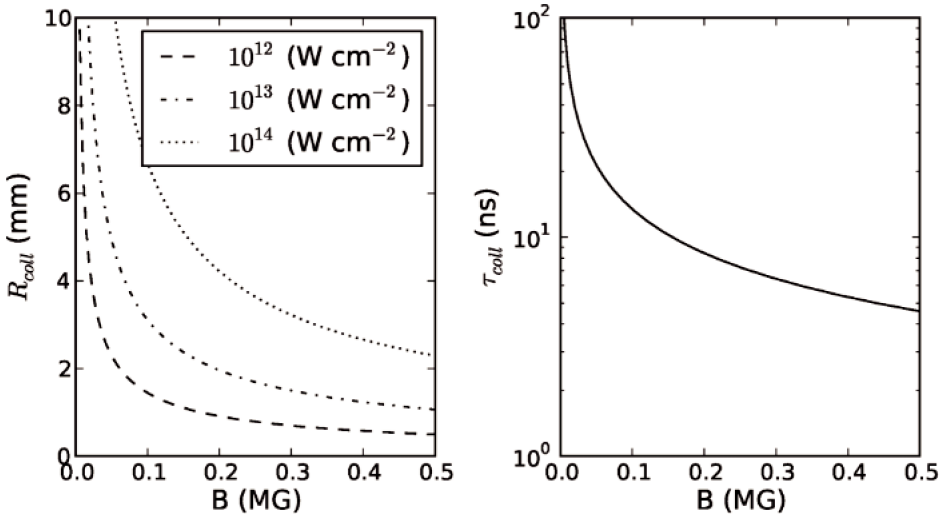

Figure 7.7: *Left panel*: Collimation radius of the plasma plume as a function of the ambient magnetic field intensity. *Right panel*: Collimation time as a function of the ambient magnetic field intensity, from Ciardi et al. [2013].

pressure (Ciardi et al. [2013]) as $\rho v^2 \sim B_0^2/2\mu_0$, which yields:

$$R_{\rm coll}({\rm cm}) \sim 0.8 \left(\frac{E_K(J)}{B_0(T)}\right))^{1/3} \tag{7.23}$$

where $E_K = fE_L$ with E_k the bulk kinetic energy, E_l the laser energy deposited on the target and f a laser acceleration efficiency coefficient, measured experimentally to be of the order 0.1 (Meyer and Thiell [1984]). A collimation time $\tau_{\rm coll}$ may then be calculated as:

$$\tau_{\rm coll} = \frac{R_{\rm coll}({\rm cm})}{v_{\rm exp}({\rm cm.s}^{-1})} \tag{7.24}$$

where $v_{exp} = 4.6 \times 10^7 I^{1/3}\lambda^{2/3}$ (Tabak et al. [1994]) is the expansion velocity with I the laser intensity in units of 10^{14} W.cm^{-2} and λ the laser wavelength in μm. The collimation time is independent of the laser intensity because of the expansion velocity scaling as $I^{1/3}$. The collimation time and radius are shown in Fig. 7.7 considering $f = 0.1$ and $\lambda = 1.064\ \mu m$. One obtains that an expanding plasma may be collimated in less than 10 ns by an ambient magnetic field above 10 T. The collimation radius for laser intensities in the range $I = 10^{12} - 10^{14}$ W.cm^{-2} is of the order of a few millimeters.

7.4.2 Experimental setup

The experimental setup may be described as follows: two solid targets opposite to each other are irradiated by nanosecond laser pulses, generating two counter-propagating plasma plumes. These plumes are embedded in an ambient magnetic field generated by an Helmholtz coil, parallel to the targets normal. This leads to the one-dimensional propagation of the plasmas parallel to the magnetic field, ensured by the collimation driven by the magnetic field, and allows the growth of the non-resonant instability. A schematic of the situation is given in Fig. 7.8. The non-resonant instability may be destabilized in the regions close to the two targets. On the *left side*, the left plasma plume (noted with

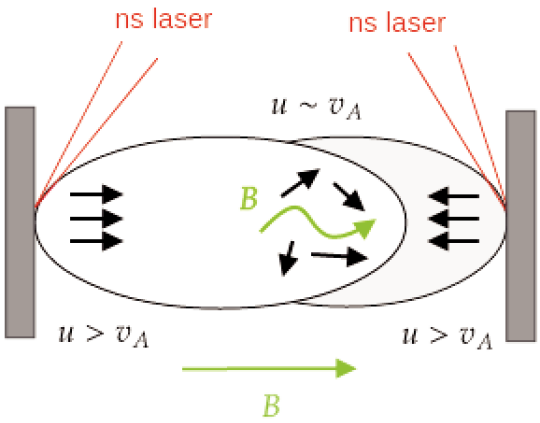

Figure 7.8: Schematic of the counter-propagating plasma plumes experimental setup. The region of development of the instability is shown for the case where the plume from the right side plays the role of the background.

the subscript "1") plays the role of the background plasma whereas the plume coming from the right (noted with the subscript "2") plays the role of the streaming population, hence $n_m \equiv n_1$ and $n_s \equiv n_2$. On the *right side* the inverse situation occurs such that $n_m \equiv n_2$ and $n_s \equiv n_1$.

Assuming an adiabatic, one-dimensional expansion along the ambient magnetic field, the collimated plasma plumes density and velocity profiles may be calculated analytically for a given time t and distance from the source z. The full derivation can be found in classical textbooks (Zeldovich and Raizer [1965], L.D. Landau and E.M. Lifshitz [2013]), and yield the density for symmetric counter-propagating plasma plumes as:

$$n_1(z,t) = n_0 \left(1 - \frac{\gamma - 1}{\gamma + 1}(1 + \frac{z}{c_{s,0}t})\right)^{2/(\gamma-1)} \tag{7.25}$$

for the left side, and:

$$n_2(z,t) = n_0 \left(1 - \frac{\gamma - 1}{\gamma + 1}(1 + \frac{z_2 - z}{c_{s,0}t})\right)^{2/(\gamma-1)} \tag{7.26}$$

for the right side, where $c_{s,0} = \sqrt{Zk_BT_{e,0}/m_i}$ is the ion acoustic speed at the source, $\gamma = 5/3$ is the heat capacity ratio, and z_2 is the position of the source of the plume coming from the right, with the origin fixed on the source of the plasma plume coming from the left at $z_1 = 0$. The source of the collimated expanding plasma plume can be estimated as being away from the solid target surface by a distance R_{coll}. The velocity profiles are given by:

$$u_1(z,t) = c_{s,0} + \frac{z}{t} \tag{7.27}$$

$$u_2(z,t) = -c_{s,0} - \frac{z_2 - z}{t} \tag{7.28}$$

This corresponds to a ballistic expansion with a minimum velocity equal to the sound speed. The relative velocity $\Delta u = u_1 - u_2 = 2c_{s,0} + z_2/t$ is independent of the position. Relative velocities of the order $\Delta u = 10^3$ km.s^{-1} can be obtained in the laboratory, which may be

sufficient to destabilize the non-resonant mode depending on the plasma parameters and ambient magnetic field intensity considered.

7.4.3 Collisionless shock formation, modified Weibel instability

Depending on the parameters of the background and streaming populations, one may observe the formation of a shock when two plasma interpenetrate, characterized by a jump in density, velocity and magnetic field at the shock front. Shocks are ubiquitous across a wide range of astrophysical environments. Supernova remnants shocks (Völk et al. [2005]), galaxy clusters shocks (van Weeren et al. [2017]) and the Earth bow shock (Winske and Leroy [1984], Johlander et al. [2016]) are a few non-exhaustive examples of such astrophysical shocks, which may develop even in collisionless plasmas by the interaction of the flow with the background via the electromagnetic field on scales larger than the Debye length. The upstream particles may be scattered off the electromagnetic fluctuations, generated by instabilities arising from the plasma interpenetration, and effectively reducing the fluid drift velocity. The formation of collisionless shocks in laboratory experiments is still an active field of research and poses challenging experimental and technological difficulties (Grassi and Fiuza [2021]). Such shocks should be avoided in experiments on the non-resonant instability to prevent any substantial loss of drift velocity before the non-resonant mode may grow.

Weibel [1959] showed that counter propagating plasmas may excite the exponential growth of purely growing transverse electromagnetic waves with respect to the drift velocity, on time scales of the order of the ion plasma frequency and on spatial scales of the order of the ion inertial length, and therefore providing the necessary electromagnetic fluctuations for the formation of a collisionless shock (Spitkovsky [2005], Bohdan et al. [2021]). The Weibel instability is modified by the presence of an ambient magnetic field which acts as a stabilizing factor because of the associated magnetic tension in the parallel and oblique case, preventing the growth of the unstable waves at large scales. Supposing non-relativistic drift velocities and purely growing modes, the unstable wavelengths are bounded by the maximum spatial scale (Stockem et al. [2006]):

$$L_{\max}^{\text{Weibel}} = 2\pi \frac{c}{\omega_p} \sqrt{\frac{g}{\mu} - 1} \tag{7.29}$$

where $\omega_p = (1+\mu)\omega_{ps}^2 \dfrac{1+r_n}{r_n}$, $\mu = m_e/m_s$, $\omega_{ps} = \sqrt{n_s e^2/\epsilon_0 m_e}$, $r_n = n_s/n_m$ and $g = (\omega_p/\Omega^2) r_n (u_s/c)^2$ with $\Omega = eB/m_e c$. In addition, one may obtain the relative drift velocity threshold for the Weibel instability as:

$$u_s \geq v_{As}\sqrt{1+r_n} \tag{7.30}$$

with u_s the relative drift velocity, and $v_{As} = B/\sqrt{n_s(m_s+m_e)\mu_0}$. In order for the particles to not be scattered by the Weibel electromagnetic perturbations, the Larmor radius of the upstream particles should be larger than the Weibel instability wavelength. This yields the condition to avoid the formation of a collisionless shock mediated by the Weibel instability,

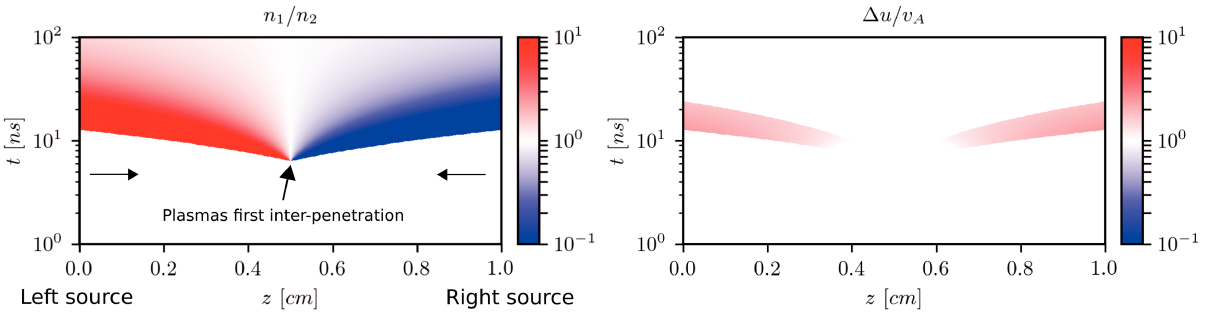

Figure 7.9: *Left panel*: Density ratio n_1/n_2 as a function of the distance (abscissa) and time (ordinate). The white regions before ~ 10 ns corresponds to times and positions where the two plasma plumes have not interpenetrated yet. The first encounter position is indicated with the central arrow, wheres the left and right arrow indicate the direction of propagation of the plumes. *Right panel*: Relative velocity Δu normalized to the Alfvén speed v_A. The relative velocity is of the order $\Delta u = 10^3 \text{km.s}^{-1}$. The white regions correspond to times and positions where the two plasma plumes have either not interpenetrated yet, or where the density ratio is larger than 0.1, or where the local Alfvén velocity is larger than the relative drift velocity Δu.

modified by a strong ambient magnetic field:

$$r_{Ls} > L_{\text{max}}^{\text{Weibel}} \tag{7.31}$$

where $r_{Ls} = m_s u_s / q_s B$. In practice this condition is easily fulfilled for typical laser plasma experiments, involving magnetic fields of the order of 10 T with drift velocities larger than 10^3 km.s^{-1}.

7.4.4 Plasma plumes analytical predictions

A map of the density ratio n_1/n_2 as a function of time and space considering the counter-propagating plasma plumes setup is shown in Fig. 7.9 upper panel, calculated with Eqs. 7.25 and 7.26. The ambient magnetic field intensity is $B = 50\ T$, and the plasmas are made of fully ionized carbon ($A = 12$, $Z = 6$) with densities at the source $n_0 = 10^{19}$ cm^{-3} and an electronic temperature $T_{e,0} = 10^7\ K$. The two plasmas sources are separated by a distance $2L = 1$ cm. The counter-propagating plumes interpenetrate after ~ 10 ns of expansion, yielding a density ratio equal to unity at the center of the experiment. After a few additional nanoseconds, the plasma plumes further propagate and permit the growth of the non-resonant instability on the left and right sides. The relative density plays a critical role in the determination of the largest unstable wavelength. In order to avoid the Hall effect to modify the instability, one needs to consider scales above the ion inertial length. Together with the requirement of super-Alfvénic drift velocities, one obtains that the density ratio must be smaller than unity (2.34). The conditions that the streaming population must be less dense than the background, together with the condition of a super-Alfvénic relative velocity, restrain the regions of interest to a region with a length of the order of 4 mm away from the sources, for a duration of ~ 10 ns. The growth rate and unstable wavelengths must therefore fit into this region in space and time. This is shown in Fig. 7.9 lower panel, which presents the relative fluid velocities normalized to the local Alfvén velocity. The white regions in the figure correspond to times and positions where

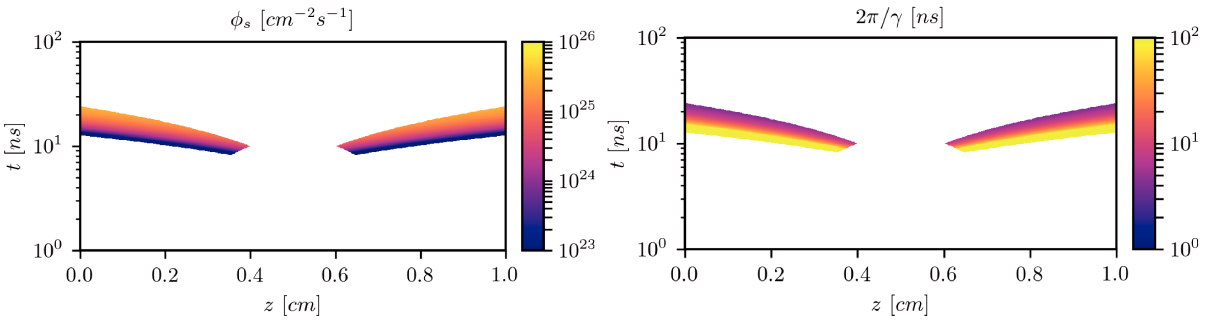

Figure 7.10: *Left panel*: Streaming population flux ϕ_s as a function of the distance (abscissa) and time (ordinate). *Right panel*: Non-resonant mode growth time $2\pi/\gamma$.

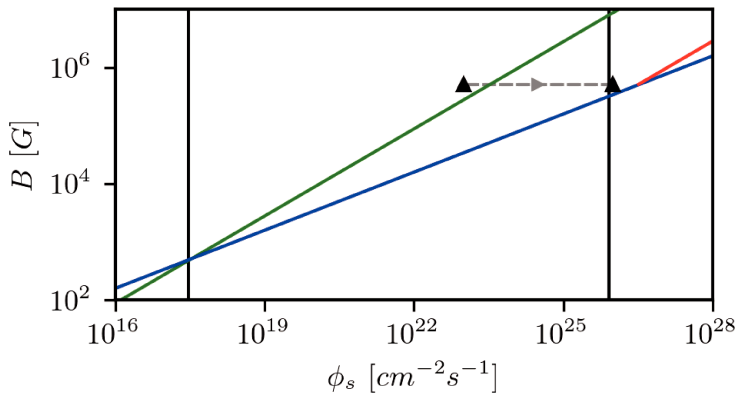

Figure 7.11: Instability regimes as a function of the streaming particle flux ϕ_s and of the ambient magnetic field B as in Fig. 7.1, and considering $n_m = 10^{19}$ cm^{-3} and $T_m = 10^7$ K. The black triangles correspond to the fluxes $\phi_s = 10^{23}$ cm^{-2}s^{-1}, reached at $t \sim 10$ ns, and $\phi_s = 10^{26}$ cm^{-2}s^{-1}, reached at $t \sim 30$ ns, for a magnetic field intensity $B = 50$ T $(0.5MG)$. The grey dashed line illustrates the range of streaming particle flux explored in the proposed experiment, where the arrow indicates the time evolution of the flux.

the two plasma plumes have either not interpenetrated yet, or where the density ratio is larger than 0.1, or where the local Alfvén velocity is larger than the relative drift velocity Δu. For times longer than ~ 30 ns the instability growth is halted as the density ratio becomes close to $n_1/n_2 \sim 1$, and the relative velocity decreases as the space between the two targets is progressively filled with both plasma plumes.

The local streaming population flux $\phi_s(z,t) = n_s(z,t)\Delta u(t)$, together with the local growth time $2\pi/\gamma$ of the non-resonant instability are presented in Fig. 7.10. The flux during the early times of interactions for $t = 10$ ns is of the order $\phi_s = 10^{27}$ m^{-2}s^{-1}, which corresponds to growth time in the range of hundreds of nanoseconds. As the plasma plumes interpenetrate, the particle flux increases and reaches values up to $\phi_s = 10^{29}$ m^{-2}s^{-1}. After 15 ns, the growth time has strongly decreased and reaches values compatible with the interaction duration. For late times $t \gtrsim 25$ ns the flux is too large and the background plasma becomes demagnetized. This is illustrated in Fig. 7.11, which shows that the flux remains in the standard regime of the non-resonant mode where thermal effects do not modify the instability, during most of the proposed experiment duration. The e-folding

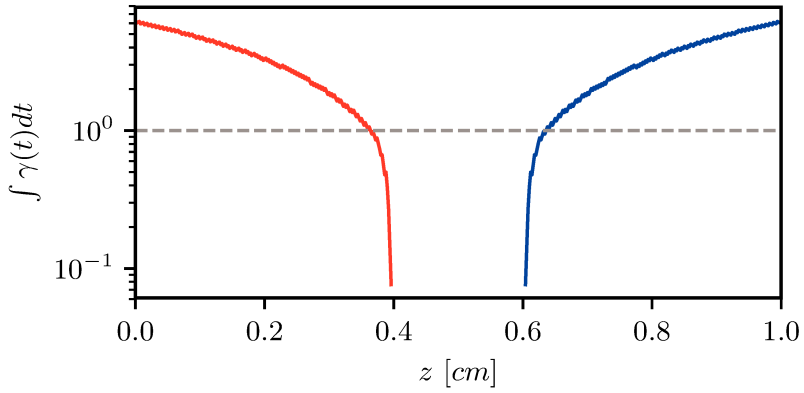

Figure 7.12: Integrated growth rate (or e-folding) over the interaction time as a function of the position between the two targets as from Eq. 7.32 while considering the growth rate in the standard, cold regime. The red and blue lines indicate the e-folding in the left and right regions of the proposed experiment respectively. The dashed grey line indicates the limit above which the instability can substantially amplify electromagnetic perturbations.

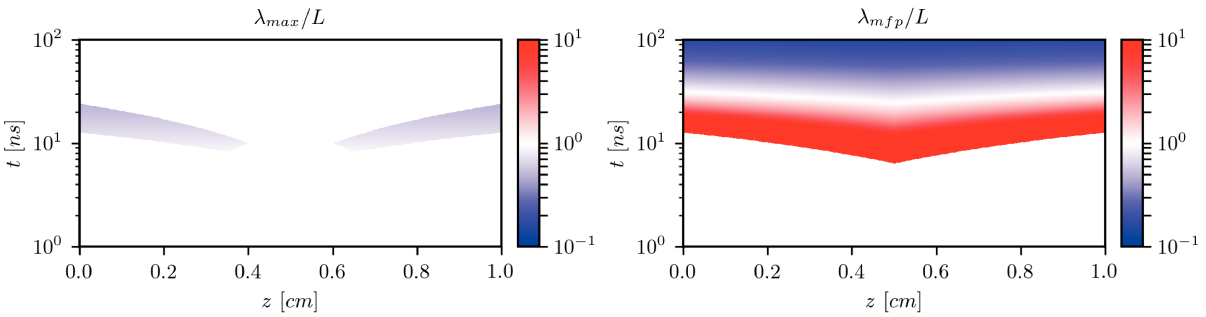

Figure 7.13: *Left panel*: Maximum unstable wavelength $\lambda_{\max}$ as from Eq. 7.33. *Right panel*: Collisional mean free path λ_{mfp} as a function of space (abscissa) and time (ordinate), normalized to the half distance between the two sources L.

can then be calculated as:

$$\int_{t_0(z)}^{t_{end}(z)} \gamma(z,t)\mathrm{d}t = \frac{1}{2}\frac{q_s}{e}\sqrt{\frac{m_p}{m_m}}\Omega_0 \int_{t_0(z)}^{t_{end}(z)} \frac{\phi_s(z,t)}{n_m(z,t)v_A(z,t)}\mathrm{d}t \tag{7.32}$$

where $t_0(z)$ is the beginning and $t_{end}(z)$ the end time of the stream-background interaction at a given position z. The result is presented in Fig. 7.12. One obtains a maximum e-folding of 5 close to the expanding plasma plume source, gradually decreasing up to 4 mm away from the source, where the instability cannot grow because of the large density ratio in the central region. In addition to the e-folding, the largest unstable wavelengths, calculated as:

$$\lambda_{\max} = 2\pi\frac{\Delta u}{\Omega_0}\frac{e}{q_s}\frac{m_s}{m_p} \tag{7.33}$$

must fit in the size of the experiment. Finally the condition that the plasma plumes propagation remains collisionless must also be fulfilled. Fig. 7.13 presents the maximum unstable wavelength together with the collisionless criterion as from Eq. 7.9, normalized to the half distance between the plasma plume sources L. Owing to the large relative velocity

between the counter-propagating plumes and to the large ambient magnetic field of 50 T, the maximum wavelength is contained in the interaction region of 4 mm during the entire duration of the experiment. Similarly the Coulomb collision mean free path between the plasma plumes is larger than the interaction region. It becomes comparable for times $t \sim 30$ ns, where the instability has already substantially developed, such that particle collisions should not modify the drift velocities of the plumes on time scales comparable to the instability growth time. In this configuration, the instability should be able to grow before the two inter-penetrating plasmas become collisional.

The modelizations presented in this chapter are based on predictions of the instability growth rate and spatial scales considering analytical density profiles and particle flux. Numerical simulations will be necessary to assess the non-linear evolution of the plasma, and validate the simplifying assumptions used. Additional physical effects such as a finite plasma resistivity will also be needed to be taken into account, as well as potential competing unstable modes, such as the fire-hose instability which may disrupt the propagation of the plasma plumes before the growth of the non-resonant mode.

7.5 References

Aharonian, F., Akhperjanian, A., Barrio, J., Bernlöhr, K., Börst, H., Bojahr, H., Bolz, O., Contreras, J., Cortina, J., Denninghoff, S., Fonseca, V., Gonzalez, J., Götting, N., Heinzelmann, G., Hermann, G., Heusler, A., Hofmann, W., Horns, D., Ibarra, A., Iserlohe, C., Jung, I., Kankanyan, R., Kestel, M., Kettler, J., Kohnle, A., Konopelko, A., Kornmeyer, H., Kranich, D., Krawczynski, H., Lampeitl, H., Lopez, M., Lorenz, E., Lucarelli, F., Magnussen, N., Mang, O., Meyer, H., Mirzoyan, R., Moralejo, A., Ona, E., Padilla, L., Panter, M., Plaga, R., Plyasheshnikov, A., Prahl, J., Pühlhofer, G., Rauterberg, G., Röhring, A., Rhode, W., Rowell, G. P., Sahakian, V., Samorski, M., Schilling, M., Schröder, F., Siems, M., Stamm, W., Tluczykont, M., Völk, H. J., Wiedner, C. A., and Wittek, W. (2001). Evidence for TeV gamma ray emission from Cassiopeia A. *A&A*, 370(1):112–120.

Aharonian, F. A., Akhperjanian, A. G., Aye, K.-M., Bazer-Bachi, A. R., Beilicke, M., Benbow, W., Berge, D., Berghaus, P., Bernlöhr, K., Bolz, O., Boisson, C., Borgmeier, C., Breitling, F., Brown, A. M., Bussons Gordo, J., Chadwick, P. M., Chitnis, V. R., Chounet, L.-M., Cornils, R., Costamante, L., Degrange, B., Djannati-Ataï, A., Drury, L. O., Ergin, T., Espigat, P., Feinstein, F., Fleury, P., Fontaine, G., Funk, S., Gallant, Y. A., Giebels, B., Gillessen, S., Goret, P., Guy, J., Hadjichristidis, C., Hauser, M., Heinzelmann, G., Henri, G., Hermann, G., Hinton, J. A., Hofmann, W., Holleran, M., Horns, D., de Jager, O. C., Jung, I., Khélifi, B., Komin, N., Konopelko, A., Latham, I. J., Le Gallou, R., Lemoine, M., Lemière, A., Leroy, N., Lohse, T., Marcowith, A., Masterson, C., McComb, T. J. L., de Naurois, M., Nolan, S. J., Noutsos, A., Orford, K. J., Osborne, J. L., Ouchrif, M., Panter, M., Pelletier, G., Pita, S., Pohl, M., Pühlhofer, G., Punch, M., Raubenheimer, B. C., Raue, M., Raux, J., Rayner, S. M., Redondo, I., Reimer, A., Reimer, O., Ripken, J., Rivoal, M., Rob, L., Rolland, L., Rowell, G., Sahakian, V., Saugé, L., Schlenker, S., Schlickeiser, R., Schuster, C., Schwanke, U., Siewert, M., Sol, H., Steenkamp, R., Stegmann, C., Tavernet, J.-P., Théoret, C. G., Tluczykont, M., van der Walt, D. J., Vasileiadis, G., Vincent, P., Visser, B., Völk, H. J., and Wagner, S. J. (2004). High-energy particle acceleration in the shell of a supernova remnant. *Nature*, 432(7013):75–77.

Albertazzi, B., Béard, J., Ciardi, A., Vinci, T., Albrecht, J., Billette, J., Burris-Mog, T., Chen, S. N., Da Silva, D., Dittrich, S., Herrmannsdörfer, T., Hirardin, B., Kroll, F., Nakatsutsumi, M., Nitsche, S., Riconda, C., Romagnagni, L., Schlenvoigt, H.-P., Simond, S., Veuillot, E., Cowan, T. E., Portugall, O., Pépin, H., and Fuchs, J. (2013). Production of large volume, strongly magnetized laser-produced plasmas by use of pulsed external magnetic fields. *Review of Scientific Instruments*, 84(4):043505.

Albertazzi, B., Ciardi, A., Nakatsutsumi, M., Vinci, T., Béard, J., Bonito, R., Billette, J., Borghesi, M., Burkley, Z., Chen, S. N., Cowan, T. E., Herrmannsdörfer, T., Higginson, D. P., Kroll, F., Pikuz, S. A., Naughton, K., Romagnani, L., Riconda, C., Revet, G., Riquier, R., Schlenvoigt, H.-P., Skobelev, I. Y., Faenov, A., Soloviev, A., Huarte-Espinosa, M., Frank, A., Portugall, O., Pépin, H., and Fuchs, J. (2014). Laboratory formation of a scaled protostellar jet by coaligned poloidal magnetic field. *Science*, 346(6207):325–328.

Bohdan, A., Pohl, M., Niemiec, J., Morris, P. J., Matsumoto, Y., Amano, T., Hoshino, M., and Sulaiman, A. (2021). Magnetic field amplification by the Weibel instability at planetary and astrophysical high-Mach-number shocks. *arXiv:2102.04328 [astro-ph, physics:physics]*.

Bolton, P., Borghesi, M., Brenner, C., Carroll, D., De Martinis, C., Fiorini, F., Flacco, A., Floquet, V., Fuchs, J., Gallegos, P., Giove, D., Green, J., Green, S., Jones, B., Kirby, D., McKenna, P., Neely, D., Nuesslin, F., Prasad, R., Reinhardt, S., Roth, M., Schramm, U., Scott, G., Ter-Avetisyan, S., Tolley, M., Turchetti, G., and Wilkens, J. (2014). Instrumentation for diagnostics and control of laser-accelerated proton (ion) beams. *Physica Medica*, 30(3):255–270.

Callen, J. D. (2006). Coulomb Collisions. In *Fundamentals of Plasma Physics*. University of Wisconsin, Madison, Wisconsin, draft edition.

Ciardi, A., Vinci, T., Fuchs, J., Albertazzi, B., Riconda, C., Pépin, H., and Portugall, O. (2013). Astrophysics of Magnetically Collimated Jets Generated from Laser-Produced Plasmas. *Physical review letters*, 110:025002.

Grassi, A. and Fiuza, F. (2021). Efficient generation of turbulent collisionless shocks in laser-ablated counter-streaming plasmas. *Phys. Rev. Research*, 3(2):023124.

Heuer, P. V., Weidl, M. S., Dorst, R. S., Schaeffer, D. B., Bondarenko, A. S., Tripathi, S. K. P., Van Compernolle, B., Vincena, S., Constantin, C. G., Niemann, C., and Winske, D. (2018). Observations of a field-aligned ion/ion-beam instability in a magnetized laboratory plasma. *Physics of Plasmas*, 25:032104.

Higginson, D. P., Revet, G., Khiar, B., Béard, J., Blecher, M., Borghesi, M., Burdonov, K., Chen, S. N., Filippov, E., Khaghani, D., Naughton, K., Pépin, H., Pikuz, S., Portugall, O., Riconda, C., Riquier, R., Ryazantsev, S. N., Skobelev, I. Y., Soloviev, A., Starodubtsev, M., Vinci, T., Willi, O., Ciardi, A., and Fuchs, J. (2017). Detailed characterization of laser-produced astrophysically-relevant jets formed via a poloidal magnetic nozzle. *High Energy Density Physics*, 23:48–59.

Hinton, J. (2004). The status of the HESS project. *New Astronomy Reviews*, 48(5):331–337.

Ivanov, V. V., Maximov, A. V., Betti, R., Leal, L. S., Moody, J. D., Swanson, K. J., and Huerta, N. A. (2021). Generation of strong magnetic fields for magnetized plasma experiments at the 1-MA pulsed power machine. *Matter and Radiation at Extremes*, 6(4):046901.

Johlander, A., Schwartz, S. J., Vaivads, A., Khotyaintsev, Y. V., Gingell, I., Peng, I. B., Markidis, S., Lindqvist, P.-A., Ergun, R. E., Marklund, G. T., Plaschke, F., Magnes, W., Strangeway, R. J., Russell, C. T., Wei, H., Torbert, R. B., Paterson, W. R., Gershman, D. J., Dorelli, J. C., Avanov, L. A., Lavraud, B., Saito, Y., Giles, B. L., Pollock, C. J., and Burch, J. L. (2016). Rippled Quasiperpendicular Shock Observed by the Magnetospheric Multiscale Spacecraft. *Phys. Rev. Lett.*, 117(16):165101.

L.D. Landau and E.M. Lifshitz (2013). *Fluid Mechanics*, volume 6. Elsevier Science.

Leneman, D., Gekelman, W., and Maggs, J. (2006). The plasma source of the Large Plasma Device at University of California, Los Angeles. *Review of Scientific Instruments - REV SCI INSTR*, 77.

Malka, V., Coulaud, C., Geindre, J., Lopez, V., Najmudin, Z., Neely, D., and Amiranoff, F. (2000). Characterization of neutral density profile in a wide range of pressure of cylindrical pulsed gas jets. *Review of Scientific Instruments*, 71.

Mancic, A., Robiche, J., Antici, P., Audebert, P., Blancard, C., Combis, P., Dorchies, F., Faussurier, G., Fourmaux, S., Harmand, M., Kodama, R., Lancia, L., Mazevet, S., Nakatsutsumi, M., Peyrusse, O., Recoules, V., Renaudin, P., Shepherd, R., and Fuchs, J. (2010). Isochoric heating of solids by laser-accelerated protons: Experimental characterization and self-consistent hydrodynamic modeling. *High Energy Density Physics*, 6(1):21–28.

Meyer, B. and Thiell, G. (1984). Experimental scaling laws for ablation parameters in plane target–laser interaction with 1.06 Mm and 0.35 Mm laser wavelengths. *The Physics of Fluids*, 27(1):302–311.

Mora, P. (2003). Plasma Expansion into a Vacuum. *Phys. Rev. Lett.*, 90(18):185002.

Revet, G., Khiar, B., Filippov, E., Argiroffi, C., Béard, J., Bonito, R., Cerchez, M., Chen, S. N., Gangolf, T., Higginson, D. P., Mignone, A., Olmi, B., Ouillé, M., Ryazantsev, S. N., Skobelev, I. Y., Safronova, M. I., Starodubtsev, M., Vinci, T., Willi, O., Pikuz, S., Orlando, S., Ciardi, A., and Fuchs, J. (2021). Laboratory disruption of scaled astrophysical outflows by a misaligned magnetic field. *Nature Communications*, 12:762.

Roth, M. and Schollmeier, M. (2016). Ion Acceleration—Target Normal Sheath Acceleration. *CERN Yellow Reports*, page 231 Pages.

Spitkovsky, A. (2005). Simulations of relativistic collisionless shocks: Shock structure and particle acceleration. *AIP Conference Proceedings*, 801:345–350.

Stockem, A., Lerche, I., and Schlickeiser, R. (2006). On the Physical Realization of Two-dimensional Turbulence Fields in Magnetized Interplanetary Plasmas. *ApJ*, 651(1):584–589.

Tabak, M., Hammer, J., Glinsky, M. E., Kruer, W. L., Wilks, S. C., Woodworth, J., Campbell, E. M., Perry, M. D., and Mason, R. J. (1994). Ignition and high gain with ultrapowerful lasers*. *Physics of Plasmas*, 1(5):1626–1634.

Thaury, C., Mora, P., Adam, J. C., and Heron, A. (2009). Regimes of expansion of a collisional plasma into a vacuum. *Physics of Plasmas*, 16(9):093104.

Trubnikov, B. A. (1965). Particle interactions in a fully ionized plasma. *Reviews of Plasma Physics*, 1:105.

van Weeren, R. J., Andrade-Santos, F., Dawson, W. A., Golovich, N., Lal, D. V., Kang, H., Ryu, D., Brüggen, M., Ogrean, G. A., Forman, W. R., Jones, C., Placco, V. M., Santucci, R. M., Wittman, D., Jee, M. J., Kraft, R. P., Sobral, D., Stroe, A., and Fogarty, K. (2017). The case for electron re-acceleration at galaxy cluster shocks. *Nat Astron*, 1(1):1–6.

Völk, H. J., Berezhko, E. G., and Ksenofontov, L. T. (2005). Magnetic field amplification in Tycho and other shell-type supernova remnants. *Astronomy & Astrophysics*, 433(1):229–240.

Weibel, E. S. (1959). Spontaneously Growing Transverse Waves in a Plasma Due to an Anisotropic Velocity Distribution. *Phys. Rev. Lett.*, 2(3):83–84.

Winske, D. and Leroy, M. M. (1984). Diffuse ions produced by electromagnetic ion beam instabilities. *Journal of Geophysical Research: Space Physics*, 89(A5):2673–2688.

Zeldovich, Y. B. and Raizer, Y. P. (1965). Physics of shock waves and high-temperature hydrodynamic phenomena. Technical report, Foreign technology division wright-patterson AFB OH.

Zou, J. P., Blanc, C. L., Audebert, P., Janicot, S., Sautivet, A. M., Martin, L., Sauteret, C., Paillard, J. L., Jacquemot, S., and Amiranoff, F. (2008). Recent progress on LULI high power laser facilities. *Journal of Physics: Conference Series*, 112(3):032021.

Zweibel, E. G. and Everett, J. E. (2010). Environments for Magnetic Field Amplification by Cosmic Rays. *The Astrophysical Journal*, 709(2):1412–1419.

Chapter 8

Conclusions and future prospects

This thesis aims to pursue the ongoing effort of describing the non-resonant streaming instability in non-ideal plasma environments, where the effects of finite plasma temperature and collisions may modify significantly the unstable waves growth and saturation. These effects are crucial to understand cosmic rays acceleration and propagation in many astrophysics environments as well as to design future laboratory experiments.

A first approach in the theoretical developments presented in this thesis was to describe the non-resonant instability using an MHD model, considering the background plasma as an electrically charged fluid traversed by a population of drifting cosmic rays. Such model allows to describe all of the essential features of the instability. In particular, the fundamental mechanism leading to the unstable feedback loop between the plasma and the electromagnetic waves was investigated. The specific spatial structure of the waves was described, and its importance on the non-linear evolution of the instability was highlighted. Quantitative predictions on the fastest growing modes and associated unstable wavelengths were obtained for arbitrary ion mass and charge, and were compared to the existing kinetic and fluid theory for protons population, in the limit of negligible plasma temperature and low density streaming population. It is found that heavy elements can destabilize the non-resonant mode on larger spatial scales, which may help to better confine lighter elements with a smaller Larmor radius at shock and thus ease the first order Fermi acceleration process to high energies for these lighter populations. It would be interesting to study such effects in shocks simulations by considering heavy cosmic rays, and look at their impact on the acceleration of lighter populations of energetic particles.

The effects of the ambient plasma temperature on the instability were then investigated within the framework of kinetic theory, where analytical expressions of its growth rate were derived in the hot, demagnetized regime of interaction for which the background ions Larmor radius is larger than the unstable wavelengths. The results obtained in this thesis were obtained with simplifying assumptions on the electrons population, assumed to remain cold. Their precise distribution function is difficult to infer in the astrophysical context, but complementary calculations with various possible distributions, including electrons thermal effects, could be attempted in the future. The prediction of the saturated magnetic field intensity is also a challenging issue. The existing estimates were obtained by assuming a cold background plasma. In the hot regime, additional work is needed to obtain corrected estimates. A promising lead is to adapt the results from quasi-linear theory to account for finite Larmor radius effects, in order to derive energy exchange rate

which could then be extrapolated to obtain a prediction on the saturated magnetic field. I have done preliminary work during this thesis, which will need to be pursued to obtain analytical results.

Using the massively parallelized hybrid-Particle-In-Cell code Heckle, numerical simulations of the instability were performed for a wide range of background ions temperature. The simulations explored the cold regime, expected to be correctly described by the modified fluid model, the warm regime where the background ions Larmor radius is no longer negligible but remains smaller than the unstable wavelengths, and hot, demagnetized regime. The results were compared to theoretical predictions, and allowed to better constrain the saturation mechanism of the non-resonant mode. This in turn is crucial to determine the saturated magnetic field intensity as a function of the streaming ions and background plasma temperature. In particular, Bell's saturation mechanism was investigated, where the combined effect of the increasing magnetic tension at small scales and magnetization of the streaming population at large scales breaks the instability feedback loop. Despite this effect, the simulations presented in this thesis showed the existence of a non-linear phase of growth, where further magnetic field amplification can occur because of the background fluid inertia. In the cold limit about two-thirds of the cosmic rays drift kinetic energy is converted into magnetic energy. Increasing the temperature of the ambient plasma can substantially reduce the growth rate and the magnitude of the saturated magnetic field, which may hinder magnetic field amplification in astrophysical environments such as supernova propagating in superbubbles, and in galaxy cluster shocks. The simulations have been performed both in 1D and 2D geometry, which yielded qualitatively and quantitatively similar results. The conduct of 3D simulations is a computational challenge that will need to be tackled to validate this tendency, and to better model the spatial structure of the regions of magnetic field amplification in the simulations. Moreover, the numerical setup used in this work was adapted to study the non-resonant mode microphysics, but does not include the interplay of the instability with the shock itself in the context of cosmic rays acceleration in supernova remnant and protostellar jets. The transition from the micro (electrons and ions scales) to the macro scale (shock and high energy particles scale) is the subject of active research in the astrophysical plasmas community, which will need to be pursued to understand high energy particles acceleration in a self-consistent way.

Significant pressure anisotropies in the background plasma were observed in the simulations. Owing to the helical spatial structure of the unstable electromagnetic waves, strong gradients of the non-diagonal terms of the full ions pressure tensor are created and oppose the instability growth, which leads to a reduced magnetic field growth rate and intensity at saturation. This result suggests that MHD and MHD-PIC simulations with isotropic closure may not be adequate to describe all of the essential features of the non-resonant mode, as a more sophisticated closure may be required to reproduce the anisotropic heating. These limitations of a fluid description of the background ions may restrict its range of applicability. In this direction, it would be interesting to perform comparative simulations between hybrid-PIC and MHD-PIC models in order to assess precisely the effects overlooked by the fluid description.

The mitigation of the anisotropies by particle collisions, which are important in denser environments such as H II regions and molecular clouds, was also investigated numerically. The Coulomb collisions between the background ions were shown to promote the growth

of the instability, provided that the collision frequency is sufficiently large. In addition, protons-neutral hydrogen collisions have been implemented using a Monte-Carlo method, and are found to rapidly damp the unstable waves, confirming previous linear theory calculations. Other types of interactions could be considered in the future, such as charge exchange which may further damp the electromagnetic waves.

Studying the non-resonant mode in the laboratory is potentially within the reach of laser experiments with tens of Tesla externally applied magnetic fields. However the large beam densities, drift velocities and ambient magnetic field required, together with the lack of theoretical knowledge on the effects of particle collisions on the development of the instability, have made its experimental investigations elusive. This work constitutes an additonal step toward filling this gap in our knowledge. Two possible setups which may allow us to observe the non-resonant mode in the laboratory were described, as well as theoretical predictions on the expected time and spatial scales involved. Several considerations which need to be taken into account when attempting to observe the instability in laboratory conditions were presented, from the effects of temperature and collisions in typical laboratory plasmas, to the possible formation of a Weibel-mediated shock. The experiments involve high intensity lasers, coupled with source of strong magnetic field ($\sim 0.1MG$) on typical scales of the order of the centimeter for tens of nanoseconds. They satisfy the condition of super-Alfvénic flows propagating in a magnetized, collionless background, and may excite waves on time and spatial scales compatible with the constraints on the size and lifetime of strongly magnetized laboratory plasmas. Such experiments will allow us to observe the instability for the first time in laboratory conditions, and permit to confront the results to the existing fluid and kinetic theory, in addition to constrain the saturation mechanism of the non-resonant instability. Their modelling with state-of-the-art numerical codes is the object of on-going studies, and will require a multi-scale approach to model the whole interaction, from the laser energy deposition of the target to the propagation of the plasma plumes or TNSA accelerated protons. In addition, other potentially important effects such as the plasma resistivity will need to be taken into account. During this thesis I carried out preliminary work to obtain the dispersion relation while including such effects, and the non-analytical expressions obtained will require additional developments to be applied for future experiments.

Appendix A

Fluid linear theory for arbitrary ions

The following derivations complement those presented in Sec. 2.2 and retain the effects of arbitrary charges and masses.

A.1 Growth rate and unstable wavelengths

The plasma is supposed quasi-neutral:

$$Q_e + Q_m + Q_{cr} = 0 \tag{A.1}$$

where $Q_e = -en_e$ is negative with e the elementary charge, such that the background plasma (main ions and electrons) is electrically charged: $Q_e + Q_m = -Q_{cr}$. This property will be characterized by the parameter:

$$\chi = -\frac{Q_m}{Q_e} = 1 + \frac{Q_{cr}}{Q_e} \tag{A.2}$$

which is positive. In the case of multiple ion species, this parameter would be written $\chi = -\sum_\alpha Q_\alpha/Q_e$. The total current can be expressed with Maxwell-Ampère's law as:

$$\boldsymbol{\nabla} \times \mathbf{B} = \mu_0(Q_e\mathbf{u}_e + Q_m\mathbf{u}_m + Q_{cr}\mathbf{u}_{cr}) + \frac{1}{c^2}\frac{\partial \mathbf{E}}{\partial t} \tag{A.3}$$

where μ_0 is the magnetic permeability and c is the speed of light. The electron population possess a drift velocity relative to the main ions, in the same direction as the cosmic rays such that:

$$\mathbf{u}_e = -\frac{Q_{cr}}{Q_e}\mathbf{u}_{cr} = (1-\chi)\mathbf{u}_{cr} \tag{A.4}$$

In the case of cosmic rays made of multiple ion species, one would also need to take into account the contribution of the current these species carry in Ampère's law. In this case the effective cosmic rays current is the sum of each individual ion component. Performing a summation of the main ions and electrons momentum conservation equations, and

inserting Ampère's law, one finds:

$$\rho\frac{\mathrm{d}\mathbf{u}}{\mathrm{d}t} = \frac{1}{\mu_0}(\nabla\times\mathbf{B})\times\mathbf{B} - \nabla\cdot\mathbf{P} - Q_{cr}(\mathbf{E}+\mathbf{u}_{cr}\times\mathbf{B}) \tag{A.5}$$

where $\mathrm{d}/\mathrm{d}t = \partial/\partial t + \mathbf{u}\cdot\boldsymbol{\nabla}$ is the material derivative. The density, fluid velocity and pressure tensor associated to the background plasma are defined as:

$$\mathbf{u} = \frac{\rho_e\mathbf{u}_e + \rho_m\mathbf{u}_m}{\rho_e+\rho_m} \tag{A.6}$$

$$\rho = \rho_e + \rho_m \tag{A.7}$$

$$P_{ij} = \sum_{\alpha=e,m} P_{ij,\alpha} \tag{A.8}$$

such that $\rho \approx \rho_m$. In the case of multiple ion species the sum should be performed over the ion populations. Considering $m_e \ll m_p$ and neglecting the electron pressure gradients by supposing a negligible electron temperature, Ohm's law can be written as:

$$\mathbf{E} = -\frac{\mathbf{J}\times\mathbf{B}}{Q_e} - \chi\mathbf{u}_m\times\mathbf{B} + (\chi-1)\mathbf{u}_{cr}\times\mathbf{B} \tag{A.9}$$

If one supposes spatial scales above the ion inertial length, the Ohm's law can be written while neglecting the Hall term $-\mathbf{J}\times\mathbf{B}/Q_e$. Using $\mathbf{u}_m\times\mathbf{B}\approx\mathbf{u}\times\mathbf{B}$, one obtains:

$$\mathbf{E} = -\chi\mathbf{u}\times\mathbf{B} + (\chi-1)\mathbf{u}_{cr}\times\mathbf{B} \tag{A.10}$$

Inserting Eq. A.10 in Eqs. A.5 and in Faraday's law, and supposing an incompressible plasma such that $\boldsymbol{\nabla}\cdot\mathbf{u}=0$ as from the density conservation equation, one obtains:

$$\frac{\mathrm{d}\mathbf{u}}{\mathrm{d}t} = \frac{1}{\mu_0\rho}(\boldsymbol{\nabla}\times\mathbf{B})\times\mathbf{B} - \frac{1}{\rho}\boldsymbol{\nabla}\cdot\mathbf{P} + \chi\frac{Q_{cr}}{\rho}\mathbf{u}\times\mathbf{B} - \frac{\chi}{\rho}\mathbf{j}_{cr}\times\mathbf{B} \tag{A.11}$$

$$\frac{\partial\mathbf{B}}{\partial t} = \chi\left[(\mathbf{B}\cdot\boldsymbol{\nabla})\mathbf{u} - (\mathbf{u}\cdot\boldsymbol{\nabla})\mathbf{B}\right] + \frac{1}{Q_e}(\mathbf{j}_{cr}\cdot\boldsymbol{\nabla})\mathbf{B} \tag{A.12}$$

with $\mathbf{j}_{cr} = Q_{cr}\mathbf{u}_{cr}$ the cosmic rays current, supposed constant. Linearizing Eqs. A.11 and A.12 while neglecting second order terms yields:

$$\frac{\partial\mathbf{u}_1}{\partial t} = \frac{(\mathbf{B}_0\cdot\boldsymbol{\nabla})\mathbf{B}_1}{\mu_0\rho} + \frac{\chi}{\rho}\frac{m_p}{e}Q_{cr}\Omega_0\left(\mathbf{u}_1\times\frac{\mathbf{B}_0}{B_0}\right) - \frac{\chi}{\rho}\mathbf{j}_{cr}\times\mathbf{B}_1 \tag{A.13}$$

$$\frac{\partial\mathbf{B}_1}{\partial t} - \frac{1}{Q_e}(\mathbf{j}_{cr}\cdot\boldsymbol{\nabla})\mathbf{B}_1 = \chi(\mathbf{B}_0\cdot\boldsymbol{\nabla})\mathbf{u}_1 \tag{A.14}$$

where $\Omega_0 = eB_0/m_p$ is the proton cyclotron frequency, m_p is the proton mass and $\mathbf{j}_{cr}$ the constant, zeroth order cosmic rays current. The subscripts "0" and "1" refer to the order of the linearization.

The fluid velocity and magnetic field perturbations in Eqs. A.13 and A.14 are coupled by only certain terms, which allows to distinguish coupling and non-coupling contributions. First, considering only the non-coupling terms (i.e. neglecting the first and third terms

of Eq. A.13 and the right-hand side of Eq. A.14) one directly obtains a rotation of the background fluid at a frequency:

$$\omega_u = \frac{\chi}{\rho}\frac{m_p}{e}Q_{cr}\Omega_0 \tag{A.15}$$

and a rotation of the magnetic field perturbation at a frequency:

$$\omega_r = \frac{kj_{cr}}{Q_e} \tag{A.16}$$

Retaining only the coupling terms (i.e. neglecting the second term in the right-hand side of Eq. A.13 and the second term in the left-hand side of Eq. A.14) and in Fourier space, the equations become:

$$-i\omega\mathbf{u}_1 = i\frac{B_0 k}{\mu_0\rho}\mathbf{B}_1 - \frac{\chi}{\rho}\mathbf{j}_{cr}\times\mathbf{B}_1 \tag{A.17}$$

$$-i\omega\mathbf{B}_1 = i\chi B_0 k\mathbf{u}_1 \tag{A.18}$$

Rewriting as a function of the magnetic field perturbation yields:

$$i\frac{\omega^2}{B_0 k\chi}B_{1y} = i\frac{B_0 k}{\mu_0\rho}B_{1y} + \frac{\chi}{\rho}j_{cr}B_{1z} \tag{A.19}$$

$$i\frac{\omega^2}{B_0 k\chi}B_{1z} = i\frac{B_0 k}{\mu_0\rho}B_{1z} - \frac{\chi}{\rho}j_{cr}B_{1y} \tag{A.20}$$

By isolating ω one finds the dispersion relation of the non-resonant mode as:

$$\omega^2 = \chi\frac{n_m m_p}{\rho}k^2 v_{A0}^2 \pm \chi^2\frac{m_p}{e}\Omega_0\frac{kj_{cr}}{\rho} \tag{A.21}$$

One obtains an instability for $|k| < k_{\max}$ with:

$$k_{\max} = \frac{j_{cr}}{en_m}\frac{\Omega_0}{v_{A0}^2}\chi \tag{A.22}$$

The growth rate $\gamma(k)$ may then be obtained in the form:

$$\gamma(k) = \sqrt{\alpha k + \beta k^2} \tag{A.23}$$

Searching for an extremum of the growth rate yields the fastest growing wavenumber:

$$k_{\text{fast}} = -\frac{\alpha}{2\beta} = -\frac{1}{2}\frac{j_{cr}}{en_m}\frac{\Omega_0}{v_{A0}^2}\chi \tag{A.24}$$

which is half of the maximum unstable wavenumber. Inserting in the growth rate expression, one obtains the fastest growing mode for the non-resonant instability for arbitrary ions as:

$$\gamma_{\text{fast}} = \frac{1}{2}\frac{j_{cr}}{e}\frac{\Omega_0}{v_{A0}}\left(\frac{m_p\chi^3}{\rho n_m}\right)^{1/2} \tag{A.25}$$

In the range of wave numbers $|k| \ll k_{\max}$, the contribution of the first term in the right-hand side of Eq. A.13 corresponding to the magnetic tension can be neglected. The instability may then be described by the simplified system of equations:

$$\frac{\partial \mathbf{u}_1}{\partial t} = -\frac{\chi}{\rho}\mathbf{j}_{cr} \times \mathbf{B}_1 \tag{A.26}$$

$$\frac{\partial \mathbf{B}_1}{\partial t} = \chi(\mathbf{B}_0 \cdot \boldsymbol{\nabla})\mathbf{u}_1 \tag{A.27}$$

One obtains an exponential growth of the electromagnetic wave with a growth rate $\gamma(k)$ varying as $k^{1/2}$:

$$\gamma(k) \approx \left(j_{cr}|k|\Omega_0\frac{\chi^2}{\rho}\frac{m_p}{e}\right)^{1/2} \tag{A.28}$$

A lower limit for the unstable wave numbers can be obtained by considering the time $(|k|u_{cr})^{-1}$ for cosmic rays to cross one wavelength, which has to be smaller than the cyclotron period $(\frac{m_p}{m_{cr}}\frac{q_{cr}}{e}\Omega_0)^{-1}$. This gives the minimum k as:

$$k_{\min} = \frac{m_p}{m_{cr}}\frac{q_{cr}}{e}\frac{\Omega_0}{u_{cr}} \tag{A.29}$$

These results are further investigated in hybrid-PIC simulations in Sec. 5.2.3. The results in this appendix can be compared with the existing literature, which is focused on astrophysical applications where the streaming ions population is made of very tenuous and essentially protons cosmic rays. In this case $n_{cr}/n_e \ll 1$, $n_e \approx n_m$, $\chi \approx 1 - n_{cr}/n_m \approx 1$, $\rho \approx n_m m_p$ such that:

$$\gamma_{\text{cold}} = \frac{1}{2}\frac{n_{cr}}{n_m}\frac{u_{cr}}{v_{A0}}\Omega_0 \tag{A.30}$$

$$k_{\text{cold}} = -\frac{1}{2}\frac{n_{cr}}{n_m}\frac{u_{cr}}{v_{A0}^2}\Omega_0 \tag{A.31}$$

$$k_{\max} = \frac{n_{cr}}{n_m}\frac{u_{cr}}{v_{A0}^2}\Omega_0 \tag{A.32}$$

$$k_{\min} = \frac{\Omega_0}{u_{cr}} \tag{A.33}$$

and one recovers the existing linear theory results for a low temperature plasma.

A.2 Energy conservation, anisotropic heating

In the following, the pressure and heat flux terms will be neglected with respect to the terms involving the electromagnetic field. The conservation equation for the background plasma kinetic and internal energies can be expressed as:

$$\rho \frac{\mathrm{d}}{\mathrm{d}t}\left(\frac{u^2}{2}+U\right)=\mathbf{j}_b\cdot\mathbf{E} \tag{A.34}$$

where $\rho U = 3p/2$ with p the isotropic part of the pressure tensor, $\mathbf{j}_b = Q_m\mathbf{u}_m + Q_e\mathbf{u}_e = \boldsymbol{\nabla}\times\mathbf{B}/\mu_0 - \mathbf{j}_{cr}$ the background current and $\mathbf{j}_{cr} = Q_{cr}\mathbf{u}_{cr}$ the current carried by the ions cosmic rays. One may separate the internal and kinetic part of the energy conservation equation by calculating the kinetic energy conservation equation, which can be obtained from the background plasma momentum density conservation equation:

$$\rho\frac{\mathrm{d}\mathbf{u}}{\mathrm{d}t}=-\boldsymbol{\nabla}\cdot\mathbf{P}-Q_{cr}\mathbf{E}+\mathbf{j}_b\times\mathbf{B} \tag{A.35}$$

Multiplying this equation by *vecu* and neglecting the pressure gradients, one obtains the balance equation for the kinetic (directed) energy of the background as:

$$\rho\frac{\mathrm{d}}{\mathrm{d}t}\left(\frac{u^2}{2}\right)=-Q_{cr}\mathbf{E}\cdot\mathbf{u}+(\mathbf{j}_b\times\mathbf{B})\cdot\mathbf{u} \tag{A.36}$$

Subtracting Eq. A.36 from Eq. A.34, one obtains the conservation equation for the internal energy of the background fluid:

$$\rho\frac{\mathrm{d}U}{\mathrm{d}t}=\mathbf{E}\cdot(\mathbf{j}_b+Q_{cr}\mathbf{u})-(\mathbf{j}_b\times\mathbf{B})\cdot\mathbf{u} \tag{A.37}$$

The electromagnetic energy density conservation, neglecting the electric energy with respect to the magnetic energy, gives:

$$\frac{\partial}{\partial t}\left(\frac{B^2}{2\mu_0}\right)+\boldsymbol{\nabla}\cdot\left(\frac{\mathbf{E}\times\mathbf{B}}{\mu_0}\right)=-(\mathbf{j}_b+\mathbf{j}_{cr})\cdot\mathbf{E} \tag{A.38}$$

Finally the cosmic rays kinetic energy conservation equation reads:

$$\rho_{cr}\frac{\mathrm{d}}{\mathrm{d}t}\left(\frac{u_{cr}^2}{2}\right)=\mathbf{j}_{cr}\cdot\mathbf{E} \tag{A.39}$$

The sum of these conservation equations yields zero, which corresponds to the conservation of the total (kinetic, internal and electromagnetic) energy of the system. Using the electric field obtained from Ohm's law $\mathbf{E} = -\chi\mathbf{u}\times\mathbf{B} + (\chi-1)\mathbf{u}_{cr}\times\mathbf{B}$ (Eq. A.10), one obtains the intermediary relations:

$$\mathbf{E}\cdot\mathbf{j}_b=\chi\mathbf{u}\cdot\mathbf{F}_L+(1-\chi)\mathbf{u}_{cr}\cdot\mathbf{F}_L+\chi\mathbf{j}_{cr}\cdot(\mathbf{u}\times\mathbf{B}) \tag{A.40}$$

$$Q_{cr}\mathbf{E}\cdot\mathbf{u}=(\chi-1)\mathbf{u}\cdot(\mathbf{j}_{cr}\times\mathbf{B}) \tag{A.41}$$

$$\mathbf{E}\cdot\mathbf{j}_{cr}=-\chi\mathbf{j}_{cr}\cdot(\mathbf{u}\times\mathbf{B}) \tag{A.42}$$

$$(\mathbf{j}_b \times \mathbf{B}) \cdot \mathbf{u} = \mathbf{u} \cdot \mathbf{F}_L - \mathbf{u} \cdot (\mathbf{j}_{cr} \times \mathbf{B}) \tag{A.43}$$

where $\mathbf{F}_L = (\boldsymbol{\nabla} \times \mathbf{B}) \times \mathbf{B}/\mu_0$ is the Lorentz force. Reporting in the conservation equations gives:

$$\rho_{cr} \frac{\mathrm{d}}{\mathrm{d}t} \left(\frac{u_{cr}^2}{2} \right) = -\chi \mathbf{j}_{cr} \cdot (\mathbf{u} \times \mathbf{B}) \tag{A.44}$$

$$\rho \frac{\mathrm{d}}{\mathrm{d}t} \left(\frac{u^2}{2} \right) = \chi \mathbf{j}_{cr} \cdot (\mathbf{u} \times \mathbf{B}) + \mathbf{u} \cdot \mathbf{F}_L \tag{A.45}$$

$$\rho \frac{\mathrm{d}U}{\mathrm{d}t} = (\chi - 1) \mathbf{F}_L \cdot [\mathbf{u} - \mathbf{u}_{cr}] \tag{A.46}$$

$$\frac{\partial}{\partial t} \left(\frac{B^2}{2\mu_0} \right) + \boldsymbol{\nabla} \cdot \left(\frac{\mathbf{E} \times \mathbf{B}}{\mu_0} \right) = -\chi \mathbf{u} \cdot \mathbf{F}_L + (\chi - 1) \mathbf{u}_{cr} \cdot \mathbf{F}_L \tag{A.47}$$

with $\chi = -Q_m/Q_e$ defined positive.

Appendix B

Growth rate numerical measurement

The growth rates γ measured in Chapters 5 and 6 are obtained by calculating the norm of the perturbed magnetic field $\mathbf{B}_1 = \mathbf{B} - \mathbf{B}_0$, averaging the result over the simulation domain, and fitting an exponential function of the form $f(t) = Ae^{\gamma t}$ to the average perturbed magnetic field as a function of time. The fit is performed over the linear phase of the instability, which end is found by calculating the non-linear transition condition $k_{\min} = k_{\max}$.

This appendix presents a critical analysis of this method of growth rate measurement in the simulations. Indeed, care must be taken when comparing the fitted numerical growth rate to the analytical expressions of the non-resonant mode growth rate at the fastest growing wavenumber. This growth rate corresponds, by its very definition, to a monochromatic perturbation. Of course in the simulations all the spectrum of wavenumbers can develop, bounded by the spatial size and resolution used. Obtaining a growth rate for a specific wavenumber can be achieved by performing a Fourier transform of the perturbed magnetic field, and by selecting the negative helicity part of the spectrum associated to the non-resonant mode, as done in Sec. 5.2.4). The main advantage of this procedure is that a direct comparison with the linear theory results can potentially be made, however the results are sensitive to the numerical noise present in the simulations. This may render the growth rate measurement delicate, and may require prior filtering and smoothing, by convoluting the signal with a Gaussian for example, at the cost of physical accuracy. In addition to these numerical concerns, the physics of the non-resonant mode must also be taken into account when trying to compare numerical and analytical growth rates. The growth rate obtained in the linear theory does not take into account the reduction of the maximum unstable wavenumber with increasing magnetic field over time, nor the increase in minimum wavenumber. Consequently the growth rate should be measured during a short period of time, i.e. before being modified by the increasing magnetic pressure at small scales or the cosmic rays magnetization at large scales. The time period should be adjusted for each individual wavenumber for a given simulation. The period is a function of the growth rate, and can be short (of the order $\Delta t \sim 5\ \Omega_0^{-1}$) which increases the noise in the results.

An example of a measurement of the magnetic field growth rate is given in Figs. B.1 and B.2. The results presented are for a simulation with the parameters $n_{cr}/n_m = 0.01, u_{cr}/v_{A0} = 100$, $T_m = T_0$ and no collisions such that $\gamma_{cold} = 0.5\ \Omega_0$. The same problematic of growth rate measurement arises in simulations including collisions, being

with neutrals or among charged particles. The measured growth rate is given for a short time period of $t = 5\ \Omega_0^{-1}$ for the linear phase, together with the theoretical prediction (Eq. 2.2.3) as a function of the wavenumber. The "goodness" of the fit R^2 is also shown, calculated with the Pearson's test as $R^2 = \sum(f(t) - y)^2 / \sum(y - \bar{y})^2$ with $f(t)$ the fitting function, y the data and $\bar{y}$ the mean, and is an indicator of the quality of the numerical fit with $R^2 \to 0$ corresponding to a good fit with the data. The spectrum can be decomposed into three parts. Above $k = k_{\max}$ (rightmost dashed line), the signal is very noisy, and the R^2 is large indicating that the exponential fit is a bad approximation of the data, consistent with the fact that the non-resonant mode is stable above $k_{\max}$. The second part, corresponding to wave numbers $0.1\ l_0^{-1} < k < k_{\max}$, is well described by an exponential function, and fits well with the theoretical prediction. Finally the third part $k < l_0^{-1}$ is poorly described by an exponential, relative to the second part. Increasing the duration of the time period over which the fit is made to $t = 10\ \Omega_0^{-1}$, one obtains a reduced growth rate for $k = k_{\text{fast}}$ (Eq. 2.36) illustrating that those wavenumbers have started to saturate due to the increasing magnetic tension. This is in contrast to lower wavenumbers for which the growth rate remains very similar. In both cases, the exact value of the growth rate at a given wavenumber is noisy in the simulations, and varies with the fitting time window. Since there is no clear criteria to define the duration of this window, one could be tempted to choose the one that best fits the theoretical prediction, which contradicts the original goal of verifying theoretical results with simulations.

For this reason, growth rate measurements on a monochromatic perturbation of the non-resonant mode in the simulations can be misleading. In the work presented in this thesis, the growth rate measurements in the simulations have been obtained by studying space averaged quantities and over the entire linear phase, thus integrating over the whole k spectrum. Given the bell-shaped growth rate $\gamma(k)$, the measured growth rate is smaller than the maximum monochromatic value, by a factor ~ 2 for the parameters considered in the simulations, and represents an average growth rate over space and over the exponential phase.

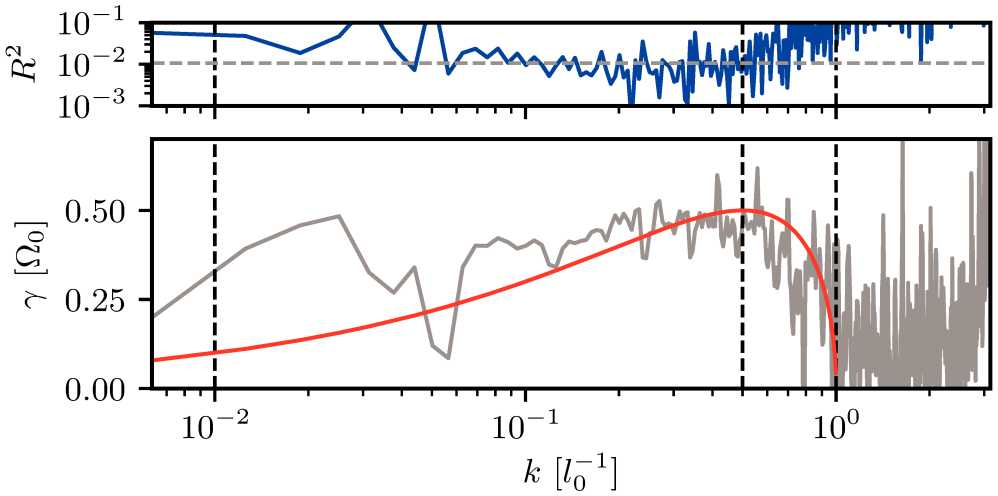

Figure B.1: *Upper panel*: "Goodness" R^2 of the numerical fitting with an exponential function, calculated with the Pearson's chi-squared test. The vertical dashed lines correspond, from left to right, to the minimum, fastest growing, and maximum unstable wavenumbers. The horizontal grey dashed line corresponds to R^2 at $k = k_{\rm fast}$, which is used as a reference for the relative goodness of the fit for other wavenumbers. *Lower panel*: Measured growth rate of the negative helicity component of the fourier transformed perturbed magnetic field (grey line) and fluid linear theory prediction (red line), as a function of the wavenumber k for a time period for the linear phase of $\Delta t = 5\ \Omega_0^{-1}$.

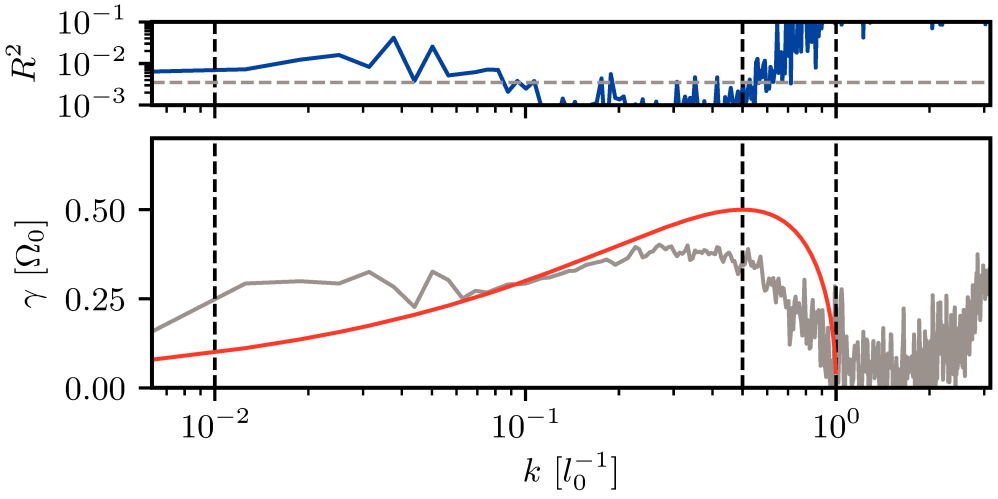

Figure B.2: Same as Fig. B.1 while considering a time period for the linear phase of $\Delta t = 10\ \Omega_0^{-1}$.

List of figures

List of tables

RÉSUMÉ

Les rayons cosmiques peuvent alimenter la croissance exponentielle d'un champ magnétique préexistant en déclenchant des instabilités qui grandissent grâce au mouvement de dérive collectif des particules. Parmi les différentes instabilités de dérive, le mode non-résonnant, aussi appelé mode de Bell, a fait l'objet d'une attention croissante car il peut amplifier le champ magnétique au-delà de son intensité initiale, et génère la turbulence nécessaire pour aider au confinement et à à accélération des rayons cosmiques. De manière générale, il peut se développer dans une grande variété d'environnements, allant des nuages moléculaires froids et denses au milieu intergalactique chaud et diffus. Cette thèse vise à élucider le comportement de l'instabilité non-résonante de dérives des rayons cosmiques dans de tels environnements, où les effets thermiques peuvent modifier considérablement sa croissance et sa saturation. Dans les environnements plus froids et plus denses, comme les régions H II et les nuages moléculaires, les collisions entre particules dans le plasma ambiant doivent également être prises en compte. Nous étudions numériquement leur impact en incluant dans les simulations avec une méthode Monte-Carlo les collisions proton-proton et proton-hydrogène. La dernière partie de cette thèse est consacrée à la conception d'expériences dédiées à la vérification des prédictions de la théorie linéaire et des simulations. Nous décrivons les conditions requises sur les paramètres du plasma pour générer l'instabilité dans une expérience, et proposons deux configurations possibles basées sur les installations laser haute puissance existantes, en visant à observer et caractériser le mode non-résonant pour la première fois en laboratoire.

MOTS CLÉS

instabilités - plasmas - rayons cosmiques

ABSTRACT

Cosmic rays can power the exponential growth of a seed magnetic field by exciting instabilities that feed on the kinetic energy of the particles collective streaming motion. Of the different streaming instabilities, the non-resonant mode, also called Bell's mode, has received growing attention as it can amplify the magnetic field well beyond its initial intensity, and generate the necessary turbulence to help confine and accelerate cosmic rays in supernovae remnants and young stellar jets shocks via the first order Fermi mechanism. In general, it can develop in a large variety of environments, ranging from the cold and dense molecular clouds to the hot and diffuse intergalactic medium. This work aims at elucidating the behaviour of the non-resonant cosmic rays streaming instability in such environments, where thermal effects can substantially modify its growth and saturation. In colder and denser environments, such as H II regions and molecular clouds, particle collisions in the background plasma must also be taken into account. We investigate numerically their impact by including Monte-Carlo Coulomb and neutral collisions in the simulations. The final part of this thesis is devoted to answer the growing need for an experimental verification of the linear theory and simulations predictions. We describe the requirements on the plasma parameters to generate the instability in an experiment, and propose two possible setups based on existing high-power laser facilities, aiming at observing and characterizing the non-resonant mode for the first time in the laboratory.

KEYWORDS

instabilities - plasmas - cosmic rays